Uptake and release of cargo molecules from responsive surfaces

MERCIER, CELINE,LUCIE

Uptake and release of cargo molecules from responsive surfaces

A thesis submitted in partial fulfilment of the requirements for the degree of Doctor of Philosophy in the University of Durham by,

Céline L. Mercier

Department of Chemistry

University of Durham

2018

Abstract

The development of smart surfaces is of interest for a wide range of applications such as drug-delivery, anti-fouling and lubrication. These layers are stimuli-responsive enabling the controlled uptake and release of a cargo molecule. The aim of this work is to develop methods for monitoring such processes in thermoresponsive systems. To do so, it is required to produce responsive surfaces and design methods to probe their responsiveness as well as the binding of cargos.

I present synthetic strategies to graft poly(*N*-isopropylacrylamide) (pNIPAM), a pNIPAM-based diblock copolymer and polyvaline from silica substrates as well as a procedure for generating mixed surfactant layers of didodecyldimethylammonium bromide (DDAB), and deuterated sodium dodecylsulfate (d-SDS) with defined composition. The main technique for investigating these films is Total Internal Reflection (TIR) Raman spectroscopy. This chemically specific and surface selective technique allows the monitoring of phase transitions inside the layers. It also provides insight on the accumulation of cargo molecules or changes in the layers' composition. A novel Raman imaging technique provides insight into the uniformity of the layers and cargo distribution within them.

First, I studied the potential of the cationic surfactant DDAB to transport the anionic surfactant d-SDS onto a silica surface. I show that the adsorption was possible only when the mixture is on the cationic side implying the electrostatic interactions between the vesicles and the surface govern the adsorption. Once the coadsorption had taken place, I triggered the gel-liquid phase transition of DDAB in order to induce a phase separation on the surface. No preferential desorption of d-SDS was observed.

Second, I looked at grafted pNIPAM at the silica-water interface and present data on the phase transition showing a change in the hydration of the polymer. I then introduce three cargo molecules — benzamide, d-malonamide and potassium thiocyanate — which have the potential to bind onto one state of pNIPAM via hydrophobic interactions, hydrogen bonding or specific ion interactions. TIR Raman spectroscopy was shown to be able to detect small quantities of the molecules but ultimately showed no selective binding.

Third, the focus shifts to grafted polyvaline layers since they are less hydrophobic than pNIPAM. I determine the secondary structure of the grafted chains and present the impact of temperature. All adsorption measurements with the cargo molecules introduced in the previous chapter showed no selective binding.

Fourth, I report on a diblock copolymer with an inner cationic block poly((2-dimethylamino) ethyl methacrylate) (pDMAEMA) and an outer neutral thermoresponsive block, pNIPAM. The copolymer was thermoresponsive. Cargo adsorption measurements showed accumulations of each molecule inside the film. The electrostatics-driven adsorption of KSCN was stronger at higher temperatures.

Acknowledgments

I would like to thank my supervisor Prof. Colin Bain for his mentoring and support over the years and from whom I tried to learn as much as I could.

I would like to acknowledge the European Commission for funding through a Marie Curie scholarship. I am grateful to Dr. Imre Varga (Eötvös Loránd University, Budapest) and Dr. Eric Tyrode (KTH, Stockholm) for guidance and useful discussions. Additional thanks to Dr. Eric Tyrode for helping me getting started in surface science (rinse[20]) a long time ago, as well as initiating the work on the multiangle model during my time in his group.

Special thanks must go to Dr. David Johnson for his precious help in polymer synthesis. I would also like to thank Prof. Karl Coleman for letting me use the equipment of his lab. I appreciate the help I have received from the machinists and glassblowers in the Department of Chemistry for building and repairing the custom apparatus I used throughout this work.

Furthermore, I would like to thank my examiners, Dr. Simon Titmuss and Dr. Eckart Wrede, for their helpful comments and suggestions.

I would like to thank the Bain group members – past and present. A special thank you to Dr. Lisong Yang for her kindness and unique combination of creativity and optimism. A particular mention goes to my friends and colleagues Andy, Antoine, Ceyla, David, Marie-Capucine and Mario for adventures in and out of the lab. Special mentions to MC for our regular scientific discussions and our friendship, and to Mario for teaching me how to code, align optics or tune up a computer fan, all in an *ordentliche* manner. Thanks to Anne, David and Fanny for their friendship over the years.

I would like to thank my family for their encouragement whenever I was staring into the void during my PhD, while secretly hoping they'll never have to read the result of it.

Finally, a special thanks must go to Mario for his support and good humour, which softened most of my bitterness.

À ma Pilou,

Ich pflege Fragen dadurch zu lösen, daß ich mich von ihnen auffressen lasse.

— Franz Kafka

List of abbreviations

AFM	atomic force microscopy
APTAC	3-acrylamidopropyl trimethylammonium chloride
APTMS	aminopropyltrimethoxysilane
ATR-FTIR	attenuated total reflection Fourier-transform infrared spectroscopy
ATRP	atom transfer radical polymerisations
BSA	bovine serum albumin
CAC	critical aggregation concentration
CD	circular dichroism
CF	carboxyfluorescein
CIPAAm	2-carboxyisopropylacrylamide
CMC	critical micelle concentration
CTAB	cetyl trimethylammonium bromide
CTAT	cetyl trimethylammonium tosylate
DDA	didocyldimethylamine
DDAB	didodecyldimethylammonium bromide
DFT	density functional theory
DMAEMA	(2-dimethylamino)ethyl methacrylate
DMF	*N*,*N*-dimethylformamide
DODAB	dioctadecyldimethylammonium bromide
DOPC	1,2-dioleoyl-*sn*-glycero-3-phosphocholine
DOPS	1,2-dioleoyl-*sn*-glycero-3-phospho-L-serine
DSC	differential scanning calorimetry
d-SDS	deuterated sodium dodecylsulfate
DTAB	dodecyltrimethylammonium bromide
EMA	ethyl acrylamide
FIB	human fibrogen
FJC	freely-jointed chain
FRC	freely rotating chain
FWHM	full width at half maximum
GPC	gel permeation chromatography
HMTETA	1,1,4,7,10,10-hexamethyltriethylenetetramine
IPA	ion-pair amphiphile
IPN	interpenetrating polymer network
IRSE	infrared-spectroscopic ellipsometry
LCST	lower critical solution temperature
Me_6TREN	tris(2-dimethylaminoethyl)amine
NCA	*N*-carboxyanhydrid
NIPAM	*N*-isopropylacrylamide
NMA	*N*-methylacetamide
pAA	poly(acrylic acid)
pBMA	poly(n-butyl methacrylate)
pDEAA	poly(*N*,*N*-diethylacrylamide)
pDMAEMA	poly((2-dimethylamino) ethyl methacrylate)

pEG	polyethylene glycol
pEO	poly(ethylene oxide)
pGMA	poly(glycidyl methacrylate)
PMDETA	N,N,N',N'',N''-pentamethyldiethylenetriamine
pMMA	poly(methyl methacrylate)
pNIPAM	poly(N-isopropylacrylamide)
pNIPMAM	poly(N-isopropylmethacrylamide)
pOEGMA	poly(oligo(ethylene glycol) methacrylate)
pSBMA	poly(sulfobetaine methacrylate)
QCM-D	quartz microbalance with dissipation
SDBS	sodium dodecylbenzenesulfonate
SDS	sodium dodecylsulfate
SEC	size exclusion chromatography
SFA	surface force apparatus
SLB	solid-supported lipid bilayer
SOS	sodium octyl sulfate
TBAF	tetrabutylammonium fluoride
TIR	total internal reflection
uHP	ultra high purity
XPS	X-ray photoelectron spectroscopy

Copyright notice

Contents

Chapter 1: Introduction

1.1 Motivation and aims

This project is part of the Marie Curie Initial Training Network NanoS3 (standing for "Smart, Small and Soft"), a network which assembles eight academic groups and two industrial partners. This project aims at increasing collaboration between research teams with complementary knowledge in polymer synthesis, self-assembly and surface science. The NanoS3 network aims at delivering a design guide for soft nanoparticles and at providing characterisation methods for their behaviour in bulk and at interfaces. A polymer nanoparticle consists of polymer chains assembled in structures of one or a couple of hundreds of nanometres in diameter. The development of simple polymer nanoparticles has already triggered several recent breakthroughs (*e.g.* delivery vehicles and contrast agents for magnetic resonance imaging). Nevertheless, there is a need for more complex structures able to deliver more functionalities.[1] Polymer nanoparticles have been studied intensively over the last two decades as they have the potential to deliver complex responses required for drug delivery, lubrication and clean tech applications.

Recent achievements in polymer chemistry have opened the way to create more sophisticated objects which can achieve more advanced performances. The strategy chosen by this network is to produce nanoparticles of polymers with a hierarchical structure, with the aim of adding the functionality of each group to the final structure. A typical design comprises a core loaded with a potential active agent — a cargo —, a protective shell to compartmentalise the core, and often an outer shell to control the surface chemistry of the particle and improve stability. Only the bulk characterisation of these nanoparticles is routinely done. A chemically selective technique (^{1}H NMR for instance) confirms the proportion of the different blocks, gel permeation chromatography or light scattering characterise the hydrodynamic size of the nanoparticles and the phase transition is monitored by turbidity or rheology measurements at different temperatures.[1,2,3] If these techniques give a good insight on the polymer aggregates on average, they do not reveal the dynamic structure which is often key to an effective delivery.

The successful delivery of a cargo molecule relies on the fulfilment of several requirements. Firstly, the control of the hydrodynamic diameter [1] or the surface chemistry [4,5] is critical. Delivery systems for biological applications such as drug delivery or targeted imaging require a careful control over the size distribution and surface charge. They need to be big enough to not be filtered out by the kidney and to remain in the blood stream long enough to access the targeted cells. Secondly, the kinetics of the delivery needs to be controlled for a long lasting effect while avoiding any overdoses. Polymer self-assemblies remain stable at lower concentrations than *e.g.* surfactants and have been used as stable vehicles which alter the kinetics of delivery by physically reducing the rate of diffusion. Another strategy to control the kinetics of delivery consists of designing a stimulus-responsive or smart nanoparticle. The polymer chains of smart nanoparticles will change conformation in a sharp and selective manner. Typical stimuli include a change in temperature, pH or ionic strength.

The NanoS3 network furthermore aims at characterising polymers and their assemblies at interfaces. Theoretical descriptions of model chains at interfaces were developed some 30 years ago, namely the scaling theory of De Gennes and Alexander. Experimental studies, however, are still ongoing. The NanoS3 network aims at using the most advanced techniques available for describing soft matter at interfaces to observe polymers adsorbed (physisorbed) or grafted (chemically bound) to an interface and assess whether their functionalities and responsiveness are modified by their structure onto a surface.

The aim of my project is to develop a method to assess the potential of nanoparticles to uptake and release a cargo molecule. To do so, I have designed the synthetic strategies required to grow polymers from surfaces. I have then used a surface selective spectroscopy technique — total internal reflection (TIR) Raman spectroscopy — to probe the polymer layers and investigate their interactions with cargo molecules. Raman spectroscopy allows the identification of chemicals by their vibrational spectra. Surface selectivity was achieved through total internal reflection illumination where an evanescent field selectively probes materials close to the surface. In addition to giving insight on how the nanoparticles will behave once attached or adsorbed onto a surface, this work can also be applicable to particles if they are large enough so that their surface can be locally considered as flat. This is true when the particle radius is much larger than the radius of gyration of a single polymer chain inside the particle. This work will give a proof of principle of both, the synthetic procedures as well as the analytical techniques, for the development of the first generation of polymer nanoparticles within the NanoS3 network.

1.2 Thesis outline

This thesis is structured as follows. The introduction, this first chapter, covers a range of subjects to provide the background for the work presented in this thesis. Polymers at interfaces are covered as the first topic. This includes an overview of the scaling theory of neutral, charged and grafted polymer chains. The section concludes with a brief review of experimental techniques for the study of grafted polymer layers.

The thermodynamics of the uptake and release of cargo molecules from films are covered in the next part of this chapter. This explanation is followed by a review of existing delivery systems and characterisation methods. The basics of optics are introduced in the last part of this chapter. The explanations include reflection and refraction of light at interfaces leading to a description of total internal reflection. Together with an introduction to Raman scattering at the end of the first chapter, these descriptions will explain the principles behind TIR Raman spectroscopy.

Chapter 2 contains a description of the experimental and synthetic methods employed in this thesis. The chapter starts with a description of TIR Raman spectroscopy and Raman imaging. The section on the former technique furthermore includes a model developed to determine the thickness of polymer layers at the solid-water interface. The next part introduces techniques employed for the characterisation of polymers, namely ellipsometry, circular dichroism spectroscopy and gel permeation chromatography. The final part of chapter 2 describes the synthetic and preparative methods used for this thesis. This includes the preparation of mixed surfactant solutions as well as different methods for coating surfaces with polymers.

Experimental results and their discussion are presented in the next chapters. Chapter 3 looks at the transport of an anionic surfactant (and deuterated sodium dodecylsulfate (d-SDS)) by vesicles of a cationic surfactant (didodecyldimethylammonium bromide (DDAB)) onto a negatively charged surface. The chapter starts with a review on surfactant assembly and a comparison to liposomes. The results section presents the coadsorption of oppositely charged surfactants as well as the impact of temperature on the mixed layer. Chapter 4 shifts the focus to polymers grafted from silica. The chapter contains the work on poly(*N*-isopropylacrylamide) (pNIPAM) at the silica-water interface and starts off with a discussion on the phase diagram of pNIPAM as well as a review on pNIPAM films. The results section includes the band assignment of the Raman spectrum and presents the impact of temperature on the polymer film. Following a discussion of three types of binding that can lead to the association of polymer and cargo, three cargo molecules are introduced. The interactions between the polymer brush and those molecules are shown at the end of the chapter. Chapter 5 contains work on polyvaline films grafted from fused silica at the silica-water interface. The beginning of the chapter gives an overview on the published work on polyvaline and polyaminoacids. The following results section includes the temperature response of the polymer as well as its interactions with the cargo molecules introduced in the previous chapter. Chapter 6 summarises the work done on a grafted layer of a diblock copolymer made of an inner cationic block (poly((2-dimethylamino) ethyl methacrylate) (pDMAEMA)) and an outer block of pNIPAM. The chapter first gives a review on pDMAEMA and on the work done on grafted copolymer layers. Results on the temperature response of the layer as well as its interactions with the cargo molecules are also reported.

1.3 Polymers at interfaces

Several delivery systems studied in this work are grafted polymer layers. pNIPAM and polyvaline are polyamides, and neutral in aqueous solutions. The diblock copolymer has a polyelectrolyte core. In this section, I will therefore describe the behaviour of neutral polymers and polyelectrolytes in solutions before getting into their grafted versions.

1.3.1 Neutral polymer solutions

This section provides the basics of a theoretical description of neutral polymers in solution. A polymer can be described as a chain of N segments or bonds. Each bond can be expressed as a bond vector $\mathbf{r}_\mathrm{i}$ with $i = 1, ..., N$. For the whole chain, the end-to-end vector, $\mathbf{R}$, can be defined as the sum of all vectors, $\mathbf{r}_\mathrm{i}$:

$$\mathbf{R} = \sum_{i=1}^{N} \mathbf{r}_\mathrm{i} \tag{1.1}$$

Flexible polymer chains contain a very large number of degrees of freedom. In addition to the translational and rotational degrees of freedom also found in particles and molecules, flexible polymer chains can adopt a large number of conformations. A statistical description of the chain conformation is therefore required. The mean square end-to-end distance for all possible conformations is:

$$\langle \mathbf{R^2} \rangle = \sum_{i=1}^{N} \sum_{j=1}^{N} \langle \mathbf{r}_\mathrm{i} \cdot \mathbf{r}_j \rangle \tag{1.2}$$

This expression can be rewritten by introducing the angle between two segments, ϑ,

$$\langle \mathbf{R^2} \rangle = a^2 \sum_{i=1}^{N} \sum_{j=1}^{N} \langle \cos \vartheta_{ij} \rangle \tag{1.3}$$

a is defined as $|\mathbf{r}_\mathrm{i}|$ and the term $\langle \cos \vartheta_{ij} \rangle$ refers to the correlation between the segments.

Freely-jointed chain (FJC) model

The freely-jointed chain model or ideal chain is the simplest description of a flexible polymer (see figure 1.1).

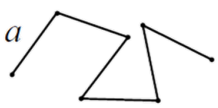

Figure 1.1: Freely-jointed chain (FJC) model where N bonds of length a form a flexible chain. Reproduced with permission from reference [6].

In this model, segments do not interact with each other or with the solvent. There is therefore no correlation between the segments, and the cross term, $\langle \mathbf{r}_j \cdot \mathbf{r}_k \rangle$, is null for $j \neq k$. The mean square end-to-end distance is then

$$\langle \mathbf{R^2} \rangle = Na^2 \tag{1.4}$$

and consequently $R \propto N^{1/2}$.

No preferential orientation is adopted by the different links and the chain follows a random walk. The set of conformations of the polymer chain resembles the trajectory of a freely diffusing particle and the end-to-end distance shows a Gaussian distribution. It is then possible to calculate the free energy, F, of the ideal polymer chain:[6]

$$\frac{F}{k_\mathrm{B}T} = \frac{R^2}{a^2 N} \tag{1.5}$$

with k_B is the Boltzmann constant and T the temperature in Kelvin. Equation 1.5 shows that an ideal polymer chain behaves like a spring. If the polymer chain is stretched beyond its mean end-to-end distance, R, there is a force that brings it back to its random walk size. The force constant is $2/a^2N$ (in $k_\mathrm{B}T$ units). This normalised restoring force is independent of the temperature, showing that it is a purely entropic effect.

Real chains can be described with the FJC model if a, also referred to as the Kuhn length, is adjusted carefully. a is always related to the monomer size but not identical to it.

Freely rotating chain (FRC) model

In this model, conformations are restricted by bonds of fixed length b and fixed bond angle while torsional rotations are permitted (see figure 1.2).

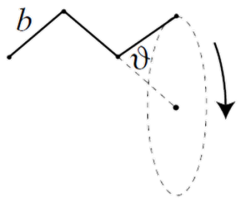

Figure 1.2: Freely-rotated chain (FRC) model where N bonds of lengths b have a fixed bond angle ϑ. The position of the further nearest neighbours are correlated to account for the chemistry of the bond. Reproduced with permission from reference [6].

Torsional rotations are described with the torsion angle ϑ. This model is closer to real synthetic polymers than the previous one. The correlation term does not vanish in this model and is $\langle \mathbf{r}_j \cdot \mathbf{r}_{j+1} \rangle = b^2 \cos\vartheta$ for neighbouring bonds. Correlations are thus transmitted through the chain leading to the general correlation term $\langle \mathbf{r}_j \cdot \mathbf{r}_k \rangle = b^2(\cos\vartheta)^{|j-k|}$.[7] The mean square end-to-end distance for infinitely long chains is given by[7]

$$\langle \mathbf{R^2} \rangle = Nb^2 \frac{1+\cos\vartheta}{1-\cos\vartheta} \tag{1.6}$$

The introduction of the correlation term has not modified the scaling relation with the bond length ($R \propto N^{0.5}$). The mean square end-to-end distance is, however, larger than in the FJC model since $\frac{1+\cos\vartheta}{1-\cos\vartheta} > 1$.

Interactions with a solvent

The free energy of a chain in a solvent is the sum of an entropic contribution associated with stretching the chain (equation 1.5) and an enthalpic contribution. The latter contribution accounts for the monomer-monomer and the monomer-solvent interactions. It will not be possible to treat each pairwise interaction to estimate the free energy of a chain in a solvent. A much simpler approach has been proposed by Flory to account for all the interactions on a monomer using a mean-field treatment.[8] Following this approach, the enthalpic contribution, $F_{\text{int}}/k_{\text{B}}T$, is described with interaction parameters by introducing the virial coefficients:

$$\frac{F_{\text{int}}}{k_{\text{B}}T} \simeq \nu_2 R^3 \left(\frac{N}{R^3}\right)^2 + \nu_3 R^3 \left(\frac{N}{R^3}\right)^3 + ... \tag{1.7}$$

A solvent is considered a good solvent if the interactions between the monomers are repulsive and $\nu_2 > 0$. It follows that

$$\frac{F}{k_{\text{B}}T} \simeq \frac{R^2}{a^2 N} + \nu_2 R^3 \left(\frac{N}{R^3}\right)^2 \tag{1.8}$$

The optimal radius minimising the free energy can be expressed as

$$R \sim a(\nu_2/a^3)^{1/5} N^{3/5} \tag{1.9}$$

For a good solvent, the radius of the polymer coil thus scales with $N^{3/5}$. In situations where there are no additional interactions between monomers other than the pure hard-core interactions, the second virial coefficient corresponds to the excluded volume, $\nu_2 = a^3$, giving $R \sim aN^{3/5}$.

Solvents are considered bad or poor when interactions between monomers are attractive ($\nu_2 < 0$) and are balanced by the third virial term which is assumed to be repulsive ($\nu_3 > 0$). It follows that:

$$\frac{F}{k_{\text{B}}T} \simeq \frac{R^2}{a^2 N} + \nu_2 R^3 \left(\frac{N}{R^3}\right)^2 + \nu_3 R^3 \left(\frac{N}{R^3}\right)^3 \tag{1.10}$$

The first term can be neglected for a poor solvent. The optimum radius scales with:

$$R \sim (\nu_2/\nu_3)^{1/3} N^{1/3} \tag{1.11}$$

The third case, where $\nu_2 = 0$, is the theta condition where monomer-monomer interactions on one hand and monomer-solvent interactions on the other cancel out the steric repulsion. The polymer then behaves like an ideal chain where

$$R \sim N^{1/2} \tag{1.12}$$

In summary, the radius of a polymer scales with N^{ν} where ν depends on the goodness of the solvent. A good solvent ($\nu = 3/5$) will overcome the attraction between monomers and swells the chain. In a poor solvent ($\nu = 1/3$), however, the attractive forces dominate and the radius shrinks compare to the ideal chain ($\nu = 1/2$).

1.3.2 Charged polymer chains

A polyelectrolyte is a polymer where a fraction, f, of its monomers are charged. The fraction of charge can, for example, be controlled by the pH of the solution. The polyelectrolyte can be described by its charge density, τ, defined as f/b, and its contour length, L. Polyelectrolytes are usually stiffer than neutral polymers due to the long-range electrostatic interactions between the monomers. Unlike neutral polymers, which will often show ideal-chain behaviour, polyelectrolytes adopt a rigid rod-like conformation. The stiffness of the chain can be described by the persistence length, ℓ_0, which is defined as the length over which two vectors on the chains are correlated.[6] In addition, polyelectrolytes tend to be more swollen than their neutral counterparts due to an electrical double layer. The characteristic thickness of this double layer, the Debye length, κ^{-1}, is a function of the salt concentration, c_{salt}, and the Bjerrum length, ℓ_{B}:

$$\kappa^{-1}(\text{nm}) = (8\pi z^2 \ell_{\text{B}} c_{\text{salt}})^{-1/2} \tag{1.13}$$

where z is the charge. The Bjerrum length characterises the medium and defines the distance at which Coulomb interactions of two charged units match the thermal energy. It is about 0.7 nm in water at room temperature.

For systems where $\tau(\ell_{\text{B}}\ell_0)^{1/2} < 1$ the electrostatic repulsion between two segments is smaller than the thermal energy, the polyelectrolyte chains cannot extend and the polymer remains in a collapsed configuration. On the other hand, electrostatic chain repulsion leads to an extension of the chains when $\tau(\ell_{\text{B}}\ell_0)^{1/2} > 1$. The polyelectrolytes can show three distinct scaling ranges in this regime depending on the contour length, L, and the effective persistence length, ℓ_{eff}. ℓ_{eff} is related to the bare persistence length, ℓ_0, by

$$\ell_{\text{eff}} = \ell_0 + \frac{\ell_{\text{B}}\tau^2}{4\kappa^2} \tag{1.14}$$

For short polyelectrolytes where $L \ll \ell_{\text{eff}}$, self avoidance is not relevant due to the short chain length, and R scales with L. In the case of long chains where $L \gg \ell_{\text{eff}}$, interactions can be again treated as a virial expansion. Similarly to neutral polymers, the free energy can be expressed as the sum of two terms:[6]

$$\frac{F}{k_{\text{B}}T} \simeq \frac{R^2}{\ell_{\text{eff}}L} + \nu_2 R^3 \left(\frac{L/\ell_{\text{eff}}}{R^3}\right)^2 \tag{1.15}$$

The first term of equation 1.15 corresponds to the elastic energy associated with entropy, while the second term denotes the virial expansion of the electrostatic inter-

actions. Above the critical contour length $\ell_{\text{eff}}^3/\nu_2^2$, the optimal radius is given by

$$R \sim (\nu_2/\ell_{\text{eff}})^{1/5} L^{3/5} \tag{1.16}$$

This condition is not met in elongated or highly charged polyelectrolytes. Chain lengths are then in an intermediate range and the radius scales with

$$R \sim \ell_{\text{eff}}^{1/2} L^{1/2} \tag{1.17}$$

1.3.3 Grafted polymer chains

Polymers can be chemically or physically bound onto a surface. The conformation then depends not only on the interactions with the solvent but also on the grafting density and interactions with the substrate.

The simplest description of a grafted polymer brush is a step-like monomer density profile. The layer has a height, h, which is a function of the length of the polymer, N, the grafting density, ρ, and the quality of the solvent. The neighbouring distance, $\rho^{-1/2}$, is defined as the distance between two neighbour chains on the surface. At low grafting density, — when the neighbouring distance is low compared to the radius, R — chains will have minimal interactions with each other. This is the mushroom regime (see figure 1.3a). Above a critical grafting density the chains start to overlap. In good solvent conditions, the monomers will repel each other and the chain will extend away from the surface (see figure 1.3b). This is the brush regime.

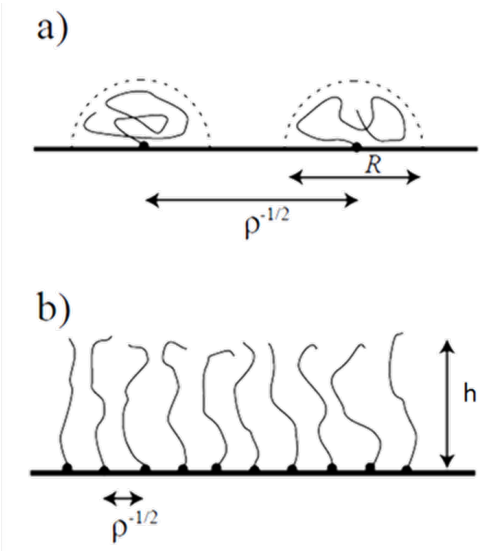

Figure 1.3: Typical structure of a grafted polymer layer in the mushroom regime a) and in the brush regime b). In the mushroom regime, polymer chains do not interact with their neighbours since the distance between two chains is large compared to their radius, R. In the brush regime, the polymer chains stretch out of the plane due to inter-chain repulsions. Reproduced with permission from reference [6].

Similarly to the bulk description, scaling laws can be obtained using the Flory description. In a good solvent, the optimal brush height, h, scales with $N\rho^{1/3}$. This scaling law implies that, at constant grafting density, the height of the brush grows

linearly with the number of monomers. In comparison, an ideal chain scales with $N^{0.5}$. The brush height also depends on the grafting density, ρ. In a poor solvent, h scales with $N\rho$ while $h \sim N\rho^{1/2}$ for a theta solvent. It thus follows that a decrease in solvent quality can impact the height of a grafted polymer and, ultimately, lead to a collapse of the brush. This behaviour is dependent on the grafting density where higher densities will lead to a weaker collapse.

A different framework is provided by self-consistent field calculations and molecular simulations. These techniques do not just provide information on the height of the polymer layer but also give insights into the density profiles. Lei *et al.* calculated the inner structure of grafted polymer brushes for a range of parameters.[9] Figure 1.4 shows their results on the impact of grafting density on the polymer profile. At low grafting densities, the brushes show a parabolic distribution of segment ends with respect to the distance from the surface. The profile becomes more step-like with increasing grafting density. Parabolic profiles have previously been observed experimentally in grafted polymer brushes.[10,11]

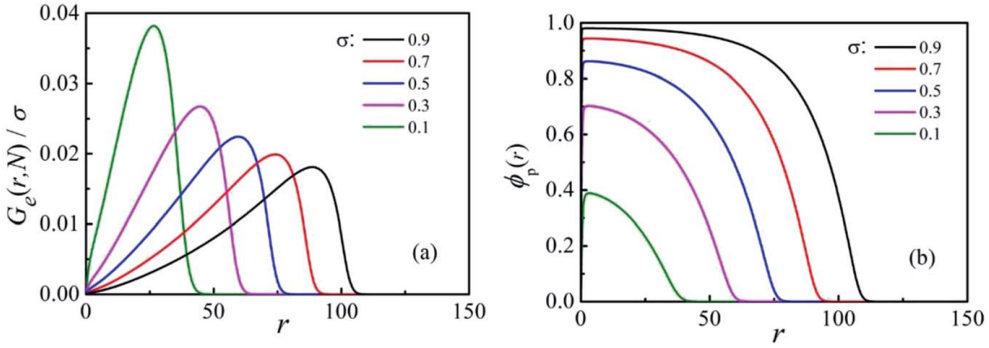

Figure 1.4: Normalised distributions of chain free ends, G_e, over the normalised grafting density, σ, and polymer volume fraction profiles, ϕ_p over the height above substrate, r, for brushes of various grafting densities (0.1, 0.3, 0.5, 0.7 and 0.9) on a planar surface. Data is obtained using self-consistent field calculations. Reproduced with permission from reference [9].

1.3.4 Experimental methods for studying grafted polymer layers

The list of experimental techniques presented here is not exhaustive and this review will cover the most common ones in soft matter science for characterising polymers at interfaces. This review will focus on grafted rather than adsorbed polymer layers. Polymer adsorption at the air–liquid interface or the solid–liquid interface has received a lot of attention but is beyond the scope of this thesis.

Ellipsometry Ellipsometry is a popular tool for the characterisation of films at interfaces. It is fast and local. It can be used for characterising polymer brushes grafted with a typical length scale of 10s to 100s of nm, as the typical incident wavelength is 633 nm (HeNe laser). In short, a laser beam is incident onto the sample at a defined

angle. The reflected light is collected and its polarisation parameters determined. Models can be fitted to the data to access film thicknesses and refractive indices. A more detailed explanation is given in section 2.3.

Measurements are commonly carried out on dry polymer films. For example, Jones and co-workers used this technique to investigate the impact of initiator density on the grafting of poly(methyl methacrylate) and poly(glycidyl methacrylate) (pGMA) brushes on gold.[12] Liu *et al.* used ellipsometry in their work on grafted pGMA layers to measure thickness and grafting density gradients.[13] In addition, most of the research presented in the remainder of this section also includes ellipsometry measurements.

Additional approaches have been developed over the years to carry out *in situ* ellipsometry measurements. Kostruba *et al.* used ellipsometry to study the properties of poly(*N*-isopropylacrylamide) (pNIPAM) brushes grafted from silane-terminated glass substrates and the impact of grafting time on the brush thickness.[14] Ellipsometry measurements of the dry polymer films gave access to properties such as the film thickness and its refractive index. In addition, they employed a modified version of their ellipsometer to measure the temperature-dependent chain collapse *in situ*. They attached glass window-terminated tubes on the polariser and analyser arms allowing their immersion in water. It was thus possible to deliver the laser beam to the glass substrate located at the bottom of a water-filled cuvette.

A different approach was reported by Habicht *et al.* in 1999 who studied the temperature-dependent swelling of a grafted polystyrene brush.[15] The polymer brush was grafted from a high-refractive-index glass prism and brought in contact with cyclohexane. The laser beam was incident through the side of the glass prism and reflected at the glass-polymer-cyclohexane interface and collected with the analyser arm of the ellipsometer after exiting the other side of the prism. Through this technique, they were able to study how the decrease of the solvent quality of cyclohexane with temperature impacts the brush thickness. Decreasing solvent quality was shown to lead to a continuous collapse of the brush towards the glass surface.

Ellipsometry was used in this work to measure the thickness of grafted polymer layers and is described in more detail in section 2.3.

Neutron Reflectometry A complementary technique to ellipsometry is neutron reflectometry. By directing a beam of collimated neutrons onto a surface and counting the collected neutrons as a function of the angle of incidence, neutron reflectometry gives access to the reflectivity profile of a surface with a very high spatial resolution. The data is then fitted by various layer models and the best fit is extracted. The wavelength of the probe is in the order of magnitude of an Ångström and so is the spatial resolution in the direction perpendicular to the surface. This technique is very popular and powerful tool for the study of thin films at interfaces.

Neutron reflectometry has been used to study ultrathin films of polymer-coated solid–liquid interfaces. Ghoussoub *et al.* have used neutron reflectometry to observe the growth of a polyelectrolyte onto the surface. Layers of poly(diallyldimethyl-

ammonium) and poly(styrenesulfonate) were successively deposited and held together by electrostatic forces between both polymers and screened by an added counterion acetate. The radio-labelled acetate was found to be uniformly distributed in the polymer film.[16] A similar study by Lösche *et al.* showed that the thickness of a poly(styrenesulfonate) and poly(allylamine hydrochloride) film made by layer-by-layer deposition increased with the number of layers until reaching an equilibrium thickness. The thickness of the film could be tuned with the ionic strength.[17] Neutron reflectometry was also used at the air-liquid interface of polydimethylsiloxane solutions to measure the density of polymer chains inside the film.[18]

Neutron reflectometry was not the method of choice for this project since it requires a neutron source. This limits the number of measurements that can be carried out which can be a challenge for new projects where synthetic and experimental parameters have not been optimised yet. The low time resolution effectively limits experiments to equilibrated or slowly varying systems and makes it difficult to follow the kinetics of polymerisation on the time scales of minutes. Neutron reflectometry does not have the spatial resolution necessary to determine whether the film is homogeneous. Small features would be averaged out and not be detected during the measurement.

QCM-D Quartz microbalance with dissipation (QCM-D) is a popular tool for measuring the mass of molecules or material attached to a quartz crystal in a liquid environment. The mass is determined via changes in the resonant frequency of the crystal. In addition, QCM-D is monitoring the energy dissipation factor and is therefore able to determine viscoelasticity of the attached film. In the past, this technique has been used to study the swelling and collapse of grafted polymer layers at a solid-liquid interface,[19,20] where it delivered information on the hydration of the polymer as well as its rigidity. Dunér *et al.* showed that this technique is also suitable for investigating kinetic processes by following the growth of polymer brushes *in situ* with a time resolution of about 1 second.[21]

While QCM-D has been shown to be useful for the study of grafted polymer films it will not be suitable for the investigation of cargo binding and release processes. The technique will not allow the direct detection of cargo molecules. Changes in the resonant frequency and the energy dissipation alone would not be sufficient for determining if and how cargo binds to a polymer brush.

Surface force apparatus The surface force apparatus (SFA) for the direct measurement of molecular forces, has first been developed by Tabor and Winterton,[22] and later improved by Israelachvili and Adams.[23] The instrument consists of two mica surfaces in a crossed-cylinder configuration. Sensitive force-measuring springs detect the interactions between the surfaces while the separation distance is measured optically through interference fringes. This sensitive technique allows force measurements down to $\sim$1 nN with a distance resolution in the Ångström region.[24,25]

The SFA is mainly used to investigate coated and adsorbed polymer films since

the surface is limited to mica. Sheth and Leckband, however, used the SFA to study the interactions between poly(ethylene glycol), grafted onto lipid bilayers, and the protein streptavidin.[26] A polymer-terminated lipid bilayer was formed on one mica surface and the protein was adsorbed to a lipid bilayer on the other mica surface. Their investigation revealed repulsive forces at low compressive loads. Attractive forces, however, were detected at high loads when the proteins were pushed into the polymer layer. This attraction was found to be high enough that the separation of the two surfaces led to removal of polymers from their supporting membrane.

An example of coated polymer films is the work of Zhang *et al.* who investigated the molecular interactions of the comb-type polymer polystyrene-*g*-poly(ethylene oxide).[27] Mica surfaces were spin-coated with the polymer to measure its interactions in NaCl solutions as well as air. Belder and co-workers used the SFA to study the adsorption of various polystyrene/poly(2-vinylpyridine) block copolymers on mica.[28] The polymers were dissolved in toluene which is a good solvent for the polystyrene and a bad solvent for the poly(2-vinylpyridine) block. By varying the size of the adsorbing poly(2-vinylpyridine) block, referred to as "anchor block", they were able to control the surface density of the adsorbed polymer. Except for the highest surface densities, the adsorbed layers were found to form mushroom-like profiles. Brushlike layers were formed for the highest densities although it was not possible to form true brushes.

Although SFA is a very sensitive technique for the study of molecular forces of thin films, it is not suitable for the work presented in this thesis. The lack of chemical information means that the study of interactions between grafted polymer brushes and cargo molecules would rely purely on changes in the interactions between the two substrates. Interactions between polymer-grafted surfaces, however, are not the subject of this research. The limitation of mica as the substrate material might furthermore introduce challenges for the grafting-from process.

AFM Atomic force microscopy (AFM) is a technique where the sample is scanned with a sharp tip attached to a cantilever spring. The AFM provides information on the sample thickness, its mechanical properties as well as surface forces through force-distance measurements.[24,25] Kidoaki *et al.* utilised this technique to study the temperature-dependent structural changes of pNIPAM grafted to glass substrates at different grafting densities.[29] Thickness and force-distance measurements were carried out at 25 °C and 40 °C and showed the collapse of the polymer layer at high temperatures. The thickness of the layer at high temperature was found to be one-half to one-fourth of the values measured for 25 °C. They furthermore detected an increase in the film thickness with grafting density confirming that higher densities lead to the expected extension of the polymer chains.

AFM furthermore allows the study of interactions between surfaces and colloidal particles. Yamamoto *et al.* attached hydrophobic silica spheres to AFM probes and successfully measured the interaction forces between the spheres and poly(methyl methacrylate) (pMMA) brushes grafted from silicon substrates.[30] Their results also showed that a higher grafting density leads to an extension of the polymer chains

and thus to an increase in the film thickness. Their results further showed that high-density brushes were more resistant to compression than low-density brushes.

In 2008, Kelley *et al.* published their work on poly(2-vinylpyridine)-polystyrene brushes adsorbed to mica where they compared the results of force-distance measurements obtained through AFM and SFA.[31] Overall, SFA force-distance profiles where found to be steeper than the AFM data which was thought to be caused by the AFM tip splaying the polymer chains. Interestingly, the AFM data showed a bimodal distribution of the force-distance results which was consistent with the topographical images that showed areas of high and low polymer density. Their results thus raise questions regarding the interpretation of SFA data. They note that such data might conventionally be interpreted using models based on homogeneous brushes although the layer might in practice be heterogeneous. Atomic force microscopy, however, allows the measurement of brush heterogeneity on a $\sim$10 nm length scale and might consequently be more suitable fo heterogeneous systems.

AFM measurements can be used to determine the thickness of grafted polymer layers at, both, the solid-air and solid-water interface. Beyond that, the technique would be of limited use for this project since it does not deliver chemical information. Due to the inability to directly confirm polymer-cargo binding, the main application of the AFM in this project would be the determination of the polymer brush thickness. In this work, such measurements were carried out using ellipsometry.

ATR-FTIR Spectroscopy Attenuated total reflection Fourier-transform infrared spectroscopy (ATR-FTIR) is a surface-selective measurement technique where, similarly to total internal reflection Raman spectroscopy, the sample is illuminated by an evanescent wave. An infrared beam is send through an ATR crystal where it undergoes total internal reflection at the crystal-sample interface. Depending on the design of the crystal, multiple reflections are possible increasing signal quality. The beam is sent to a detector after exiting the crystal. This technique has been utilised successfully to characterise grafted polymers in a range of applications including membrane functionalisation[32,33] and the fabrication of cell sheets.[34,35,36]

ATR-FTIR is a surface-selective and chemically-specific technique for the study of processes at interfaces. Due to the strong IR-absorption of water, measurements at the solid-water interface result in spectra with strong water signals. As a consequence, spectra of polymers at this interface would be dominated by the water background, reducing the detection limit and potentially swamping weak cargo signals.

Degrafting Another interesting approach is called degrafting, where a polymer is detached from the surface it was grafted from. The polymer can be degrafted by, *e.g.*, attacking the bond between the substrate and the surface initiator. Degrafted polymer layers are subsequently analysed like bulk-initiated polymers would be. Patil *et al.* used this technique to study PMMA brushes grafted from silica substrates.[37] Following the characterisation of the grafted brush using X-ray photoelectron spectroscopy (XPS), ellipsometry and contact angle measurements, the polymer was degraf-

ted using tetrabutylammonium fluoride (TBAF). TBAF attacks the Si-O bonds which anchor the polymer to the surface and was used as an alternative to hydrofluoric acid. The free polymer chains were then analysed using size exclusion chromatography. This technique gives access to properties such as the molecular weight distribution and, if the area of the substrate is known, the grafting density. Degrafting can thus give valuable insight into the characteristics of the polymer chains that might otherwise not be accessible when the chains are bound to the substrate. It is however necessary to be able to degraft polymers from a large surface area in order to obtain a sufficient amount of material for analysis.

Degrafting is an invasive technique that has the potential to give access to information on parameters such as grafting density and polymer weight. It does not allow *in situ* studies on the interactions of the polymer with its surroundings. This technique is thus not suitable for investigations such as this work that focus on interactions between the grafted brush and cargo molecules.

1.4 Uptake and release of cargo molecules from films

1.4.1 Thermodynamic description

The association of a cargo molecule with a nanoparticle or a polymer film is characterised with a binding constant K_{binding}. This constant reflects the potential of interaction between a carrier and a cargo molecule at a given temperature, pH, cargo concentration and polymer density at equilibrium. The binding constant is then defined as

$$K_{\text{binding}} = \frac{k_{\text{a}}}{k_{\text{d}}} = \frac{[\text{polymer-cargo}]_{\text{eq}}}{[\text{polymer}][\text{cargo}]_{\text{eq}}} \tag{1.18}$$

where k_{a} and k_{d} are the association and dissociation rate constants, respectively. K_{binding} thus denotes the equilibrium of the two reactions, shown as a schematic representation in figure 1.5. In the case of a polymer film, an effective binding constant $K^{\text{eff}}_{\text{binding}}$ can be defined as the ratio of the concentrations of bound to free cargo molecules at equilibrium:

$$K^{\text{eff}}_{\text{binding}} = \frac{[\text{cargo}_{\text{bound}}]_{\text{eq}}}{[\text{cargo}_{\text{free}}]_{\text{eq}}} \tag{1.19}$$

$$[\text{polymer}] + [\text{cargo}] \underset{k_{\text{a}}}{\overset{k_{\text{d}}}{\rightleftharpoons}} [\text{polymer-cargo}]$$

Figure 1.5: Schematic representation of the association of a cargo molecule to a polymer forming a complex polymer-cargo. The association is an equilibrium with an association and a dissociation reaction.

The successful uptake and release of a cargo molecule from a polymer layer relies on the carrier's ability to change its binding affinity with the cargo. In the ideal scenario, the polymer exhibits two distinct states: one state where $k_{\text{a}} \gg k_{\text{d}}$ favouring the association of polymer and cargo, and a second state where $k_{\text{a}} \ll k_{\text{d}}$ and the cargo is released. The switch between the states might be triggered through changes

in parameters such as temperature, pH and ionic strength. Throughout this work, temperature changes are used as the trigger in the investigated systems.

Binding between carrier and cargo can be due to a range of interactions. Typical interactions involved in the work presented here are hydrophobic and electrostatic interactions as well as hydrogen bonding. Binding occurs if these interactions are attractive enough to overbalance the entropic penalty of burying the cargo molecule in the polymer layer.

1.4.2 Literature review

Delivery systems Several delivery strategies involving the release of cargo from films are under consideration for biomedical applications. Liposomes, or lipid vesicles, are popular system for forming protective shells around hydrophobic drugs.[38] The vesicles can be coated with polyethylene glycol (pEG) to extent their retention time in the body. Due to the non-targeted delivery, only a fraction of the liposomes end up reaching the targeted area. This approach, called passive targeting, can be applied in cancer treatments since cancerous cells are well irrigated by blood vessel. Targeted delivery can be achieved by covering the surface of the liposomes with more active substances such as antibodies or ligands which can react to hormones.

pNIPAM is an interesting candidate for the use in drug delivery systems due to its phase transition temperature close to the human body temperature. For example, Zhang *et al.* designed magnetic microcapsules of chitosan and pNIPAM to encapsulate and release sodium salicylate as a model cargo.[39] Polystyrene beads were used as a template for deposited chitosan from which pNIPAM was grafted. Iron ions were adsorbed onto the particles before the polystyrene core was removed through repeated washes with tetrahydrofuran and water. The capsules are magnetic and can therefore be transported towards a target organ easily through the application of an external magnetic field. They are pH and temperature responsive due to the chitosan and pNIPAM block, respectively. The particles were then loaded with sodium salicylate by immersing them in a solution of sodium salicylate for 48 h. The subsequent release was diffusion limited with a diffusion coefficient tunable through pH and temperature. Half-times were ranging from 2 to 5 hours.

Kroning and co-workers investigated the protein-adsorbing and -repelling properties of a range of responsive polymer brushes.[40] The systems they investigated included poly(*N*-isopropylacrylamide) and poly(acrylic acid) (pAA) brushes grafted to pGMA-coated (poly(glycidyl methacrylate)) silicon wafers as pNIPAM-pGMA block-copolymers. The researchers employed *in situ* infrared-spectroscopic ellipsometry (IRSE) to study the adsorption of human serum albumin (HSA) and human fibrogen (FIB) onto the model surfaces. The thermoresponsive pNIPAM and pNIPAM-pGMA brushes showed a consistently repelling behaviour when exposed to HSA and FIB, respectively. This protein-repellent characteristic was observed for the swollen and collapsed states of the brushes. The pH-responsive pAA brushes, however, showed a different behaviour. Time-dependent IRSE measurements showed the adsorption of HSA at ph 5 and confirmed the stability of pAA-HSA when exposed to protein-free

solutions of a similar pH. Raising the pH to 7 lead to a controlled desorption of the proteins until nearly 90 % of HSA had desorbed. Throughout the adsorption and desorption processes, IRSE revealed no changes in the amide I and II bands of HSA that are highly sensitive towards changes its secondary structure. This shows that the protein's structure was not altered upon adsorption.

Characterisation methods The uptake and release of cargo molecules from a polymer film or a soft nanoparticle can be followed either directly or indirectly. An example for indirect measurements on nanoparticles is dynamic light scattering [41] which measures a change in the particle's diameter during loading and release. This technique is not chemically specific but nevertheless an effective method for studying cargo release from nanoparticles. UV/vis spectroscopy is a chemically specific alternative that measures depletion in the solution. [42] Aliquots are taken from the solution at different times and cargo concentrations are determined *ex situ*. Methods for the case of films on planar substrates include ATR-IR spectroscopy, neutron reflectometry and QCM-D measurements which have been reviewed in section 1.3.4 above.

In this thesis, I am studying the interactions between polymers grafted from planar substrates and cargo molecules mainly using TIR Raman spectroscopy. This is a chemical specific, surface selective and quantitative technique that allows *in situ* measurements of processes at the solid-water interface.

1.5 Optics

1.5.1 Reflection and refraction at interfaces

This section contains a description of reflection and refraction at an interface using the electromagnetic approach. Through Snell's law and the subsequent derivation of the Fresnel equations, we will be able to calculate the relative amplitudes of the incident, reflected and transmitted rays. I will also describe the case of total internal reflection and the impact on the electric field at the interface. Knowledge of these processes is important for understanding the principle behind TIR Raman spectroscopy which has been the main tool for the work presented in this thesis. The equations derived in this section will furthermore allow us to understand the origin of the relative scattered intensities generated by the different polarisation combinations. To start with, we consider an interface as shown in figure 1.6. This figure defines the coordinate system used for the remainder of this section. The incident monochromatic light wave can be expressed as: [43]

$$\mathbf{E}_{\mathrm{i}} = \mathbf{E}_{0\mathrm{i}} e^{i(\mathbf{k}_{\mathrm{i}} \cdot \mathbf{r} - \omega_{\mathrm{i}} t)} \,. \tag{1.20}$$

The initial electric field vector, $\mathbf{E}_{0\mathrm{i}}$, is assumed to be constant, and gives the orientation of the initial field and the amplitude of the wave. $\mathbf{k}$ is the propagation vector with the magnitude $2\pi/\lambda$ giving the direction of the incident light and ω is the angular frequency given by $2\pi/\tau$. The time period, τ, is defined as $\tau = \lambda/v$ where v is the velocity. The velocity itself can be expressed as $v = c/n$. The reflected and

transmitted waves can be expressed similarly as

$$\mathbf{E}_\mathrm{r} = \mathbf{E}_{0\mathrm{r}} e^{i(\mathbf{k}_\mathrm{r}\cdot\mathbf{r}-\omega_\mathrm{r}t+\phi_\mathrm{r})} \tag{1.21}$$

and

$$\mathbf{E}_\mathrm{t} = \mathbf{E}_{0\mathrm{t}} e^{i(\mathbf{k}_\mathrm{t}\cdot\mathbf{r}-\omega_\mathrm{t}t+\phi_\mathrm{t})}\,, \tag{1.22}$$

respectively. ϕ_r and ϕ_t are introduced as phase constants relative to $\mathbf{E}_\mathrm{i}$ since the position of the origin is not unique.

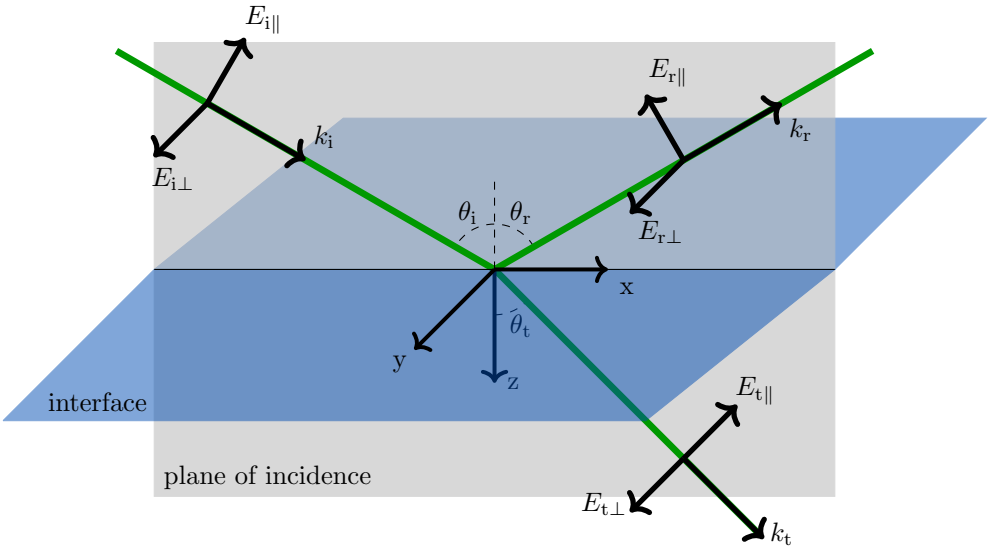

Figure 1.6: Schematic representation of reflection and refraction at an interface showing the direction of the parallel and perpendicular components of the electric field vectors as well as the direction of the propagation vectors.

The laws of electromagnetic theory dictate multiple boundary conditions, one of which being that the total tangential component of the electric field, $\mathbf{E}$, must be equal across the interface. Consequently

$$\hat{\mathbf{u}} \times \mathbf{E}_\mathrm{i} + \hat{\mathbf{u}} \times \mathbf{E}_\mathrm{r} = \hat{\mathbf{u}} \times \mathbf{E}_\mathrm{t}\,, \tag{1.23}$$

where $\hat{\mathbf{u}}$ is the unit vector normal to the interface. This relationship can be expressed as

$$\hat{\mathbf{u}} \times \mathbf{E}_{0\mathrm{i}} e^{i(\mathbf{k}_\mathrm{i}\cdot\mathbf{r}-\omega_\mathrm{i}t)} + \hat{\mathbf{u}} \times \mathbf{E}_{0\mathrm{r}} e^{i(\mathbf{k}_\mathrm{r}\cdot\mathbf{r}-\omega_\mathrm{r}t+\phi_\mathrm{r})} = \hat{\mathbf{u}} \times \mathbf{E}_{0\mathrm{t}} e^{i(\mathbf{k}_\mathrm{t}\cdot\mathbf{r}-\omega_\mathrm{t}t+\phi_\mathrm{t})}\,, \tag{1.24}$$

which must be true at any time and at all points on the interface. As a consequence, $\mathbf{E}_\mathrm{i}$, $\mathbf{E}_\mathrm{r}$ and $\mathbf{E}_\mathrm{t}$ must share the same dependence on t and r. The time-dependent terms are thus identical giving

$$\omega_\mathrm{i} = \omega_\mathrm{r} = \omega_\mathrm{t}\,, \tag{1.25}$$

while the constrained spatial variation leads to

$$(\mathbf{k}_\mathrm{i}\cdot\mathbf{r}) = (\mathbf{k}_\mathrm{r}\cdot\mathbf{r}+\phi_\mathrm{r}) = (\mathbf{k}_\mathrm{t}\cdot\mathbf{r}+\phi_\mathrm{t})\,. \tag{1.26}$$

This expression can be transformed into two equations giving the relative phases of the reflected and transmitted waves:

$$(\mathbf{k}_\mathrm{i} - \mathbf{k}_\mathrm{r}) \cdot \mathbf{r} = \phi_\mathrm{r} \,, \tag{1.27a}$$

$$(\mathbf{k}_\mathrm{i} - \mathbf{k}_\mathrm{t}) \cdot \mathbf{r} = \phi_\mathrm{t} \,. \tag{1.27b}$$

These two equations define a plane swept out by the endpoint of $\mathbf{r}$ perpendicular to $\mathbf{k}_\mathrm{i} - \mathbf{k}_\mathrm{r}$ and $\mathbf{k}_\mathrm{i} - \mathbf{k}_\mathrm{t}$ which is the interface. The incident and reflected waves are in the same medium and consequently the magnitude of the incident and reflected wave vectors are identical, $k_\mathrm{i} = k_\mathrm{r}$. Since $\mathbf{k}_\mathrm{i} - \mathbf{k}_\mathrm{r}$ has no component in the plane of the surface, defined as $\hat{\mathbf{u}} \times (\mathbf{k}_\mathrm{i} - \mathbf{k}_\mathrm{r}) = 0$, we can conclude that

$$k_\mathrm{i} \sin\theta_\mathrm{i} = k_\mathrm{r} \sin\theta_\mathrm{r} \,, \tag{1.28}$$

leading to the law of reflection:

$$\theta_\mathrm{i} = \theta_\mathrm{r} \,. \tag{1.29}$$

Similarly, following on from equation 1.27b, $\mathbf{k}_\mathrm{i} - \mathbf{k}_\mathrm{t}$ is also normal to the interface and parallel to $\hat{\mathbf{u}}$ giving

$$k_\mathrm{i} \sin\theta_\mathrm{i} = k_\mathrm{t} \sin\theta_\mathrm{t} \,. \tag{1.30}$$

The media on both sides of the interface are different and consequently $k_\mathrm{i} \neq k_\mathrm{t}$. However, since $\omega_\mathrm{i} = \omega_\mathrm{t}$ (see equation 1.25) both sides can be multiplied with c/ω_i to finally give Snell's law:

$$n_\mathrm{i} \sin\theta_\mathrm{i} = n_\mathrm{t} \sin\theta_\mathrm{t} \,. \tag{1.31}$$

1.5.2 Fresnel equations

In the previous section, I have shown the relationships between the phases of the three waves $\mathbf{E}_\mathrm{i}$, $\mathbf{E}_\mathrm{r}$ and $\mathbf{E}_\mathrm{t}$. We can now investigate the connection between the amplitudes of the incident, reflected and transmitted waves, $\mathbf{E}_{0\mathrm{i}}$, $\mathbf{E}_{0\mathrm{r}}$ and $\mathbf{E}_{0\mathrm{t}}$, respectively. As above, we consider a plane monochromatic wave incident at the interface between between two isotropic media. We can separate the $\mathbf{E}$ and $\mathbf{B}$ fields of the wave into components that are parallel and perpendicular to the plane of incidence. This allow us to express any polarisation of the incident wave as a linear combination of those two orthogonal polarisations. In the first case, we assume that $\mathbf{E}$ is perpendicular to the plane of incidence and $\mathbf{B}$ parallel to it. Since $E = vB$,

$$\hat{\mathbf{k}} \times \mathbf{E} = v\mathbf{B} \tag{1.32}$$

follows and since $\mathbf{k}$ is perpendicular to $\mathbf{E}$

$$\hat{\mathbf{k}} \cdot \mathbf{E} = 0. \tag{1.33}$$

The propagation vector $\hat{\mathbf{k}}$, $\mathbf{E}$ and $\mathbf{B}$ are thus forming a right-handed system (see figure 1.6). The boundary condition of the continuity of the tangential electric field

applies again, giving

$$\mathbf{E}_{0\mathrm{i}} + \mathbf{E}_{0\mathrm{r}} = \mathbf{E}_{0\mathrm{t}} \,. \tag{1.34}$$

There is no such continuity of the component normal to the electric filed. However, the normal component of the product of $\epsilon\mathbf{E}$ — ϵ being the permittivity of the medium — is the same on both sides of the interface. In a similar fashion, the normal component of the magnetic field $\mathbf{B}$ and the tangential component of $\mu^{-1}\mathbf{B}$ — μ being the permeability of the medium — are continuous across the interface. Through this continuity of the tangential component, also referred to as the magnetic intensity vector $\mathbf{H}$, we can write that

$$-\frac{B_\mathrm{i}}{\mu_\mathrm{i}}\cos\theta_\mathrm{i} + \frac{B_\mathrm{r}}{\mu_\mathrm{r}}\cos\theta_\mathrm{r} = -\frac{B_\mathrm{t}}{\mu_\mathrm{t}}\cos\theta_\mathrm{t} \,. \tag{1.35}$$

Following on from equation 1.32 we obtain

$$B_\mathrm{i} = E_\mathrm{i}/v_\mathrm{i} \,, \tag{1.36a}$$

$$B_\mathrm{r} = E_\mathrm{r}/v_\mathrm{r} \,, \tag{1.36b}$$

$$B_\mathrm{t} = E_\mathrm{t}/v_\mathrm{t} \,. \tag{1.36c}$$

Since the incident and reflected waves are in the same medium, $\mu_\mathrm{i} = \mu_\mathrm{r}$, $v_\mathrm{i} = v_\mathrm{r}$ and $\theta_\mathrm{i} = \theta_\mathrm{r}$, allowing us to substitute the above expressions into equation 1.35 to obtain

$$\frac{1}{\mu_\mathrm{i} v_\mathrm{i}}(E_\mathrm{i} - E_\mathrm{r})\cos\theta_\mathrm{i} = \frac{1}{\mu_\mathrm{t} v_\mathrm{t}} E_\mathrm{t}\cos\theta_\mathrm{t} \,. \tag{1.37}$$

We can further simplify this expression as we know that E_i, E_r and E_t must have the same time dependence:

$$\frac{n_\mathrm{i}}{\mu_\mathrm{i}}(E_{0\mathrm{i}} - E_{0\mathrm{r}})\cos\theta_\mathrm{i} = \frac{n_\mathrm{t}}{\mu_\mathrm{t}} E_{0\mathrm{t}}\cos\theta_\mathrm{t} \tag{1.38}$$

Combining this expression with equation 1.34 yields the Fresnel equations for the reflected and transmitted light:

$$\left(\frac{E_{0\mathrm{r}}}{E_{0\mathrm{i}}}\right)_\perp = \frac{\frac{n_\mathrm{i}}{\mu_\mathrm{i}}\cos\theta_\mathrm{i} - \frac{n_\mathrm{t}}{\mu_\mathrm{t}}\cos\theta_\mathrm{t}}{\frac{n_\mathrm{i}}{\mu_\mathrm{i}}\cos\theta_\mathrm{i} + \frac{n_\mathrm{t}}{\mu_\mathrm{t}}\cos\theta_\mathrm{t}} \,. \tag{1.39}$$

$$\left(\frac{E_{0\mathrm{t}}}{E_{0\mathrm{i}}}\right)_\perp = \frac{2\frac{n_\mathrm{i}}{\mu_\mathrm{i}}\cos\theta_\mathrm{i}}{\frac{n_\mathrm{i}}{\mu_\mathrm{i}}\cos\theta_\mathrm{i} + \frac{n_\mathrm{t}}{\mu_\mathrm{t}}\cos\theta_\mathrm{t}} \,. \tag{1.40}$$

The subscript $\perp$ highlights that these equations are valid when $\mathbf{E}$ is perpendicular to the plane of incidence. We can further simplify the above equations for dielectric materials where $\mu_\mathrm{i} \approx \mu_\mathrm{r} \approx \mu_\mathrm{t}$. This transformation returns the common forms of those two Fresnel equations

$$r_\perp = \left(\frac{E_{0\mathrm{r}}}{E_{0\mathrm{i}}}\right)_\perp = \frac{n_\mathrm{i}\cos\theta_\mathrm{i} - n_\mathrm{t}\cos\theta_\mathrm{t}}{n_\mathrm{i}\cos\theta_\mathrm{i} + n_\mathrm{t}\cos\theta_\mathrm{t}} \tag{1.41}$$

and

$$t_\perp = \left(\frac{E_{0\mathrm{t}}}{E_{0\mathrm{i}}}\right)_\perp = \frac{2n_\mathrm{i}\cos\theta_\mathrm{i}}{n_\mathrm{i}\cos\theta_\mathrm{i} + n_\mathrm{t}\cos\theta_\mathrm{t}} \,. \tag{1.42}$$

$r_\perp$ and $t_\perp$ denote the amplitude reflection coefficient and amplitude transmission coefficient, respectively. It is possible to further simplify the expressions using Snell's Law giving

$$r_\perp = -\frac{\sin(\theta_\mathrm{i} - \theta_\mathrm{t})}{\sin(\theta_\mathrm{i} + \theta_\mathrm{t})} \tag{1.43}$$

and

$$t_\perp = \frac{2\sin\theta_\mathrm{t}\cos\theta_\mathrm{i}}{\sin(\theta_\mathrm{i} + \theta_\mathrm{t})}\,. \tag{1.44}$$

We can derive the Fresnel equations for light polarised parallel to the plane of incidence in a similar manner. From the boundary conditions of the continuity of the electric field it follows that

$$E_{0\mathrm{i}}\cos\theta_\mathrm{i} - E_{0\mathrm{r}}\cos\theta_\mathrm{r} = E_{0\mathrm{t}}\cos\theta_\mathrm{t}\,. \tag{1.45}$$

The continuity of the tangential component of $\mu^{-1}\mathbf{B}$ across the interface consequently leads to

$$\frac{1}{\mu_\mathrm{i} v_\mathrm{i}} E_{0\mathrm{i}} + \frac{1}{\mu_\mathrm{r} v_\mathrm{r}} E_{0\mathrm{r}} = \frac{1}{\mu_\mathrm{t} v_\mathrm{t}} E_{0\mathrm{t}}\,. \tag{1.46}$$

Similar to the previous case, we can now use the fact that $\mu_\mathrm{i} = \mu_\mathrm{r}$ and $\theta_\mathrm{i} = \theta_\mathrm{r}$ to arrive at the Fresnel equations for light where $\mathbf{E}$ is parallel to the plane of incidence.

$$\left(\frac{E_{0\mathrm{r}}}{E_{0\mathrm{i}}}\right)_\parallel = \frac{\frac{n_\mathrm{t}}{\mu_\mathrm{t}}\cos\theta_\mathrm{i} - \frac{n_\mathrm{i}}{\mu_\mathrm{i}}\cos\theta_\mathrm{t}}{\frac{n_\mathrm{i}}{\mu_\mathrm{i}}\cos\theta_\mathrm{t} + \frac{n_\mathrm{t}}{\mu_\mathrm{t}}\cos\theta_\mathrm{i}} \tag{1.47}$$

$$\left(\frac{E_{0\mathrm{t}}}{E_{0\mathrm{i}}}\right)_\parallel = \frac{2\frac{n_\mathrm{i}}{\mu_\mathrm{i}}\cos\theta_\mathrm{i}}{\frac{n_\mathrm{i}}{\mu_\mathrm{i}}\cos\theta_\mathrm{t} + \frac{n_\mathrm{t}}{\mu_\mathrm{t}}\cos\theta_\mathrm{i}} \tag{1.48}$$

The subscript $\parallel$ indicates the polarisation the equations are valid for. As above, we can simplify the expressions for dielectric materials giving

$$r_\parallel = \left(\frac{E_{0\mathrm{r}}}{E_{0\mathrm{i}}}\right)_\parallel = \frac{n_\mathrm{t}\cos\theta_\mathrm{i} - n_\mathrm{i}\cos\theta_\mathrm{t}}{n_\mathrm{i}\cos\theta_\mathrm{t} + n_\mathrm{t}\cos\theta_\mathrm{i}} \tag{1.49}$$

and

$$t_\parallel = \left(\frac{E_{0\mathrm{t}}}{E_{0\mathrm{i}}}\right)_\parallel = \frac{2n_\mathrm{i}\cos\theta_\mathrm{i}}{n_\mathrm{i}\cos\theta_\mathrm{t} + n_\mathrm{t}\cos\theta_\mathrm{i}}\,. \tag{1.50}$$

Further simplifications using Snell's law finally lead to the amplitude reflection and amplitude transmission coefficients

$$r_\parallel = \frac{\tan(\theta_\mathrm{i} - \theta_\mathrm{t})}{\tan(\theta_\mathrm{i} + \theta_\mathrm{t})} \tag{1.51}$$

and

$$t_\parallel = \frac{2\sin\theta_\mathrm{t}\cos\theta_\mathrm{i}}{\sin(\theta_\mathrm{i} + \theta_\mathrm{t})\cos(\theta_\mathrm{i} - \theta_\mathrm{t})}\,, \tag{1.52}$$

respectively.

1.5.3 Total internal reflection

Let us now imagine a system where the incident medium is of a higher optical density than the transmission medium and thus $n_\mathrm{i} > n_\mathrm{t}$. Based on the amplitude reflection coefficients we derived in the previous section, we know that gradually increasing θ_i will increase $r_\perp$ and $r_\parallel$, and consequently decrease $t_\perp$ and $t_\parallel$. Snell's law moreover dictates that $\theta_\mathrm{t} > \theta_\mathrm{i}$. The transmitted ray therefore gradually approaches tangency with the interface as θ_i increases. At some point $\theta_\mathrm{t} = 90°$ and all available energy appears in the reflected beam. Figure 1.7 shows this change in the amplitude reflection coefficients for a silica–water interface. Since $\sin\theta_\mathrm{t} = 1$ we can use Snell's law to calculate this value of θ_i for which $\theta_\mathrm{t} = 90°$, known as the critical angle θ_c:

$$\theta_\mathrm{c} = \sin^{-1}\left(\frac{n_\mathrm{t}}{n_\mathrm{i}}\right) \tag{1.53}$$

Above this critical angle, all incident energy is reflected back into the incident medium. This process is called total internal reflection.

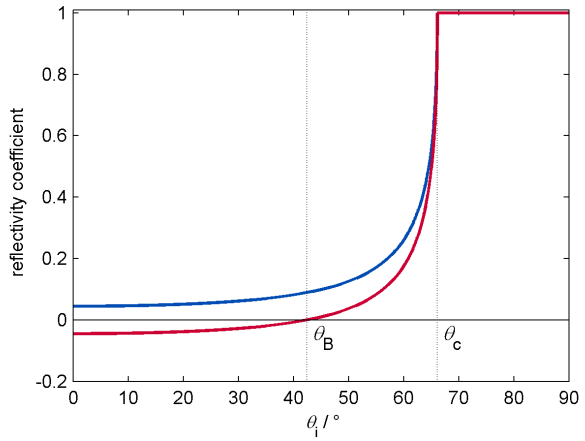

Figure 1.7: Amplitude reflection coefficient for perpendicular (blue line) and parallel (red line) polarised light as a function of incident angle, θ_i, for the internal reflection at the silica–water interface ($n_\mathrm{i} = 1.461$, $n_\mathrm{t} = 1.336$). No parallel polarised light is reflected at the Brewster angle, θ_B, and all light is reflected above the critical angle, θ_c (66°).

Since there is now no transmitted wave inside the second medium, the incident and reflected fields are not sufficient to satisfy the boundary conditions. The tangential components of the electric field must be continuous across the interface. Consequently, there must be a transmitted wave but simultaneously, on average, no energy transfer across the interface. We can express the transmitted electric field as

$$\mathbf{E}_\mathrm{t} = \mathbf{E}_{0\mathrm{t}} e^{i(\mathbf{k}_\mathrm{t}\cdot\mathbf{r}-\omega t)} \tag{1.54}$$

where

$$\mathbf{k}_\mathrm{t}\cdot\mathbf{r} = k_{\mathrm{t}x}x + k_{\mathrm{t}z}z \tag{1.55}$$

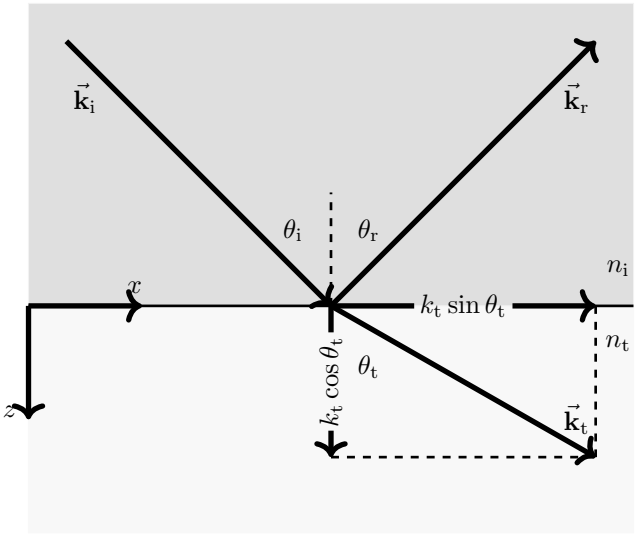

Figure 1.8: Schematic representation showing the propagation vectors for internal reflection.

as $\mathbf{k}$ has no y-component. The x- and z-components are

$$k_{\mathrm{t}x} = k_\mathrm{t} \sin\theta_\mathrm{t} \tag{1.56}$$

and

$$k_{\mathrm{t}z} = k_\mathrm{t} \cos\theta_\mathrm{t}\,, \tag{1.57}$$

respectively, as shown in figure 1.8. Through Snell's law it now follows that

$$k_\mathrm{t} \cos\theta_\mathrm{t} = \pm k_\mathrm{t} \left(1 - \frac{\sin^2\theta_\mathrm{i}}{n_\mathrm{ti}^2}\right)^{1/2} \tag{1.58}$$

where $n_\mathrm{ti} = n_\mathrm{t}/n_\mathrm{i}$. For cases where $\sin\theta_\mathrm{i} > n_\mathrm{ti}$, *i.e.* total internal reflection occurs, the two components can be expressed as

$$k_{\mathrm{t}z} = \pm i k_\mathrm{t} \left(\frac{\sin^2\theta_\mathrm{i}}{n_\mathrm{ti}^2} - 1\right)^{1/2} \equiv \pm i\beta \tag{1.59}$$

and

$$k_{\mathrm{t}x} = \frac{k_\mathrm{t}}{n_\mathrm{ti}} \sin\theta_\mathrm{i}\,. \tag{1.60}$$

Finally, we can rewrite the transmitted electric field as

$$\mathbf{E}_\mathrm{t} = \mathbf{E}_{0\mathrm{t}} e^{\pm\beta z} e^{i(k_\mathrm{t} x \sin\theta_\mathrm{i}/n_\mathrm{ti} - \omega t)}\,. \tag{1.61}$$

We can ignore the positive exponential in equation 1.61 since it would result in an electric wave with an ever increasing amplitude away from the interface. The transmitted wave thus advances in the x-direction of the interface with its amplitude decaying exponentially in the z-direction. It is this evanescent wave that we use in TIR Raman spectroscopy to stimulate Raman scattering at an interface. The exponential decay of this wave is governed by the attenuation coefficient β introduced above which can

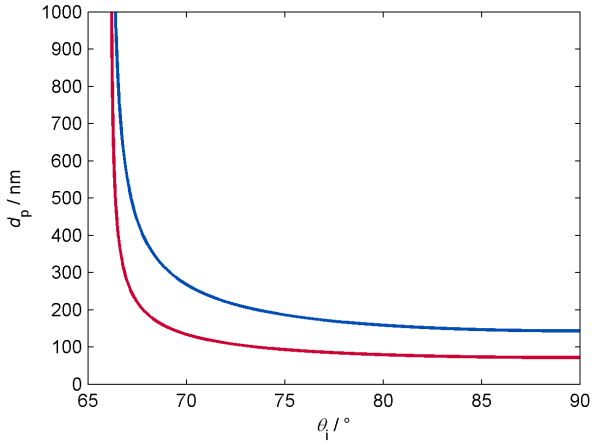

Figure 1.9: Penetration depth of the evanescent wave (blue) and the square of the evanescent wave (red) for total internal reflection at the silica-water interface ($n_i = 1.461$, $n_t = 1.335$) at a wavelength of 532 nm with respect to the angle of incidence.

be rewritten as

$$\beta = \frac{2\pi n_t}{\lambda_0}\left[\left(\frac{n_i}{n_t}\right)^2 \sin^2\theta_i - 1\right]^{1/2} . \tag{1.62}$$

Its characteristic decay length, referred to as the penetration depth d_p, is defined as the point where the strength of the electric field drops to $1/e$ of its initial value at $z = 0$. The penetration depth is thus defined as $d_p = 1/\beta$. In Raman spectroscopy, the intensity of the light defined as the square of the electric field is of interest and has a decay length of $\beta^{-1}/2$. Figure 1.9 shows the penetration depth at the silica-water interface for a wavelength of 532 nm. I used an angle of incidence of 73° for the majority of my TIR Raman measurement resulting in the penetration depth of the square of the electric field to be 103.5 nm.

Above the critical angle, $r_\perp$ and $r_\parallel$ are becoming complex quantities. We can thus rearrange the Fresnel coefficients to give

$$r_\perp = \frac{\cos\theta_i - i(n_{ti}^2 - \sin^2\theta_i)^{1/2}}{\cos\theta_i + i(n_{ti}^2 - \sin^2\theta_i)^{1/2}} \tag{1.63}$$

and

$$r_\parallel = \frac{n_{ti}^2\cos\theta_i - i(n_{ti}^2 - \sin^2\theta_i)^{1/2}}{n_{ti}^2\cos\theta_i + i(n_{ti}^2 - \sin^2\theta_i)^{1/2}} . \tag{1.64}$$

The overlap of the incident and reflected beams leads to an enhancement of the Fresnel factors of the transmitted beam. Rather then simply giving one Fresnel factor for each polarisation, they are now split up into separate factors for each of the three axes. This distinction is important since the presence of the interface means that molecules might be ordered with respect to the z axis. It is thus of interest for TIR Raman measurements to know the relative intensities generated by the different planes relative to the interface for each of the two polarisations. Perpendicular polarised incident light (**E** perpendicular to plate of incidence) has no components in the x and z axes, whilst parallel polarised light has no components in the y axis. Consequently,

$t_{\perp x} = t_{\perp z} = t_{\parallel y} = 0$. The three remaining non-zero coefficients are:[44]

$$t_{\parallel x} = \frac{2\cos\theta_\mathrm{i}(\sin^2\theta_\mathrm{i} - n_\mathrm{ti}^2) + i(2n_\mathrm{ti}^2\cos^2\theta_\mathrm{i}\sqrt{\sin^2\theta_\mathrm{i} - n_\mathrm{ti}^2})}{n_\mathrm{ti}^4\cos^2\theta_\mathrm{i} + \sin^2\theta_\mathrm{i} - n_\mathrm{ti}^2}\,, \tag{1.65a}$$

$$t_{\perp y} = \frac{2\cos^2\theta_\mathrm{i} - i(2\cos\theta_\mathrm{i}\sqrt{\sin^2\theta_\mathrm{i} - n_\mathrm{ti}^2})}{1 - n_\mathrm{ti}^2}\,, \tag{1.65b}$$

$$t_{\parallel z} = \frac{2n_\mathrm{ti}^2\cos^2\theta_\mathrm{i}\sin\theta_\mathrm{i} - i(2\cos\theta_\mathrm{i}\sin\theta_\mathrm{i}\sqrt{\sin^2\theta_\mathrm{i} - n_\mathrm{ti}^2})}{n_\mathrm{ti}^4\cos^2\theta_\mathrm{i} + \sin^2\theta_\mathrm{i} - n_\mathrm{ti}^2}\,. \tag{1.65c}$$

Figure 1.10 shows a plot of the absolute values of the three Fresnel factors for the silica-water interface. $t_{\perp y}$ and $t_{\parallel z}$ show maximum enhancement at the critical angle, 66°, while $t_{\parallel x}$ is zero. Minimising $t_{\parallel z}$ would have simplified spectral analysis and, combined with the enhancement of $t_{\parallel x}$ and $t_{\perp y}$, implies that θ_c is the preferred angle of incidence for TIR Raman measurements. To work at this angle, however, is not feasible for a variety of reasons: Reliably aligning the experiment, including the beam delivery optics and the sample interface, exactly to the critical angle would be very challenging. In addition, the finite numerical aperture of the pump laser would cause some of the light to be incident below the critical angle. Finally, the infinite penetration depth would cause a massive increase in the water signal and thus swamp any signals arising from species at the interface. This would, as a consequence, defeat the point of using TIR Raman spectroscopy for its surface selectivity.

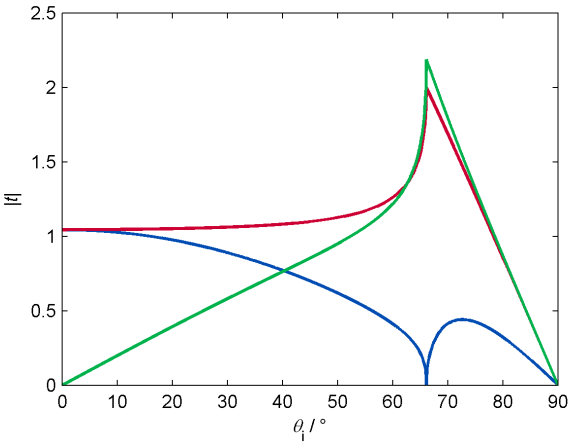

Figure 1.10: Absolute values of the Fresnel factors at the silica-water interface ($n_\mathrm{i} = 1.461$, $n_\mathrm{t} = 1.336$) as a function of the angle of incidence. $t_{\parallel x}$ is shown in blue, $t_{\perp y}$ in red and $t_{\parallel z}$ in green.

The angle of 73° used in most of my measurements was chosen as a compromise between maximising the electrical field and minimising the penetration depth. $t_{\parallel z}$ is close to its local maximum at this angle of incidence. Note that $\perp$ and $\parallel$ are replaced by S and P, respectively, in the subsequent chapters.

1.6 Raman spectroscopy

1.6.1 Vibrations in molecules

Raman spectroscopy is a type of vibrational spectroscopy probing vibrational modes of molecules. We will thus briefly discuss vibrations in polyatomic molecules. Non-linear molecules containing N atoms need $3N$ coordinates the specify the location of all atoms. Three coordinates are required to describe the location of the molecule's centre of mass. The rotation of the molecule about the centre of mass is specified with three more coordinates. Changes in the remaining $3N-6$ coordinates describe vibrations of the molecule. The number of coordinates corresponding to vibrational modes is $3N-5$ for linear modules since there are only two angles needed to specify their orientation.[45] All atoms of a polyatomic molecule are participating in vibrations and the potential energy depends on all displacements of atoms from their equilibrium positions. The potential energy can be expressed through a Taylor series expansion giving

$$V(x) = V(0) + \left.\frac{\partial V}{\partial x}\right|_0 x + \frac{1}{2}\left.\frac{\partial^2 V}{\partial x^2}\right|_0 x^2 + \dots, \tag{1.66}$$

where x is the displacement of an atom away from the equilibrium distance R_0. At the equilibrium where $x = 0$, the first derivatives can be set to zero. Since the absolute energy of the molecule is not of interest here, $V(0)$ can be set to zero as well. For small displacements from the equilibrium, the expression can be simplified the neglecting the terms after the second derivative. The potential energy can now be expressed as

$$V(x) = \frac{1}{2}kx^2 \tag{1.67}$$

where k, the force constant, is defined as

$$k = \left.\frac{\partial^2 V}{\partial x^2}\right|_0 \tag{1.68}$$

arising from the second derivative. The discrete energy levels of this harmonic oscillator are given as

$$E = \left(v + \frac{1}{2}\right)\hbar\omega \tag{1.69}$$

for each normal mode where v is the vibrational quantum number defined as an integer ≥ 0. ω, the angular frequency, is given by $\sqrt{k/\mu}$ where μ is the reduced mass of the system. The uniform spacing between the levels is consequently $\hbar\omega$ while the zero-point energy is $\frac{1}{2}\hbar\omega$ when $v = 0$. The total vibrational energy is then the sum of the energies of each normal mode. This harmonic treatment implies the existence of an infinite number of discrete energy levels for each normal mode. The potential energy of real molecules, however, does not actually follow this harmonic shape but can be described as an anharmonic vibration. The differences become more important at higher quantum numbers and are a consequence of the simplifications in equation 1.66 where the Taylor expansion was truncated after the quadratic term. Equation 1.69 is, however, still a good approximation at low quantum numbers. The different

shapes of harmonic and anharmonic potentials together with the associated energy levels are shown in figure 1.11. One way of modelling the anharmonic vibration is the Morse potential given by

$$V(x) = hcD_e(1 - e^{-1ax})^2 \tag{1.70}$$

where D_e is the wavenumber associated with the depth of the minimum of the potential curve and a defined as

$$a = \sqrt{\frac{k}{2hcD_e}} \tag{1.71}$$

The Morse potential shows that the molecule has enough vibrational energy at high quantum number to break the bonds. It follows, that there is actually a finite number of available vibrational energy levels. Another difference is the separation between vibrational levels. The energy levels of the Morse potential are given by [45]

$$E = \left(v + \frac{1}{2}\right)\hbar\omega - \left(v + \frac{1}{2}\right)^2 \hbar\omega x_e \tag{1.72}$$

with

$$\omega x_e = \frac{a^2\hbar}{2\mu} \tag{1.73}$$

and are not equally spaced like as they are for a harmonic oscillation but are converging with increasing quantum number. It should be noted that the Morse potential is still an approximation.

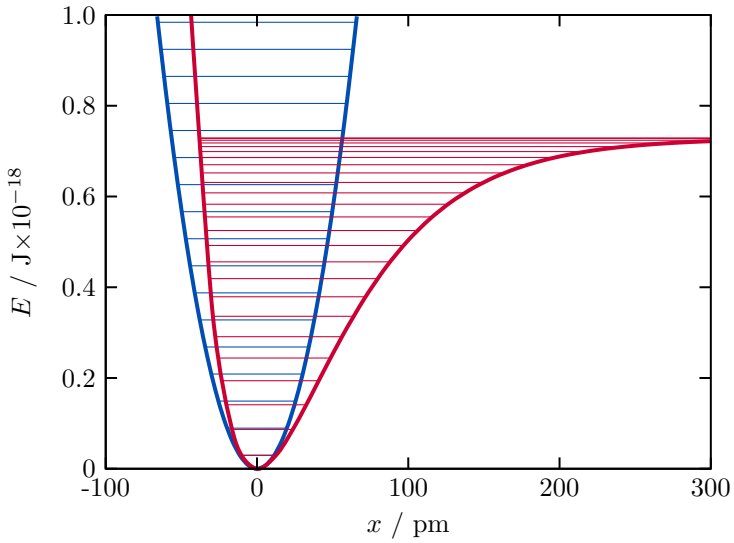

Figure 1.11: Harmonic (blue) and anharmonic (red) potentials as a function of atomic displacement with added energy levels (horizontal lines). The constants used to generate this figure were chosen to be close to the values for a C−H stretch at 2900 cm^{-1}.

These vibrational modes can be probed through techniques such as Raman spectroscopy and infrared spectroscopy. Raman spectroscopy was utilised extensively throughout this work and will be discussed in detail in the remainder of this chapter.

1.6.2 Raman scattering

Background Whenever monochromatic light is incident on a transparent medium such as a dust-free gas or an optically perfect solid, most of the light will be transmitted.[46] In addition, some of the light is scattered. The vast majority of the scattered light is of the same frequency as the incident light. This is the result of an elastic scattering process is called Rayleigh scattering. An even smaller portion of the light (typically 10^{-6} of the incident light), however, is scattered inelastically and thus at a frequency different from the one of the incident light.[47] The underlying process is called Raman scattering, named after C. V. Raman who first observed it in 1928 following its theoretical prediction by A. Smekal in 1923. The Raman effect can be described through classical and quantum mechanical descriptions. This section will only include a classical description since it is sufficient for explaining the vibrational transitions that are relevant to this work. A quantum mechanical treatment, based on the work of Placzek in 1934, would be necessary to, for example, describe electronic transitions seen in resonance Raman scattering.

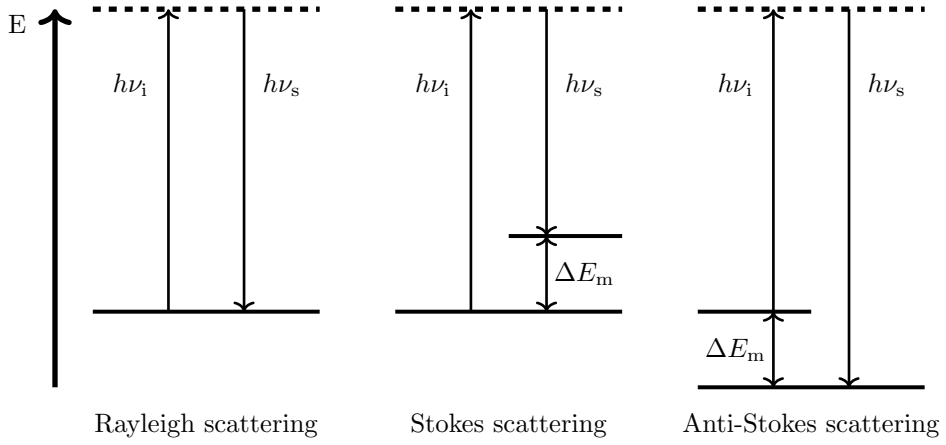

Figure 1.12: Diagram showing Rayleigh, Stokes and anti-Stokes scattering.

The Raman scattered light has a lower or higher frequency than the incident light, and is referred to as Stokes or anti-Stokes scattering, respectively. All three possible types of scattering are illustrated in figure 1.12. In each case, the photon interacting with the molecule raises it to a so-called virtual energy level that does not correspond to a normal vibrational level. The difference between this level and the molecule's initial vibrational level matches the energy of the incident photon, $h\nu_\mathrm{i}$. In the case of Rayleigh scattering, the molecule returns to its initial state and the energy of the scattered photon matches the incident photon. Conversely, the energy of the molecule changes by ΔE_m during inelastic scattering which is given by

$$\Delta E_\mathrm{m} = h\nu_\mathrm{i} - h\nu_\mathrm{s} \tag{1.74}$$

where $h\nu_\mathrm{s}$ is the energy of the scattered photon. In the case of Stokes scattering, ν_s is smaller than ν_i resulting in a positive ΔE_m. The molecule gains energy. Conversely, the molecule loses energy during anti-Stokes scattering where $\nu_\mathrm{s} > \nu_\mathrm{i}$ resulting in a negative ΔE_m. The magnitude of the shift between the incident and scattered

photons can be expressed as

$$\Delta\nu = |\nu_\mathrm{i} - \nu_\mathrm{s}| \tag{1.75}$$

and is the called the Raman shift which is commonly given in wave numbers and forms the x axis of a Raman spectrum.

Anti-Stokes scattering is usually much weaker in a Raman spectrum than Stokes scattering. This can be explained by the Boltzmann distribution

$$\frac{N_1}{N_0} = e^{-\Delta E_\mathrm{m}/k_\mathrm{B}T} \tag{1.76}$$

where N_0 and N_1 are the populations the ground and a higher vibrational level, respectively. k_B is the Boltzmann constant and T the temperature. At room temperature, essentially only the lowest vibrational levels are occupied. The exponentially smaller number of occupied higher levels results in most of the inelastic scattering being Stokes scattering.

Note that Raman scattering is not an absorption/emission process like the one seen in IR spectroscopy. The photon interacting with the molecule raises the molecule to a so-called virtual energy level that does not correspond to a normal vibrational level. The energy of the photon does not match the match the energy difference between two vibrational states. Additionally, Raman scattering can not be distinguished into two processes. For comparison, in IR spectroscopy, where the sample is irradiated with a range of infrared frequencies, light is only absorbed if the photon's energy matches the energy difference ΔE_m between two vibrational states. In the second step, the energy can be spread amongst a large number of vibrations and transferred to translational energy.

Classical description When the electric field of incident light is applied to a molecule, the electrons and protons are forced to respond by moving in opposite directions. The field is thereby inducing a temporary dipole moment within the molecule. This induced dipole moment, $\boldsymbol{\mu}_\mathrm{ind}$, is linearly proportional to the applied electric field and can be expressed as

$$\boldsymbol{\mu}_\mathrm{ind} = \boldsymbol{\alpha}\mathbf{E} \tag{1.77}$$

where $\mathbf{E}$ is the electric field inducing the dipole and $\boldsymbol{\alpha}$ the polarisability of the molecule which will be discussed further at the end of this section. The electric field of the incident light with its maximum electric field strength $\mathbf{E}_0$ and frequency ν_i is given by

$$\mathbf{E} = \mathbf{E}_0 \cos 2\pi\nu_\mathrm{i} t\,. \tag{1.78}$$

Substituting the above expression into equation 1.77 returns the expression for the induction of Rayleigh scattering

$$\boldsymbol{\mu}_\mathrm{ind} = \boldsymbol{\alpha}\mathbf{E}_0 \cos 2\pi\nu_\mathrm{i} t\,, \tag{1.79}$$

where an oscillating electric field induces an oscillating dipole in the molecule. Expanding the polarisability using a Taylor series leads to

$$\boldsymbol{\alpha} = \boldsymbol{\alpha}_0 + \left.\frac{\partial \boldsymbol{\alpha}}{\partial \mathbf{Q}}\right|_0 \mathbf{Q} + ... \tag{1.80}$$

where $\boldsymbol{\alpha}_0$ is the equilibrium polarisability, $\mathbf{Q}$ the normal mode displacement vector and $\partial\boldsymbol{\alpha}/\partial\mathbf{Q}$ the change of polarisability with respect to $\mathbf{Q}$ at the equilibrium configuration. The vibrational mode behaves as a harmonic oscillator with a vibrational frequency ν_v and can be expressed as

$$\mathbf{Q} = \mathbf{Q}_0 \cos 2\pi\nu_{\mathrm{v}} t\,. \tag{1.81}$$

We can now substitute equations 1.80 and 1.81 into equation 1.79 giving

$$\boldsymbol{\mu}_{\mathrm{ind}} = \boldsymbol{\alpha}_0 \mathbf{E}_0 \cos 2\pi\nu_{\mathrm{i}} t + \left.\frac{\partial \boldsymbol{\alpha}}{\partial \mathbf{Q}}\right|_0 \mathbf{E}_0 \mathbf{Q}_0 (\cos 2\pi\nu_{\mathrm{i}} t)(\cos 2\pi\nu_{\mathrm{v}} t)\,. \tag{1.82}$$

Since $\cos(\alpha)\cos(\beta) = \frac{1}{2}\cos(\alpha-\beta) + \frac{1}{2}\cos(\alpha+\beta)$, we can rewrite the above equation as

$$\boldsymbol{\mu}_{\mathrm{ind}} = \boldsymbol{\alpha}_0 \mathbf{E}_0 \cos 2\pi\nu_{\mathrm{i}} t + \frac{1}{2}\mathbf{E}_0 \mathbf{Q}_0 \left.\frac{\partial \boldsymbol{\alpha}}{\partial \mathbf{Q}}\right|_0 [\cos 2\pi(\nu_{\mathrm{i}} - \nu_{\mathrm{v}})t + \cos 2\pi(\nu_{\mathrm{i}} + \nu_{\mathrm{v}})t] \tag{1.83}$$

to return a classical description of Raman scattering. The unshifted first term on the right-hand side corresponds to Rayleigh scattering, while the lower frequency second term and higher frequency third term correspond to Stokes and anti-Stokes scattering, respectively. Importantly, equation 1.83 shows that Stokes and anti-Stokes scattering only occur when $\frac{\partial \boldsymbol{\alpha}}{\partial \mathbf{Q}} \neq 0$, that is, when the polarisability changes during the vibration, the fundamental requirement of the Raman effect.

Chapter 2: Methods

This thesis required the development of novel synthetic and analytic methods to produce and characterise films of polymers and surfactants. This chapter describes different techniques used for both types of films, including total internal reflection Raman spectroscopy, a recently developed Raman imaging technique — which has been used to evaluate the uniformity of the films with micrometre resolution as well as the distribution of different components inside the layers — ellipsometry and circular dichroism spectroscopy. This chapter also details the methods used to produce the soft matter films, including synthetic procedures to attach polymer layers chemically to silica substrates and the formation of surfactant films by fusion of vesicles onto a surface.

2.1 Total Internal Reflection (TIR) Raman Spectroscopy

2.1.1 Optical set up

The total internal reflection (TIR) Raman set up of the Bain group (see figure 2.1), has been built around a Renishaw spectrometer (Ramascope 1000, Renishaw) and a Leica upright microscope equipped with an Olympus objective (×50, NA 0.55).

The laser (Opus 532, Laser Quantum) emits a green light ($\lambda = 532\,\text{nm}$) horizontally polarised with tunable power of up to 2 W. The laser beam is expanded via a telescope **L1-2** ($f_1 = -25\,\text{mm}$ and $f_2 = +125\,\text{mm}$) and directed onto the sample stage with a controlled angle of incidence via a periscope. The telescope is used so that the beam spot is smaller on the sample, thus improving spectral resolution. The beam is focussed onto the sample via a convex gradient index lens **L3** ($f_3 = +120\,\text{mm}$) to a diameter of 10 µm. The reflected beam is blocked by a beam dump. The polarisation of the beam can be changed using a half-wave plate. Scattered light is collected and collimated by the objective lens, and directed into the spectrometer. The path of the scattered light is shown in figure 2.2.

In short, the Rayleigh-scattered and anti-Stokes scattered light are removed with an edge filter **EF**. A half-wave plate can be flipped into the beam path to selectively probe the different polarisations of the scattered light. A lens focusses the light onto the entrance slit **ES** of the spectrometer. The light is then re-collimated and dispersed by a grating (1800 lines/mm). The spectrum is focussed onto a CCD camera.

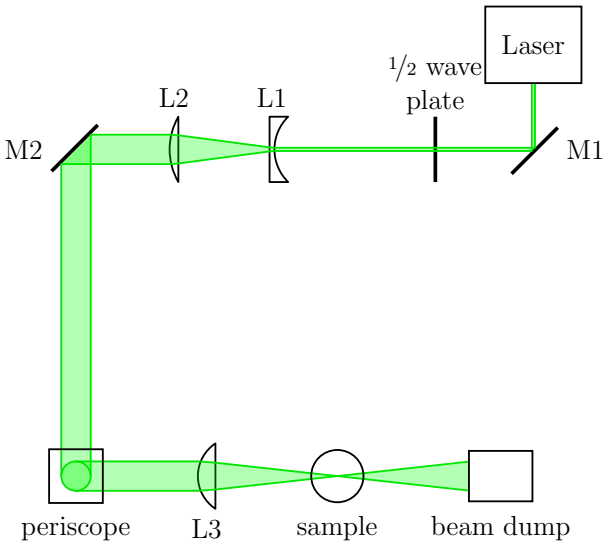

Figure 2.1: The optical beampath of the Raman spectrometer as set up in the Bain laboratory, seen from above.[48] The laser beam is expanded by a telescope **L1-2**, directed by a periscope and focused by **L3** onto the sample.

2.1.2 Alignment

The laser power is reduced to 10 mW using a OD1 neutral density filter added to the beampath. The expanded beam is set to a desired angle of incidence by two mirrors acting as a periscope. The first mirror sends the light in the vertical direction, while the second mirror defines the beam height and angle of incidence. The angle of incidence is set by measuring the height of the beam between two points. The height of the beam is measured in two known points from either side of the microscope. Once the angle is set, the focussing lens is positioned perpendicularly to the beam. This is achieved by checking the height of the beam as well as the back-reflected light. The position of the lens is finely adjusted by moving the lens along the direction of the beam using a translational stage (Thorlabs) to get a minimal spot size on the sample. The position of the lens before the entrance slit of the spectrometer is adjusted to maximise the intensity and reduce the full width at half maximum (FWHM) of the 520 cm^{-1} silicon band of a silicon wafer. This band is used to relate the position of a peak on the CCD camera to the Raman shift.

2.1.3 Data acquisition and data analysis

Operating parameters

The Renishaw spectrometer possesses two modes of data acquisition. In the extended scan mode, the grating rotates while the CCD is read out simultaneously. This mode enables the collection of spectra with a large spectral window which are not limited by the size of CCD. Internal reference spectra are collected using this mode. The main disadvantage of this mode is the long acquisition time required, as the grating is moving at low speed. In the single scan mode, the entire width of the CCD is read at once. This mode enables the acquisition of spectra covering a 660 cm^{-1}

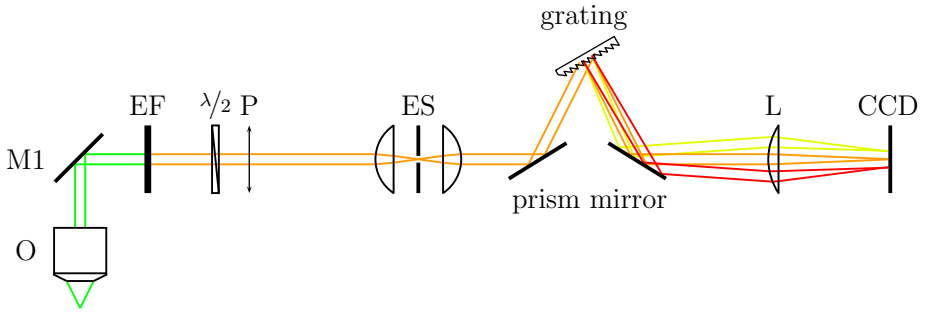

Figure 2.2: The travel of the scattered light inside the Renishaw spectrometer seen from the side.[48] Scattered light from the sample is collected by a microscope objective, **O**, the Raman scattered light is passed through a high-pass edge filter, **EF**, polarised (**P** and $\frac{\lambda}{2}$), focussed onto the entrance slit of the spectrometer, **ES**, dispersed by a grating and focussed on the CCD.

spectral window in one second. After selecting the region of interest in the extended scan spectrum, the single scan mode is used to collect all further Raman spectra.

The polarisation of the incident light can be selected with the half-wave plate of the beam delivery optics (see figure 2.1). S polarised light has an electric field vector perpendicular to the plane of incidence and P has an electric field vector parallel to the plane of incidence. In the lab coordinate system, described in chapter 1, the electric field of S polarised light is pure y while the electric field of P polarised light has components in x and z. The polarisation of the scattered light is also selected with the half-wave plate and polariser in the spectrometer (see figure 2.2). The y-polarised scattered light is in the same plane as both the surface and the S-polarised light. The x component is in the same plane as the surface but perpendicular to y. The four possible combinations of polarisations probe different elements of the Raman tensor (see table 2.1). The different polarisations are used for the final assignment of the Raman bands. All data are collected with the Sy polarisation combination, unless specified otherwise.

Table 2.1: Elements of the Raman tensor probed by the polarisation combinations in the TIR Raman set up. It is worth noting that some of the equivalences assume that the sample is symmetric in the plane of the sample.

Experimental polarisation	Detected tensor elements	Equivalent tensor elements
Sy	α_{yy}	α_{xx}
Sx	α_{yx}	α_{xy}
Px	α_{xx}, α_{zx}	α_{yy}, α_{xz}, α_{yz}, α_{zy}
Py	α_{xy}, α_{zy}	α_{yx}, α_{yz}, α_{xz}, α_{zx}

Typical acquisitions consist of five accumulations of 30-second scans. This mode has been preferred to a single scan of 150 seconds as no saturation of the detector from the water band is observed at any polarisation or laser power used. Also, the extra noise and readout time resulting from the multiple scans is negligible compared to the shot noise in the Raman signal.

When cosmic rays, high energy particles from outer space, hit the CCD, it liberates many electrons causing artefacts in the data. Cosmic ray peaks are unavoidable but can be removed as they are sharper and more intense than the Raman scattering bands. A Matlab code developed by a former PhD student of our group, Dr. David Woods, has been used to find and remove cosmic ray peaks from all spectra. Alternatively, the Renishaw software possesses an automatic cosmic ray removal function which records two additional scans and remove any spike present in only one of them. This alternative works well but requires extra measuring and readout time.

Background subtraction

Fused silica hemispheres used as substrate have a large spectral window enabling the measurement of most organic bands. All peaks above $1100\,\mathrm{cm}^{-1}$ are detected. Characteristic bands are shown in figure 2.3. The signals between 2700–$3300\,\mathrm{cm}^{-1}$ can be attributed to the water OH stretch. At lower Raman shift, between 2700–$3000\,\mathrm{cm}^{-1}$, lie CH stretches. CD stretches are located between 2000 and $2300\,\mathrm{cm}^{-1}$. In the region between 1400–$1700\,\mathrm{cm}^{-1}$ lie different bands: aromatic C−C stretches, CH deformations, features of ketones or amides.

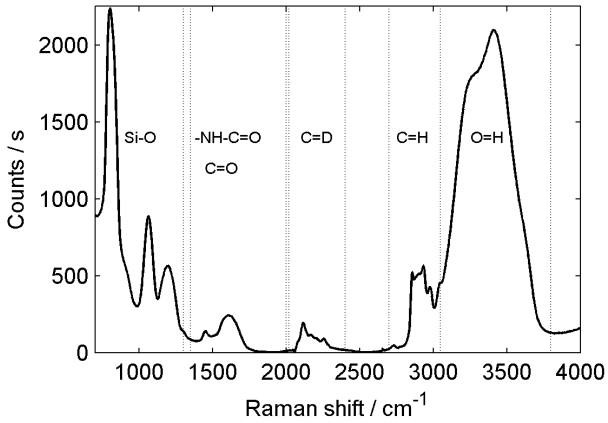

Figure 2.3: TIR Raman spectrum of a mixed layer of surfactants — one being deuterated — showing the regions of interest.

Water OH stretches are sensitive to temperature. As the temperature increases, hydrogen bonded networks are disrupted. Thus, the OH stretches of water become freer and vibrate at higher frequencies leading to a larger Stokes shift. Sets of water reference spectra are collected for every degree between 5 °C and 60 °C in the regions of interest.

A Matlab function written jointly with another PhD student, Mario Possiwan, has been used to estimate the peak position, half-width, amplitude and Gaussian and Lorentzian fractions. Raman spectra are fitted by minimising the mean squared error, ε, between the fitted and original spectra. If two sets lead to a similar error (less than 0.5 % difference), the one requiring fewer peaks is chosen.

Bulk contribution and quantitative analysis

The Raman effect is linear and it is therefore possible to relate the Raman intensity of a band to the number of induced dipoles in the probed volume. To do so, adsorption isotherms are collected. Solutions of increasing concentration are prepared and inserted into the cell. The variation of intensity of the Raman signal with respect to the bulk concentration is called an isotherm, see figure 2.4.

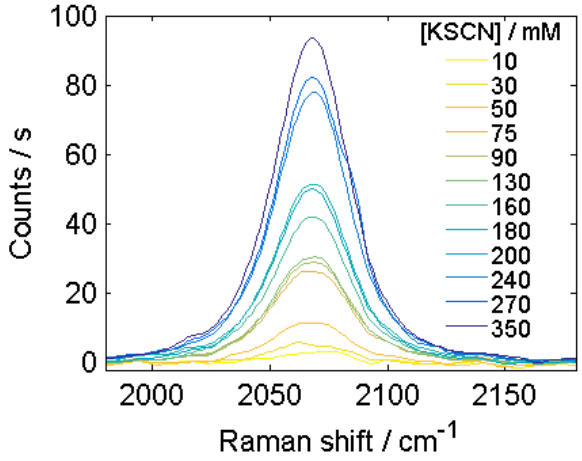

(a) TIR Raman spectra of potassium thiocyanate solutions at various concentrations

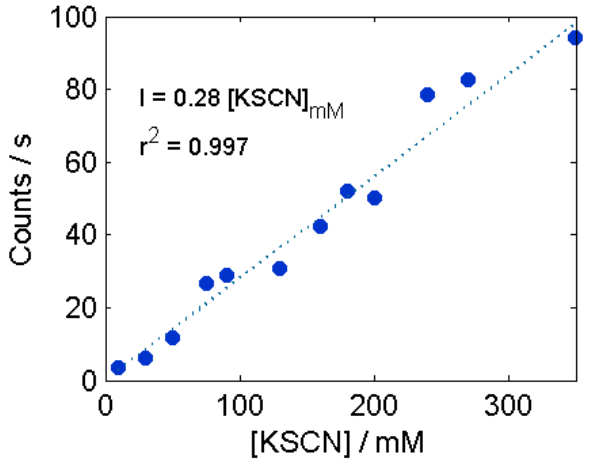

(b) Amplitude of $\nu_s(SCN^-)$ as a function of concentration of potassium thiocyanate in bulk (right).

Figure 2.4: TIR Raman spectra and amplitude of $\nu_s(SCN^-)$ from solutions of potassium thiocyanate.

Above a certain concentration, the surface excess remains constant and the increase in the Raman intensity is linear and arises from the contribution of bulk solution within the evanescent wave. In the example shown above, this is true at all concentrations, since SCN^- does not adsorb onto silica. The slope of this increase gives the calibration factor between the Raman intensity and the concentration, and the contribution from bulk can be thus removed. The remaining Raman intensities arose only from adsorbed material, *i.e.* all material in the probed volume that is

actually on the surface. The surface excess can be calculated as follows: all detected signals arise from the exponentially decaying evanescent wave. A recorded signal is thus the integral of this profile which is equivalent to a layer of solution with a thickness of $d_p/2$. Because of this relationship, the surface excess can be calculated by multiplying the concentration by the sampling depth ($d_p/2$).

The detection limit is calculated by comparing the concentration-dependent integrated signal to the noise level in the same integrated region in absence of the species. The detection limit is given by the standard deviation (65 % confidence limit).

2.1.4 Wall-jet cell

The glass cell used in this thesis has been made in the glass–blowing workshop of the Durham Chemistry Department (see figure 2.5). This cell has been designed

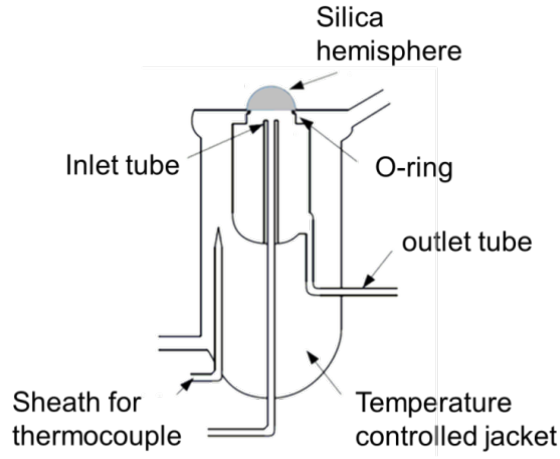

Figure 2.5: The glass cell as designed for TIR Raman experiments and made by the glass blowers of the Department of Chemistry of the University of Durham.

to control the hydrodynamics close to the interface in order to observe the kinetics of adsorption of surfactants and surfactant mixtures, using a wall-jet geometry. This geometry allows the distribution of the solution onto the surface with a zero radial speed. Transport of material onto the surface is diffusion limited. This assumption is valid only if the flow is laminar which gives restrictions on the tubing size and the flow speed. The wall–jet cell is surrounded by a glass jacket which can be filled with water to control temperature using a circulating water bath. The temperature close to the interface is measured by a thermocouple placed in a sheath inside the jacket. The injection and outlet ports of the cell are attached to tubing and connectors made from Teflon. Sealing is enabled by small O-rings inside the connectors. Solutions are injected using syringe pumps providing control over flow speed and volume.

The substrates are hemispherical to prevent chromatic aberrations in the scattered light, to make the collection more efficient and to get a better control over the angle of incidence at the interface. The hemisphere is held in place by a Teflon plate screwed on top of the cell. As the hemisphere can be slightly tilted from the platform, the glass cell is mounted onto an optical mount (Thorlabs) enabling to compensate for this tilt.

The procedure to align the platform so that the bottom surface of the hemisphere lies perpendicular to the plane of incidence requires the researcher to repeat two steps alternately until the reflection from the bottom surface of the hemisphere is at the right height and in the plane of incidence. Firstly, the central position on the bottom surface of the hemisphere is found, which is achieved by locating the position of a bright spot within the hemisphere using the microscope. The bright spot is caused by the hemisphere focussing the light of the microscope illumination. This point is located slightly above the actual interface. Secondly, the cell is tilted so that the reflection from the hemisphere is at the same angle as the angle of incidence.

2.1.5 Sample preparation

Fused silica hemispheres (IR-grade, diameter 10 mm, CVI) used for Raman spectroscopy are thoroughly cleaned prior to use. Hemispheres are placed in a Teflon beaker and sonicated in ethanol for 5 minutes, rinsed 5 times with ultra high purity (uHP, Millipore) water and immersed in a solution of chromium sulfuric acid for 30 minutes. Chromium sulfuric acid solution is a powerful oxidizing agent removing any organic contamination from the surface; it requires careful handling and precaution, and should not be used without prior training. The acid is stored in a 100 mL glass jar on a chemical resistant tray inside the fumehood to ease handling and prevent spillage of large quantities. The mixture can be used several of times before it should be carefully neutralised and disposed of. The substrates are rinsed with a small amount of Milli-Q water to remove any remaining acid. The rinsing water is then transferred to a specific waste bottle since it now contains toxic chromium IV and VI ions. The substrates are then rinsed 10 times with uHP water. The presence of any organics is assessed by taking a TIR Raman spectrum at the silica–water interface.

Silicon wafers were placed in a Teflon beaker and sonicated in ethanol for 5 minutes, rinsed 5 times with uHP water and immersed in a solution of 3:1 sulfuric acid:hydrogen peroxide solution 30 % for 30 minutes. This mixture — often referred to as piranha solution — is a powerful oxidizing agent and requires careful handling and precautions. After use, the acidic mixture is allowed to cool and carefully diluted with water before disposal.

All glassware is sonicated in a solution of Decon 90, a commercial detergent, for 15 minutes and left to soak overnight. Glassware is rinsed 10 times in uHP water, sonicated for 15 minutes and rinsed again 10 times. The contact angle of uHP water on the glassware should be close to 0° and is verified through visual inspection. Stainless steel spatulas and tweezers are sonicated in a solution of Decon 90 for 15 minutes and rinsed with copious amount of uHP water. Teflon connectors, O-rings and syringe plungers are cleaned in a similar manner.

2.1.6 Film thickness model

Introduction

The penetration depth of the electric field is a function of the angle of incidence. Varying the angle of incidence thus changes the probed volume below the interface.

If a uniform polymer layer of a volume fraction y and thickness h is present at the interface, the relative intensities of the Raman signals originating from the polymer and water layers will then vary with the angle of incidence. The magnitude of this change is a function of y and h. Figure 2.6 shows a schematic diagram of such a polymer layer grafted onto a silica substrate in water.

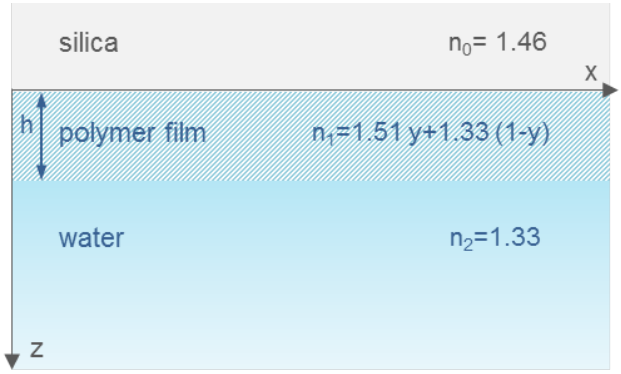

Figure 2.6: Schematic diagram of the multilayer model used in this work. The polymer layer is a uniform film of thickness h and volume fraction y, lying between two media of infinite thickness, silica and water.

This section outlines a model that calculates the Raman intensities originating from polymer layers at the silica-water interface, as a function of the angle of incidence, polymer film volume fraction and thickness. TIR Raman spectra of polymer films recorded at a range of angles of incidence can then be matched to the model, returning the volume fraction and thickness of the grafted polymer layer.

Description of the algorithm

The algorithm calculates the relative Raman intensities scattered from the polymer grafted onto silica and from water for a range of angles of incidence. Raman intensities are simulated over a range of polymer densities and thickness. The polymer volume fraction ranges from 0.1 to 1 and the thickness from 1 to 500 nm.

The refractive index n_1 of the polymer layer is a function of the polymer volume fraction, y, and calculated in the first step from the refractive indices of pNIPAM [49] and water: [50]

$$n_1 = 1.51\ y + 1.33\ (1 - y) \tag{2.1}$$

An effective medium approximation would be a more accurate way of calculating the refractive index. The linear relationship is, however, a good approximation and sufficient for this algorithm.

The Fresnel factors of the y-component of the electric field, in transmission and reflection, $r_\perp$ and $t_\perp$ respectively, are calculated as shown in equation 2.2. [51]

$$r_\perp = \frac{r_\perp^{0,1} + r_\perp^{1,2} e^{2i\phi}}{1 + r_\perp^{0,1}\ r_\perp^{1,2} e^{2i\phi}} \quad t_\perp = \frac{t_\perp^{0,1} t_\perp^{1,2} e^{i\phi}}{1 + t_\perp^{0,1}\ t_\perp^{1,2} e^{2i\phi}} \tag{2.2}$$

ϕ refers to the phase change between the reflected beams at the two interfaces

and is defined in equation 2.3. $r_{\perp}^{m,n}$ and $t_{\perp}^{m,n}$ are the Fresnel factors in transmission and reflection at the interface between the media m and n. The silica substrate, the polymer film and the water bulk phase are denoted by the number 0, 1 and 2, respectively. The Fresnel factors at each of the two interfaces are calculated as shown in equation 2.4 where $\xi_{\mathrm{i}} = \sqrt{n_{\mathrm{i}}^2 - n_0^2 \ \sin^2\theta}$.

$$\phi = \frac{2\pi h \ \sqrt{n_1^2 - n_0^2 \ \sin^2\theta}}{\lambda} \tag{2.3}$$

$$\begin{aligned} r_{\perp}^{01} &= \frac{\xi_1 - \xi_2}{\xi_1 + \xi_2} \quad r_{\perp}^{12} = \frac{\xi_2 - \xi_3}{\xi_2 + \xi_3} \\ t_{\perp}^{01} &= \frac{2\xi_1}{\xi_1 + \xi_2} \quad t_{\perp}^{12} = \frac{2\xi_2}{\xi_2 + \xi_3} \end{aligned} \tag{2.4}$$

The average electric fields inside the polymer layer, $\langle E_{y,1}^2 \rangle$, and inside the water layer, $\langle E_{y,2}^2 \rangle$, can now be defined as shown in equations 2.5 and 2.6, respectively.[51]

$$\frac{\langle E_{y,1}^2 \rangle}{\langle E_0^2 \rangle} = \left| (1 + r_{\perp}) \ \cos\left(\frac{2\pi \ z \ \xi_2}{\lambda}\right) + i \ \frac{\xi_1}{\xi_2} \ (1 - r_{\perp}) \ \sin\left(\frac{2\pi \ z \ \xi_2}{\lambda}\right) \right|^2 \tag{2.5}$$

$$\frac{\langle E_{y,2}^2 \rangle}{\langle E_0^2 \rangle} = |t_{\perp}|^2 \exp\left(\frac{-4\pi \ (z - h) \ n_2 \cos(\theta_i)}{\lambda}\right) \tag{2.6}$$

The polymer layer has a defined thickness, h, and volume fraction y. Thus only a fraction of the electric field inside the polymer layer $\langle E_{y,1}^2 \rangle$ contributes to the Raman intensity of the polymer, I_p. The Raman intensity of water, I_w, is a combination of the water inside the polymer layer and the water layer. The two Raman intensities are consequently defined as follows:

$$\begin{aligned} I_p(\theta) &\propto \int_0^h y \frac{\langle E_{y,1}^2 \rangle}{\langle E_0^2 \rangle} dz \\ I_w(\theta) &\propto \int_0^h (1 - y) \frac{\langle E_{y,1}^2 \rangle}{\langle E_0^2 \rangle} dz + \int_h^{\infty} \frac{\langle E_{y,2}^2 \rangle}{\langle E_0^2 \rangle} dz \end{aligned} \tag{2.7}$$

This process generates a look-up table of the expected Raman intensities for the set of possible polymer layers defined by the input ranges of y and h.

Experimental data set and fitting

Figure 2.7 shows the dataset of Raman spectra from a layer of grafted pNIPAM at the silica–water interface, collected for a range of angles of incidence between 66° and 80°. The Raman spectra are all normalised to the water maximum. After subtraction of the water background, the integral of the spectra are calculated in the range of 2800–3050 cm^{-1}, and plotted against the angle of incidence. As the angle of incidence increases, the penetration depth decreases. Consequently, the water layer contributes less to the Raman spectrum leading to the increase in I_{p} shown in the figure below.

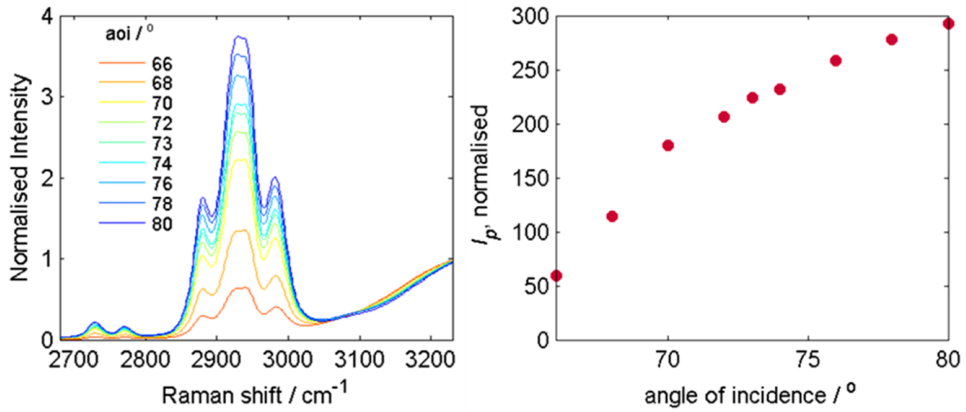

Figure 2.7: Multi-angle data set collected from a swollen pNIPAM film at room temperature. The spectra are collected at various angles of incidence between the critical angle (66°) and grazing incidence. The spectra have been normalised to the maximum of the water band (left). The water background is subtracted and the resulting integrals are plotted against the angle of incidence (right).

It is not possible to directly compare the absolute values of the simulated and measured Raman intensities. The algorithm thus compares the relative change in the signal of the polymer layer. All simulated data therefore has to be scaled to the observed intensities first. Scaling is carried out for each modelled set of intensities using Matlab's mrdivide function. This function solves the equation $s\phi_{\text{model}} = \phi_{\text{real}}$ for s, where ϕ_{model} and ϕ_{real} are row vectors containing the integrated polymer intensities of the model for one combination of y and h, and the input data, respectively. The solution s can then be used to scale the modelled Raman intensities. The degree of agreement between the simulated and measured intensity profiles is assessed through the coefficient of determination, r^2*.

The map in figure 2.8 shows the r^2 for all simulated polymer films and the experimental data shown above. Areas plotted in red show the highest agreement between the simulated and measured data. Blue areas have the lowest r^2 values.

There are multiple suitable (y, h) combinations matching the experimental dataset. An isotherm of pNIPAM solutions had been recorded at an angle of incidence of 73° (shown in figure 2.24). The isotherm enables the conversion of the polymer/water signal ratio to a polymer concentration. The Raman data of the grafted polymer film at the same angle of incidence can thus be converted into an equivalent polymer concentration, C_0, using the relationship shown in equation 2.8. The term on the left-hand side represents the polymer signal in a grafted film, while the term on the right hand side represents the polymer signal in a solution of a concentration C_0.

However, film density and thickness are related to the total amount of polymer in the probed volume by equation 2.8. The TIR Raman spectrum of a pNIPAM film collected at the angle of incidence of 73° can relate the polymer to water ratio signal

*Here, the coefficient of determination is 1 minus the ratio of the sum of squares of residuals to the total sum of squares, *i.e.* $r^2 = 1 - \frac{\sum_{i=1}^{n}(y_i - \hat{y}_i)^2}{\sum_{i=1}^{n}(y_i - \bar{y})^2}$ with n, y_i, $\hat{y}_i$ and $\bar{y}_i$ being the number of data points, the measured values, the predicted values and the mean of the observed data, respectively.

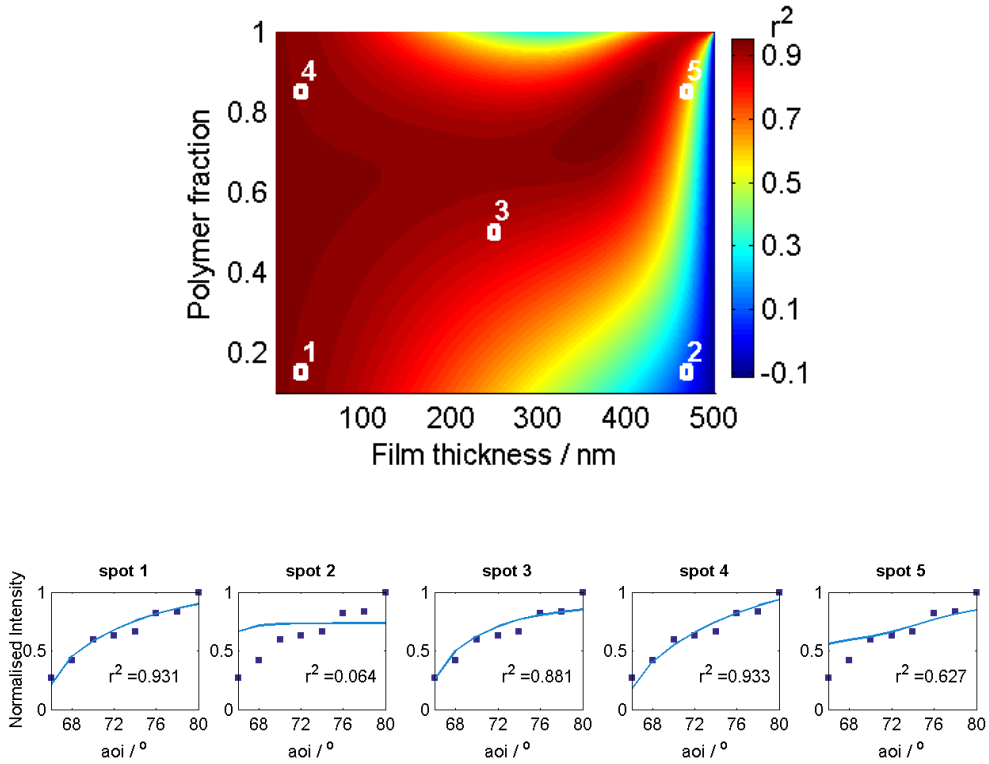

Figure 2.8: Map showing the goodness of the fit using the film thickness and polymer fraction as parameters. The goodness of the fit is determined by calculating the coefficient of determination, r^2, between the shape of the multiangle data (squares) and the modelled data (line).

to the total amount of material in the probed volume C_0. The (y, h) combination solution verifies equation 2.8.

$$\int_0^h y\ e^{-z/d_p}\ dz = \int_0^\infty C(z)e^{-z/d_p}\ dz \tag{2.8}$$

y can therefore be expressed as a function of h:

$$y = \frac{C_0}{1 - e^{-h/d_p}} \tag{2.9}$$

Figure 2.9 shows the overlap of the map of coefficient of determination with this concentration band. The solution is found by taking the (y, h) combination on this concentration band with the highest coefficient of determination.

I grafted pNIPAM from eight hemispheres with identical reaction mixtures and removed individual hemispheres at different times to control the reaction for each surface. Raman spectra of the grafted polymers in contact with water were then recorded at 20 °C with seven different angles of incidence (66°, 68°, 70°, 74°, 76°, 78° and 80°). The spectra were analysed with the multiangle algorithm. The algorithm considered film thicknesses in 1 nm steps in a 1–500 nm range. Volume fractions between 0.1 and 1 with a step size of 0.002 were permitted. The results are summarised

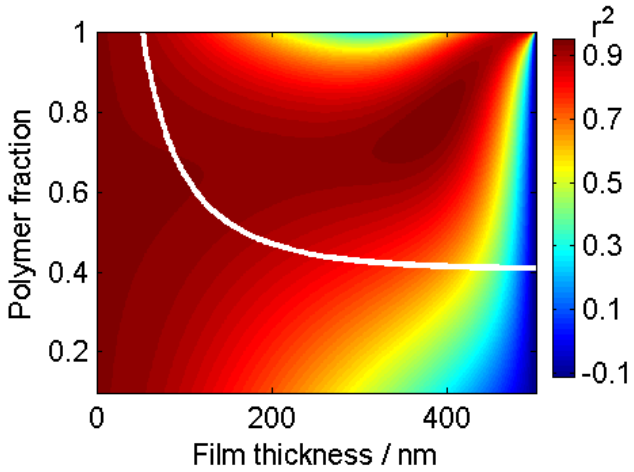

Figure 2.9: Overlap of the coefficient of determination map with the concentration band. The thickness and density of the film are determined by taking the (y, h) with the highest r^2 on the concentration band. On this map, $y = 0.63$ and $h = 81\,\text{nm}$.

in the table 2.2 below.

Table 2.2: Fitting results of the multiangle measurements.

Reaction time / h	thickness / nm	polymer fraction
0.3	60	1.00
1.0	98	0.70
2.0	81	0.63
4.0	83	0.72
8.0	60	1.00
12.0	108	0.52
24.0	84	0.62
30.0	86	0.80

The thickness data shows no correlation between the film thickness and reaction time. The film thickness is expected to increase with time as the chains are growing. Polymer fractions of 1 were determined for two of the datasets which is unlikely to be real. The thickness are also very similar to each other when the Raman spectra, shown in figure 2.10 for an angle of incidence of 72°, are actually quite different in intensity. The apparent errors in the calculated results might be due to experimental errors. Note that the overall intensity is not strictly increasing with reaction time. This might be due to the reaction having terminated prematurely on some hemispheres. Additional possible errors might stem from the beam delivery alignment, resulting in errors in the angle of incidence, as well as experimental errors during the recording of the concentration line.

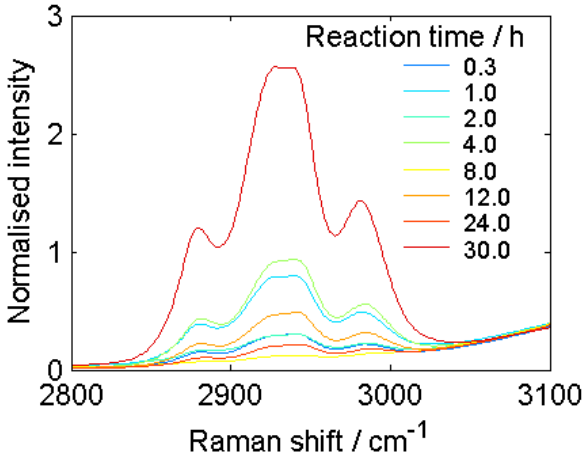

Figure 2.10: TIR Raman of eight grafted pNIPAM layers produced with varying reaction times. The spectra are normalised the the water signal.

The results show that more work needs be done to deliver reliable thickness and volume fraction data. The next step in the development should be the addition of a more realistic polymer profile. The step function could, for example be replaced with a parabolic profile. In terms of experiments, it would be beneficial to complement the TIR Raman spectroscopy with a second technique such as AFM measurements of the swollen chains to validate the model.

Since the model does not return reliable data yet, I am limiting thickness measurements to ellipsometry on dry films. The technique is described in section 2.3.

2.2 Raman imaging of surfaces

2.2.1 Optical path

The Raman imaging set up is an extension to the TIR Raman spectrometer described above (section 2.1). In the original setup, a telescope is introduced into the beam path to increase the laser beam diameter, which results in a smaller sized focus on the sample and increases the spectral resolution. In Raman imaging, a larger laser spot is of advantage since it increases the field of view. Therefore, additional mirrors (**M3-7**) are added to circumvent the telescope and deliver an unexpanded beam to the sample. Mirrors **M3** and **M7** are mounted on flip mounts and can be added easily to the beampath.

Inside the spectrometer (figure 2.12), additional mirrors **M2-5** steer the collected light around the grating. As a result, an undispersed image of the scattered light is formed on the CCD sensor. A tunable bandpass filter (TBP01-628/14-25x36, Semrock) (**TBF**) is mounted on a motorised rotation stage (CR1/M-Z7, Thorlabs) between **M3** and **M4**. The center of its transmission band changes with the angle of incidence from 630 nm at 0° to 589 nm at 40°. For this setup with a laser wavelength of 532 nm, the tuning range of the filter corresponds to 1450–3250 cm^{-1}. The image on the CCD camera is thus formed by only a defined part of the Raman spectrum.

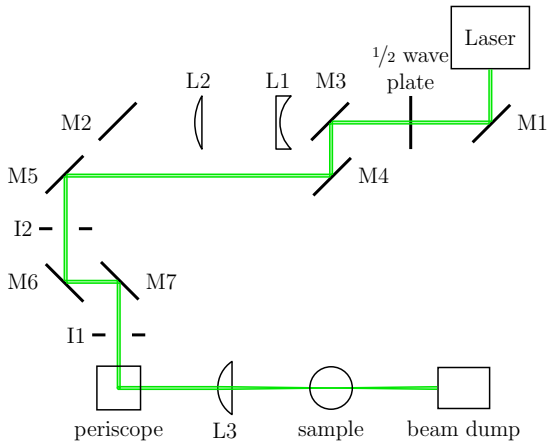

Figure 2.11: Beam delivery of the Raman imaging setup in the Bain laboratory, seen from above.[48] The laser beam bypasses the telescope (L1-2) before reaching the sample.

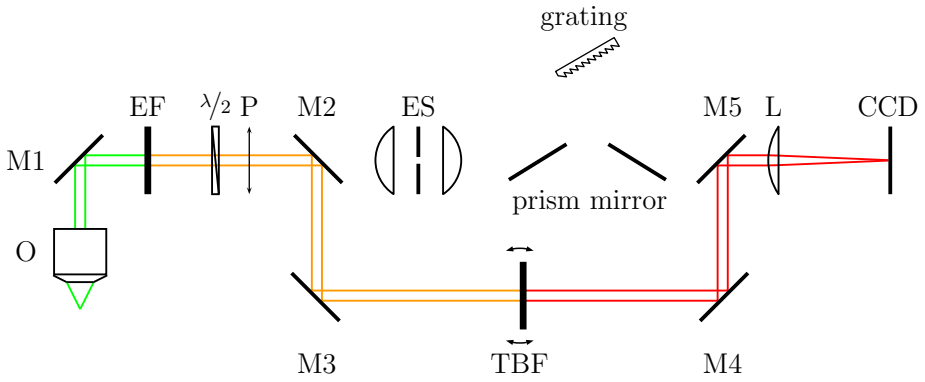

Figure 2.12: The beam path of the Raman imaging extension inside the Renishaw spectrometer, seen from the side.[48] Additional mirrors (**M2-5**) deflected the Raman scattered light from the grating onto a tunable bypass filter (**TBF**). The filtered light is focussed onto the CCD.

In order to be able to determine the spatial distribution of the different components in the sample, multiple images at different filter angles have to be collected. The four mirrors of the imaging path are aligned using a 632.8 nm HeNe laser light since the centre of the transmission band of the tunable filter at 0° is close to the HeNe laser emission wavelength. During alignment with the HeNe laser, a ND filter is added to the optical path to avoid any damage to the CCD.

2.2.2 Image collection and reconstruction

Choice of filter angles

To collect a Raman image of N components, a minimum of N filter angles is required. For each component there needs to be at least one filter angle with a transmission band that overlaps with its Raman spectrum. Recording images at more filter angles can improve the quality of the data and lower the noise.

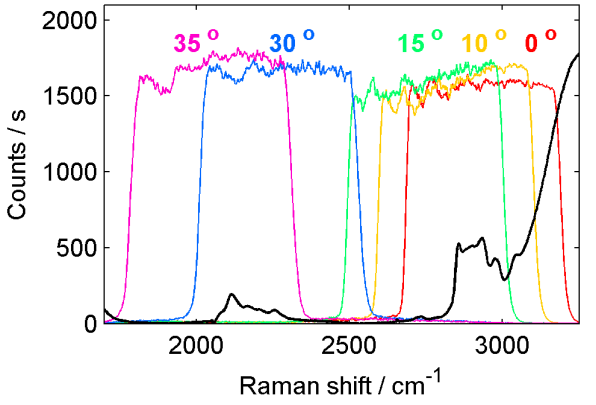

(a)

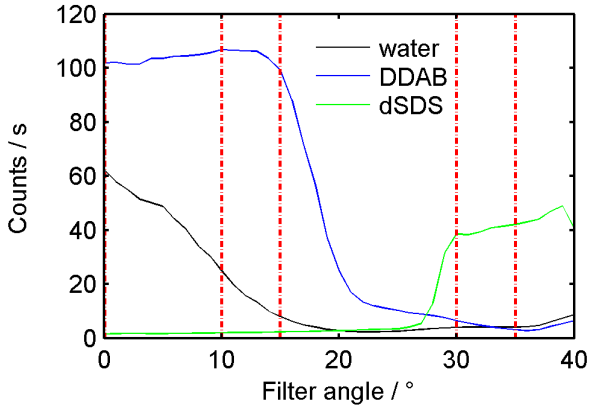

(b)

Figure 2.13: (a) Transmission curves of the tunable band pass filter for different filter angles overlapping with the spectrum of a mixed layer of DDAB–d-SDS. The corresponding filter angle is indicated above each filter curve. (b) Filter curves of water, DDAB and d-SDS. These curves were obtained from the transmission curves (a) and the Raman spectrum of each component. Vertical red lines show the chosen filter angles for the DDAB–d-SDS–water system.

Figure 2.13a shows the TIR Raman spectrum of a mixed layer of didodecylammonium bromide (DDAB) and deuterated sodium dodecyl sulfate (d-SDS) at the silica–water interface (black line). Superimposed are the transmission bands of the filter at five different angles. Using the reference spectra of each component, so-called filter curves can be plotted (see figure 2.13b). These curves show how much signal of each component is transmitted as a function of the filter angle. An algorithm has been developed in our group to find the best combinations of angles. [48] This algorithm simulates measurements obtained with a combination of all available filter angles. The number of angles is then reduced one at a time, removing the angle whose absence causes the smallest increase of error in the simulated component weights. For the layer of DDAB–d-SDS, these filter angles are: 0°, 10°, 15°, 30° and 35°. Figure 2.14 shows the Raman images collected at various filter angles. These images are then analysed to access the distribution of the different components.

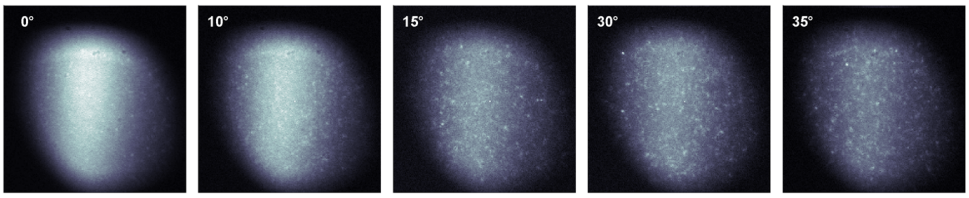

Figure 2.14: Raman images of a mixed layer of DDAB and d-SDS at each filter angle.

Sub-pixel precision image matching

As the Raman imaging technique requires the acquisition of a set of images, the information relating to a pixel is disseminated into a set of images. This relies on the hypothesis that there is enough commonalities between the images. This had been true for all images collected for this thesis. Therefore, it is essential to make sure that all images match with a pixel or even a sub-pixel resolution and any possible sample movement during the image acquisition is corrected. Cross correlation with the image collected at a filter angle of 0° has been calculated for each filter angle. The method relies on finding the maximum of the correlation surface, which gives the translational shift between the two images. Parabola fitting is used to determine the maximum of the peak, with a sub-pixel resolution. The correlation surface is computed using Fourier-transforms methods as they are fast and not resource-intensive. [52]

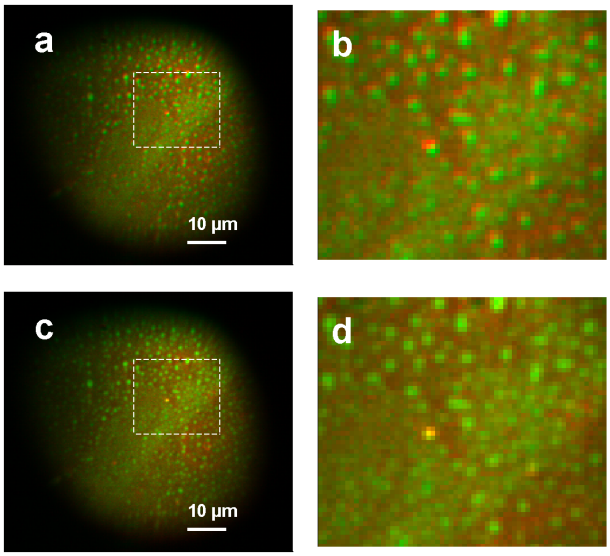

Figure 2.15: Raman images of adsorbed pNIPAM at 35 °C, showing the impact of sub-pixel matching on the quality of the reconstructed image. Image (a) and zoomed-in view (b) are reconstructed without the matching correlation fitting program while image (c) and zoomed-in view (d) are reconstructed with it. The detail images cover an area of 20 × 20 µm.

Figure 2.15 shows the impact of the matching correlation fitting program on the reconstructed image. In the zoomed-in view (b), the distribution of pNIPAM (in red) is systematically translated from the distribution of water (in green). This aberration is corrected by the image matching algorithm, as shown in the zoomed-in view (d).

Image reconstruction

Once the N images have been collected, a fitting algorithm is carried out to extract the contribution of each component in every pixel. Each pixel of the collected images can be expressed as a linear system of equations:

$$\begin{pmatrix} I_1 & I_2 & \cdots & I_n \end{pmatrix} = \begin{pmatrix} c_1 & c_2 & \cdots & c_m \end{pmatrix} \begin{pmatrix} f_{1,1} & f_{1,2} & \cdots & f_{1,n} \\ f_{2,1} & f_{2,2} & \cdots & f_{2,n} \\ \vdots & \vdots & \ddots & \vdots \\ f_{m,1} & f_{m,2} & \cdots & f_{m,n} \end{pmatrix} \tag{2.10}$$

where I_i is the observed intensity of that pixel at the i^{th} filter angle, c_j the unknown weight of the j^{th} component, and $f_{i,j}$ the convolution of the filter curve at the i^{th} angle with the spectrum of the j^{th} component weight.

The filter curves have been previously collected for any angle, so the matrix F is known. If $N \geqslant m$, this system can be solved through matrix inversion for each pixel giving the weight of each component. Figure 2.16 shows an example of the solution of the linear system.

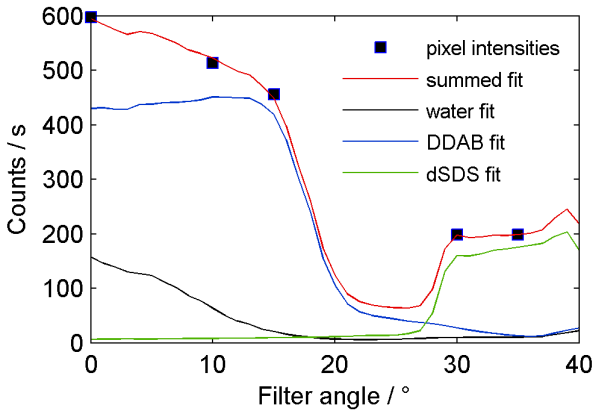

Figure 2.16: Solution of equation 2.10 for one pixel of a Raman image of mixed layer of DDAB and d-SDS. The graph shows the agreement between the recorded intensities (black squares) and the combined component weights (red line).

Pixels located at the edge of the field of view — where signal intensities are lower — might show negative component weights. As they have no physical meaning, such values are set to zero and the fitting procedure is repeated.

To allow the simultaneous visualisation of up to three components, RGB plots are created. Each component is expressed in either red, green or blue. The colour of the pixel in the RGB plot is a combination of the three colours. Pixels where all three components are present with similar weights will thus be shown as white. In this thesis, two-component RGB plots are shown where one component is set to red and one to green. Overlaps will appear consequently in yellow.

2.2.3 Calibration and post-processing

Scale bars of images are obtained by imaging a LaVision calibration ruler. This ruler has metallic spots of 5 µm of diameter, 20 µm apart. Figure 2.17a shows the images of the calibration rule obtained with a traditional white light microscope. The metallic dots have no spectra in the CH region as opposed to the glass they are deposited on. We can therefore obtain the Raman images shown in figure 2.17b.

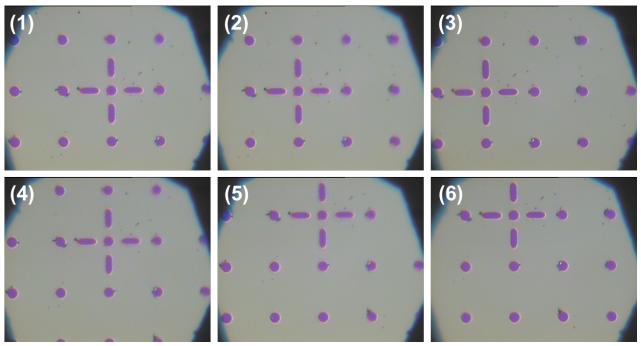

(a) Microscope images of the LaVision calibration ruler. The metallic cross is moved side ways and up and down.

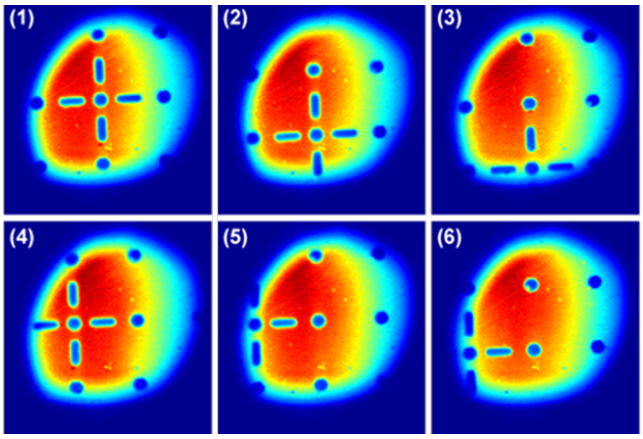

(b) Raman images collected from the LaVision calibration ruler. The letters correspond to the configuration of the microscope images shown above.

Figure 2.17: Microscope (a) and Raman (b) images of the LaVision calibration ruler.

The metallic cross of the ruler is used as the reference object to visualise the potential rotation and inversion operations required to overlap both images. The images read from the CCD and plot in Matlab undergo a counter clockwise rotation of 90° as compared to the microscope images.

After the Raman images are rotated, they are scaled by finding the positions of the center of the spots in pixels (see figure 2.18a), and converting a distance in pixels into a distance at the interface using an in-house written Matlab code. Final images are plotted with a scale bar calculated from this conversion. An example image is shown in figure 2.18b.

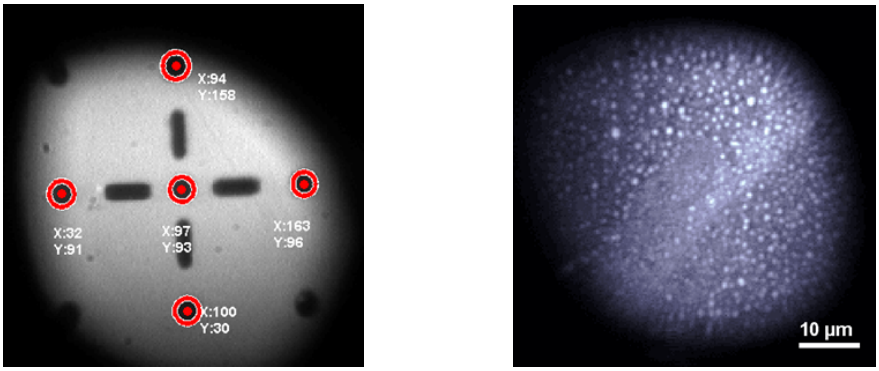

(a) (b)

Figure 2.18: Raman image of the LaVision calibration target (a) used for the image calibration and final Raman image of a layer of adsorbed pNIPAM at 35 °C (b). Scale bars are calculated from imaging the calibration ruler.

2.3 Ellipsometry

This section introduces ellipsometry which I have used to measure the dry thickness of grafted-from polymer films. Ellipsometers measure a change of polarisation of light upon reflection (or transmission) from a substrate. This change of polarisation is due to the dielectric nature of the interface and can be assigned to the presence of one or multiple film layers. Ellipsometry has been used previously to determine the thickness and/or the optical constants of thin polymer films, after being spin coated,[53] adsorbed[54] or grafted.[55]

2.3.1 Principle

Reflection ellipsometry determines the complex ratio r of the Fresnel coefficients in reflection for the S and P polarisations, $r_\perp$ and $r_\parallel$, as defined in section 1.5.2.

$$r = \frac{r_\parallel}{r_\perp} = \tan(\psi)e^{j\Delta} = \tan(\psi)\cos(\Delta) + i\tan(\psi)\sin(\Delta) = \mathrm{Re}(r) + i\mathrm{Im}(r) \quad (2.11)$$

with $\tan(\psi)$ and Δ being the relative change in amplitude and in phase of the two polarisations upon reflection. The Fresnel factors are related to the thickness and refractive index of the film.

2.3.2 Instrument

The Picometer Ellipsometer (Beaglehole Instruments, Wellington New Zealand) is equipped with a HeNe 632.8 nm laser source (Melles Griot, Germany). The sample is mounted on an anti-vibration table.

Figure 2.19 shows the set-up of the Picometer ellipsometer, which consists of a laser light source, a polariser producing linearly polarised light, a birefringence modulator, a second polariser and a detector. The birefringence modulator modulates the polarisation of the incident light at high frequency. The modulation has two advantages. Firstly, the polarisation of the light can be changed at high speed (1.5 Hz)

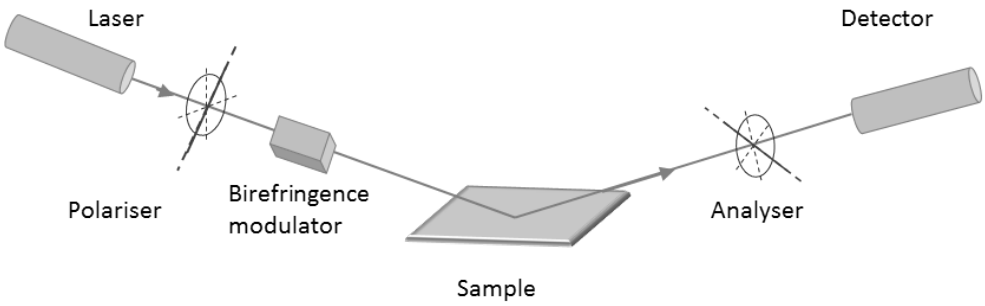

Figure 2.19: Layout of the Picometer ellipsometer.

and without moving any optics enabling fast and accurate measurement. Secondly, the modulation at a 50 kHz frequency reduces the noise.

The optics are mounted on two motor-controlled arms allowing computer control of the angle of incidence. The sample is placed on a kinematic platform mount attached to a Z-translation stage, enabling the sample to be positioned and levelled at the intersection between the laser and detection arms.

The laser spot at the sample is 1 mm wide. Temporal resolution can be as low as 1 ms. Data was averaged over 1 second for the measurements presented in this thesis.

2.3.3 Optical model and data analysis

The interface of a polymer-coated silicon wafer consists of three interfaces as a film of silicon dioxide forms on the chemically oxidised silicon wafer (see figure 2.20).

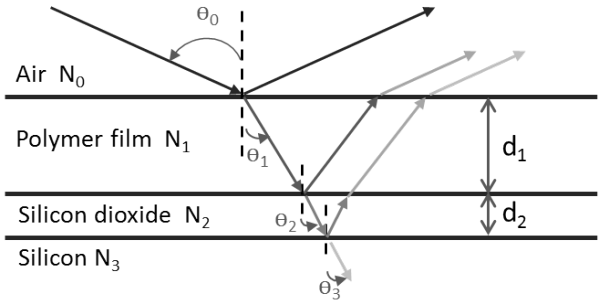

Figure 2.20: Reflection and transmission of a plane wave at the air-solid interface of a polymer-coated silicon wafer

Prior to polymerisation, the thickness, d_2, of the silicon dioxide layer is obtained by measuring the ellipticity at the air–silicon dioxide interface at 8 angles of incidence between 40° and 80°. The measurement is repeated after the polymerisation. In the thin film approximation, $\mathrm{Im}(r)$ is directly proportional to the ellipsometric thickness defined as:

$$\eta = \int \frac{(\varepsilon_1 - \varepsilon_0)(\varepsilon_1 - \varepsilon_2)}{\varepsilon_1} dz \tag{2.12}$$

with ε_0, ε_1, and ε_2 being the relative permittivities of the substrate, the thin film and

the medium at the laser frequency, respectively. This equation is used successively for a film of silicon dioxide on a silicon wafer in air, and a film of polymer on a silicon wafer in air. The relative permittivities and thickness used in the optical model are tabulated in 2.3. The thin film approximation breaks down when λ/d is not much smaller than 1.

Table 2.3: Relative permittivities and thicknesses used in the modelling of the polymer layer grafted onto silicon.

Layer	Relative permittivities [56]	Thickness
air	1.00	n/a
polymer and silane	2.25	d_1
silicon dioxide	3.90	d_2
silicon	11.68	semi-infinite

2.4 Circular Dichroism Spectroscopy

Most biopolymers in solution feature secondary structures stabilised by weak bonds. These structures are key to their biological functions and significant efforts have been made to establish spatial conformation of biomacromolecules in solution. Circular dichroism spectroscopy utilises the difference of absorptivity from these secondary structures to measure the conformation of macromolecules.

2.4.1 Principle

When a polarised electric field penetrates an anisotropic medium, such as a solution of macromolecules with a secondary structure, its amplitude and polarisation can be modified. Circular dichroism measures the difference in absorptivity of two electric field polarised circular left and right by a solution (see in figure 2.21a) .

Hence, at a given wavelength λ, the difference of absorptivity or extinction coefficients between a left (L) and right (R) circularly polarised light is:

$$\Delta\varepsilon_\lambda = \varepsilon_L - \varepsilon_R \tag{2.13}$$

The unequal absorption of the right-handed and left-handed polarised electric fields defines an ellipticity θ:

$$\tan\theta_\lambda = \frac{E_R - E_L}{E_R + E_L} \tag{2.14}$$

Figure 2.21b shows the components of the electric field in each polarisation of both the incident and emergent light. Circular dichroism measures this asymmetric absorption at different wavelengths in the UV range.

The ellipticity, θ_λ, is a linear combination of the ellipticity of its constitutive secondary structures:

$$\theta_\lambda = \Sigma\gamma_i\theta_{\lambda_i} \tag{2.15}$$

where γ_i is the fraction of each secondary i, and θ_{λ_i} is the ellipticity at each wavelength

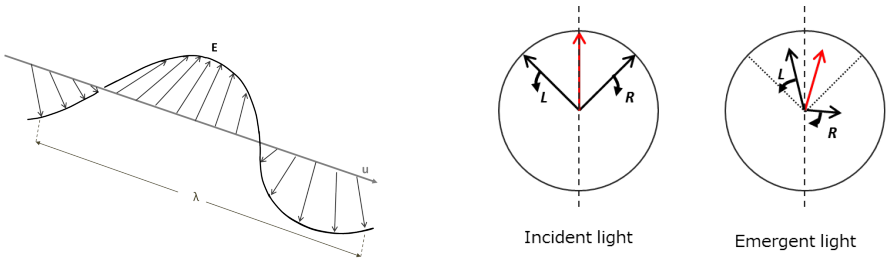

(a) An electric field E polarised circular clockwise, propagating along the u direction.

(b) Components of the electric field in each polarisation (black arrows) and their sum (red arrows), The comparison is made between the incident light and the light emerging through a CD active sample.

Figure 2.21: Asymmetric absorption of two circular polarised electric field induced by local anisotropy in a solution of macromolecules with secondary structures.

of each i^{th} secondary structural element. Analysing a CD spectrum consists in finding the fraction of each basis secondary structure as shown in figure 2.22.

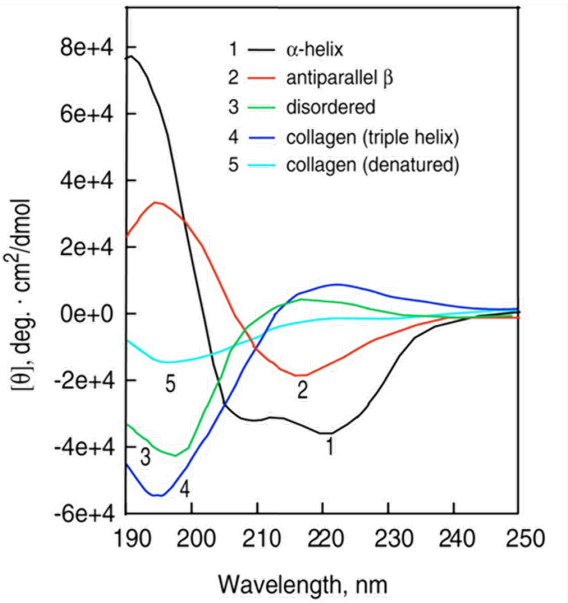

Figure 2.22: Circular dichroism (CD) spectra of polypeptides and proteins with representative secondary structures. Reproduced from reference [57].

Several algorithms are available to find the weight of each secondary structure. These algorithms use reference CD spectra of proteins whose secondary structure has been determined independently, for example by X-ray crystallography.[57] The reference data set of these algorithms influence the accuracy of the analysis of the secondary structure. I used the algorithm using natural and synthetic polypeptide based reference sets, LINCOMB, as recommended in the literature.[57] The Institute of Structural and Molecular Biology of Birkbeck College (University of London) has a server holding the fitting algorithms and reference data sets in open access for academics.

2.4.2 Experimental details

In a circular dichroism spectropolarimeter, a polarised monochromatic light is shone through a sample and the relative intensity of the transmitted light is detected with a photomultiplier. A schematic representation of a CD spectropolarimeter is shown in figure 2.23. As the difference of absorption between both polarised light is much smaller than the absorption of each, the CD signal can be quite noisy. Hence, the polarisation is modulated to high frequency via a photoelastic modulator. Thus, a fair fraction of the noise can be filtered out. Inside the spectrometer, a powerful UV lamp is used to generate the incident light. This lamp promotes the ionisation of oxygen in ozone, which in addition to be toxic, damages the optics. Therefore, the Jasco spectrometer is flushed with nitrogen to make sure all the oxygen is removed from the light chamber before the lamp is turned on.

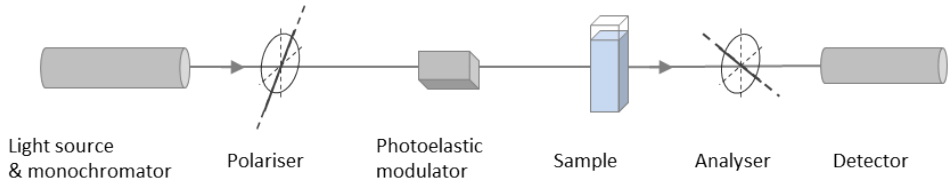

Figure 2.23: Layout of the Jasco circular dichroism spectrometer. For every wavelength (selected by a monochromator), the incident light is polarised. The polarisation is modulated by a photoelastic modulator. For every wavelength, the polarisation of the transmitted light is measured.

I used high-transparency quartz rectangular cuvettes with path length of 1 cm (Hellma, OG, 10 mm) as fewer artefacts are produced compared to the cuvettes with a smaller path length.[57] These cuvettes can be used to analyse very small quantities of material or when a buffer is not completely transparent. As no CD transparent buffer has dissolved polyvaline at detectable concentration, I chose to graft polyvaline from the cuvette to analyse its secondary structure in water or buffer. The grafting procedure is described in section 2.7.5. Prior to the measurement, the reference cuvette (with no polymer on its surface) is cleaned by a piranha mixture (see section 2.1.5) and rinsed with Milli-Q water. Both cuvettes are immersed in ultrapure water in a sealed container until use. A spectrum in air is first collected to make sure the lamp is stable and the optics aligned, which is confirmed by a non-drifting baseline. A background spectrum of water is collected with the reference cuvette. The wavelength is tuned at 5 nm per minute allowing a spectra resolution of 0.1 nm. Typical acquisitions consist of five accumulations.

The equivalent concentration of polyvaline is determined by measuring the absorption at 214 nm.[58] Assuming a uniform degree of polymerisation, a_{DP}, the molar extinction coefficient for a chain of length a_{DP} is:

$$\varepsilon_{\mathrm{polyvaline}} = \varepsilon_{\mathrm{valine}} \times a_{\mathrm{DP}} + \varepsilon_{\mathrm{peptide\ bond}} \times (a_{\mathrm{DP}} - 1) \tag{2.16}$$

with $\varepsilon_{\mathrm{polyvaline}}$, $\varepsilon_{\mathrm{valine}}$ and $\varepsilon_{\mathrm{peptide\ bond}}$ the molar extinction coefficient of respectively polyvaline chains, valine and peptide bond in $\mathrm{M^{-1}\,cm^{-1}}$.

2.5 Gel Permeation Chromatography

Gel permeation chromatography (GPC) or size exclusion chromatography (SEC) is a liquid chromatography technique separating polymer chains according to their hydrodynamic volume. Macromolecules dissolved in a solvent form coils with a size dependent on their molecular weight, M_w, and interaction with the solvent. Size exclusion chromatography uses a column filled with an insoluble porous material with pores of known sizes to separate macromolecules according to their molecular weight. Coils diffuse in and out from the pores, with larger coils being excluded from most pores. Therefore, the retention time (or retention volume) of analytes is inversely proportional to their hydrodynamic size. All GPC data are collected on a microporous silica column (Viscotek TDA 302, Malvern Instruments) with *N*,*N*-dimethylformamide (DMF) as eluent. Using a calibration curve (log M_w against retention volume) obtained from polystyrene standards, the retention volume is converted into molecular weight. Concentrations of chains at a given retention volume are determined by refractometry as shown in equation 2.17.

$$n_\mathrm{retention} = K_\mathrm{I} \left.\frac{dn}{dc_\mathrm{i}}\right|_{c_\mathrm{i}\to 0} c_\mathrm{i} \tag{2.17}$$

with $n_\mathrm{retention}$ being the refractive index, K_I an instrument dependent constant, n the refractive index of a solution of polymer in the eluent, c_i the concentration of polymer at a given retention volume.

Knowing the molecular weights, $M_\mathrm{w,i}$, and concentrations, c_i, of all retention volumes enables one to calculate the weight average $\overline{M}_\mathrm{w}$, number average $\overline{M}_\mathrm{n}$ and hence the polydispersity index, defined as the ratio of $\frac{\overline{M}_\mathrm{w}}{\overline{M}_\mathrm{n}}$. Calibration standards are linear chains of polystyrene. Molecular distributions are converted for linear chains of pNIPAM. The chemistry and the architecture of the sample lead to different values of $\left.\frac{dn}{dc_\mathrm{i}}\right|_{c_\mathrm{i}\to 0}$, hence to different concentrations, and different retention volumes. The variation of refractive index for pNIPAM in DMF at 20 °C is substituted to the polystyrene value,[59] and the chains are assumed linear.

In a typical experiment, 1 mg of polymer is placed in a glass vial with 1 mL of solvent and placed on a roller overnight until dissolution is complete. The sample is filtered and pushed into the column.

2.6 Preparation of mixed surfactant solutions

I have examined the potential of surfactant vesicles for transporting and releasing a cargo molecule from a surface. The model cargo is an anionic surfactant which does not adsorb onto the negatively charged silica surface on its own. I chose a cationic surfactant as a vehicle for transporting an anionic surfactant onto a negatively charged surface. This transport is made possible by the stability of catanionic surfactant system. In particular, DDAB–SDS form remarkably stable vesicles over a wide range of concentrations and ratios.[60]

Recrystallisation of deuterated sodium dodecylsulfate

Both surfactants are carefully recrystallised to ensure purity. For instance, SDS hydrolyses to dodecanol when dissolved in water reaching concentrations of up to 1 % within one day. Deuterated sodium dodecylsulfate (d-SDS) (Cambridge Isotope, 98 %) is recrystallised from ethanol following a procedure previously described.[61] All glassware, including Pasteur pipettes, is cleaned following the procedure described in section 2.1.5 and placed in an oven at 100 °C until use. In a typical recrystallisation procedure, 0.5 g of d-SDS is placed in a 10 mL glass beaker with a magnetic stirrer bar. 5 mL of ethanol (99 % high purity grade) is heated up in a 10 mL conical flask. 1 mL of hot ethanol is added to the beaker placed onto a hot plate. Hot ethanol is then added dropwise until all the d-SDS is dissolved. The mixture is left to cool down for 15 minutes so that crystals would form. Most of the solvent is then removed with a pipette. The procedure is repeated twice. White crystals are then dried under vacuum overnight. Purity is checked by equilibrium pendant drop tensiometry. The surface tension of a 5 mM solution of d-SDS freshly prepared is 35 $\mathrm{mN\,m^{-1}}$, which is in agreement with previous report for SDS.[62]

Recrystallisation of didodecyldimethylammonium bromide

Similarly, didodecyldimethylammonium bromide (DDAB) (Sigma Aldrich, 98 %) is recrystallised from acetone.[63] Crystals of both surfactants are placed in tubes filled with argon and stored in the freezer. The tubes are removed from the freezer 30 minutes prior to the sample preparation, the tubes are then dried with paper and opened inside the glovebox to prevent water crystals from forming on the surfactants. Purity is checked by equilibrium pendant drop tensiometry. The surface tension of a 1 mM solution of DDAB freshly prepared is 23 $\mathrm{mN\,m^{-1}}$, which is in agreement with previous report.[63]

Solution preparation

In a typical experiment, 10 solutions with a total surfactant concentration of 2.5 mM are prepared from fresh stock solutions. The concentration of the stock solutions is chosen to be 3 or 4 times higher than the final solutions in order to prepare all solutions from the same stock. At these concentrations, d-SDS remains below its critical micelle concentration (CMC), while DDAB forms unilamellar vesicles.[64]

Vesicles of DDAB are prepared by hydrating a thin film, following a similar method used in our group to form lipid vesicles. Typically, 0.1 g of recrystallised DDAB are placed in a 50 mL round bottom flask with ∼500 µL of chloroform. Chloroform is slowly evaporated by reducing the pressure to 70 mbar at 25 °C for 30 minutes. As the round bottom flask is slowly rotated, a homogeneous thin film of DDAB is formed on the bottom of the flask. The pressure is further reduced to 1 mbar to ensure evaporation of all chloroform. 40 mL of Milli-Q water is added to the thin film and the round bottom flask is sonicated for 30 minutes at 40 °C, so that DDAB is in its liquid crystalline state. The solution takes light blue turbid appearance, confirming the presence of vesicles. The solution is transferred to a 100 mL volumetric flask and

the concentration adjusted to 4 mM. The mixture is sonicated further for 30 minutes at 40 °C.

Stock solutions of d-SDS are prepared by dissolving 0.040 g of recrystallised deuterated sodium dodecylsulfate in 100 g of Milli-Q water and sonicated for 10 minutes at 40 °C.

The surfactant mixture solutions are prepared by slowly adding the d-SDS solution onto the DDAB solution, while maintaining the temperature of the mixture above the the transition temperature of DDAB (T_m = 16 °C). The turbidity of the mixed solution increases rapidly, indicating the formation of bigger aggregates. Milli-Q water is added as necessary, to reach lower surfactant concentrations.

2.7 Coating surfaces with polymers

The production of polymer films for releasing and uptaking cargo molecules has two prerequisites. First, the synthesis of polymer layers layer needs to be stable towards solutions of cargo molecules. Second, the layer has to be uniform and dense enough to prevent any interaction between the cargo molecule and the substrate. This section introduces two approaches for coating substrates with polymers, first by physical adsorption from polymer solutions and second by grafting polymers onto the surface. I will evaluate each of these approaches regarding the two criteria previously described.

2.7.1 Adsorption of polymers

The adsorption of polymers from a solution is a simple way of getting macromolecules onto a surface. This section presents the adsorption from aqueous poly(*N*-isopropylacrylamide) solutions.

Poly(*N*-isopropylacrylamide) chains with an average molecular weight M_w = 5000 g mol^{-1}, bearing uncharged end group were dissolved in Milli-Q water. The TIR Raman spectra of the solutions of pNIPAM at the silica–water interface are shown in figure 2.24a. Band assignment of pNIPAM spectra will be detailed in chapter 4. Spectra are collected from lowest to highest concentrations. After the highest concentration has been recorded, the cell is rinsed with 20 mL of ultrapure water. The surface excess is calculated by assuming that the surface is saturated at high concentrations. Further signal increase then corresponds to bulk polymer only. This slope can be used to determine the adsorbed amount from the excess signal at lower concentrations. The resulting isotherm is plotted in figure 2.24b. The detection limit of pNIPAM corresponds to 0.02 mg m^{-2}. pNIPAM adsorbs weakly onto hydrophilic silica with a maximum surface coverage, Γ_{max}, of ≈0.075 mg m^{-2}. However, once adsorbed the chain is difficult to lift off. Even if the attractive interaction between a segment of pNIPAM is small (compared to the thermal energy $k_B T$), there is a strong entropy penalty to lift off all the segment at once. Therefore once adsorbed, a polymer chain is more likely to remain on the surface.

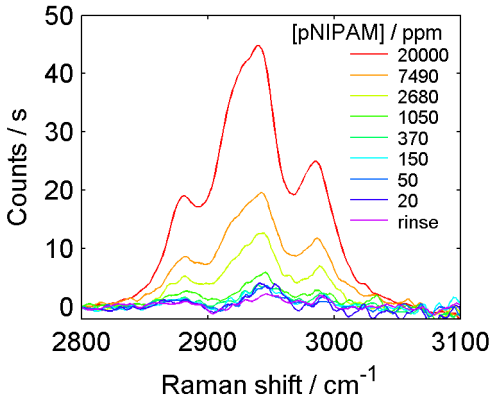

(a)

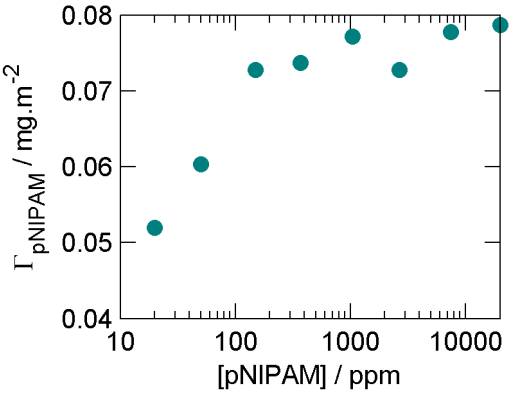

(b)

Figure 2.24: (a) TIR Raman spectra of solutions of pNIPAM at a silica–water interface and (b) isotherm of adsorption of pNIPAM onto hydrophilic silica at 20 °C.

2.7.2 "Grafting onto" and "grafting from" polymer layers

This section reports the synthesis of polymer layers chemically bound onto surfaces. The methods described in this section are not only applicable to the modification of planar silica surfaces, but can be transferred to other materials and to curved surfaces. There are two approaches of attaching polymers onto a surface called "grafting onto" and "grafting from", as represented in figure 2.25. These two methods differ by the order in which immobilisation and polymerisation occur. In the grafting onto approach, a pre-formed polymer chain is attached by its end group onto the surface. Typical protocols add an amine end-group onto an electrophile bound to the surface, such as an epoxide or a ketone. The main advantage of this approach is the possibility to measure the molecular weight and polydispersity index of the polymer chain before grafting. The only unknown left is the grafting density. The main disadvantage is the poor surface coverage, due to the steric hindrance between the chains.

The grafting from approach entails immobilisation of the initiator on the surface and a subsequent polymerisation step from the monomers in solution. This method enables a denser and more uniform coverage while leaving the grafting density, the molecular weight and chain polydispersity unknown. In spite of the difficulty of

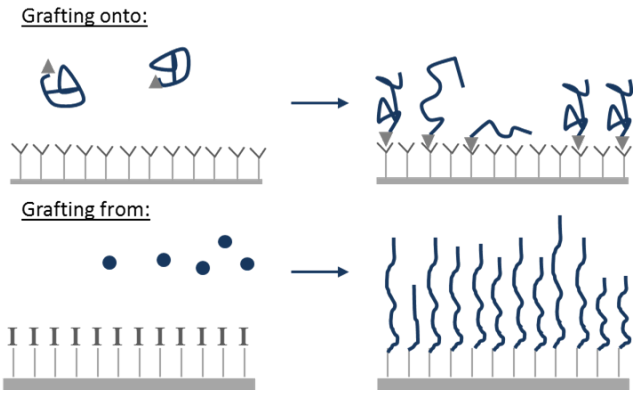

Figure 2.25: Drawings of the two grafting approaches.

getting structural parameters of the polymer layers, I opted for the grafting from method as it gives the means to prepare denser layers. Steric hindrance between preformed chains block the access to the surface and reduce the amount of material on the surface. Both grafting methods require the modification of silica substrates by fixing either the initiator of the polymerisation reaction, or a reactive group to the surface. The next section will detail the methods used to modify silica surfaces.

2.7.3 Modification of silica substrates

The surfaces of silica and silicon substrates is a network of Si−O bonds. These bonds are rather strong and organised in multivalent structures as shown in figure 2.26.

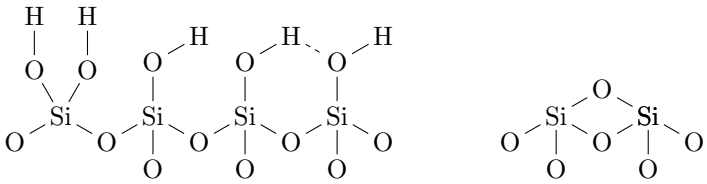

Figure 2.26: Si−O bonds are organised in silanols and siloxanes.

Silanols and siloxanes are composed of three or four Si−O bonds. Therefore, substrates are modified by condensation of a coupling agent, a silane which bears siloxanes which are easily connected to the silanol bonds. Silanes have been used extensively to modify the wettability of glass, for example to promote adhesion or hydrophobicity, or to add a new chemical moiety to the surface. In this work, silanes are used to couple an inorganic and unreactive surface with a highly reactive initiator of polymerisation. A wide range of silanes are available. Chain length, end group or number of silicate bonds can be easily tailored. I chose the coupling silane based on two criteria:

(i) a silane bearing a versatile end-group

(ii) a short hydrocarbon chain for sterics to get dense coverage and to enhance the sensitivity of polymers

The aminosilane aminopropyltrimethoxysilane (APTMS), see figure 2.27, is a good candidate as it satisfies both conditions.

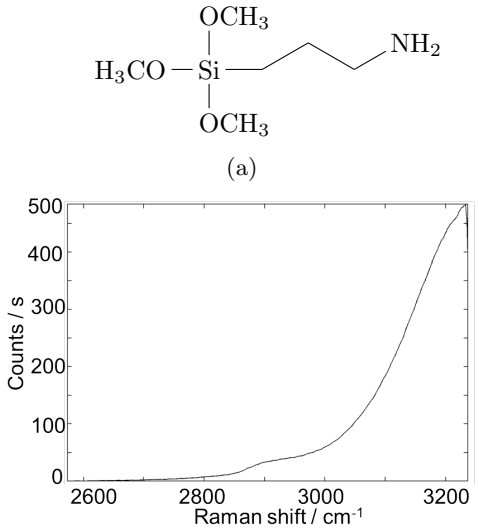

Figure 2.27: (a) Structure of aminopropyltrimethoxysilane (APTMS) and (b) TIR Raman spectrum of a layer of APTMS at the silica–water interface. The weak Raman intensity of APTMS makes it a good candidate as a first building block of grafted layers. Aminopropyltrimethoxysilane (APTMS) has been used as a coupling agent to modify silica and silicon substrates.

Aminosilanes are versatile and various chemical groups can be added onto the amine site, subsequently to the silanization. Also, APTMS bears a short hydrocarbon chain, thus giving a small Raman intensity, required to detect the subsequent spectra of polymer-coated prisms. Figure 2.27 shows the Raman spectrum of a silica hemisphere coated with aminopropyltrimethoxysilane at the silica–water interface. The weak TIR Raman spectrum of a layer of APTMS makes it a good candidate for a base for grafting polymer layers.

The general mechanism to covalently bind methoxysilanes onto a silica substrate involves the hydrolysis of the methoxy groups. The silanols formed react onto the silanols of the substrate by condensation. Aminopropyltrimethoxysilane can form three silica bonds, enabling horizontal polymerisation forming a dense and connected network of silane bonds. Vertical polymerisation is also possible. The consensus for producing reproducible, stable and homogeneous layers of aminosilanes by liquid silanization includes the following criteria:

(i) an anhydrous solvent. Controlling the amount of water is key for producing homogeneous and stable layers in a reproducible way. 10 mL of anhydrous toluene 99.8 % contain 20 µL of water.

(ii) low silane concentration to avoid self-polymerisation, typically 1 % v/v are used

(iii) after silanization, rinsing substrates with toluene, ethanol and water to displace

weakly bonded silane molecules. This step can also trigger the hydrolysis of residual alkoxy groups in the silane layer.

(iv) after the substrate is dried with a stream of nitrogen, a curing step (110 °C for 1 hour) promotes the conversion of silanol bond into siloxanes. This step also converts the ammonium ion into more reactive amines.

The bottle of APTMS is opened and stored in the glovebox to limit any extra adsorption of water supporting the polycondensation of APTMS. In a typical experiment, surfaces are placed into a Teflon beaker in an argon-purged glovebox, immersed in a solution 1 % v/v of APTMS in anhydrous toluene 99.8 % and left to stir for about 12 h at room temperature. Substrates are washed with copious amounts of toluene, taken out of the glovebox, immersed in ethanol and sonicated for 10 minutes to remove unbound silane molecules. The formation of the siloxane bond network is favoured by curing the substrates at 110 °C for an hour. To remove any silane non-covalently bound to the surface, the substrates are immersed in deionised water and sonicated for 30 minutes, see figure 2.28. Substrates are then dried with a stream of nitrogen. This protocol led to the formation of silane and polymer layers. The layers are stable in water for more than 24 hours.

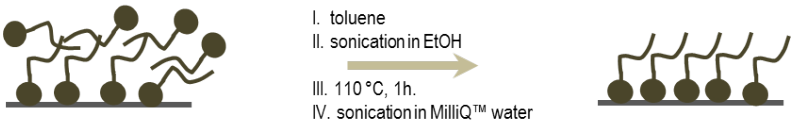

Figure 2.28: Removal of unbound APTMS, formation of a network of siloxane bonds onto the substrates.

2.7.4 Atom Transfer Radical Polymerisation

Controlled radical polymerisations — as opposed to free radical polymerisations — have enabled the synthesis of a variety of polymers with control over structure, polydispersity and molecular weight.[65,66] In a free radical polymerisation, a radical is created from the homolytic breakage of a bond (initiation) and monomers successively add onto the radical site (propagation) until termination occurs caused by, for example, a recombination of two radicals. In free radical polymerisations, the concentration of radicals is not controlled creating multiple active sites. Conversely, in controlled radical polymerisations, the availability of radicals is limited, slowing down the propagation step and having a small fraction of the chains active. In atom transfer radical polymerisations (ATRP), the concentration of radicals is controlled by an equilibrium between active and dormant chains. This is enabled by a catalytic agent transferring a labile atom (in general a halogen) to and from the chains as shown in figure 2.29.

The polymerisation rate, K_p, and the polydispersity index, $Đ_\mathrm{M}$, are then expressed as follows:[65]

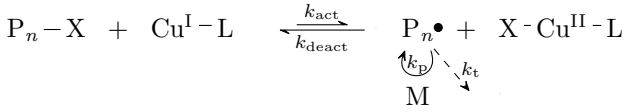

Figure 2.29: General mechanism of atom transfer radical polymerisation. The addition of monomer M onto a radical P$_n$• is controlled by an equilibrium of activation. A halogen atom X is transferred from a deactivated chain to a catalytic agent, here copper–based.

$$K_{\mathrm{p}} = k_{\mathrm{p}}[\mathrm{M}][\mathrm{R}^{\bullet}] = \frac{k_{\mathrm{p}} k_{\mathrm{act}}[\mathrm{RX_0}][\mathrm{M}][\mathrm{Cu^I}]}{k_{\mathrm{deact}}[\mathrm{Cu^{II}X}]}$$
$$Đ_{\mathrm{M}} = 1 + \left(\frac{k_{\mathrm{p}}\ [\mathrm{RX_0}]}{k_{\mathrm{deact}}[\mathrm{Cu^{II}}X]}\right)\left(\frac{2}{p} - 1\right). \tag{2.18}$$

with k_{p} being the propagation rate constant, k_{act} the activation rate constant, k_{deact} the deactivation rate constant, p the monomer conversion, [M] the concentration of monomer, [R$^{\bullet}$] the radical concentration, [Cu$^{\mathrm{I}}$] the activator concentration and [Cu$^{\mathrm{II}}$X] the deactivator concentration. Equations 2.18 show that the polydispersity index can be modulated with the addition of copper(II) (see the section below).

Transfer agents are often copper-based because copper can be easily oxidised by one degree and is readily available. Copper(I) is not very soluble in a lot of organic solvents and the equilibrium between the metal in its two oxidation states is fragile. To overcome this difficulty, an organic ligand folds around copper, stabilises it and keeps the activation or deactivation of the chain equally facile. The choice of the ligand is a function of the solvent and the acidity of the monomer. The stability constants of the complexes of copper(I) and copper(II), β^{I} and β^{II} in the chosen solvent, should also be high enough to overcome the larger concentrations of monomer and polymer which are competing ligands to copper. High catalytic activity also requires the additional condition of β^{II} being much larger than β^{I}. The geometry of the complex depends on the state of oxidation as the exchangeable atom is either present or absent in the coordination sphere. I opted for a normal ATRP *i.e.* using a catalytic system based on copper(I). This choice has been motivated by the possibility to use of anhydrous solvents, access to a glovebox and commercial availability of high purity copper(I). Copper chloride (CuCl(I)) has been used in this thesis with a content of copper(I) higher than 99.99 %. Copper(I) is stored in the glovebox to avoid oxidation. It is sold as beads and embedded in a glass ampule as it is sensitive to moisture. The glass ampule is opened inside the glovebox and CuCl(I) is partitioned into small batches that are weighed with a balance with a precision of 0.1 mg. The mass of each sample is used as a reference to calculate masses and volumes of the other reactants.

Atom Transfer Radical Polymerisation of *N*-isopropylacrylamide

In an attempt to follow the kinetics of *in situ* surface polymerisation of *N*-isopropylacrylamide (NIPAM) by Total Internal Reflection Raman spectroscopy (see

section 2.1), I aimed at polymerising in aqueous media, suitable for TIR conditions with silica substrates. Synthesis of polyacrylamides in aqueous media is reported from multiple sources[67,68,69] using multidentate ligands such as *N*,*N*,*N*′,*N*″,*N*″-pentamethyldiethylenetriamine (PMDETA) and 1,1,4,7,10,10-hexamethyltriethylenetetramine (HMTETA), shown in figure 2.33.

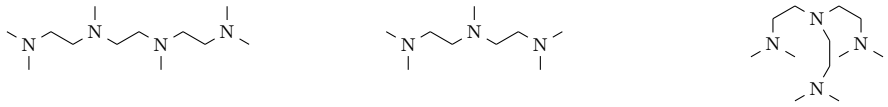

1,1,4,7,10,10-Hexamethyltriethylenetetramine
HMTETA

N,*N*,*N*′,*N*″,*N*″-Pentamethyldiethylenetriamine
PMDETA

Tris(2-dimethylaminoethyl)amine
Me_6TREN

Figure 2.33: Example of multidentate ligands used for ATRP

I carried out surface polymerisations with PMDETA and HMTETA in Milli-Q water. The conditions of polymerisation are shown in Table 2.4.

Table 2.4: Reaction parameters of surface-polymerisation of NIPAM in Milli-Q water using CuCl(I):PMDETA as catalyst and surface-attached ethyl 2-bromo-2-methylpropionate as initiator

Reactants	Mass / mg	*n* / mmol	Ratio
CuCl	3.0	0.03	1
NIPAM	342.0	3.03	100
PMDETA	10.5	0.06	2

The kinetics of the CuCl(I)/PMDETA-catalysed surface polymerisation of NIPAM was followed *in situ* using TIR Raman spectroscopy. Figure 2.34 shows the evolution of the integrated signal arising from the polymer's CH_2 stretches during the reaction.

This data indicates a fast growth of the polymer chains and a rapid termination of the reaction after about 10 minutes. This behaviour is due to PMDETA which is not binding strongly enough to copper(I) in order to overcome its disproportionation. The result is a free radical polymerisation. Copper(0), formed during the disproportionation, is embedded in the polymer layer and absorbs some of the laser light used for the Raman measurement. This causes damage to the polymer layer in the form of burn marks which are visible in the microscope image (see figure 2.35).

No polymerisation was observed with the ligand HMTETA.

These preliminary experiments showed that polymerisations in water with PMDETA and HMTETA will not yield the desired surface-grafted polymers. I thus decided to investigate protocols using different solvents even though I will not be able to follow the reaction *in situ* using TIR Raman spectroscopy.

In their work on the surface-polymerisation of NIPAM in DMSO, Suzuki *et al.* presented a thorough investigation of various reaction parameters.[66] They demonstrated their ability to produce uniform and dense pNIPAM layers with a controlled polydispersity. Silicon wafers modified with self-assembled thiols are used as substrates and the catalytic system is CuCl and Me_6TREN (figure 2.33). I decided to

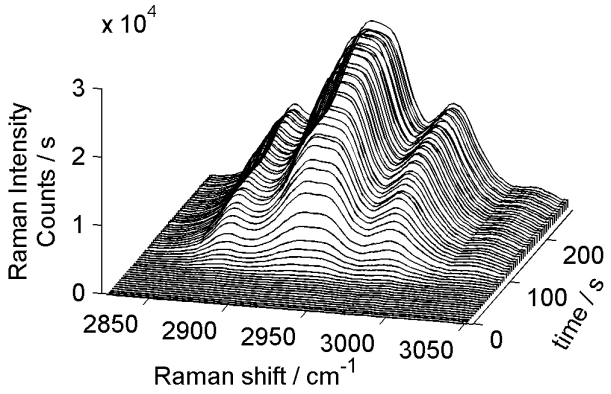

(a) Stack of Raman spectra from pNIPAM as it grows from the surface

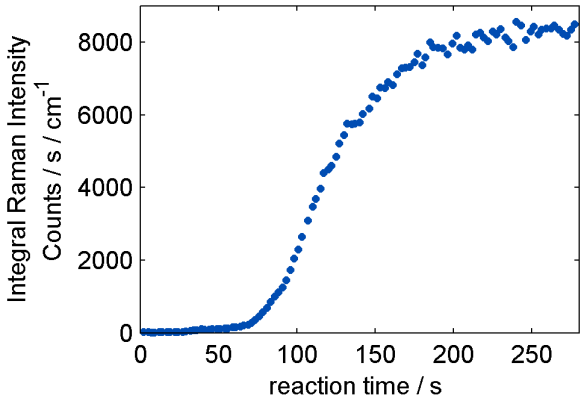

(b) Integrals of Raman intensities as a function of reaction time.

Figure 2.34: Kinetics of surface polymerisation of NIPAM in Milli-Q water using CuCl(I):PMDETA as a catalyst and surface-attached ethyl 2-bromo-2-methylpropionate as initiator.

use the findings of Suzuki *et al.* as the basis for the development of my synthetic protocol. In a typical experiment, 0.75 g of recrystallised NIPAM are dissolved in 5 mL of anhydrous DMSO and introduced in a two-neck round-bottom flask. The mixture is degassed by three freeze-thaw cycles and placed in an argon purged glovebox. In a second two-neck round-bottom flask, 30 µL of Me_6TREN are dissolved in 1 mL of anhydrous DMSO, degassed and placed in the glovebox. 10 mg of CuCl stored in the glovebox are left to stir in the DMSO/Me_6TREN mixture for 30 minutes. After dissolution of all beads of copper(I), the mixture becomes light green. 130 µL of this catalytic mixture is added to the first one and 5.6 µL of ethyl 2-chloropropionate to initiate the polymerisation. The reaction is stopped by taking out the mixture from the glovebox and left to stir overnight. The solution is concentrated to get a viscous green oil. The catalyst is removed by passing the mixture though a neutral alumina column. A transparent solution is obtained and further solvent evaporation leads to a white solid, which is analysed by NMR and gel permeation chromatography (see section 2.5).

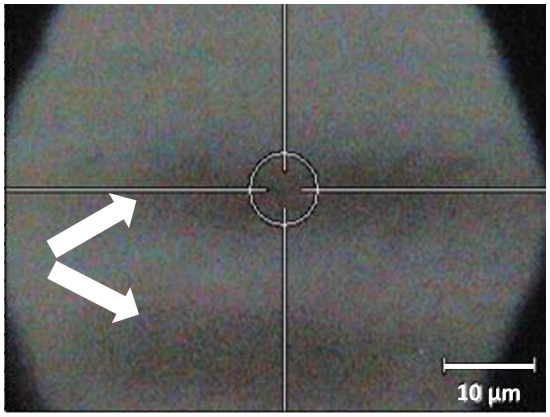

Figure 2.35: Microscope image of a surface-grown pNIPAM, presenting "burn" spots — shown by the white arrows. These burn marks are due to laser damage.

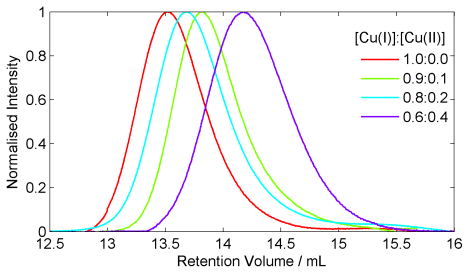

Cu(I):Cu(II)	M_w / g mol^{-1}	$Đ_M$
1.0:0.0	8000	1.3
0.9:0.1	7800	1.3
0.8:0.2	7200	1.7
0.6:0.4	3900	1.4

Figure 2.36: Gel Permeation Chromatograms of poly(*N*-isopropylacrylamide) chains obtained by ATRP for different Cu(I):Cu(II) ratios. All reactions were stopped after 7 hours. The introduction of copper(II) slows down the reaction but does not improve the polydispersity of the chains.

As the polydispersity index of the pNIPAM chains (see table 2.36) is higher than reported in the literature,[66] I decided to try to slow down the polymerisation rate by adding copper(II). As expected, the average molecular weight decreases with a rise in the concentration of copper(II) — with a similar reaction time — as shown in figure 2.36. However, the addition of copper(II) does not improve the distribution of polymer chains suggesting the ATRP is slow enough for disproportionation to occur. Therefore, a catalytic system only consisting of Cu(I) was selected. The final conditions for the surface initiated polymerisation of NIPAM are very similar to the optimised bulk one except that no free initiator is added to the mixture. Instead, the initiator of polymerisation is covalently attached to the silica surface.

Fixation of the initiator onto the surface

The initiator of the surface polymerisation has been chosen so that its activity, once at the surface, is close to the activity of ethyl 2-chloropropionate used for the bulk reaction. 2-chloropropanoyl chloride is a good candidate as the initiating site is activated in a similar manner. First, the chlorine atom regulating the activity of the chains is in the alpha position of the ester of the amide for the bulk or the surface, respectively. Second, the methyl group, also in the alpha position, stabilises the future radical and favours initiation. 2-chloropropanoyl chloride is fixed onto the

amine function of the silane by nucleophilic substitution, see figure 2.37.

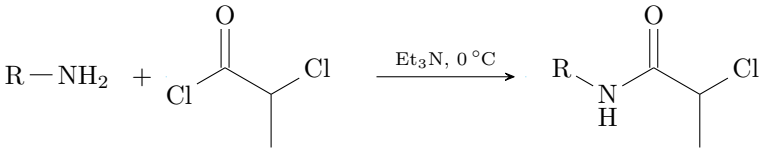

Figure 2.37: Immobilisation of the initiator of polymerisation onto an aminosilane coated substrate.

Following a procedure described in the literature,[70] substrates coated with aminosilanes are placed in 10 mL of anhydrous toluene and cooled down to 0 °C when 1 eq of trimethylamine is added. 15 minutes later, 1.1 eq of 2-chloropropanoyl chloride are added drop-wise. The reaction is stirred for an hour or until triethylammonium chlorohydrate precipitates as a yellow salt. Substrates are then washed with copious amounts of anhydrous toluene to remove unbound material and sonicated in ethanol for 10 minutes. The substrates are then dried with a stream of nitrogen and are ready for polymerisation.

Surface Initiated Atom Transfer Radical Polymerisation of poly(*N*-isopropylacrylamide)

Once the initiator is fixed, the substrates are immersed in a mixture of [NIPAM] : [CuCl] : [Me_6TREN] = 100 : 1 : 1 with a concentration of [NIPAM] = 0.3 M. The reaction is stopped by taking the sample out of the glovebox and rinsing it with DMSO and ethanol. The substrates are sonicated in ethanol for 5 minutes and in water for 30 minutes, and are then ready to be used.

With these conditions, it is possible to produce films of various thicknesses by varying the reaction time. Figure 2.38a shows the thickness of polymer films determined by ellipsometry as function of reaction time. The surface initiated ATRP is slow enough to fine tune the thickness of the polymer film.

The homogeneity of these films has been assessed by Raman imaging (see figure 2.38b). The resolution of the image is of 1 µm.

Surface Initiated Atom Transfer Radical Polymerisation of poly((2-dimethylamino)ethyl methacrylate)-*b*-poly(*N*-isopropylacrylamide)

The synthesis of the surface grafted diblock copolymer is done in two steps. First, the cationic monomer ((2-dimethylamino)ethyl methacrylate) (DMAEMA) is polymerised by ATRP following a procedure described in the literature.[71] In short, the reaction is performed in methanol — DMAEMA is not soluble in DMSO — with a [DMAEMA] : [CuBr] : [HMTETA] = 400 : 2 : 3 ratio and a DMAEMA concentration of 0.1 M. Prior to polymerisation, DMAEMA is purified by reduced-pressure distillation, to remove monomethyl ether hydroquinone. NMR confirmed the purity of the monomer and the absence of self polymerisation. After 4 hours, the substrates

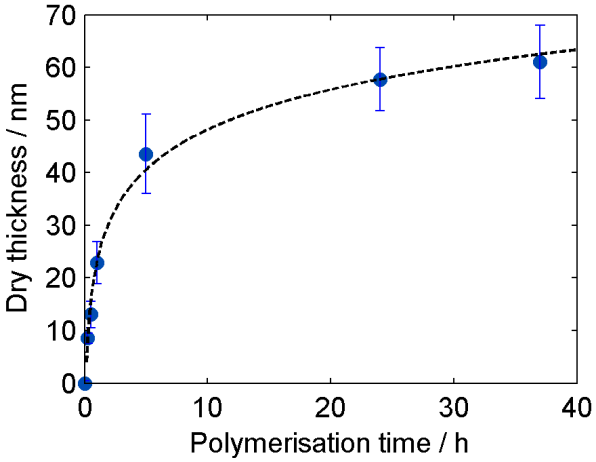

(a) Thickness of dry pNIPAM films as a function of polymerisation time. The error bars indicate the standard deviation. The dashed line is used as a guideline.

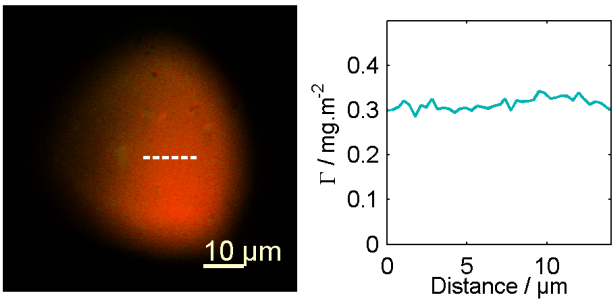

(b) Left: Raman image of a film of surface-grown pNIPAM. The resolution limit of the image is 1 µm. Right: Surface excess of pNIPAM along the cross-section highlighted in the Raman image.

Figure 2.38: Control over the production of pNIPAM in terms of thickness and homogeneity.

are sonicated in methanol and water. The polymerisation of the methacrylate is confirmed by the disappearance of the vinyl peaks in the Raman spectrum. Substrates are dried and ATRP of NIPAM is conducted following the conditions described above.

2.7.5 Ring Opening Polymerisation of polyamino acids

Polyaminoacids are synthesised by a ring-opening polymerisation of *N*-carboxyanhydrides formed from the corresponding amino acids.

Synthesis of *N*-carboxyanhydride of valine

The most common method for synthesising the anhydride is the dehydration of amino acids by phosgenation (Fuchs method). The reaction is shown in figure 2.39.

Triphosgene is preferred to diphosgene and phosgene as it is solid and safer to handle. Nevertheless, the reaction produces some lethal phosgene gas and extra care is taken to remove this gas and quench it as it is formed. The reaction is carried out in

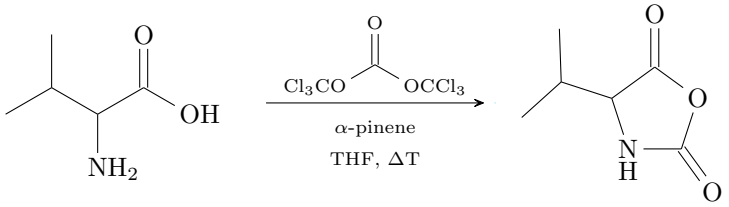

Figure 2.39: Phosgenation of valine into *N*-carboxyanhydride valine. The reaction produces the lethal gas phosgene and requires specific precautions.

a dry three-neck round-bottom flask with a condenser. A positive pressure of argon is set before the reaction is started and maintained for up to an hour after the end of the reaction. The positive pressure pushed phosgene gas out of the flask and into a beaker where it is bubbled through a sodium hydrogen carbonate solution. A pH indicator is used to monitor the accumulation of phosgene. Also, to prevent suck-back of any sodium carbonate solution into the reaction medium, a trap is inserted between the top of the condenser and the bubbling solution. Triphosgene is added via a pressure-equalised addition funnel. The dehydration of valine also produces small quantities of hydrochloric acid which can reopen the anhydride. α-pinene is therefore required as a scavenger. Typically, 2.3 g of valine (20.0 mmol, 1 eq) and 0.1 eq of α-pinene are dissolved in 20 mL of anhydrous ethyl acetate in a dry three-neck round-bottom flask. 0.34 eq of triphosgene (2.25 g, 7.5 mmol) are dissolved into 8 mL of anhydrous ethyl acetate.[72] The vessel is heated up to 50 °C, the funnel is opened and a third of the triphosgene is added. The other two thirds are added with a 30 minutes gap to avoid the accumulation of phosgene inside the round bottom flask. After 3 hours of reaction, the mixture is cooled to room temperature and the nitrogen flow is left on for 30 minutes to remove phosgene. The mixture is filtered and the solid, which is contaminated with trisphogene, dissolved in sodium hydrogen carbonate. Contaminated glassware is then immersed in a solution of sodium hydrogen carbonate. The filtrate is transferred to a rotary evaporator where most of the solvent is removed. A small quantity of sodium carbonate is placed inside the first collection flask in the rotary evaporator to quench any phosgene which would had been dissolved in the filtrate. A brown oil is obtained and washed with hexane to remove α-pinene. The valine anhydride is purified by recrystallising twice from a 1:1 hexane : anhydrous ethyl acetate mixture. Needles are dried under vacuum overnight. The 1H NMR (see Appendix) spectrum showed (d_6DMSO, 400 MHz): δH/ppm= 9.1 (1H, −NH−), 4.35 (m, 1H, −NH−CH−C=O), 2.06 (m, 1H, $(CH_3)_2CH-$), 0.96 (d, 3H, J = 6.9 Hz, $(CH_3)_2CH-$), 0.87 (d, 3H, J = 6.9 Hz, $(CH_3)_2CH-$) and confirms the cyclisation. The carboxyanhydride of valine is very sensitive to moisture and nucleophiles. Therefore, the polymerisation is carried out in a glovebox purged with argon and without exposing the sample to the environment.

Ring opening polymerisation of polyvaline from the *N*-carboxyanhydride of valine

Carbon dioxide is evolved during the ring opening polymerisation, see figure 2.40. Therefore, most procedures described in the literature[72] recommend sparging of

nitrogen into the reaction medium.

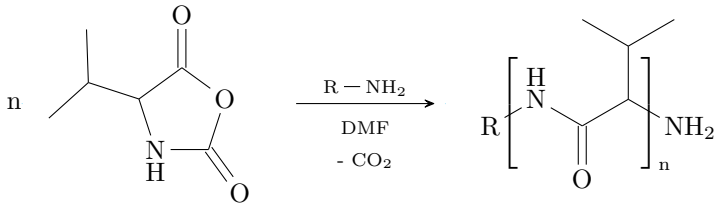

Figure 2.40: Ring opening polymerisation of *N*-carboxyanhydride valine.

Raman images from our custom rig (described in section 2.2) of polymer surfaces grown on silica surfaces using this method, showed circular patterns which may have been caused by the formation of bubbles on the surface. Since sparging did not produce homogeneous polymer layers, reactions were carried out inside a glovebox where the mixtures were simply stirred under an argon atmosphere. Specifically, aminosilane-coated silica hemispheres were placed in a Teflon beaker in the glovebox where 0.5 g of valine *N*-carboxyanhydride were dissolved in 5 mL of anhydrous dimethylformamide. The mixture was left to stir for 48 hours. Hemispheres were then taken out of the glovebox and sonicated in anhydrous dimethylformamide for 10 minutes, followed by ethanol for 5 minutes and water for 15 minutes, and dried with a stream of nitrogen. Hemispheres were stored in Teflon beakers covered with parafilm.

Chapter 3: Coadsorption and desorption of oppositely charged surfactant layers

3.1 Introduction

In this chapter, I will examine the potential of positively charged vesicles to incorporate, transport and release an anionic surfactant to and from a hydrophilic silica substrate. This ternary system (cationic vehicle, anionic cargo and solvent) is equivalent to what has been referred to as catanionic mixtures. In the first part of this chapter, I will summarise the literature on catanionic mixtures and detail some aspects of the theory of vesicles adsorption onto a surface. Then, I will present my results on the study of a double-chained cationic surfactant, didodecyldimethylammonium bromide (DDAB), used for incorporating an anionic cargo, deuterated sodium dodecylsulfate (d-SDS), onto the negatively charged interface of hydrophilic silica and water at a pH of 5.

3.2 Review

3.2.1 Surfactant assembly

Surfactants are amphiphilic molecules, with a hydrophilic head and a hydrophobic tail, which self assemble in aqueous solutions in order to minimise hydrophobic interactions. A conceptual tool for inferring the structures of surfactant assemblies from the molecule geometry is the packing parameter defined as the ratio between optimal area of the chain a_{hc} over the optimal area of the headgroup a_{hg}.[73]

$$p = \frac{a_{\mathrm{hc}}}{a_{\mathrm{hg}}} = \frac{V_{\mathrm{c}}}{A_0\ l_{\mathrm{c}}} \tag{3.1}$$

The volume of the chain, V_{c}, is calculated with the following equation established from alkane chains at their freezing point based on the number of methylene groups, $n_{\mathrm{CH_2}}$, and methyl groups, $n_{\mathrm{CH_3}}$:[74]

$$V_{\mathrm{c}}/\mathrm{\AA}^3 = 29.65 n_{\mathrm{CH_2}} + 34.81 n_{\mathrm{CH_3}} \tag{3.2}$$

The surface area of the headgroup, A_0, is determined from the aggregation number of single chains surfactant assuming they form spherical micelles. The chain length, l_c, is calculated following the Tanford formula:[75]

$$l_c/\text{Å} = 1.5 + 1.265 n_c \tag{3.3}$$

where n_c is the number of carbons in the tail.

When the area of the headgroup is about three times larger than the area of the tails ($p \approx \frac{1}{3}$), the surfactant molecules have roughly the shape of a cone, and tend to assemble as spherical micelles. When the area of the tails gets larger ($\frac{1}{3} \leq p \leq \frac{1}{2}$), the surfactant molecules look like truncated cones and assemble as cylindrical micelles. In the case of equal area between the headgroups and the tail, the surfactant molecules look like a cylinder and assemble as planar bilayers. In between the truncated cone and the cylinder, the molecule has a truncated cone shape (with a larger second base) and assembles as flexible bilayers or vesicles. When the area of the tails is larger than the headgroup, the same series of structures, although inverted, is predicted.

3.2.2 Vesicles

Among these structures, vesicles have attracted a lot of attention for their potential as encapsulating agents. Vesicles can protect the integrity of a molecule in a medium or dissolve both hydrophobic and hydrophilic molecules. The former can be trapped in the membranes while the latter are located in the aqueous internal cavity.[76] These systems have been studied as potential carriers in cosmetics,[77] pharmacology,[78,79,80] foods[81] or farming industries.[82]

In drug delivery, the compartmentalisation of a drug improves its stability in a biological medium towards hydrolysis, oxidation, and immune response and also reduces its toxicity.[76] Compartmentalisation also prevents potential incompatibilities with other drugs as recently demonstrated in a clinical study by Elsabahy *et al.*[80] who encapsulated vancomycin and acyclovir, an antimicrobial and an antiviral drug, in distinct vesicles. They found that when trapped inside separate vesicles, the co-precipitation of the two drugs was suppressed and oedema formation prevented. Oedemas are notably observed in the brain when the two drugs were injected together free in the body. The antimicrobial activity of vancomycin was preserved during the co-injection of acyclovir. Their study thus demonstrated the potential of vesicles in medical applications.

Vesicles are also capable of targeting various organs. With passive targeting, the vesicles are transported by the blood stream towards the cleaning organs or the reticuloendothelial system (liver, spleen and bone marrow) where they can be filtered out according to their size or surface charge.[83] For example, particles smaller than the renal threshold (40 kDa[84]) are filtered out by the kidneys. Passive targeting has been used to deliver contrast agents in kidney and liver imaging.[85,86] In active targeting, vesicles are tailored to increase their time in the blood stream bypassing the cleaning organs before reaching their targets where they can bind specifically.[87]

There are four typical vesicular systems: liposomes, niosomes, double tailed dialkyl surfactants and catanionic surfactant mixtures.

(i) Liposomes are vesicles made of lipids. They have been extensively studied for their potential as biocompatible drug carriers. Among them, phospholipids vesicles have attracted a lot of attention for their biomimicking properties as models of cell membranes. While their spontaneous formation has been reported in a few papers,[88,89] it is commonly accepted that their formation requires some energy such as sonication or extrusion. Vesicles of phospholipids are not thermodynamically stable structures and tend to aggregate into multilamellar structures with greater radius. They are usually quite expensive to fabricate and have a short half-life. It is possible to improve their stability by mixing phospholipids with surfactants. Such hybrid vesicles will be briefly discussed later in this section.

(ii) Niosomes are non-ionic surfactant vesicles that typically include additives such as cholesterol. These additives are often required to aid the vesicle formation[90] and make the membranes more rigid.[91] Niosomes are usually bigger than other vesicles, typically in the micrometer-range, allowing the delivery of more material. Niosomes have a longer shelf time than liposomes even though they also tend to aggregate. Their main advantage over liposomes is their stability versus osmotic pressure.[92] They share two disadvantages with liposomes: (1) they can induce hydrolysis and oxidation of the host and (2) they are permeable. Niosomes are formed by the same processes used for the vesiculation of liposomes.[93]

(iii) Spontaneous vesiculation has been observed with double tailed dialkyl surfactants. These surfactants tend to form bilayers, vesicles or sponge-like structures with packing parameters between 0.5 and 1. The resulting structures can take up a lot of water and are often used as swelling agents. In addition, due to the very low solubility of monomers in water — sometimes as low as 10^{-10} M for C18 chains[94] — the slow exchange of molecules between aggregates makes the structure of solutions of double-tailed dialklyl surfactants sensitive to their history. Among double-tailed dialkyl surfactants, quaternary ammonium salts are utilised in important applications as antimicrobial agents,[95,96] wetting agents,[97] and antistatic control agents.[98]

(iv) Mixtures of cationic and anionic surfactants can be seen as pseudo double-tailed dialkyl surfactants.[94] The term catanionic mixture was first used by Jokela *et al.* in a study on swollen lamellar phases of equimolar mixtures of oppositely charged surfactants.[99] Jokela *et al.* demonstrated that equimolar mixtures of catanionic surfactants can be used as the uncharged equivalent of zwitterionic phospholipids. They demonstrated that stable bilayers were formed simply due to repulsive hydration forces and not electrostatic interactions. In mixtures of cationic and anionic surfactants, bilayers were formed from single-tailed surfactants as a result of contraction of the polar heads due to the electrostatic interaction between the oppositely charged headgroups. The packing parameter of single-tailed surfactants could thus reach the ones of double-chained

surfactants and spontaneous vesiculation has been observed. Additional driving forces for vesiculation include the expulsion of counterions which can form a precipitate. Counterion-free catanionic surfactants, called "ion-pair amphiphiles" (IPAs), can be formed very easily by combining an organic acid and an organic hydroxide which assemble and release water rather than a salt. Various IPA systems and their properties have been described by Tondre and Caillet.[100] Their phase diagrams are similar to the ones observed for solutions of phospholipids. In addition, while vesicles of phospholipids are not thermodynamically stable and require ultrasonication and extrusion, vesicles of catanionic surfactants form spontaneously. Vesicles of surfactants give access to a larger range of compression and bending moduli than vesicles of phospholipids.[101] Their potential to replace phospholipids in formulation or drug delivery system has been investigated extensively.[102,103,104,105] In a recent paper, Dew *et al.* used the spontaneous vesiculation of catanionic mixtures to design encapsulating systems for a dozen cationic drugs such as tetracaine, lidocaine or atenolol with two anionic surfactants, capric acid and lauric acid.[106] Cryo-TEM was used to identify the composition leading to spontaneous vesiculation giving a range of ratios of drug to surfactant at constant total concentrations ($c = 40\,\mathrm{mM}$) for which vesiculation was observed. The release of the encapsulated drug from a gel (agar-agar or carbopol) was then followed using UV spectroscopy in a water-based medium. Diffusion of the encapsulated cationic drug out of the gel was 50 times slower than when free. The main disadvantage of catanionic mixtures is their poor biocompatibility. Even though strategies such has hybridation with lipids or the use of aminoacid-based surfactants[107] have been developed, there is currently no application in the medical field.

3.2.3 Catanionic surfactants mixtures

Phase diagrams

A typical catanionic phase diagram is shown in figure 3.1. At the equimolar ratio, the two surfactants form a precipitate. As one of the surfactant gets in excess, the stable structures move towards lamellar phases and charged vesicles, and finally micelles.

The interest in catanionic mixtures particularly increased when Kaler *et al.* observed spontaneous vesicle formation in aqueous mixtures of cetyl trimethylammonium tosylate (CTAT) and sodium dodecylbenzenesulfonate (SDBS).[108] The ternary phase diagram of CTAT/SDBS at 25 °C showed large vesicle domains (see figure 3.2 (b)). This diagram was constructed after equilibrium had been reached (visual observations). Equilibrium can take a couple of days to two weeks to be attained in most compositions while solutions containing vesicles usually require longer times. The presence of vesicles in these solutions was inferred by their blueish color and confirmed by cryo-TEM[108,109,110,111,112] or small-angle neutron scattering.[108,109,110,111,112,113,114] The symmetry of the phase diagram and the prevalence of the vesicle domains is related to the symmetry of the chain length of the two surfactants. Kaler *et al.* compared three ternary diagrams of mixtures of surfactant with the same headgroups

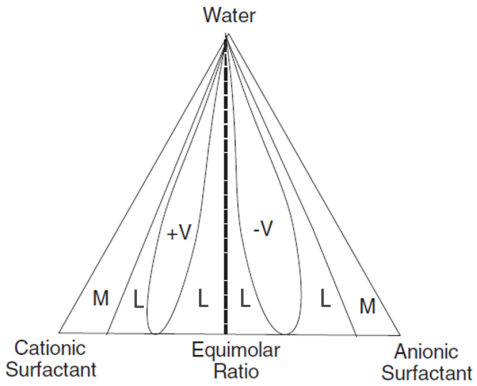

Figure 3.1: Typical phase diagram of a catanionic mixture. Upon addition of anionic surfactant to a cationic solution, the structures formed are micelles (M), positively and negatively charged vesicles (V+ and V-), a precipitate (line) and lamellar phases (L). Adapted from reference [76].

(sulfate and trialkylammonium), namely cetyl trimethylammonium bromide/sodium octyl sulfate (CTAB/SOS), cetyl trimethylammonium tosylate/sodium dodecyl benzyl sulfonate (CTAT/SDBS) and dodecyltrimethylammonium bromide/sodium dodecyl sulfate (DTAB/SDS).[115] The three diagrams are shown in figure 3.2. When the chains of the cationic and anionic surfactants are identical (DTAB/SDS), the range of compositions leading to precipitation is the largest. When the tails are highly asymmetric, such as in the CTAB/SOS system, a larger vesicular domain forms on the side of the shorter chain surfactant (i.e. SOS). Vesicles rich in the longer chain surfactant are restricted to a very narrow composition range. The phase diagram of CTAT/SDBS shows a vesicular domain in both sides with equivalent composition ranges.

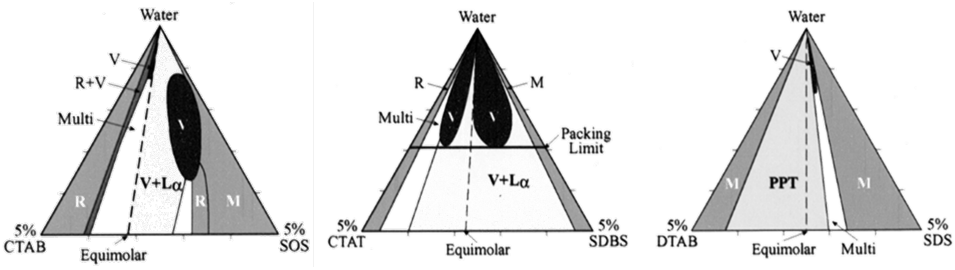

(a) (b) (c)

Figure 3.2: Phase diagrams of the catanionic mixtures of (a) CTAB/SOS, (b) CTAT/SDBS and (c) DTAB/SDS. V corresponds to vesicle, Lα to lamellar phase, M to micelles, PPT to precipitate, R to rodlike micelles. Reproduced from reference [115].

Encapsulation and permeation

Encapsulation by catanionic mixtures is typically tested on dyes for it is possible to discriminate trapped from free dye by fluorescence measurements.[116] Using this method, anionic and cationic CTAT/SDBS vesicles (V^+ and V^-) were both found to

encapsulate carboxyfluorescein (CF) much more efficiently (21 %) than phospholipids vesicles formed from egg-yolk phosphatidylcholine (1.6 %).[105] The half period of CF release was 84 days for the V^+ catanionic vesicles against 2 days for the phospholipids. Such an encapsulation efficiency for a single chain surfactant membrane is rather atypical and is associated with a specific electrostatic interaction between the anionic CF and the cationic membrane bilayer in addition to the inner water pool encapsulation. All CTAT/SOS vesicles and IPA were found to encapsulate carbofluroescein, riboflavein or glucose rather poorly[117] while SDBS-rich vesicles of SDBS/CTAT encapsulated CF sucessfully.[105] Wang *et al.* investigated the encapsulation of cationic and anionic drugs by both positively and negatively charged mixed surfactant vesicles.[116] They found that the charge effect on the encapsulation was strong enough to selectively capture and separate cargo molecules. The change in size of the vesicles due to encapsulation was determined by light scattering and small angle scattering. Vesicles of catanionic mixtures which became larger upon the uptake were separated from the rest of the vesicles by size exclusion chromatography. It was even possible to selectively retrieve a particular drug from a mixture.[116] These results highlight the subtlety of interaction between the cargo and the vesicle.

In 1998, Chung *et al.* demonstrated that vesicles formed spontaneously from multichain ion-pair amphiphiles could be a lot less permeable than catanionic mixtures. The membranes of didodecyldimethylammonium and dioctadecyldimethylammonium vesicles were very resistant to dilution and the encapsulation of carboxyfluorescein even resisted dialysis. The release could be triggered by breaking the membranes through addition of other surfactants such as SDS and Triton X. In 2012, Jiang *et al.* used the double-chained anionic surfactant bis-(2-ethylhexyl)sulfosuccinate sodium salt to transport tetracaine via mixed surfactant vesicles.[118]

Delivery of DNA material

Gene therapy is bringing immense hope for curing some genetic diseases or malignant forms of cancer by inserting missing or corrupted DNA into defective cells. Nucleic acids can be inserted inside the kernel of a cell via an impotent virus (tranfection) or via a liposome (lipofection). Transfection is the most commonly used method although the production of transfective viruses is not without difficulty or risks. In addition, the amount of material that can be delivered into the cell is rather small compared to what is required for an effective gene therapy. Lipofection is a promising alternative as it allows a denser packing of DNA. A mixture of cationic and non-ionic surfactants could provide a solution to densely pack DNA. And if positively charged, this mixture could penetrate the cell membrane and deliver the DNA material. The main advantage of lipofection is the ability to transport more material than tranfection. The efficiency of the method remains relatively poor, partly due to the little knowledge on the vesicle-DNA complex in water. The stability of the DNA strands is hindered by potential aggregation of the complexes. DNA strands are not only encapsulated inside the vesicles but also cover their surface. In buffer solutions and in the body pH, the presence of DNA around the vesicle is enough to decrease the zeta potential of the positively charged vesicles until aggregation occurs.

3.2.4 Vesicles at interfaces

Biological membranes are highly complex assemblies ensuring the cohesion of living cells as well as the transfer of information and materials in and out of it. They are made of lipid bilayers held together by hydrophobic interactions. They also contain proteins, typically anchoring proteins, ion transporters, receptors, glycolipids and glycoproteins. In biophysics, biological membranes are modelled by the homogeneous surface of confined lipid bilayers, which allows the control of global parameters such as the lipid density as well as the curvature or the stiffness of the bilayer. In practice, lipid bilayers can be simply supported by the solid. Methods include solid-supported lipid bilayers (SLB), and confinement on a polymer cushion or a self-assembled monolayer such as thiols on gold, silanes on glass or silica. Furthermore, lipids can be tethered or even freely suspended as shown in figure 3.3.

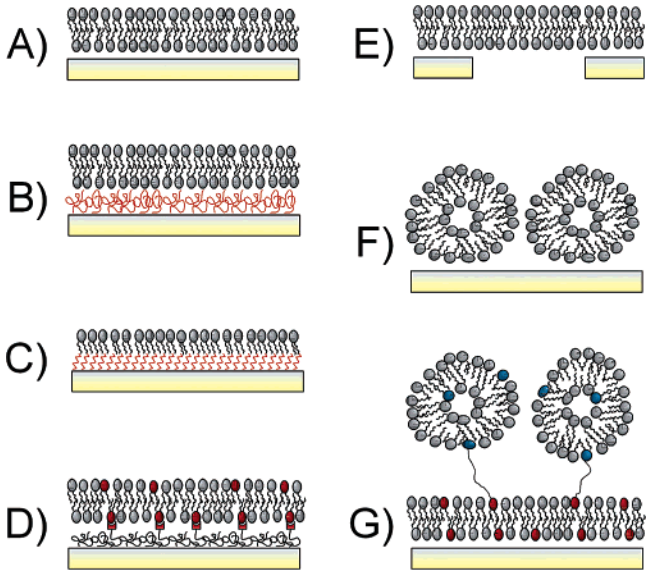

Figure 3.3: Methods to produce surface-confined lipid layers. (A) solid-supported lipid bilayer. (B) polymer-cushioned lipid bilayer. (C) lipid monolayer on a self-assembled monolayer (*e.g.* thiols on gold, or silanes on glass or silica) (D) tethered lipid bilayer (E) freely suspended lipid bilayer (F-G) supported vesicular layers. Reproduced with permission from reference [119].

The formation of a solid-supported lipid bilayer (configuration (A) in figure 3.3) is a one-step procedure allowing a simple way of producing SLBs of various lipids and lipid mixtures.[120,121,122,123] The mechanism of the formation of supported lipid bilayer has two stages: (i) the adhesion of the vesicles onto the substrate and their subsequent rupture into bilayer patches and (ii) the evolution of these patches into a complete SLB.[119] The driving force for the adsorption is the gain in adhesion energy which overbalances the energy penalty caused by the bending the vesicle, especially at its edges. Figure 3.4 shows a schematic indicating the position in the membrane of an adsorbed vesicle where bending stress is the largest.[124] The formation of a hole can release some of this stress. This local relaxation is counterbalanced by another bending penalty for the formation of the new boundaries around the hole.[125]

Some theoretical aspects on the shape of the vesicles during their adhesion process

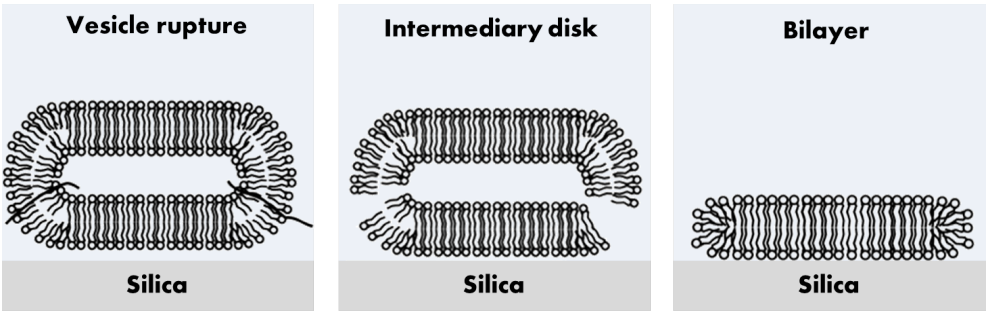

Figure 3.4: Schematic of a cross section of a vesicle rupture subsequently to its adsorption. Adapted from reference [126].

onto a surface will be described in this section. A surface can be described locally by two curvatures, $c_1 = \frac{1}{R_1}$ and $c_2 = \frac{1}{R_2}$ with R_1 and R_2 being the radii of curvature in two perpendicular directions as shown in figure 3.5. There is an energy density,

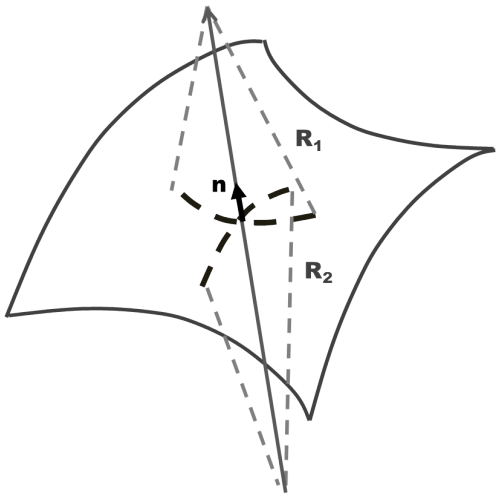

Figure 3.5: Description of the local curvatures of a lipid membrane. The first radius of curvature is defined as the radius of the largest sphere which best fits a normal section of the surface. The second radius is defined in the same way in the direction normal to the surface and perpendicular to the other normal. Adapted from reference [127].

f_c, associated with this curvature. The curvature energy density is defined assuming that the membrane is locally elastic:

$$f_c = \frac{1}{2}\,\kappa_1\,c_1^2 + \frac{1}{2}\,\kappa_2\,c_2^2 \tag{3.4}$$

with κ_1 and κ_2 being the bending rigidity in the directions 1 and 2, respectively. Equation 3.4 can be rearranged as[128]

$$f_c \;=\; \frac{1}{2}\,\kappa\,(c_1 + c_2)^2 + \overline{\kappa}\,c_1 c_2 \tag{3.5}$$

which defines two moduli with κ being the bending modulus and $\overline{\kappa}$ the saddle splay modulus. This equation assumes that the membrane is symmetric. If it is not, an additional curvature term called spontaneous curvature, c_0, is introduced and

subtracted from equation 3.5.

The gain in free energy during adhesion is proportional to the adhesion area A such as

$$f_{\mathrm{a}} \;=\; -W\ A \tag{3.6}$$

where W is the effective free energy per unit of contact area.

Vesicles will adsorb to the surface if the gain in energy due to adhesion can compensate the stretching and bending energies $f_{\mathrm{a}} \;\geq\; f_{\mathrm{c}} + f_{\mathrm{G}}$. For spherical objects, the Gaussian curvature energy is $f_{\mathrm{G}} = 0$ (Gauss Bonnet theorem). Since the adsorption energy is a function of the radius of the vesicles while the bending energy is not, there will be a critical radius R_{a} above which adsorption will become favourable:

$$R_{\mathrm{a}} \;=\; \sqrt{\frac{2\kappa}{W}} \tag{3.7}$$

Once adsorbed, a vesicle will rupture if the energy associated with the adsorbed vesicle is greater than the energy of the adsorbed disk resulting from the rupture. The free energy of an adsorbed vesicle f_{bv} is given as

$$f_{\mathrm{bv}} \;=\; -2\ \pi\ W\ R^2 \;+\; 2\ \pi\ g\ \sqrt{2\kappa W}\ R \tag{3.8}$$

with g being a numerical constant, and R the radius of the vesicle. The free energy of an adsorbed disk f_{bd} is

$$f_{\mathrm{bd}} \;=\; -4\ \pi\ W\ R^2 \;+\; 4\ \pi\ \Sigma\ R \tag{3.9}$$

with Σ being the line tension of the adsorbed disk.

There is rupture of the adsorbed vesicle if $f_{\mathrm{bd}} \leq f_{\mathrm{bv}}$. Consequently, a critical radius exists above which the vesicle ruptures:

$$R_{\mathrm{rup}} = \frac{2\ \Sigma -\ g\ \sqrt{2\kappa W}}{W} \tag{3.10}$$

Figure 3.6 shows the deformation of a single vesicle during the adsorption as a function of the interaction potential. Kasemo *et al.* have also calculated the total energy at different points of the vesicles and showed that most of the bending stress is located at the edges of the vesicles.[124]

In the same study, they also show that neighbouring vesicles or patches can induce the rupture because of the energy released from reducing the number of edges. Therefore, a critical vesicular concentration would have to be reached to observe bilayer formation at the interface. Such a scenario has been observed by QCM-D and AFM. The results presented in figure 3.7 show very stable adsorbed isolated vesicles which would, above a critical concentration, coalesce with an already adsorbed vesicle or bilayer patch, rupture and form a bilayer. Richter *et al.* have recorded AFM images of bilayer patches of various lipids on mica with increasing lipid concentration. They have observed spontaneous coalescence of the neighbouring bilayer patches. They

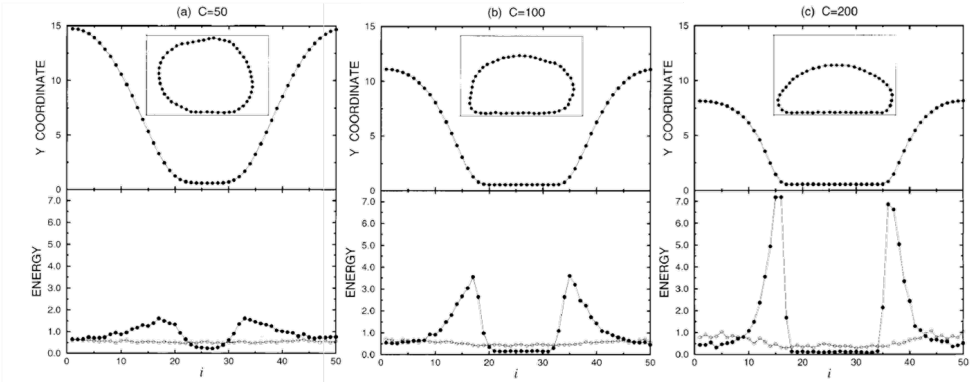

Figure 3.6: Average y coordinate of lipids (top) and bending and stretching energy (bottom) of an axisymetric vesicle made of 50 beads, for different intensity of interaction parameters with the substrate, C. Increasing C means increasing gain in adhesion energy. Reproduced with permission from reference [124].

also induced the coalescence with the AFM tip. Furthermore, they observed patches stable to both spontaneous and induced coalescence.[122] They concluded that the mobility of surface-bound vesicles was an important parameter and explained the surface aggregation or patches stability. The critical vesicular concentration is therefore related to the statistical distribution of patches or vesicles on the substrate. The other scenarios show typical QCM-D responses when the vesicles do not adsorb (A), the vesicles adsorb but do not rupture at any concentration (B) and vesicles rupture spontaneously (D).

In addition to the interaction potential of the vesicles with the substrate and their mobility once bound, other parameters can influence the SLB formation. Divalent ions and among them calcium ions in particular are promoting adsorption and rupture, even at low concentrations ($c \leq 1\,\mathrm{mM}$).[121,129,130,131] The physicochemical properties of the substrate surface are also important. For example, the basic treatment of silica substrate could reduce the hydroxylation state and modify the contact potential and alter SLB formation. The topography of the surface can bring an additional energy penalty to the SLB formation. Nevertheless, it was possible to deposit SLBs on silica films of high porosity.[132] The formation of SLBs can also be altered by modifying electrostatic interactions between the vesicles and the substrate, *e.g.* via a change of pH or ionic strength.[133]

A final consideration on lipid adsorption relevant to this chapter is the distribution of lipids in an adsorbed structure in mixed vesicles.[134,135] Richter *et al.* investigated asymmetries in mixed biyalers of 1,2-dioleoyl-*sn*-glycero-3-phospho-L-serine (DOPS) and 1,2-dioleoyl-*sn*-glycero-3-phosphocholine (DOPC) by introducing proteins that bind specifically to DOPS. For example, the bilayer formed on mica from vesicles composed of 20 % DOPS is highly asymmetric. The bulk-facing leaflet only contains 7 % of DOPS rather than the expected 20 %.[135] On the other hand, the same mixture leads to the formation of a symmetric bilayer on silica. Richter *et al.* attributed the asymmetry of the adsorption on mica to the influence of calcium ions.[134]

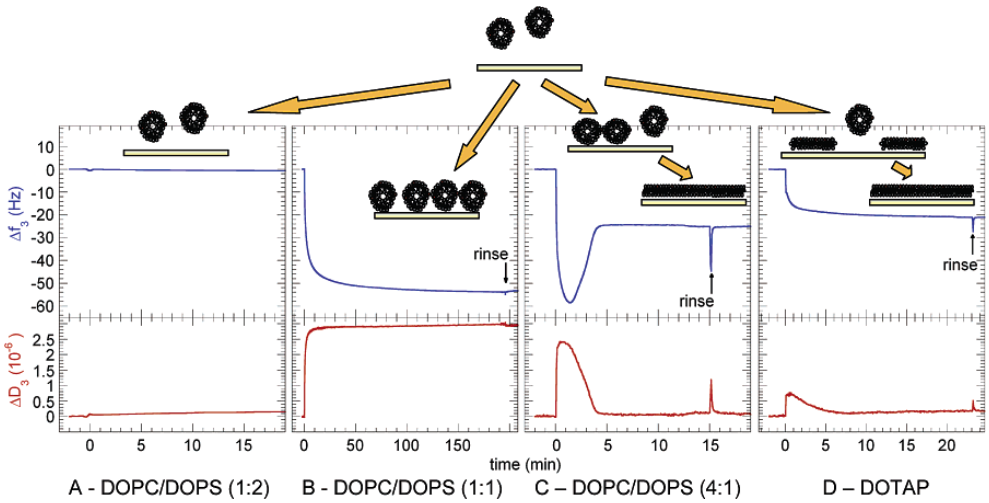

Figure 3.7: Different mechanisms of lipid vesicles adsorption onto a silica substrate identified by QCM-D. The adsorbed mass is given by the change in vibrating frequency of the quartz piezo, while the dissipation ΔD helps to distinguish between vesicles (high dissipation) and bilayer patches (low dissipation). Reproduced with permission from reference [119].

3.2.5 DDAB

Phase diagram of aqueous DDAB solutions

DDAB has a packing parameter of 0.66 and is therefore expected to form bilayers and vesicles. The packing parameter has been calculated using equation 3.1, based on a trimethylammonium headgroup size of 68 Å^2. The volume of 758 Å^3 and the l_c of 16.7 Å were calculated using equation 3.2 and the Tanford equation, respectively.

Vesicles of DDAB have been observed very early on by Kunitake *et al.* using cryo-TEM.[136] The phase diagram of DDAB solutions at 25 °C shows that vesiculation occurs at concentrations as low as 0.05 mM.[137] Additionally, scattering data showed that vesicles are unilamellar at concentrations up to 0.2 mM while multilamellar vesicles formed at higher concentrations. A cross polarisation study showed that lamellae start to form at [DDAB] = 0.7 mM. The fraction of lamellae gradually increases until the complete disappearance of vesicles at 21 mM.

The adsorption onto solid substrates from aqueous DDAB solutions has been followed by AFM[138,139,140] and neutron reflectometry.[141] Griffith *et al.* showed that DDAB adsorbs onto silica at the CMC, forming a weakly hydrated bilayer (7 % hydrated) with a thickness of 20 Å. This value is close to the l_c calculated with the Tanford equation. Surface vibrational spectroscopy showed the rather different picture of a disordered film.[142] At 0.1 CMC, a highly hydrated layer of 15 Å thickness was observed. At 0.5 CMC, the adsorbed layer thickens and gets denser (28 Å, 84 % hydrated). On mica, DDAB was found to form a complete bilayer at much lower concentrations: unhydrated layers with a thickness of 23 Å where detected at concentrations between 0.1 CMC and 0.5 CMC.[141] The adsorption of DDAB onto mica had previously been observed using AFM measurements.[138]

Phase transitions of DDAB at various concentrations have been measured by dif-

ferential scanning calorimetry (DSC).[137] Feitosa *et al.* recorded a sharp gel-to-liquid phase transition in DDAB vesicular solutions. The transition is exothermic with a critical temperature around 15 °C.[143] Baptista *et al.* measured a similar gel-to-liquid transition temperature at $T_m = 16$ °C,[144] collecting calorimetry data from liposomes of DDAB/DODAB (dioctadecyldimethylammonium bromide) mixtures of various ratios. They found that DODAB exhibits a gel-to-liquid transition temperature of 60 °C while the mixtures show two transitions: one at 15 °C and another one that varies with the mole fraction of DODAB. The authors also looked at the uptake and release of a dye by these vesicles. They found that for all compositions, cooling the mixture led to a release of the dye. For pure DDAB vesicles, the dye emission was found to be weaker above 15 °C indicating a liquid crystal phase. Additional DSC data have demonstrated the potential existence of an hysteresis in the DDAB gel-to liquid phase transition[137] since the liquid-to-gel transition was found to be at 9.5 °C.

3.2.6 Mixtures of DDAB and SDS

The phase diagram of the DDAB-SDS-water system at 40 °C was first determined by Marques *et al.* and is shown in figure 3.8. The addition of a small amount of DDAB to an aqueous SDS solution leads to the replacement of micelles by vesicles (blueish solution). The domain of stability of negatively charged vesicles is large. Further addition of DDAB leads to the formation of lamellaes. Close to the equimolar ratio, the precipitate DDA+ SD− forms but is quickly destabilised upon the introduction of a net charge.

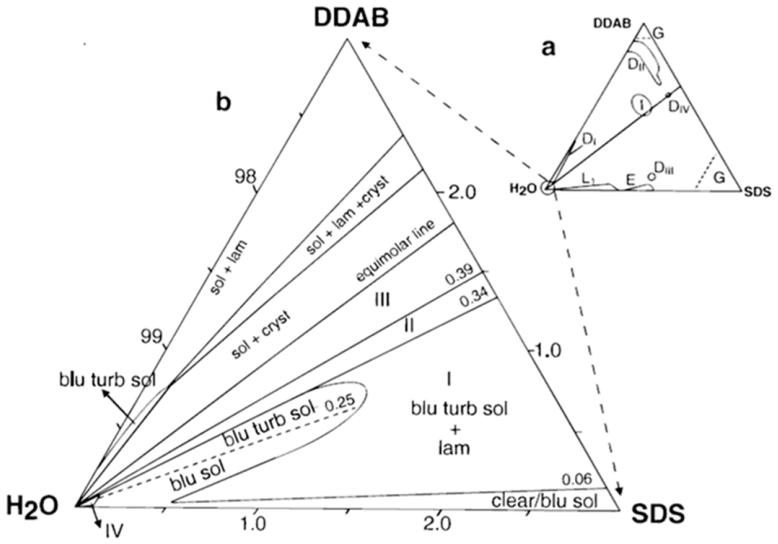

Figure 3.8: (a) Phase diagram for the SDS-DDAB-water system at 40 °C. Isotropic micellar (L_1), normal hexagonal (E), cubic (I), lamellar (D_{I-IV}) and crystals (G). (b) Phase diagram for the SDS-DDAB-water system at low surfactant concentration (lower than 3 wt%) 25 °C. Reproduced with permission from reference [145].

The phase diagram of dilute DDAB-SDS-water solutions was later determined by Marques *et al.*[145] When DDAB is added to SDS micelles (see figure 3.9) the expected

micellar growth — due to a change in the effective packing parameter and a partial screening of charged intra and inter aggregates and higher counterions concentrations — occured but on a very limited domain (up to 0.06 % of DDAB). Instead, vesicles — objects with a larger curvature — were observed very early on. The first order micelle-to-vesicle transition — common to many catanionic mixtures — was not observed for DDAB-SDS. Instead, disk shaped aggregate were formed leading to unilamellar, polydisperse and very large vesicles distributions. [145]

In the DDAB-rich region, see figure 3.10, pure vesicle solutions have a larger area upon introduction of SDS compared to the DDAB-water system. DDAB rich vesicles are unilamellar but polydisperse (the radii ranged between 0.1–5 µm). The average size of the vesicle distribution is furthermore a function of the catanionic ratio. This variation is non-monotonic and there is a critical ratio above which electrostatics replace packing effects as the dominating force. Below the critical ratio, the excess of DDAB is much lower than the salt concentration and the role of electrostatics is reduced. Tighter packing is possible via the SDS single chain which leads to a reduction of the vesicle size. Above the critical ratio, the electrostatic interactions between the DDAB molecules dominate and the vesicles are typically larger than pure DDAB vesicles.

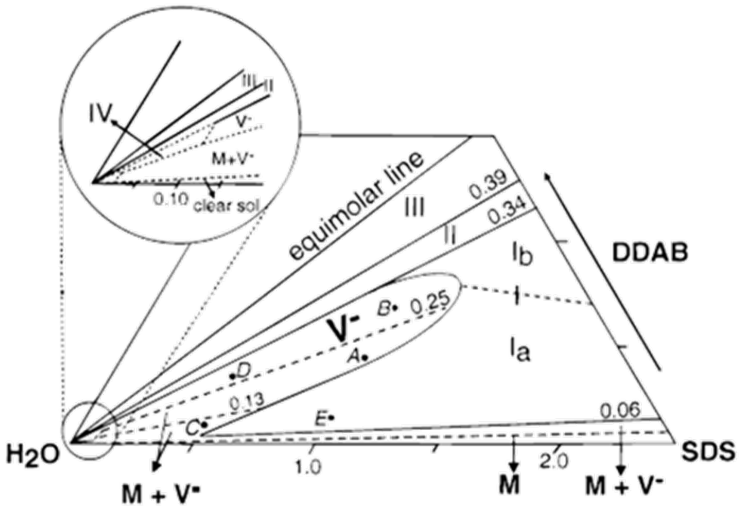

Figure 3.9: Phase diagram for the SDS–DDAB–water system at 25 °C on the anionic-rich side. The micellar region is reduced by the addition of DDAB and large domains of negatively charged vesicles V^- are formed. Reproduced with permission from reference [145].

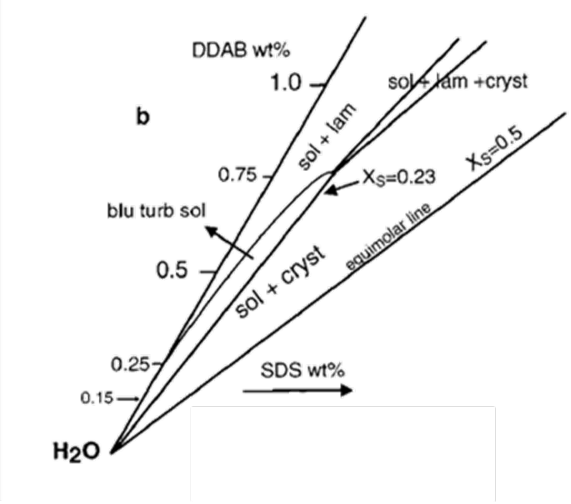

Figure 3.10: Phase diagram for the SDS–DDAB–water system at 25 °C on the cationic-rich side. Large domains of polydisperse positively charged vesicles V^+ are formed. Reproduced with permission from reference [146].

3.3 Results

In this section, I will describe and discuss the results obtained on the interaction of each surfactant and their mixtures with silica substrates. The primary aim of this chapter is to design a transport and release system for an anionic molecule to and from a silica surface. The hypothesis is that liquid-gel phase transition inside the DDAB bilayers will alter the binding constant of an anionic cargo. d-SDS is used as a model anion since it is known to form mixed vesicles with DDAB and can be easily monitored by TIR Raman scattering. The effect of temperature on the adsorbed layer has been investigated, along with the partition of d-SDS inside the two possible phases of DDAB. In addition, this chapter will also present the spectral markers to identify the onset of the phase transitions in a DDAB-based adsorbed layer.

3.3.1 Single surfactant systems

Band assignment of the d_{25}-SDS Raman spectrum

Throughout this chapter, sodium dodecylsulfate (structure shown in figure 3.11) is used in a nearly fully deuterated version ($\geq$ 98 atom% D), referred to as d-SDS. The most intense bands are located in the CD region as expected. The band assignment of the CD stretches is presented below.

The spectra of a solution of 10 mM of d-SDS in SY and SX polarisation are shown in figure 3.12. Six bands are resolved in both spectra. The assignment of deuterated aliphatic chain is established.[147] The band at 2075 cm^{-1} is assigned to the methyl symmetric stretch (r^+). The methylene symmetric stretch is located at 2107 cm^{-1}. Its higher intensity compared to the methyl symmetric stretch despite the lower Raman scattering cross section is due to the number of methylene groups in SDS. The signal at 2137 cm^{-1} corresponds to the Fermi resonance of the methyl symmetric stretch ($r^+{}_{FR}$). The band at 2204 cm^{-1} is assigned to the antisymmetric methylene stretch

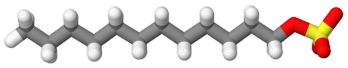

(a)

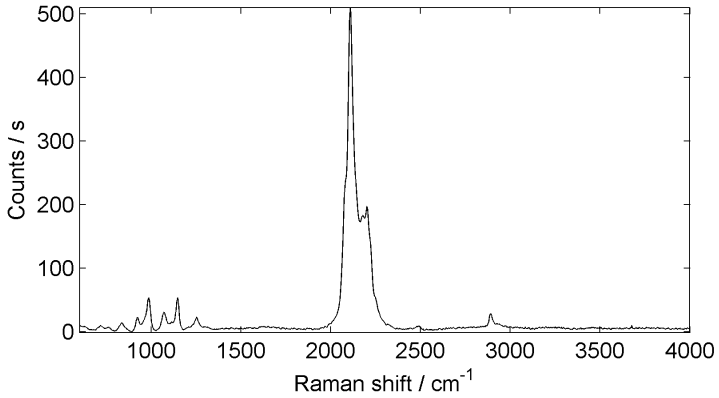

(b)

Figure 3.11: (a) Structure of sodium dodecylsulfate and (b) Raman spectrum of fully deuterated sodium dodecylsulfate (d_{25}-SDS)

.

(d^-). The antisymmetric methyl stretch is found at 2220 cm^{-1} (r^-). The band at 2173 cm^{-1} has previously been assigned to either an antisymmetric methylene stretch,[148] or to Fermi resonance of the methylene symmetric stretch.[149]

Isotherm of adsorption of d_{25}-SDS at the silica-water interface

Spectra of solutions of d-SDS with concentrations ranging from 8 µM to 13 mM were recorded to create an isotherm. Figure 3.13 shows the background-subtracted TIR spectra collected for each solution in the SY and SX polarisation.

To generate the isotherm, the spectra were normalised to the water maximum and d-SDS signals integrated. Figure 3.14 shows the isotherms collected for each polarisation. For both isotherms, the TIR Raman intensities are directly proportional to bulk concentration. This proportionality without a change of slope at the CMC (8.1 mM) demonstrates that no d-SDS adsorbs onto silica and all TIR Raman signals arise from bulk d-SDS. The slope of each isotherm allows us to relate the TIR Raman intensity to the d-SDS concentration in the probed volume and therefore to the adsorbed amount. The SX and SY polarisations are shown in this section to assign the symmetry of the CH or CD stretching bands. In the next section, I use S polarised light, the sum of SX and SY polarised light, to improve the detection limit of the technique. These isotherms later used as calibration data between TIR Raman intensities and surface coverage are obtained in a similar way as shown in the method chapter.

Band assignment of the didodecyldimethylammonium bromide (DDAB) Raman spectrum

Didodecyldimethylammonium bromide (DDAB) is a double-chained cationic surfactant (structure shown in figure 3.15). The most intense bands of the Raman

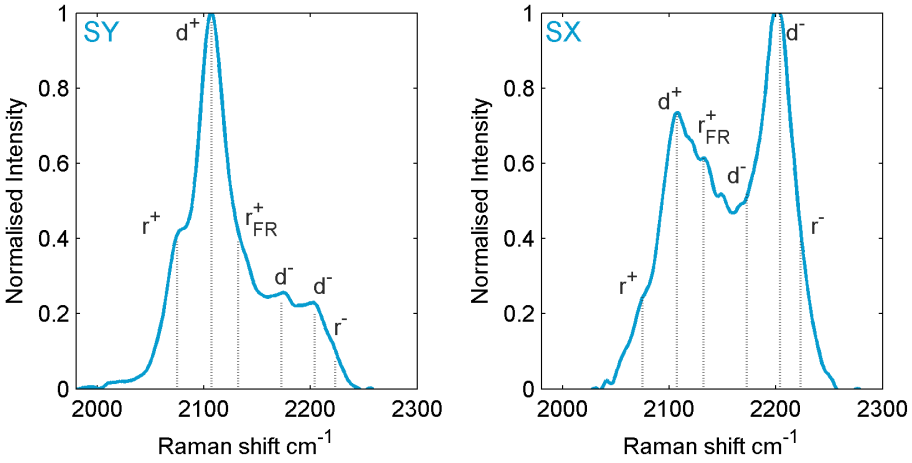

Figure 3.12: TIR Raman spectrum of bulk d-SDS in the SY and SX polarisations.

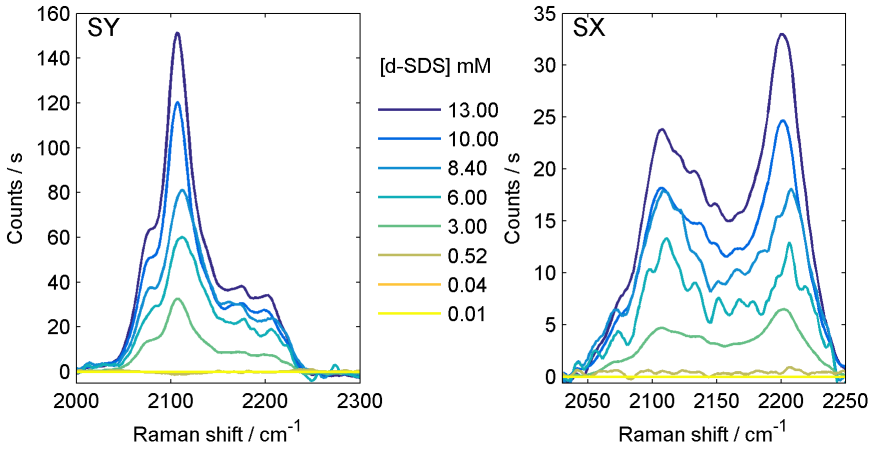

Figure 3.13: TIR Raman spectra collected from solutions of d-SDS of concentrations ranging from 10^{-3} to 1.6 times the CMC. The generally accepted value for the CMC of SDS in deionised water at 25 °C is 8.1 mM. [150,151,152]

spectrum, figure 3.15, are located in the CH stretch region as expected.

The CH region of Raman spectra of a 2.5 mM solution of DDAB in SY and SX polarisation are shown in figure 3.16. Band assignment of the CH stretches is well established. [153] The symmetric (d^+) and antisymmetric (d^-) methylene stretches are located at 2854 cm^{-1} and 2890 cm^{-1}, respectively. The band at 2932 cm^{-1} is assigned to a Fermi resonance of an overtone of a CH_2 scissoring mode (1445 cm^{-1}). The band at 2962 cm^{-1} is assigned to the antisymmetric methyl stretch (r^-). The symmetric terminal mode at 2876 cm^{-1} is not resolved and is buried under the d^- mode. The band at 2980 cm^{-1} is assigned to the symmetric methyl stretch of the headgroup r^+_{HG}, while the band at 3036 cm^{-1} is assigned to its antisymmetric methyl stretch r^-_{HG}.

Isotherm of adsorption of DDAB at the silica-water interface

Spectra of solutions of DDAB with concentrations ranging from 0.3 µM to 3.8 mM were recorded to create an isotherm. This range of concentrations corresponds to

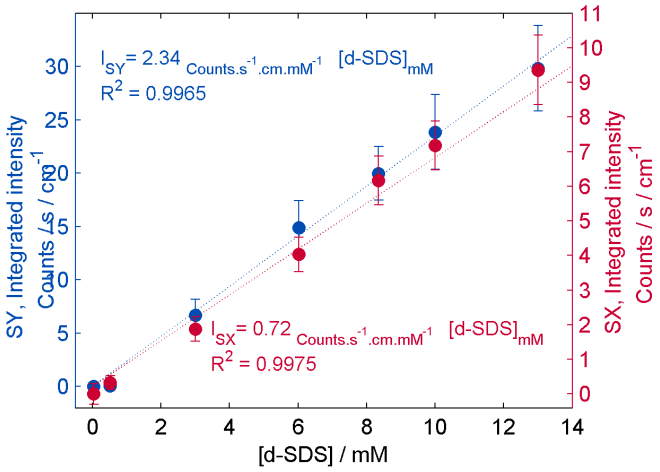

Figure 3.14: Isotherms of d-SDS at the silica–water interface at 25 °C collected in the SX and SY polarisations.

1/1000 to 22 times the critical aggregation concentration (CAC, see table 3.1). The minimum waiting time corresponding to the transport of DDAB vesicles to the interface has been estimated by recording the kinetics of adsorption from a solution of 5 mM of DDAB. All spectra were recorded after stabilisation of the signal intensity which happened 30 minutes after insertion of the solution in the cell at 0.5 mL min^{-1}. The kinetics of adsorption of DDAB is discussed later in this section.

Using the isotherm, the signal intensity can be related to the amount of DDAB present at the silica-water interface. Figure 3.17 shows the background-subtracted TIR Raman spectra collected for each solution in the SY and SX polarisation. To generate the isotherm, the DDAB signals were integrated and divided by the range of wavenumbers used for the integration. The resulting plot, figure 3.18, shows good agreement between the two polarisations. The observed signal increased up to a concentration of 0.1 mM. Above this concentration, the signal intensities level off and remain constant. The critical aggregation concentration (CAC) of DDAB has been determined by different methods which agree on a value close to 0.1 mM, see table 3.1.

Table 3.1: Critical aggregation concentration of DDAB measured by different methods.

CAC / mM	Method
0.17	surface tension [142]
0.070–0.086	surface tension [154]
0.078±0.006	conductivity [154]
0.099±0.007	potentiometry [154]

Our standard method for relating the Raman signal intensity to the amount of material at the interface could not be used for DDAB. Previous isotherms were calcu-

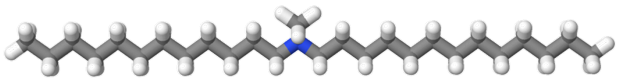

(a)

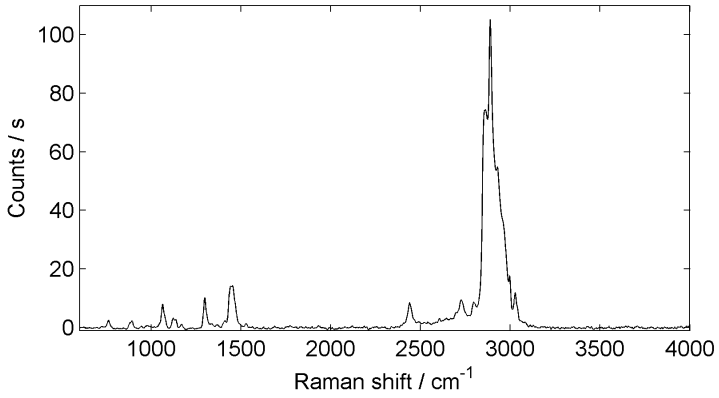

(b)

Figure 3.15: (a) Structure and (b) Raman spectrum of didodecyldimethylammonium bromide.

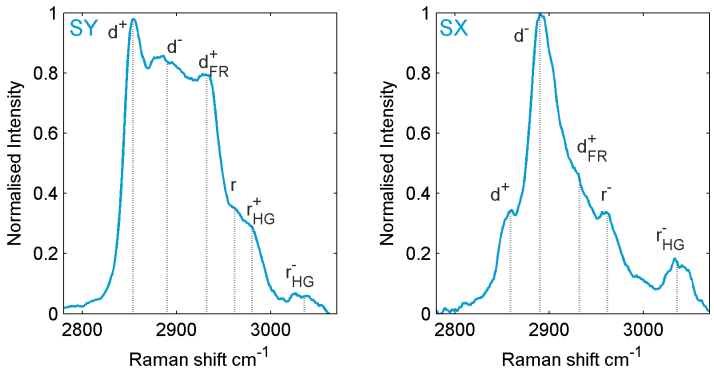

Figure 3.16: TIR Raman spectrum of a bilayer of DDAB in the SY and SX polarisations in the CH stretch region. The symmetry of the stretches is assigned by comparing the relative band intensity in the polarisation SX and SY.

lated by subtracting the bulk contribution from the Raman intensities. The isotherm of DDAB does not show a linear increase with bulk concentration in the range of measured concentrations. Above the critical aggregation concentration, there is an excluded volume near the surface where the centres of vesicles cannot lie. In addition, the electrostatic repulsion between the cationic vesicles and the cationic adsorbed layer further depletes the probed volume from bulk DDAB. Hence, the concentration of DDAB in the evanescent wave is not equal to the bulk concentration. Therefore, I decided to collect the isotherm of another surfactant, DTAB, which is the single chain equivalent of DDAB. The structure of DTAB is shown in figure 3.19.

The normalised TIR Raman spectra of both surfactants are shown on the same graph in figure 3.19. There are two minor differences between the DDAB and DTAB spectra. First, the relative amplitudes of the methyl stretches from the headgroup and the methylene stretches of the alkyl chain are different. The bands r^{-}_{HG} and r^{+}_{HG} are

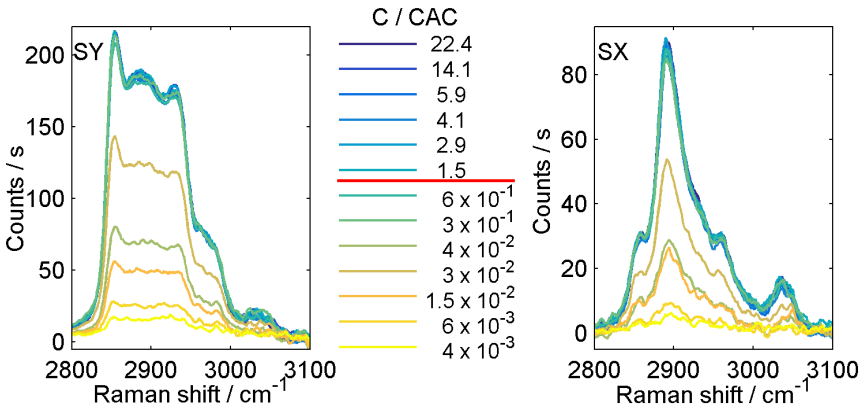

Figure 3.17: TIR Raman spectra collected from solutions of DDAB of concentration ranging from 1/1000 to 22 times the critical aggregation concentration. The red line marks the position of the CAC (see table 3.1).

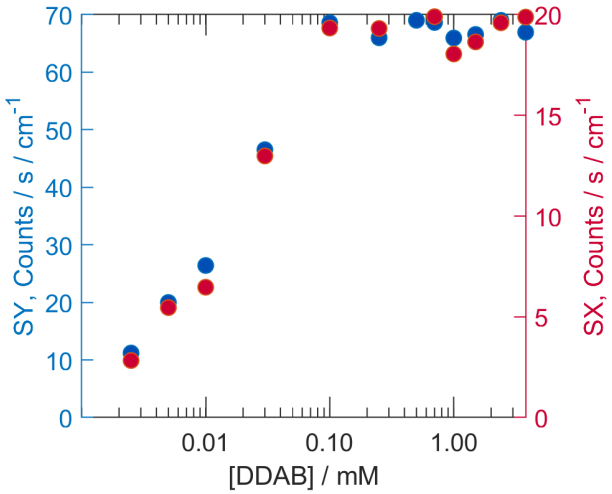

Figure 3.18: Isotherm of adsorption of DDAB at the silica–water interface at 25 °C. The isotherms were obtained by averaging the integrated TIR Raman signal over the range 2800–3085 cm^{-1}.

therefore better defined in the Raman spectrum of DTAB compared to the spectrum of DDAB, as expected. Also, the ratio between the symmetric stretch (2855 cm^{-1}) and the antisymmetric stretch (2890 cm^{-1}) is higher for DDAB. The impact of this difference on the calculation of the surface coverage will be discussed at the end of this section.

Spectra of solutions of DTAB with concentrations ranging from 1.5 µM to 220 mM were recorded. Figure 3.20 shows the background-subtracted TIR Raman spectra collected for each solution in the SY and SX polarisation. The resulting isotherm is shown in figure 3.21. The shape of the isotherm of adsorption of DTAB collected from TIR Raman spectra in the SY polarisation indicates a two-step adsorption mechanism, corresponding to the formation of a monolayer or a fraction of a monolayer of DTAB at the hydrophilic silica-water interface. The maximum adsorbed amount corresponds to a surface area per molecule of ≈60 $Å^2$. The surface area per molecule of DTAB is

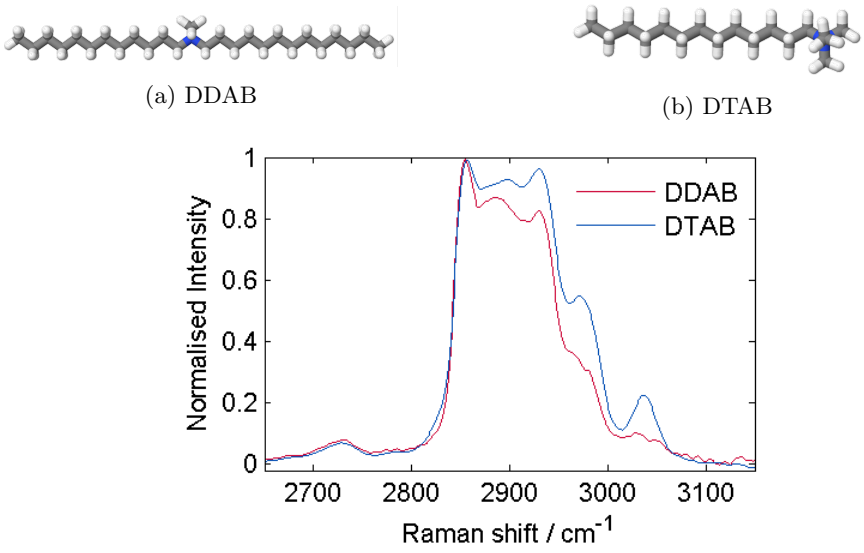

(a) DDAB (b) DTAB

(c)

Figure 3.19: (a-b) Structures and (c) TIR Raman spectra of adsorbed DDAB and DTAB in the CH region. Both spectra shown are in the SY polarisation. Spectra are normalised to 1 at the highest intensity.

therefore larger than the size of the TAB headgroup (≈68 Å^2), implying an incomplete monolayer at the hydrophilic silica–water interface. This is in agreement with previous reports.[155]

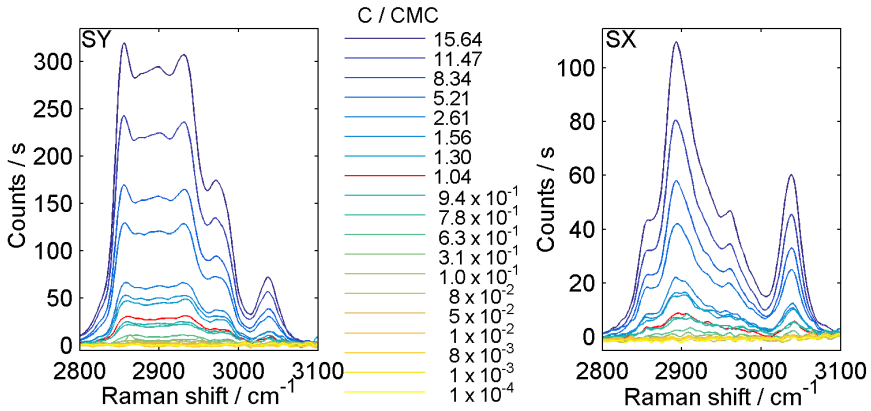

Figure 3.20: TIR Raman spectra of DTAB at the silica–water interface at 25 °C. The spectra recorded at the CMC (14 mM) are shown in red.

The bulk contribution from DTAB solutions in the TIR Raman spectra gives a scaling factor to convert the integrated Raman intensity to the amount of DTAB at the interface α_{DTAB}. Assuming the spectra of DTAB and DDAB are identical and assuming the cross sections of all C−H bonds are the same, it is possible to obtain the scaling factor for DDAB, α_{DDAB}, using equation 3.11.

$$\alpha_{\mathrm{DDAB}} = \alpha_{\mathrm{DTAB}} \frac{N_{\mathrm{DDAB}}}{N_{\mathrm{DTAB}}} \tag{3.11}$$

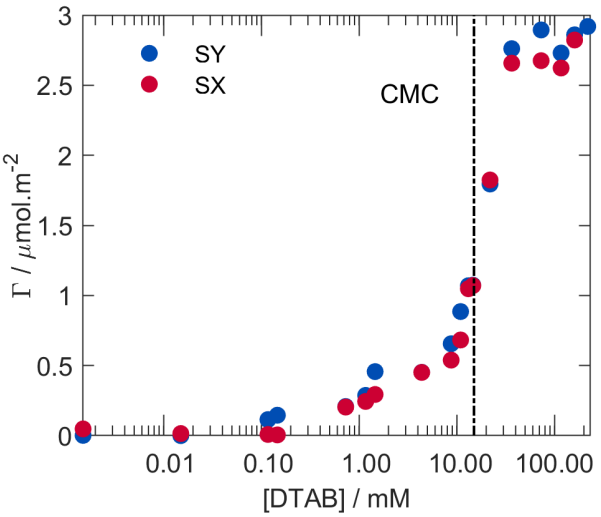

Figure 3.21: Isotherm of adsorption of DTAB at the silica–water interface at 25 °C.

where N_{DDAB} and N_{DTAB} the number of C−H bonds in DDAB and DTAB respectively. The isotherm of DDAB at the silica-water interface is then calculated for both polarisation combinations. Results are shown in figure 3.22.

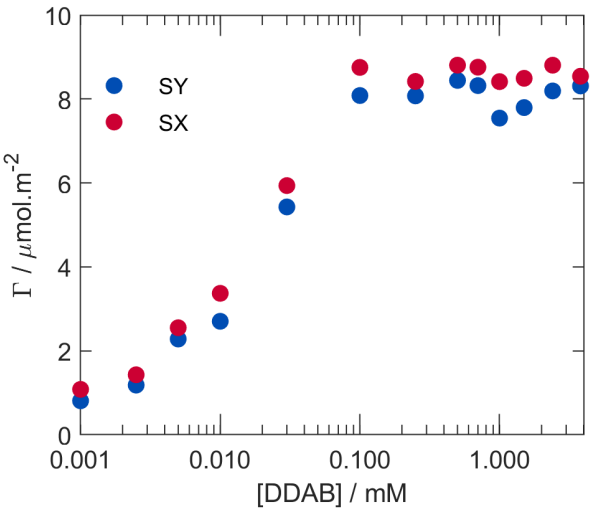

Figure 3.22: Isotherm of adsorption of DDAB at the silica–water interface at 25 °C.

The maximum adsorbed amount is found to be $8\,\mu\mathrm{mol\,m^{-2}}$, which corresponds to a minimum surface area per molecule of $A_{\mathrm{min}} = 21\,\mathrm{Å}^2$ which is about half the calculated surface area per molecule for closed-packed double chain quaternary ammonium salts ($40\,\mathrm{Å}^2$), with a vertical orientation of the alkyl chain.[143] The adsorbed amount corresponds to a tightly packed bilayer. The formation of a bilayer is in agreement with previous studies on the adsorption of DDAB at the solid–water interfaces, such as mica, silicon oxide, and silica.[141] The adsorbed amount is probably slightly overestimated by the method of conversion the Raman intensities into surface coverage. The method relies on the assumption that the Raman intensities from DDAB can be scaled from the intensities of DTAB.

Figure 3.19 shows that one difference in the shape of the spectra of DDAB and DTAB lies in the relative intensities of their antisymmetric and symmetric stretch. The intensity of the symmetric stretch in DDAB is stronger than in the spectra of DTAB. Also, the C−H bonds in the adsorbed layer aligned preferentially parallel to the surface (since the chains have a preferential orientation normal to the surface), while the C−H bonds have an isotropic orientational distribution in bulk DTAB solutions. Therefore, when the scaling method is applied to spectra acquired with the electric field parallel to the surface (S polarisation), it tends to overestimate the amount of material present on the surface.

The shape of the adsorption isotherm of surfactants also gives an insight on the type of structures formed at the interface — two models have been developed, the two-step model[156,157] and the four-region model.[158] They differ in the interplay between electrostatic and hydrophobic interactions. In the two-step model, the adsorbed amount is first very low, corresponding to the adsorption of single surfactants molecules at low density surface coverage. Then, the adsorbed amount increases steeply, corresponding to the formation of admicelles from the nucleated sites, until the CMC is reached and the adsorbed amount remains constant. This model corresponds to cases where the electrostatic interactions between the surface and the surfactant are weakly attractive and the adsorption is mainly driven by the hydrophobic interactions. For stronger electrostatic attractions, the adsorption isotherm is better described by the four-region model (see figure 3.23). At low bulk concentrations, when there is no interaction between the adsorbed molecules, the adsorbed amount increases linearly with concentration (region I). Then, due to the stronger electrostatic interactions, the surface coverage is more dense (region II) leading to the formation of hemimicelles (region III) and the attachment of a second layer. The formation of this second layer continues until the bulk concentration reaches the critical aggregation concentration. Then, the adsorbed amount remains constant (region IV). The two models do not describe all adsorption isotherms such as the adsorption of CTAB onto silica.[159] Likewise, neither model accurately described the adsorption of DTAB onto silica shown in figure 3.21. The shape of the isotherm of adsorption of DDAB onto hydrophilic silica also does not clearly match either of the two mechanisms. However, the calculated surface coverage of DDAB implies that the formation of hemimicelles is rather unlikely and that DDAB will fall into the category of surfactants adsorbing in a four-region type mechanism. In that case, it is possible that only the regions III and IV of the surface coverage evolution are visible in our adsorption isotherm. The other regions are at very low concentrations where experimental errors in the sample preparation might become too significant. Nevertheless, lower concentrations can be probed at the first stage of the adsorption kinetics of DDAB.

The resulting graph of the kinetics of adsorption is shown in figure 3.24. This data supports a four-region adsorption mechanism, although with several differences from the model usually proposed. Regions I and II have different rates of adsorption. Regions III and IV overlap quite well with the equilibrium adsorption isotherm shown in figure 3.22.

This section has shown that vesicles of DDAB formed as described in section 2.6

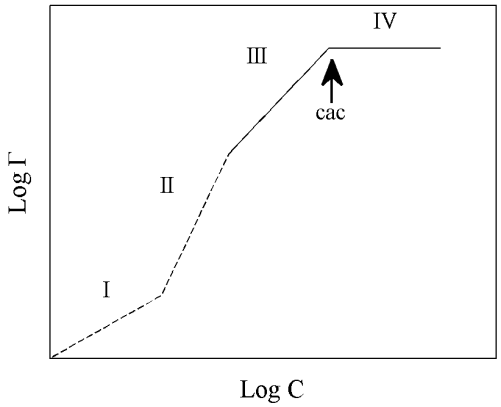

(a) Proposed shape of the adsorption isotherm of DDAB onto silica, following the four region model. Regions I and II are not visible in our data (dotted line).

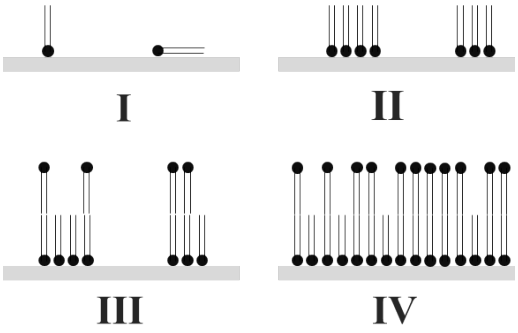

(b) Corresponding adsorption mechanism.

Figure 3.23: Proposed mechanism of adsorption of DDAB onto silica. Adapted from reference [158].

and adsorb at the silica–water interface, a process probably driven by attractive electrostatic interactions between the cationic DDAB vesicles and the negatively charged hydrophilic silica. The vesicles rupture and form a bilayer which is stable towards rinsing with water and methanol (results not shown). This is in agreement with previous studies.[141]

The influence of temperature on the supported bilayer of DDAB will be examined in the next section. A liquid-to-gel phase transition of the supported DDAB bilayer could be potentially used for releasing a coadsorbed surfactant.

Influence of temperature on a bilayer of DDAB at the silica-water interface

To assess the influence of temperature on a bilayer of DDAB at the silica–water interface, TIR Raman spectra of a bilayer of DDAB were collected in S and P polarisations at temperatures ranging from 60 °C to 10 °C (see figure 3.25). The bilayer was formed at 60 °C from a vesicular solution of DDAB in water. The vesicular solution was left in contact with the silica surface for 30 minutes after which the Raman intensity from DDAB had stabilised indicating equilibrium in the sample cell. The

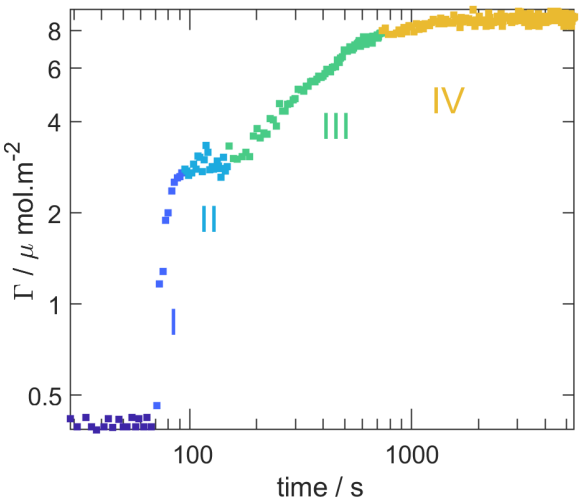

Figure 3.24: Isotherm of adsorption of DDAB on a log-log plot. The data is extracted from time series of S-polarised TIR Raman spectra collected every 2 seconds during the introduction of a solution of 1 mM of DDAB at 0.1 mL min^{-1}.

cell was then flushed with 15 mL of pure Milli-Q water, equal to two times the cell volume, at a temperature of 60 °C with a flow rate of 0.1 mL min^{-1}. The temperature was then reduced at a rate of −0.1 °C min^{-1}. Spectra were collected 5 minutes after the temperature inside the cell had reached the target value. Figure 3.25 shows the TIR spectra collected in the S and P polarisations at each temperature. As the temperature was gradually reduced to 10 °C, the band positions shifted towards lower Raman shifts. There was a simultaneous reduction in the intensity of the CH stretches observed in both polarisations. The shape of the spectra was also changing, signalling a change in the chain tilt. Figure 3.25 shows spectra normalised to their methylene symmetric stretch (2855 cm^{-1}). As the temperature decreased, the ratio between the antisymmetric to symmetric methylene stretches intensities (I(d$^-$)/I(d$^+$)), called the primary order parameter, increased. This ratio has been correlated with the chain packing of the aliphatic chains of lipids at the interface.[148] The higher this ratio, the more ordered the chain packing. This parameter thus gives information on the phase the lipids are in: when in the fluid phase, the primary order parameter is ≈ 1.05, when in the gel phase, the primary order parameter is ≈ 1.4.

Quantitative analyses are shown in figures 3.26, 3.27 and 3.28. TIR Raman spectra were fitted to obtain the position and amplitude of the symmetric and antisymmetric methylene stretches with a mixture of Gaussian and Lorentzian curves as explained in section 2.1.3.

Figure 3.26 shows the primary order parameter in the DDAB bilayer as a function of temperature. The order parameter has been calculated from S-polarised intensities. The primary order parameter at 60 °C is around 1.09 which is close to the values measured in phospholipid bilayers. The primary order parameter increases as the temperature decreases, which is in agreement with a transition from a liquid-like phase towards a gel-phase. However, the values of the primary parameter measured for the gel phase in phospholipids of around 1.4 is not reached. The tail of a DDAB

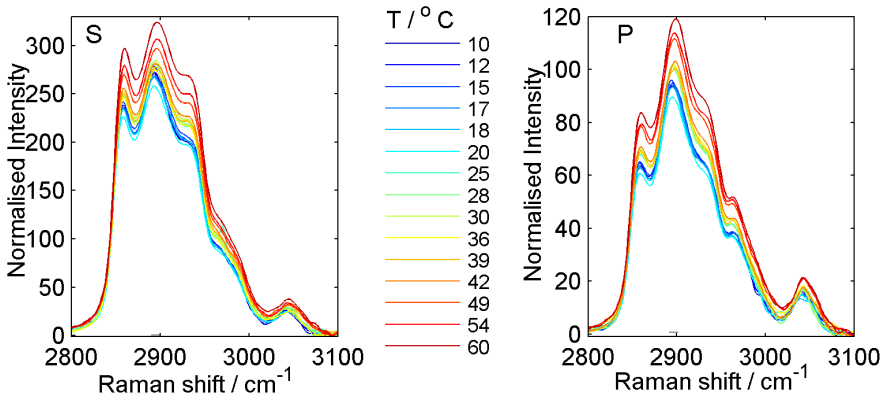

(a)

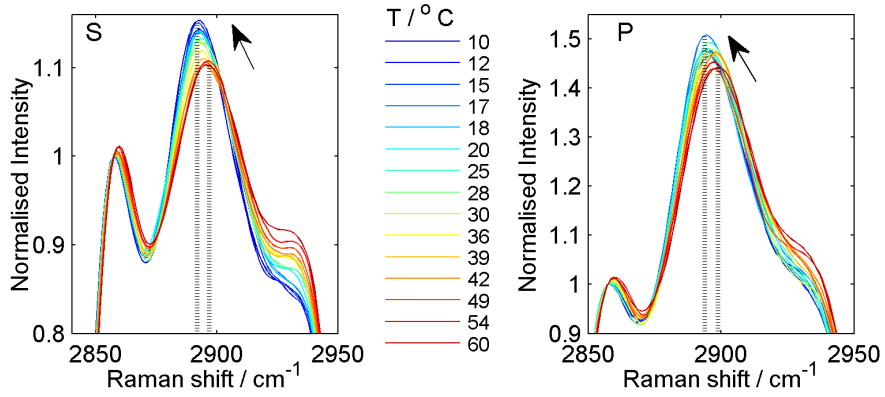

(b)

Figure 3.25: TIR Raman spectra in S and P polarisations of a DDAB bilayer recorded at different temperatures (a) and normalised to the methylene symmetric stretch (d^+) (b). The bilayer was prepared at 60 °C and the temperature was gradually decreased to 10 °C, at a rate not exceeding 0.1 °C min^{-1}. Arrows indicate the direction of decreasing temperature.

molecule is shorter than those in a phospholipid. Getting both chains parallel in a tightly packed gel-phase requires a certain number of gauche conformations to make a turn. DDAB chains are a little bit too short to get both chains parallel and tightly packed.

Figure 3.27 shows the changes in the positions of the symmetric and antisymmetric methylene stretches with temperature. Both peaks are gradually shifting towards lower wavenumbers with decreasing temperature, signalling fewer gauche defects and an ordering in the layer. This is consistent with a liquid-to-gel phase transition. This shift of around 2–3 cm^{-1} is caused by a dehydration of the layer and is similar to the one observed during the phase transition of phospholipids albeit of a lower magnitude.

Figure 3.28 shows the ratio of the integrated intensities of the CH stretches of P-polarised and S-polarised TIR spectra. This parameter has been used to characterise the average chain tilt of phospholipids in supported lipid bilayers. The amplitude of this ratio has no real physical meaning but relative changes indicate a change in the tilt of the chains: an increase in the ratio is correlated to an increase in the

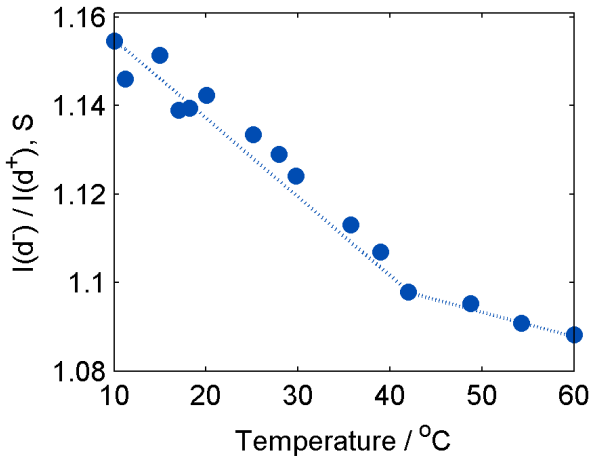

Figure 3.26: Order parameter of the DDAB bilayer as a function of temperature. The dotted line is to guide the eye only.

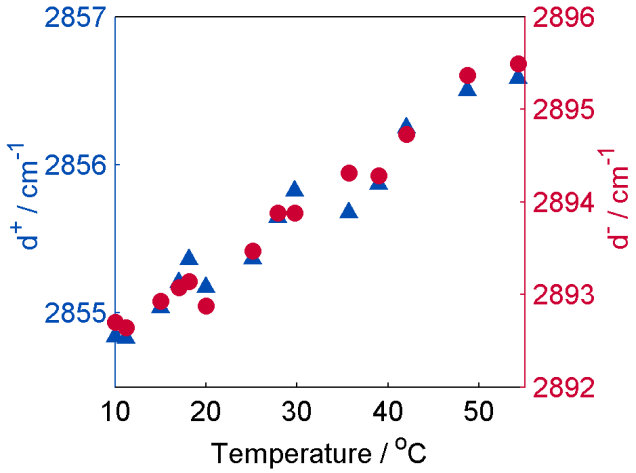

Figure 3.27: Peak position of the symmetric methylene stretch (▲) and the antisymmetric methylene stretch (●) as a function of temperature.

chain tilt away from the normal to the surface. The data can be divided into two regions of different ratios. The ratio is higher at high temperature and increases at around 42 °C where figures 3.26 and 3.27 show a change in slope. This data implies that, on average, DDAB chains are getting closer to the normal of the surface as the temperature is reduced.

These three markers of the order in the molecular chain (the primary order parameter, the peak positions, and the ratio of the P and S intensities) lead to different possible interpretations on the start of the transition, and even on its characteristic temperature. For instance, there is a concomitant change in the slope of the primary order parameter with a change of the CH intensity ratio, while the peak positions are gradually shifting throughout the studied temperature range. Previous studies have acknowledged the primary order parameter to be the marker the most sensitive to structural changes in supported lipid bilayers. [160]

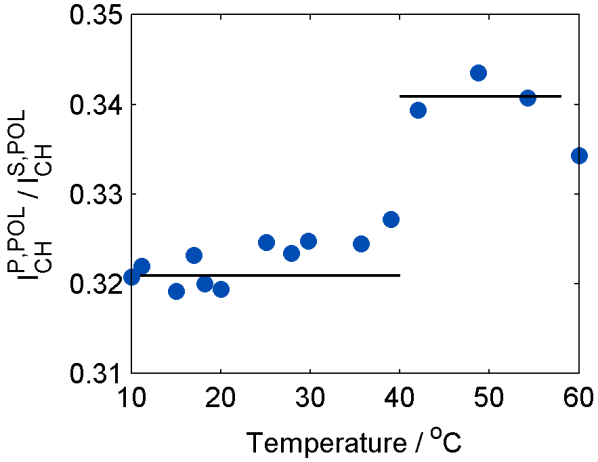

Figure 3.28: Ratio of the integrated intensities of the CH stretches of P-polarised and S-polarised TIR spectra of the DDAB bilayer, as a function of temperature.

3.3.2 Coadsorption of d-SDS–DDAB

To study the coadsorption of mixed vesicles of d-SDS–DDAB, solutions of varying surfactant ratios were prepared in Milli-Q water. The total surfactant concentration was kept at 2.5 mM whilst the d-SDS content was varied between 15 % and 80 %. For each ratio, the solution was injected into the Raman cell and left in contact with the silica surface for 30 minutes at 40 °C. This temperature was well above the phase transition temperature of DDAB and was maintained throughout the experiment. The cell was then rinsed with 15 mL of Milli-Q water at a rate of 0.1 mL min^{-1}, displacing the surfactant solutions. S-polarised TIR Raman spectra were then collected in the CH and CD regions. Figure 3.29 shows the spectra collected for each mixture. Between each solution, the cell was dismantled and cleaned thoroughly. This process includes rinsing the cell with methanol, water and sonicating it in Decon for 10 minutes. The hemisphere was cleaned with BIC following the procedure described in section 2.1.5.

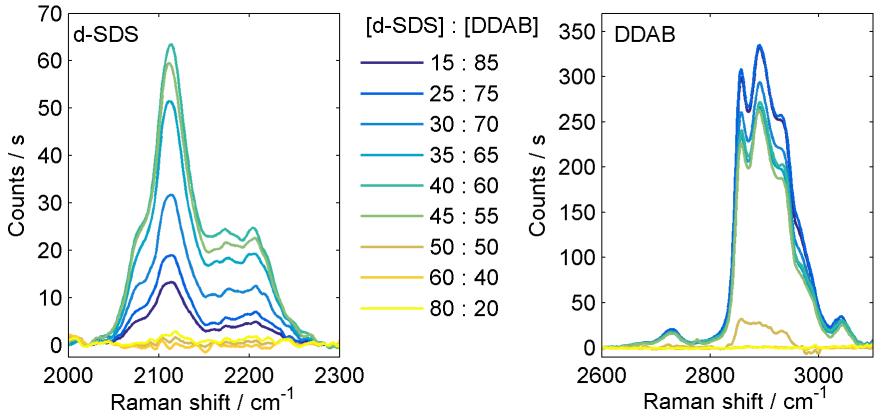

Figure 3.29: S-polarised TIR Raman spectra in the CD and CH region of the adsorbed layer from mixtures of d-SDS and DDAB, collected at different [d-SDS] : [DDAB] ratios. All spectra were collected at 40 °C.

The data falls into three categories. In the d-SDS rich region (60 % and 80 % d-SDS), the vesicles are negatively charged and do not adsorb onto the silica surface. There are consequently no signals, neither in the CD nor CH region of the Raman spectrum. In the DDAB rich region (15–45 % d-SDS), both surfactants are adsorbing at the interface. The peak intensities in the CH region are increasing with DDAB concentration, while the intensities in the CD region are decreasing. At the equimolar ratio (50 % d-SDS), a small amount of DDAB but no d-SDS is detected. The DDAB signal intensity corresponds to a surface excess of 0.3 µmol m^{-2}. The chemical potential of DDAB in the vesicle phase has to be uniform (at equilibrium). There are thus no pure DDAB vesicles and the surface excess originates from an excess of monomers of DDAB in solution. Based on the isotherm measurements (see figure 3.22), a bulk concentration of DDAB of 0.85 µM is necessary to achieve this surface coverage. This excess, deviating from the equimolar ratio, corresponds to an error in the bulk ratio of 0.03 %.

The quantitative analysis of signal intensities over the whole range of surfactant ratios is shown in figure 3.30. The data is obtained by converting the signal intensities from the CD and CH regions into the amounts of adsorbed d-SDS and DDAB using the isotherms shown in figure 3.14 and figure 3.22. For pure DDAB vesicles, a bilayer with a surface excess of 8 µmol m^{-2} is formed at the interface. The substitution of 15 % of DDAB in solution with d-SDS increases the surface excess of DDAB by 9 %. d-SDS coadsorbs with a surface excess of 1.5 µmol m^{-2}. Throughout the DDAB-rich region (mole fraction $x_{\text{d-SDS}} \leq 0.45$), the amount of d-SDS at the interface increases with its concentration in the vesicles reaching a maximum of 0.7 at the [d-SDS] : [DDAB] ratio of 0.67 in the vesicle solution.

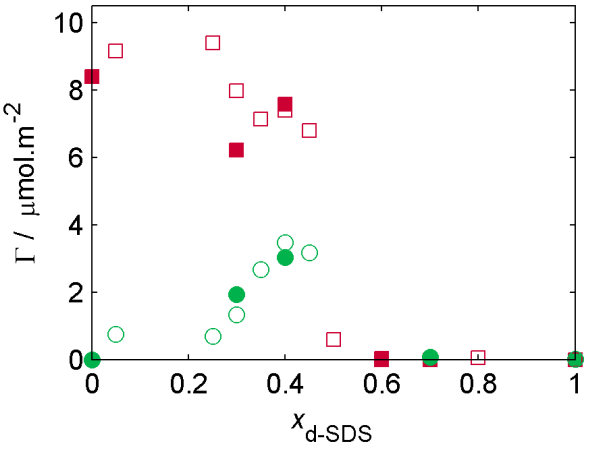

Figure 3.30: Adsorbed amount of surfactants DDAB (■ and □) and d-SDS (● and ○) as function of the mole fraction of d-SDS in bulk, $x_{\text{d-SDS}}$, at 40 °C. Quantities were determined from the TIR Raman spectra in S polarisation, in the range of Raman shift of 2800–3050 cm^{-1}. The filled and empty symbols correspond to two sets of data.

The area per chain in a monolayer is related to the surface coverage by:

$$A_{\text{min}} = \frac{1}{\Gamma_{\text{chains}}\, N_{\text{a}}} \tag{3.12}$$

where

$$\Gamma_{\text{chains}} = \frac{2 \times \Gamma_{\text{DDAB}} + \Gamma_{\text{d-SDS}}}{2} \tag{3.13}$$

with Γ_{DDAB} and $\Gamma_{\text{d-SDS}}$ being the surface coverage of DDAB and d-SDS in $\mu\text{mol}\,\text{m}^{-2}$, respectively. They are obtained from figure 3.30. The factor 2 accounts for the fact that the surfactants are packed in a bilayer.

Figure 3.31 shows the area per chain in the mixed surfactant adsorbed layer, as a function of the d-SDS mole fraction in the vesicle solutions.

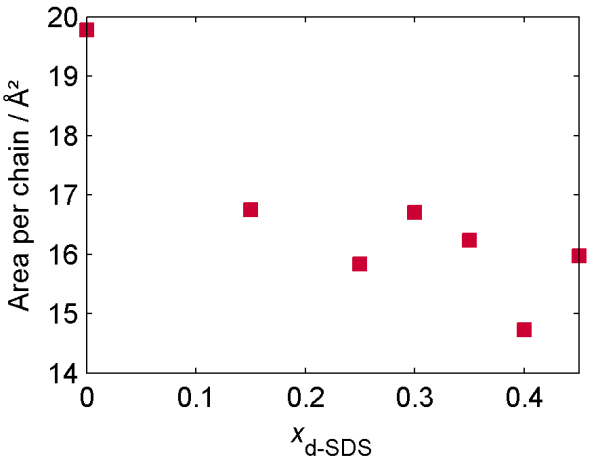

Figure 3.31: Area per chain of surfactant as a function of bulk d-SDS ratio, determined from the S polarisation spectra in CH and CD regions.

Pure DDAB layers show the lowest density with an area of 20 Å^2 per molecule. A small substitution of DDAB with d-SDS ([d-SDS] : [DDAB] = 0.15 : 0.85) is enough to lower the area per chain by 15 %. The experimental data shows a decrease in the area per chain with increasing d-SDS content down to 15 Å^2. This further decrease can be due to a change in density but might also be a consequence of experimental errors. An area per chain of 15 Å^2 is below the limit of an hexagonal packed bilayer (20 Å^2 per chain). The amount of d-SDS and DDAB in the layer is, however, overestimated since the calculation is based on isotropic solutions. As the orientation effects will be similar for both species of the mixed bilayer, mole fractions are more reliable than the absolute values of surface excess.

The mole fraction of each surfactant in the cation-rich region is shown in figure 3.32. The mole fraction of d-SDS increases until reaching an equimolar ratio with the mole fraction of [d-SDS] : [DDAB] = 0.4 : 0.6. There is therefore an excess surface coverage of d-SDS compared to the vesicles' composition. The increase in mole fraction in the adsorbed layer is not linearly increasing with the bulk d-SDS mole fraction, showing that the adsorbed surfactants are not mixing ideally on the surface.

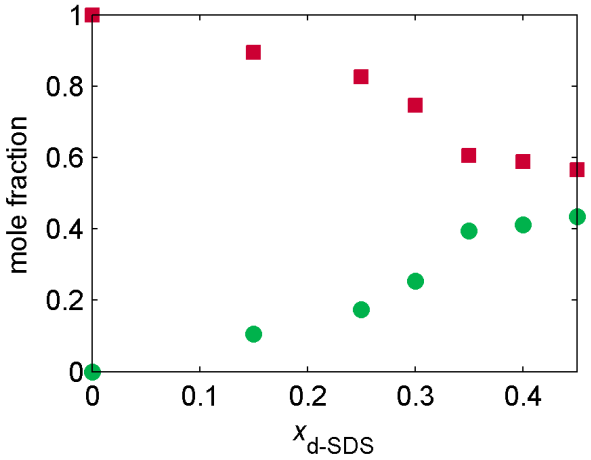

Figure 3.32: Mole fractions of DDAB (■) and d-SDS (●) within the bilayer as a function of d-SDS mole fraction in bulk, $x_{\text{d-SDS}}$, at 25 °C. Above a d-SDS mole fraction of 1.2 mM, the layer does not form.

In ideal solutions, both the enthalpy and the entropy of mixing are null. In this model, there is no preferred neighbour meaning that the enthalpy of mixing between two identical neighbours U_{ii} and the enthalpy of mixing between two different neighbours U_{ij} are the same. The simplest deviation from this model is called the regular solution theory where the enthalpy of mixing is non zero while the entropy of mixing is. In the case of oppositely charged surfactants, the electrostatic attraction and repulsion are too strong to be considered as equal. It is therefore expected for a catanionic mixture to be non ideal. In the case of an adsorbed DDAB–SDS layer, the repulsive interactions between the DDAB headgroups are screened by the sulphate headgroups. This energetic gain overcomes both the repulsive interaction between the sulphate headgroup and the negatively charged silica interface. A similar effect has been observed with mixed layers of DDAB and dodecanol.[142] The attraction between the two oppositely charged headgroups is also in favour of an excess of SDS at the interface.

In order to establish whether the DDAB–d-SDS adsorbed layers follow a regular solution mixing, I will calculate the expected molar fraction of adsorbed d-SDS as a function of its bulk concentration. The goodness of the fit to figure 3.32 will indicate whether regular solution theory is an appropriate model to the adsorbed mixture and thermodynamic constant can be extracted. In a regular solution of a cationic surfactant + and an anionic surfactant −, the chemical potential of each component μ_i is a function of the molar fraction of i in the mixture, x_i, the temperature, T, and the activity coefficient, γ_i, which marks the deviation from ideality.

$$\mu_i = \mu_i^0 + RT \ln x_i + RT \ln \gamma_i \tag{3.14}$$

where R is the gas constant and μ_i^0 the standard chemical potential, *i.e.* the chemical potential of i when pure. In a regular solution mixture of i and j, the activity

coefficient of i, γ_i, is related to the square fraction of j as follows :

$$\ln \gamma_i = \frac{\beta_j}{RT} x_j^2 \tag{3.15}$$

and symmetrically

$$\ln \gamma_j = \frac{\beta_i}{RT} x_i^2 \tag{3.16}$$

with $\beta_i = \beta_j = \beta$.

If the adsorbed layer is a regular solution, the chemical potential of d-SDS in the layer is:

$$\mu^{\mathrm{s}}_{\text{d-SDS}} = \mu^{\mathrm{s0}}_{\text{d-SDS}} + RT \ln x^{s}_{\text{d-SDS}} + \frac{\beta}{RT} (x^{\mathrm{s}}_{\mathrm{DDAB}})^2 \tag{3.17}$$

and similarly for DDAB

$$\mu^{\mathrm{s}}_{\mathrm{DDAB}} = \mu^{\mathrm{s0}}_{\mathrm{DDAB}} + RT \ln x^{\mathrm{s}}_{\mathrm{DDAB}} + \frac{\beta}{RT} (x^{\mathrm{s}}_{\text{d-dSDS}})^2 \tag{3.18}$$

If the bulk mixture is also a regular solution and assuming the potential of interaction of the two surfactants is the same in bulk and at the interface, the chemical potential of d-SDS in the bulk is:

$$\mu^{\mathrm{b}}_{\text{d-SDS}} = \mu^{\mathrm{b0}}_{\text{d-SDS}} + RT \ln x^{\mathrm{b}}_{\text{d-SDS}} + \frac{\beta}{RT} (x^{\mathrm{b}}_{\mathrm{DDAB}})^2 \tag{3.19}$$

and similarly for DDAB

$$\mu^{\mathrm{b}}_{\mathrm{DDAB}} = \mu^{\mathrm{b0}}_{\mathrm{DDAB}} + T \ln x^{\mathrm{b}}_{\mathrm{DDAB}} + \frac{\beta}{T} (x^{\mathrm{b}}_{\text{d-dSDS}})^2 \tag{3.20}$$

At equilibrium, $\mu^{\mathrm{b}}_{\mathrm{DDAB}} = \mu^{\mathrm{s}}_{\mathrm{DDAB}}$ and $\mu^{\mathrm{b}}_{\text{d-SDS}} = \mu^{\mathrm{s}}_{\text{d-SDS}}$.

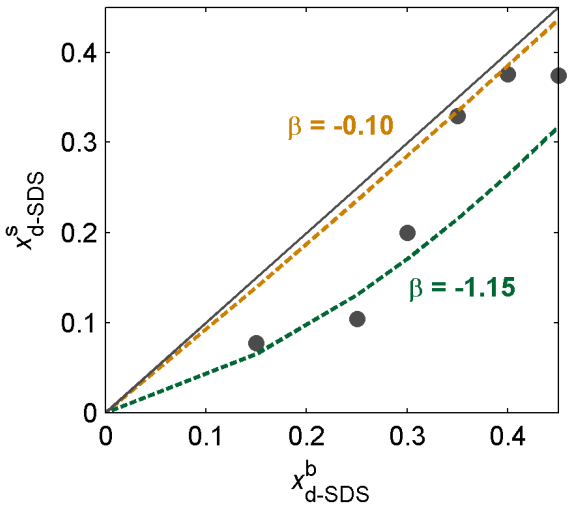

Figure 3.33: Composition of the adsorbed layer as measured by TIR Raman ● and as predicted by different models: ideal solution (black line), regular solution with two attractive interactions with $\beta = -1.15$ (green dashed line) and $\beta = -0.10$ (orange dashed line).

Figure 3.33 shows that the composition of the adsorbed layer deviates strongly from ideality (black dashed line). Deviation to ideality can not be fitted by a regular solution model over the whole range of study. Instead, two interaction parameters can be calculated, one for the lowest d-SDS fractions ($x_{\text{d-SDS}} \leq 0.3$, $\beta = -1.15$) and one for the highest d-SDS fractions ($x_{\text{d-SDS}} \geq 0.35$, $\beta = -0.10$).

The insertion of d-SDS into the adsorbed DDAB layer has an impact on the CH region of the DDAB Raman spectrum. The data shown in figure 3.34a is normalised to symmetric methylene stretch at around 2855 cm^{-1}. The antisymmetric methylene stretch at 2894 cm^{-1} increases in intensity with the d-SDS content in the mixed-surfactant vesicles.

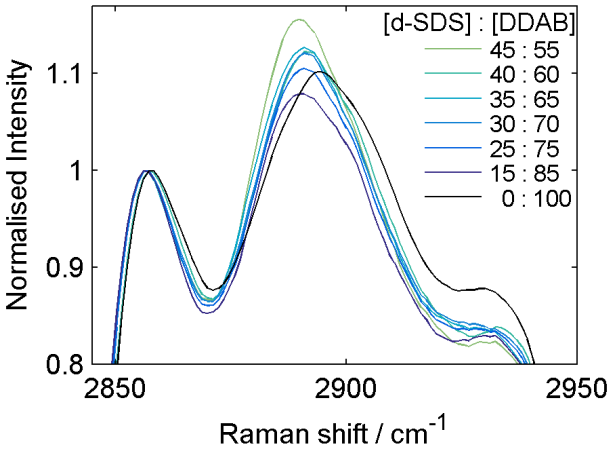

(a)

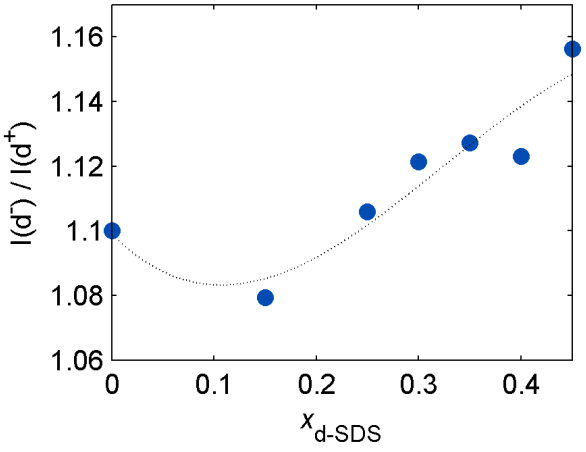

(b)

Figure 3.34: (a) S polarised TIR Raman spectra of DDAB in the coadsorbed d-SDS–DDAB layer as a various d-SDS mole fractions in bulk, $x_{\text{d-SDS}}$. The spectra are normalised to the symmetric methylene stretch, d^+. (b) Primary order parameter of the DDAB chains in the d-SDS–DDAB adsorbed layer. The dotted line is to guide the eye only.

The corresponding primary order parameter $I(d^-)/I(d^+)$, shown in figure 3.34b, increases from 1.10 for a pure DDAB layer to 1.16 in the equimolar mixed layer. These

values have also been observed during the fluid-gel phase transition occurring in the DDAB bilayer between 50 °C and 10 °C (see figure 3.26). This behaviour implies that the presence of d-SDS in the adsorbed layer induces a phase transition well above the transition temperature of DDAB. This would imply that the chemical potential of d-SDS in DDAB in the gel phase is lower than in liquid phase DDAB. It might therefore be possible to trigger the release of d-SDS from a mixed layer could happen via a gel-to-fluid phase transition. This possibility is addressed in the next section.

3.3.3 Temperature induced gel-to-liquid phase transition in a mixed d-SDS–DDAB layer.

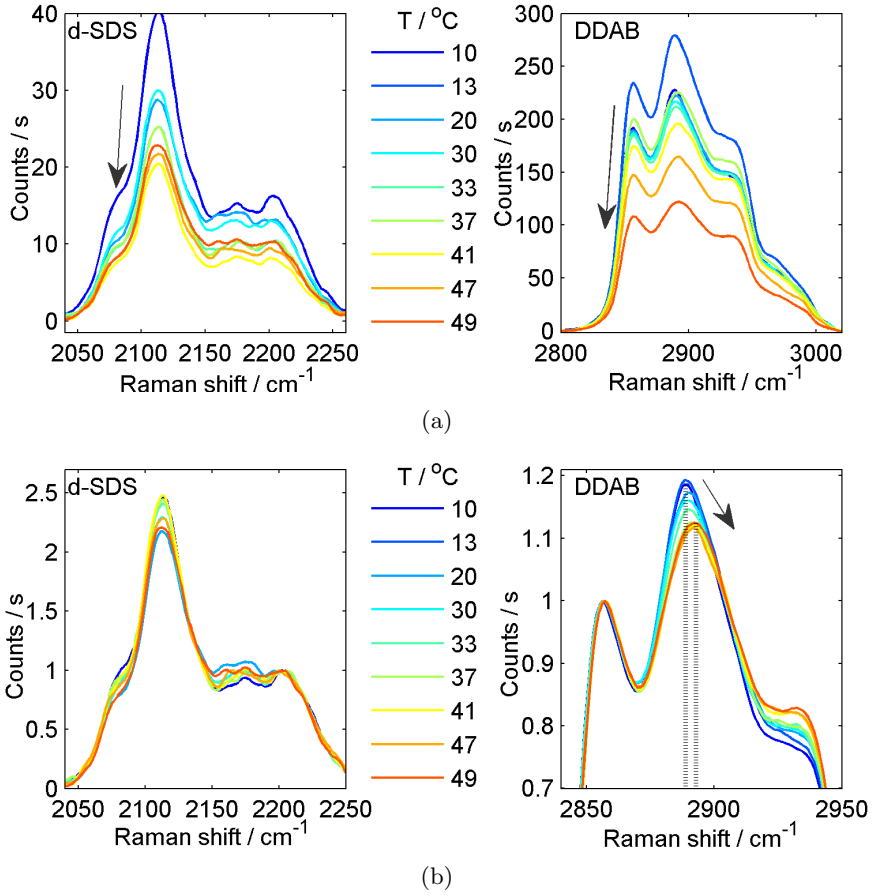

Figure 3.35: TIR Raman spectra of d-SDS and DDAB in S polarisation during the temperature increase raw (a) and normalised to the methylene antisymmetric stretch, d^-, at 2200 cm^{-1} and the methylene symmetric stretch, d^+, at 2855 cm^{-1}, respectively (b). Arrows indicate the direction of increasing temperature.

The release of d-SDS from a coadsorbed d-SDS–DDAB layer could potentially be triggered by the gel-fluid phase transition. The solution of d-SDS–DDAB was chosen so that the composition of the resulting layer contains the maximum amount of d-SDS, *i.e.* when [d-SDS] : [DDAB] = 0.4 : 0.6. The solution was inserted at 40 °C and the cell was gradually cooled down to 10 °C with a rate of 0.05 °C min^{-1} with the vesicle solution still inside the cell. This way, the adsorbed mixed layer was gradually

getting denser. The solution was rinsed out of the cell with 15 mL of Milli-Q water at 10 °C. The temperature was then gradually increased up to 50 °C. Figure 3.35 shows the TIR Raman spectra collected from the mixed bilayer at various stages of the temperature rise. As the temperature was gradually increased, the signal intensities and shapes were changing.

Changes in the spectrum of DDAB mark that the layer is gradually changing from gel-like to more fluid-like. Quantitative analysis is shown in figure 3.36a where the amounts of each surfactant have been extracted from the S polarised TIR Raman spectra. Up to 40 °C, d-SDS is released down to 40 % of the initial amount measured at 10 °C, while the amount of DDAB is relatively constant. At higher temperatures, fractions of DDAB are irreversibly removed while the amount of d-SDS remains stable. The ratio of the adsorbed DDAB and d-SDS is shown in figure 3.36b. At 12 °C, 20 °C, 30 °C and 50 °C, the composition is richer in anionic species which could imply that the system has not reached equilibrium.

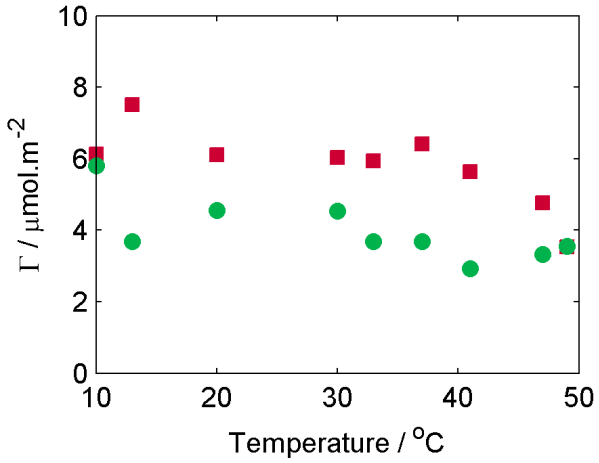

(a)

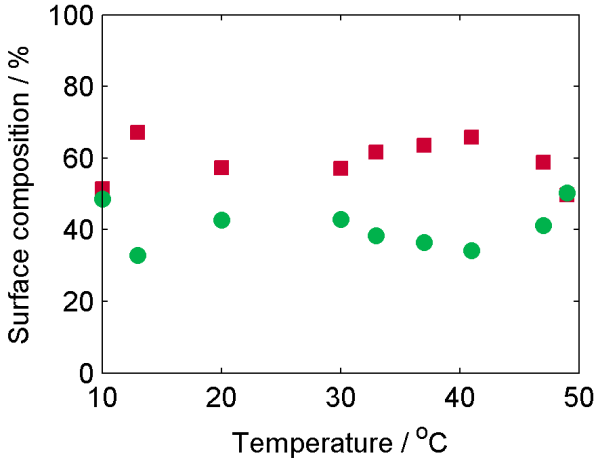

(b)

Figure 3.36: Surface coverage (a) and fractions (b) of DDAB (■) and d-SDS (●) in the coadsorbed layer as function of temperature. The quantities were determined from the S polarisation spectra.

Images collected at different stages of the temperature rise are shown in figure 3.37 along with illumination-corrected cross-sections. The overall intensities are not uniform, which is due to a non-uniform illumination of the sample. To account for this variation, I fitted the water signal with a polynomial which I then used to scale the d-SDS and DDAB signal. Figure 3.38 shows the intensities of the three components along the cross section of the image recorded at 50 °C. Also, the surfactants to water ratios are related to the concentration of each surfactant and therefore, the signal intensities can be converted into surface coverage. The image analysis confirms the

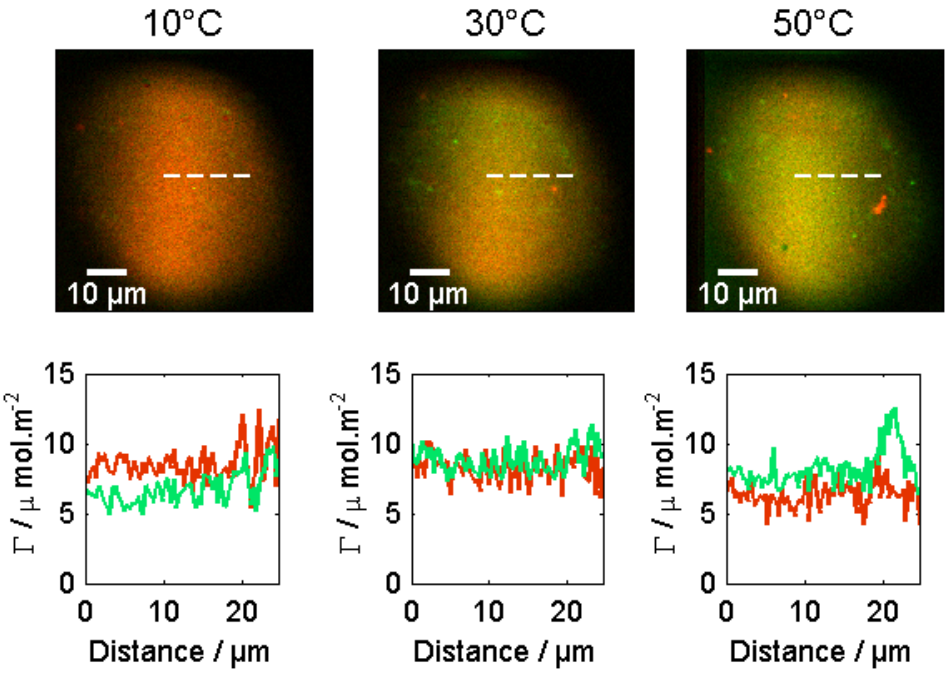

Figure 3.37: TIR Raman images of a DDAB–d-SDS layer formed from a [DDAB]:[d-SDS] = 0.60 : 0.40 solution, during the heating up step from 10 °C back to 70 °C. DDAB is shown in red and d-SDS in green. The amounts of each surfactant along the cross sections determined after image flattening are shown below each image.

inversion of the ratio d-SDS–DDAB with the temperature rise. The amounts of surfactant at 10 °C and 30 °C are close to the ones determined by spectral analysis shown in figure 3.36a. At 50 °C, the reduction of DDAB is also observed although not at the level measured by spectral analysis. The images furthermore show the presence of aggregates on the surface. For example, the cross-section at 50 °C shows a d-SDS rich aggregate at 20 µm.

3.4 Conclusion

In this chapter, I used TIR Raman spectroscopy to measure the adsorption of a pure anionic surfactant (d-SDS), a dibranched cationic surfactant (DDAB) and their mixtures onto hydrophilic silica. After demonstrating the formation of a stable bilayer of DDAB, I described a phase transition inside the adsorbed layer similar to a gel-liquid phase transition observed in supported lipid bilayers. Quantitative parameters such as the primary order parameter, the position of the peaks and the ratio between

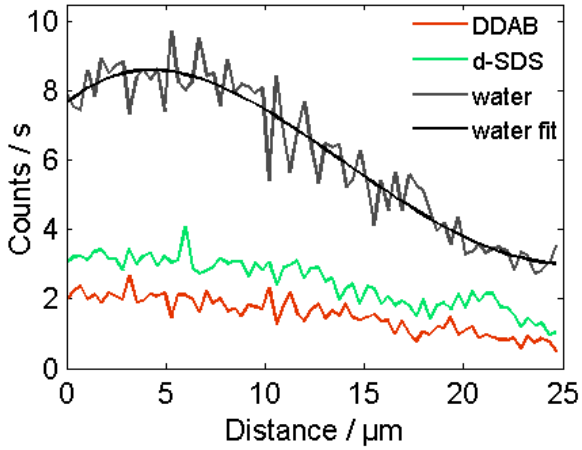

Figure 3.38: Untreated cross-section of the Raman image shown in figure 3.37 ($T = 50\,°C$). The black line is a polynomial fit of the water signal used for flattening the cross-section.

S and P intensities have been introduced. All these parameters are mildly changing in the range of temperatures studied. The peak positions of the methylene stretches shifted gradually over the temperature range. The lowest temperatures show the lowest peak positions, demonstrating that less hydrogen bonds were formed between the CH groups of the methylene and the water molecules. This is in agreement with a gel phase and an increased packing density. However, the shape of this shift does not correlate with the change of amplitude of Raman intensities or the primary order parameter. The ratio of S and P intensities changes weakly during the phase transition showing that the chain tilt is not varying significantly. The more sensitive primary order parameter $I(d^+)/I(d^-)$ is not reaching the value of 1.4 which would mark the formation of a complete gel phase, observed for longer dibranched alkylammonium or phospholipids. Instead, the phase transition in the DDAB bilayer is milder and has probably been completed at the experimental temperature limit of 10 °C.

Deuterated SDS was incorporated in the DDAB vesicles in various mole fractions in Milli-Q water. On the anion-rich side, no adsorption was observed. The vesicles are repelled from the negatively charged silica surface. On the cation-rich side, both surfactants adsorbed in concentrations that depend on the ratio between their molar fraction. The total surface coverage was higher in all compositions compared to pure DDAB, reaching a maximum around [d-SDS] : [DDAB] = 0.4 : 0.6. The composition of the layer deviates strongly from an ideal mixture. This deviation can not be fitted by one regular solution model over the whole range of concentrations. Instead, two interaction parameters can be calculated, one for high and one for low d-SDS bulk fractions. The composition of the adsorbed layer at higher d-SDS bulk fractions ($x_{\text{d-SDS}} \geq 0.35$), is close to the bulk fraction. The presence of d-SDS additionally shifts the DDAB phase transition towards high temperatures, demonstrating the better affinity of SDS with DDAB in its gel phase, compared to DDAB in its fluid phase. The primary aim of this chapter was to design a transport vehicle for SDS onto a negatively charged surface, which will undergo a phase transition in the range

of temperatures studied triggering an asymmetric release of SDS by changing the temperature. Mixed bilayers containing an equimolar ratio of d-SDS and DDAB were adsorbed with DDAB in the gel phase and release was tentatively triggered by the transition of DDAB towards the liquid phase where SDS is less soluble. However, the ratio of [d-SDS] : [DDAB] does not undergo a clear change although the gel-liquid phase transition of DDAB is happening inside the layer.

An additional attempt was carried out with the amine equivalent of DDAB, didocyldimethylamine (DDA) to tune the electrostatic attraction with d-SDS by changing the pH. However, it has not been possible to prepare vesicles by hydrating films of DDA, above the pKa of DDA.

This chapter has pointed out the difficulty of designing a transport vehicle which would also release the cargo once both are coadsorbed on the surface. The following chapters will focus on the release of cargo molecules from responsive surfaces. To do so, polymers undergoing phase transition in water will be chemically attached onto the substrates and the binding constant of various cargo molecules will be measured.

Chapter 4: pNIPAM films

4.1 Introduction

The aim of this chapter is to examine the potential of poly(*N*-isopropylacrylamide) films to take up and release a cargo molecule to and from a coated surface. In the first part of this chapter, I will given an overview of the research that has been done on pNIPAM films. Then, I will present and discuss my results on the interactions between the polymer film and potential cargo molecules. I will also discuss the selection of cargo models for the following chapters.

4.2 Review

pNIPAM has been intensely studied since the seminal publication by Heskins and Guillet in 1968 where they presented the phase diagrams of the polymer in water.[161] The polymer showed a macroscopic phase separation over a small temperature range close to the human body temperature. pNIPAM has now become one of the most studied thermoresponsive macromolecules with researchers studying its behaviour with a wide range of techniques including NMR,[162,163,164,165] light scattering,[166,167,168,169,170,171] turbidity measurements,[161,172,173,174,175] fluorescence microscopy,[176,177] IR spectroscopy,[178,179,180,181] and Raman spectroscopy.[182,183] There are multiple reasons for its popularity: The location of the phase transition close to the body temperature makes it an interesting candidate for biomedical applications such as drug delivery. pNIPAM is as a model system for the study of hydrogen-based interactions since it is neutral in water and its behaviour is mainly driven by hydrogen bonding. The polymer's amide bonds and conformational changes during the phase transition furthermore make it a good model for the study of folding mechanisms in proteins where pNIPAM and its derivatives are *e.g.* used to assess the impact of the chemical structure on sterical hindrance.

This review will first focus on the phase diagram on pNIPAM and spectroscopic techniques used to study the associated changes in the polymer structure. The next part discusses the behaviour of grafted pNIPAM films while the last section provides an overview of pNIPAM-based cargo delivery systems.

4.2.1 Phase diagram of aqueous solutions of pNIPAM

The thermoresponsiveness of pNIPAM in water is due to a change in solubility of pNIPAM chains in water. Above a critical temperature, the solution demixes

into a polymer-rich phase and a water-rich phase. This behaviour has also been observed in other neutral polymers such as poly(ethylene oxide) (pEO) or poly(*N*-vinylpyrrolidone) and has been attributed to the formation of a network of hydrogen bonds around the chains. The high entropy penalty for breaking these networks results in peculiar phase diagrams. For example, the phase diagram of pEO in aqueous solutions contains a closed loop. Outside the loop, pEO chains are dissolved in water, inside there is phase separation.[184] The shape of the miscibility line is a function of the molecular weight of the chains. The lowest temperature upon which such a solution demixes is called the lower critical solution temperature (LCST). A number of small molecules also show a closed loop phase diagram in water such as triethylamine[185] (LCST = 19 °C) and nicotine (LCST = 61 °C).[186]

In contrast to pEO, the phase diagram of pNIPAM shows that the LCST is rather independent of the concentration of pNIPAM at low polymer concentrations (see figure 4.1). The closed loop becomes closer to a square. This behaviour has been rationalised by Tanaka *et al.* who demonstrated sequential adsorption of water molecules onto the pNIPAM chains. In other words, once a water molecule is bound onto a NIPAM monomer, the neighbouring water molecules adsorb much more easily onto the neighbouring site. This sequential adsorption is related to the steric hindrance resulting from the large hydrophobic isopropyl group.[187] The amide is then by far the preferred binding site onto pNIPAM. The resulting domino effect leads to a sharp transition. Using this model, Tanaka *et al.* were able to find good agreement with their own experimental data using polymer samples with various chain lengths.

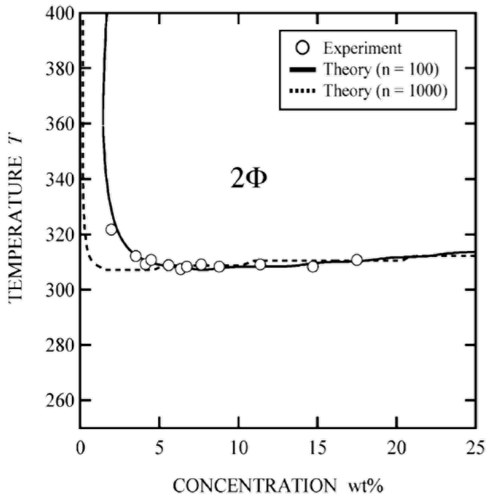

Figure 4.1: Phase diagrams of pNIPAM aqueous solutions as predicted by Tanaka *et al.* (lines) and reproduced with permission from reference [187].

The first phase diagram of pNIPAM was measured by Heskins and Guillet[161] in 1968 who reported a LCST of 32 °C. However, additional measurements show a variety of phase diagrams. In a recent review,[188] Halperin *et al.* plotted them altogether as shown in figure 4.2. The diversity of phase diagrams can be due to differences in the polydispersity of the chains, different chain ends or experimental errors such as overheating. They can also be related to slow equilibration between

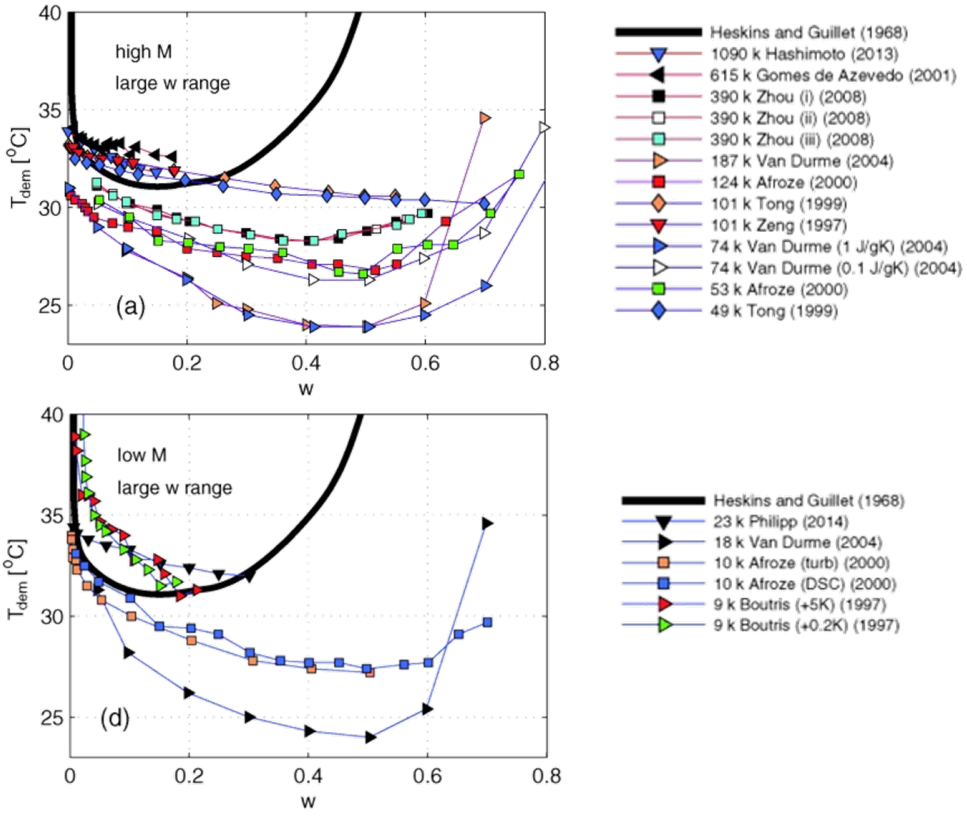

Figure 4.2: Phase diagrams of aqueous pNIPAM solutions as reported in the literature where w denotes the weight fraction of pNIPAM in water. Low molecular weight (left) and high molecular weight (right) samples were plotted separately. The seminal paper of Heskins and Guillet [161] was taken as reference (thick black line). Other papers are labelled with the name of the first author and year of publication. Reproduced with permission from reference [188].

the different states of hydration of the polymer. There is overall a high variation in the phase behaviour plotted in figure 4.2 but we can conclude that the LCST depends on the polymer concentration.

An elegant method for constructing the phase diagrams of pNIPAM in water has been developed by Zhou *et al.* using a microfluidic system to enable a rapid heat exchange in the solution. [189] The concentration of pNIPAM was varied by a controlled evaporation and phase diagrams were obtained very easily and quickly. The results proved to be very reproducible and allowed the study a large range of concentrated solutions which otherwise too viscous to measure their phase transition temperature. This way it was possible investigate solutions with more than 40 wt% pNIPAM. The LCSTs of aqueous pNIPAM solutions at various concentrations are shown in figure 4.3.

The LCST behaviour of pNIPAM has also been characterised using change of solvent. Tirrell *et al.* measured the LCST of a 0.04 wt% solution of pNIPAM in water/methanol mixtures using cloud point measurements and microcalorimetry. [190] Both measurements agreed quantitatively in showing that the LCST drops when adding methanol and rises sharply again at higher concentrations. A more expected

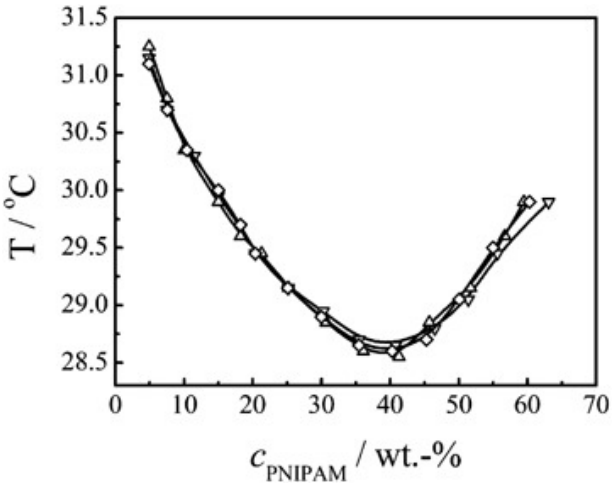

Figure 4.3: LCST of pNIPAM–water solutions prepared in a microfluidic systems. Three repetition curves showed good overlap between different set of data ($\overline{M}_w$ = 390 000 g mol^{-1}, $Đ_M$ = 1.10). Reproduced with permission from reference [189].

behaviour would have been to observe an increase in the transition temperature when adding a better solvent (methanol). The smallest LCST of −5 °C was reached for a specific volume fraction of methanol of 0.55. The first drop in the LCST marks a co-nonsolvency behaviour where a mixture of two otherwise good solvents leads to a drop in solubility. This behaviour was also observed with other water miscible polar solvents such as tetrahydrofuran[191] or in dioxane.[192] The same behaviour was recorded for 200 times more concentrated solution (8 wt%).[193] Tirrel *et al.* concluded that the interactions between water and methanol were preferred to the ones between water and pNIPAM. The co-nonsolvency phenomenon in methanol became a recurring topic and several mechanisms were inferred. In 2014, Kremer *et al.* suggested that molecules of methanol could promote the binding of two distant NIPAM monomers driving collapse.[194] Rodríguez-Ropero *et al.* suggested a preferential binding of methanol as compared to water onto collapsed pNIPAM, resulting in a shift of the LCST towards lower temperatures upon addition of methanol. This mechanism is consistent with the dependency of the reentry into the coil regime at higher concentrations on the molecular weight of the chain.[195] For Grazziano *et al.*, the competition between the two otherwise good solvents leads to a collapse in the mixed solvents region for pure geometrical reasons. Methanol binds preferably onto the isopropyl group of pNIPAM while the water molecules position themselves onto the amide. The collapse of pNIPAM reduces this frustration.[196]

Spectroscopy The phase transition of pNIPAM in aqueous solution has been the subject of multiple studies over the years, investigating the impact of temperature on the structure and hydration of the polymer. Although majority of the studies utilised IR spectroscopy, Raman spectroscopy has received some attention as well. This section outlines some of the spectroscopic studies on the chain collapse of pNIPAM giving insight on peak assignment as well as the mechanism behind the phase transition. The findings of the presented studies will help with the interpretation of spectral changes reported in the results section of this chapter.

One of the first IR spectroscopic studies on this subject was published by Maeda and coworkers in 2000.[180] They recorded IR spectra of solutions of pNIPAM and pNIPAM-d, a version of pNIPAM where the amide groups are deuterated, in water and D_2O, respectively. Spectra of the solutions were recorded between 25 °C and 40 °C, capturing the phase transition in both systems. Changes in the spectra were determined through the subtraction of spectra recorded at low temperature from high temperature spectra. The C−H stretching, amide II and C−H bending bands were found to move to lower wavenumbers during phase transition whereas only the amide I band shifted upwards to higher wavenumbers. The inflection point of all signal shifts matched the onset of the phase transition observed with DSC measurements. A closer analysis of the amide I band in pNIPAM-d, which contains contributions from C=O stretching vibrations (80 %) as well as minor contributions from N−H bending vibrations, revealed the appearance of an additional peak above the LCST located at 1650 cm^{-1}. It was determined through comparison with the IR spectrum of *N*-methylacetamide (NMA) that the first component of the amide I band, located at 1625 cm^{-1}, can be assigned to hydrogen bonding between the C=O and water. The second peak appearing above the LCST (1650 cm^{-1}) was assigned to weak intra- and intermolecular hydrogen bonding between C=O and N−H/N−D groups of pNIPAM/pNIPAM-d. Spectral analysis showed that only 13 % of the C=O groups form hydrogen bonds with amide groups above the LCST indicating that the majority of C=O is not dehydrated and still forms hydrogen bonds with water. The amide II band of pNIPAM is associated with N−H bending (60 %) as well as C−N stretching (40 %) and consists of a single peak at 1559 cm^{-1} below the LCST. The appearance of a second peak at 1535 cm^{-1} was interpreted as a consequence of a shift from hydrogen bonding between the N−H groups and water to hydrogen bonding between N−H and C=O groups. The opposite shifts of the amide I and II bands can thus be explained with weaker hydrogen bonding involving the polymer's amide groups. The deconvolution of the C−H bands revealed that all bands except the $\nu_s(CH_2)$ and $\nu(CH)$ bands experience a shift towards lower wavenumbers of up the 6 cm^{-1} during the phase transition. This change was also attributed to dehydration since C−H···OH_2 interactions lead to a contraction of the C−H bond thus shifting the signal to higher wavenumbers.

Similarly, Katsumoto and coworkers studied the phase transition in aqueous solutions of pNIPAM using IR spectroscopy but utilised Density Functional Theory (DFT) calculations to aid the interpretations of the results.[179] Their temperature-dependent IR measurements also show single peaks in the amide I and II regions located at 1624 cm^{-1} and 1562 cm^{-1}, respectively, below the LCST. The appearance of a second peak (1653 cm^{-1}) in the amide I region was attributed to free C=O groups following the breaking of C=O···H−N hydrogen bonds. They observed a gradual upward shift in the wavenumber of the amide II band of about 6 cm^{-1} which they assigned to the formation of intramolecular hydrogen bonds as well as conformational changes in the main chain. Changes observed in the amide III bands located between 1130 cm^{-1} and 1180 cm^{-1} were also attributed to conformational changes in the main chain. DFT calculations suggested that the bands located at 1173 cm^{-1} and 1155 cm^{-1} can be

attributed to contributions from trans and gauche conformations, respectively. The relative intensity increase of the two bands during the phase transition was thus seen as either a decrease in gauche or an increase in trans conformations.

In their follow-up work, Katsumoto *et al.* focussed on changes in the amide I band.[197] By adding methanol and THF to aqueous pNIPAM solution, they saw the appearance of a second peak in the amide I region previously seen above the LCST in pure pNIPAM–water mixtures. The mixtures show phase separation but redissolve again at high co-solvent concentrations. Interestingly, the second amide I peak, located at $1650\,\mathrm{cm^{-1}}$, still increases with co-solvent concentration when pNIPAM dissolves again. As a consequence, the signal at $1650\,\mathrm{cm^{-1}}$ cannot purely be a consequence of C=O···H−N interactions following the pNIPAM chain collapse. Through DFT calculations and spectral comparisons with model systems, the researchers concluded that the peak at $1624\,\mathrm{cm^{-1}}$ can be assigned to di-hydrated C=O groups as well as intramolecular C=O···H−N interactions. The amide I peak at $1650\,\mathrm{cm^{-1}}$ was assigned to mono-hydrated C=O in addition to C=O···H−N interactions. For comparison, the fully hydrated C=O bonds in the model component NMA give rise to an amide I peak at $1618\,\mathrm{cm^{-1}}$. It thus follows that the C=O groups of pNIPAM in water are not fully hydrated below the LCST. The peak observed at $1673\,\mathrm{cm^{-1}}$ in methanol and THF is assigned to weakly solvated C=O groups.

In a later study, Maeda *et al.* utilised confocal Raman microscopy to follow the phase transition of pNIPAM in water focussing on the CH part of the Raman spectrum.[183] They observed the expected formation of particles above 32 °C which adsorbed to the glass surface of their sample cell. Through Raman microscopy they were then able to determine the composition of the polymer-rich particles and the surrounding solvent phase at 40 °C as a function of bulk pNIPAM concentration. At a bulk concentration of 10 wt%, in the polymer-rich and solvent-rich phases were found to contain 51 wt% and 9 wt%, respectively. The pNIPAM concentration increased linearly in both phases with increasing bulk concentration. Monitoring the polymer concentration inside the particles during the cooling process showed a sharp decrease around 34 °C matching the endothermic peak observed in DSC measurements. A close investigation of the CH vibrations showed that the ν(C−H) vibration was located at $2924\,\mathrm{cm^{-1}}$ polymer-rich phase and at $2944\,\mathrm{cm^{-1}}$ in the solvent-rich phase. In the single-phase system below the LCST (30 °C), the signal can be found at $2943\,\mathrm{cm^{-1}}$. As mentioned above, interaction with water can shift the signal of C−H bonds to higher wavenumbers. The observed shift is consequently an indicator of a dehydration of pNIPAM's main chain. The researchers furthermore added 2-propanol-d_8 to pNIPAM solutions observing an accumulation of the co-solvent inside the polymer-rich phase. Their research thereby shows the viability of using Raman spectroscopy for the study of pNIPAM systems enabling the detection of changes within the polymer *in situ* as well as the study of species accumulating within it.

The phase transition in pNIPAM was also studied by Dybal and coworkers who compared it to the transition in poly(*N*-isopropylmethacrylamide) (pNIPMAM).[198] They combined Raman spectroscopy, ATR-IR and DFT calculations to study the impact of the α-methyl group present in pNIPMAM on the polymer's physical struc-

ture in water. Their finding include a strong hysteresis in the phase transition of pNIPMAM during cooling which was explained by the formation of larger compact structures during the chain collapse. The dissociation of those compact structures has a higher energy barrier compared to pNIPAM. They also showed that hydration of the amide group increases the strength of inter-amide hydrogen bonds compared to free dimers, leading to shorter C=O···H−N bonds. This explains the shift of pNIPAM's amide II band to lower wavenumbers during the phase transition. Their findings were confirmed by Tang *et al.* who studied similar systems using laser light scattering and ultrasensitive differential scanning calorimetry.[199] This again highlights the utility of vibrational spectroscopy for the study of changes within pNIPAM.

Sun and coworkers employed FTIR and 2D-IR correlation for a detailed study of changes in the CH and amide I signals during the phase transition of highly concentrated pNIPAM (20 wt%) in D_2O.[200] Increasing the temperature past the phase transition led to a sudden shift in the positions of peaks associated with the $\nu_{as}(CH_3)$ vibrations of the side chains and the $\nu_{as}(CH_2)$ vibrations of the main chain, located at 2981 cm^{-1} and 2938 cm^{-1}, respectively. This shift towards lower wavenumbers was, as before, associated with a dehydration of the side and main chains during the phase transition. The transition of the CH_3 groups was observed about 1 °C below the transition of the main chain's CH_2 groups indicating that the side chains are more sensitive towards temperature. 2D-IR correlation revealed two dehydration steps of the CH_3 groups: first CH_3 groups hydrated with more water molecules will change to CH_3 groups with less water molecules. In a second step, these groups will dehydrate further. The changes in the $\nu_{as}(CH_2)$ peak were interpreted to reflect main-chain aggregation. This aggregation happens following the two-step dehydration of the side chains. The process during the cooling is slightly different as the CH_3 groups surrounded by fewer water molecules hydrate partly, followed by disentanglement of the main chain. The CH_3 groups hydrate further in the final step. The amide I region showed the familiar single peak at low temperature (1624 cm^{-1}), dropping in intensity during the phase transition while a second peak (1649 cm^{-1}) emerges. The two peaks were associated with C=O···D−O−D and C=O···D−N hydrogen bonds, respectively. The changes thus indicated the dehydration of the C=O and the formation of intra- and intermolecular hydrogen bonds during the phase transition. An analysis of the signal intensities showed that only about 35 % of the C=O groups form hydrogen bonds with N−H groups after the phase transition. Consequently, 65 % of the groups are still hydrated. This observation matches the observations by Maeda *et al.* who reported a significant water content in pNIPAM-rich phases above the phase transition temperature.[183] It should be noted that Sun and coworkers observed that the molar fraction of C=O···D−N did not drop back down to zero during the cooling process which is thought to be a consequence of the high pNIPAM concentration. 2D-IR correlation analysis of the amide I region showed that a temperature rise first leads to the breaking of hydrogen bonds with water before hydrogen bonds are formed between C=O groups and D−N. A combined analysis of the phase transition indicated that these processes happen after the changes in the CH_3 and CH_2 groups.

The number of water molecules associated per monomer has been addressed by

Füllbrandt *et al.* Using dielectric relaxation spectroscopy, they demonstrated that above the LCST, pNIPAM solutions are as conductive as pure water. Below the LCST, however, strong deviations were observed and attributed to the formation of additional hydrogen bonds between water and pNIPAM. They were able to estimate that five additional water molecules per NIPAM monomer are attached to pNIPAM below the LCST which is in agreement with the vibrational spectroscopy studies presented in this section.[201]

4.2.2 pNIPAM grafted films

The previous section showed the complex phase behaviour of aqueous pNIPAM solutions as a function of temperature and polymer concentration. Grafting introduces a new parameter called grafting distance which is a measure of the average distance between the anchor points of two neighbouring chains. This parameter is therefore somewhat similar to the polymer concentration in solutions. Grafting density and molecular weight are thus expected to both have significant impact on the changes that occur within grafted pNIPAM at the LCST.[202] The understanding of this influence is consequently of high importance in order to be able to design efficient thermoresponsive polymer layers. This section explores some of the work that has been done to study the impact of the three parameters — temperature, grafting density and molecular weight — on grafted pNIPAM films including the phase behaviour, structure and topography. The majority of the studies presented in this section focus on films grafted from planar substrates but also include an example concerning spherical substrates.

An extensive study on the impact of grafting density and molecular weight on the collapse of grafted pNIPAM chains was published by Plunkett and coworkers in 2006.[203] The researchers grafted pNIPAM brushes from gold surfaces at varying grafting densities and molecular weights controlling the parameters by diluting the initiator on the substrate and limiting the reaction time, respectively. The dry polymer thickness of the brushes was determined through AFM and ellipsometry measurements. Both techniques showed an increase in film thickness with grafting density and molecular weight. AFM measurements overall returned lower values than ellipsometry which can be caused by adhesion of the AFM tip to pNIPAM and subsequent damping of the oscillation. SFA measurements of the polymer films in water were carried out at 26 °C and 36 °C, above and below the LCST. The measured thickness again increased with increasing molecular weight and grafting density. Comparing the relative changes in film thickness during the phase transition showed that the magnitude of the change also increases with an increase of the two parameters. For example, the thickness of the longest brush with the highest density (2.3 nm^2/chain, 269.0 nm at 26 °C) decreased by 30 % whereas the shortest brush with the lowest grafting density (19.3 nm^2/chain, 38.3 nm at 26 °C) showed no noticeable change in its thickness. The LCST itself, however, was independent of the two parameters and did not vary throughout the investigated systems. Force measurements indicated the existence of a two-layer structure below the LCST with a high-density inner layer and a low-density outer layer.

A different behaviour was reported by Yim *et al.* who grafted pNIPAM brushes of varying lengths but constant grafting density (3.2 nm^2/chain) from gold.[204] Concentration profiles at the gold–D_2O interface obtained through neutron reflectometry at 41 °C were step-like for all chain lengths and did not change in shape with the molecular weight. There was, however, much more variation in the low temperature concentration profiles (20 °C): the highest molecular weight (71 000 g mol^{-1}) showed a step-like profile albeit with a broader transition indicating that the brush thus existed as a single dense layer at both temperatures. The profiles became more bilayer-like with decreasing molecular weight leading to the distinct bilayer profile of the 13 000 g mol^{-1} brush. The sample had a thin layer of high segment concentration close to the substrate followed by a low concentration layer that extended far into the subphase at a distance comparable to the length of fully extended chains. The film thickness was determined to change the most during the phase transition at low molecular weights while the sample with the highest M_w showed only a small collapse. In contrast to the results reported by *e.g.* Plunket *et al.*, the fractional change of the polymer thickness between 20 °C and 41 °C decreased with increasing molecular weight. The variation in the low-temperature concentration profiles was seen as a consequence of attractive segment-segment interactions at high grafting densities matching previously reported behaviour in aqueous pNIPAM solutions. The similar profile shapes at 41 °C are explained through the much more attractive segment–segment interactions at high temperature leading to more uniform collapsed layer.

The work of Ishida and Biggs is an interesting addition to the findings of Plunket *et al.* since they worked with similar pNIPAM brushes.[205] Their brushes were grafted from silicon at varying grafting densities but constant molecular weight, comparable to the highest molecular weights used in the work above. The high and medium grafting densities in this study are comparable to the highest and lowest densities synthesised by Plunkett and coworkers, respectively. Ishida and Biggs recorded AFM images of the pNIPAM brushes at different temperatures between 26 °C and 40 °C to detect possible morphology changes during the phase transition. All brushes were virtually featureless at low temperatures. The low-density brush began to show domains close to the LCST which then increased in contrast with rising temperature indicating the formation of more rigid structures. First features appeared earlier for more dense films with the onset temperature decreasing with increasing grafting density. The domain formation in the AFM images are direct evidence of the formation of mushroom-like features during the phase transition. The researchers did not determine the changes in film thickness but compression tests with the AFM tip indicated a significant collapse of the layers towards the surface. The earlier onset of the feature formation at higher grafting densities shows a broader phase transition for denser films at constant LCST.

This formation of domains in pNIPAM brushes was investigated further by Choi and coworkers who studied the impact of the features on ellipsometric height measurements.[206] AFM images of dense pNIPAM films (11 nm^2/chain) grafted of varying molecular weights (30–85 kDa) were recorded at room temperature and above the LCST at 35 °C. Ellipsometry was then used to measure the heights of the polymers

at both temperature. The collapse of a brush with high molecular weight that was uniform at both temperatures was reflected well in the ellipsometry results. A brush of medium molecular weight did not collapse above the LCST but AFM data showed the formation of distinct domains at high temperatures. The ellipsometry measurements, however, returned identical values for the brush thickness at both temperatures. A similar behaviour was seen for a low-M_w brush although the features were smaller. The researchers also compared AFM images to data from protein adsorption measurements carried out with similar brushes. The polymer films of varying grafting densities were swollen and featureless at low temperature but exhibited domains at high densities above the LCST. Protein adsorption at high temperature initially increased with increasing grafting density but dropped with the onset of micelle formation. This behaviour is potentially caused by the micelles as dense brushes can repel proteins. It has to be noted though that the presented AFM images are not of the polymer brushes that were used for the adsorption measurements.

Suzuki and coworkers found that very high grafting densities ($\sim$2 nm^2/chain) lead to the situations mentioned before where a temperature increase above the LCST does not lead to the sudden change in film thickness usually observed in grafted pNIPAM films at the solid–water interface.[66] Instead, the physically restrained state of the polymer chains leads to a gradual decrease of the film thickness with increasing temperature. The high grafting density means that the pNIPAM chains cannot fully interact with water at low temperatures leading to the brush behaving like a partially collapsed layer at low temperatures. More interactions are possible at higher temperature, leading to the more gradual change in film thickness. IR measurements in the amide region furthermore revealed that there is still significant interaction between the chain and water above the LCST leading to the increased film thickness of the collapsed layers compared to dry films.

Variations of the polymer density within a pNIPAM brush can also lead to multiple phase transitions inside the layer. Tang and coworkers studied phase transitions in particles composed of pNIPAM grafted from poly(oligo(ethylene glycol) methacrylate) (pOEGMA) cores.[207] 2D-IR correlation showed a two-step phase transition during the temperature increase where the inner part of the pNIPAM brushes collapses first. The outer part collapses at higher temperatures forming a densely packed shell. The non-uniform collapse was due the higher packing and lower hydration of pNIPAM segments closer to the core, a consequence of the particles' spherical shape. This resulted in the lower phase transition temperature compared to the outer parts of the polymer. Similar behaviour had been observed for gold nanoparticles with grafted pNIPAM brushes albeit at lower temperatures.[208] The temperature difference is thus a consequence of the pOEGMA core which favours hydrophilic conditions and highlights the complexity of the phase transition in grafted pNIPAM layers.

This section provided an overview on the complexity of the phase behaviour of grafted pNIPAM layers. While the phase transition is generally less sharp than in solutions, it was also shown that the presence, amplitude and shape of the temperature response of grafted pNIPAM layers across the LCST is impacted by its grafting density and molecular weight. The LCST itself, however, appears to be less dependent on

those factors. It became furthermore apparent that heterogeneous structures can form inside the layers close to and above the LCST, and potentially affect cargo interactions. It is also important to note that techniques which average a relatively large sampling area, such as ellipsometry and neutron reflectometry, might make it difficult to detect the formation of such features.

4.2.3 pNIPAM-based cargo delivery systems

The close proximity of pNIPAM's phase transition temperature to the human body temperature makes it a popular candidate for controlled drug delivery. The published work can be roughly split into two main categories: carriers consisting of pNIPAM-based hydrogels and particles surrounded by pNIPAM. Hydrogels are usually simultaneously synthesised and loaded with cargo by cross-linking pNIPAM or copolymers containing NIPAM in the presence of cargo molecules to trap them inside the forming network. The second category includes core-shell particles where the phase of the pNIPAM shell controls the diffusion rate between the core and the surrounding medium. A very small number of studies focusses on trapping cargo inside pNIPAM brushes grafted from planar substrates which is more relevant to the work presented in this chapter. The following paragraphs provide a brief overview of some of the work that has been carried out to develop pNIPAM-based cargo delivery systems.

The work published by Zhang and coworkers in 2004 is an example of the advanced work on pure pNIPAM hydrogels.[42] The researchers synthesised the hydrogels by cross-linking the polymer but also explored interpenetrating polymer network (IPN) structures. IPN-pNIPAM hydrogels were synthesised through an additional cross-linking reaction between pNIPAM hydrogels and NIPAM monomers. The aim was the creation of hydrogels with an increased mechanical stability, reducing the risk of open channels inside swollen hydrogels which can lead to the undesired diffusion of cargo out of polymer assembly. The degree at which the second pNIPAM network formed was controlled through the concentrations of NIPAM and the redox initiator. The IPN structures were found to increase of the compression modulus and tensile modulus but had no significant impact on the LCST. The modified hydrogels, however, showed the formation of fibrillar structures alongside less regular pore structures compared to regular pNIPAM hydrogels. They also had an impact on the release of the protein bovine serum albumin (BSA), leading to a slower release above and below the LCST. The release of BSA at 20 °C during a period of 96 h, for example, dropped from 54 % for a normal pNIPAM hydrogel to 28 % in the hydrogel with the highest degree of second pNIPAM structures. It is important to note that the release profiles do not change considerably above the LCST: 43 % and 23 % of BSA were released at 37 °C during the same time span, respectively. The formation of additional structures thus has no significant impact apart from improved mechanical stability and does not allow the controlled release of BSA.

Hydrogels synthesised from a copolymer containing pNIPAM and a second polymer are an alternative to pure pNIPAM hydrogels. Huang and coworkers used such copolymers as the basis for their work on hydrogel nanoparticles.[41] They cross-linked

monodisperse d(NIPAM-co-allylamine) and d(NIPAM-co-acrylic acid) nanoparticles to create interconnected hydrogel nanoparticle networks consisting of a primary network of cross-linked polymers and a secondary network of cross-linked particles. The cross-linking was carried out in solutions containing dextran of varying molecular weights to trap the molecule inside the hydrogels. Pure pNIPAM gels were loaded with dextran as well to assess the impact of the copolymers on the release kinetics. Allylamine-containing hydrogels exhibited a phase transition similar to pure pNIPAM hydrogels but different release kinetics. The release of dextran from p(NIPAM-co-allylamine) and pNIPAM hydrogels was studied at 21 °C and 37 °C, and monitored by UV/vis spectroscopy. Overall, dextran-release was much slower from pNIPAM hydrogels than from the allylamine-containing derivative, *e.g.* less than 25 % within 28 h compared to 60 % after 9 h, respectively. The release rates from p(NIPAM-co-allylamine) decreased with increasing polymer weight of dextran but were higher at temperatures above the LCST than at room temperature. The p(NIPAM-co-acrylic acid) hydrogels, by contrast, showed a rather different behaviour. The hydrogels shrank much less during the temperature increase and released dextran at similar rates at both temperatures. The lack of a substantial chain collapse was thought to be the reason for this temperature-independence since it means that the mesh size did not change significantly over the studied temperature range. The results of this work nevertheless show that hydrogels based on pNIPAM derivatives can potentially be used to deliver cargo molecules that are otherwise only slowly released from pure pNIPAM hydrogels. The work also highlights the challenge of preserving the thermoresponsiveness of pNIPAM when forming copolymers.

A different study on p(NIPAM-co-acrylamide) hydrogels was published by Zhang *et al.* who studied its possible application for the delivery of anticancer drugs.[209] Their research did not focus on the controlled release of cargo but on its targeted delivery. The researchers were able to tune the LCST of their hydrogels by varying the acrylamide concentration inside the hydrogel. An increase of the acrylamide content led to a rise in the LCST ranging from 35.5 °C to 48 °C for 2.4 wt% and 16.7 wt%, respectively. The hydrogel diameter was controlled by the SDS concentration inside the reaction mixture. A SDS concentration of 0.5 mg mL^{-1} resulted in hydrogels with a diameter of 440 nm while an increase to 2 mg mL^{-1} led to smaller hydrogels with diameters of around 50 nm. The targeting behaviour of those hydrogels was studied by injecting dispersions of the hydrogels into mice. The hydrogels of the animal study had an LCST between 37 °C and 42 °C, and thus above the body temperature of the mice. Loading the hydrogels with the hydrophobic fluorescent dye NIRD-12 prior to the injection allowed the monitoring of their distribution inside the mice *in vivo* through near infrared imaging. Injecting dye-loaded hydrogels as well dye-only injections led to accumulations inside the livers. Raising the temperature of one of the legs, however, led to an additional accumulation inside that leg. Similar results were achieved in mice with tumor tissues. Raising the temperature of the tumor tissue, referred to as hyperthermia treatment, led to an accumulation of the dye-loaded thermoresponsive hydrogel inside said tissue. As before, no such accumulation was seen in the control groups. This study is an important addition to research focussed

on the controlled release of cargo from thermoresponsive pNIPAM-based structures as it shows the impact of temperature on the localised accumulation of such structures. The results highlight the potential of pNIPAM for the targeted delivery of cargo molecules such as anticancer drugs.

Another approach is to utilise changes in the shape of pNIPAM during the phase transition. You *et al.*, for example, used the collapsed polymer as a sterical barrier to control the release of a cargo molecule.[210] To do so, disulfide-pyridyl-terminated pNIPAM chains were grafted to silica nanoparticles via the particle's thiol surface modification. The particles had diameters of 80–90 nm and pore sizes of 1–4 nm. The resulting carrier particles were loaded with fluorescein through immersion in a solution of the cargo at room temperature and were subsequently filtered at high temperature and washed with a buffer solution. The concentration of fluorescein inside particles following this procedure was determined to be close to the concentration in the fluorescein solution. In contrast, immersion of the particles in solution at 38 °C, above the LCST, led to no cargo uptake. Release experiments were carried out by immersing the loaded particles in buffer solutions at 25 °C and 38 °C. Measurements of the fluorescein concentration with UV/Vis spectroscopy after 48 h showed that about 80 % were released from the particles at the lower temperature, below the LCST. The particles immersed at temperatures above the LCST, however, had only released ∼20 % of their cargo. A more detailed experiment on the temperature-dependent release of fluorescein showed a significant step-wise decrease in the amount of cargo released at temperatures above the LCST. It thus follows that the pores of the particles are blocked by collapsed pNIPAM chains. The polymer consequently acts as a barrier above the LCST, obstructing the release of the cargo molecules. This work shows that the thermoresponsive behaviour of pNIPAM can be used to create molecular gates for the controlled release of cargo from porous nanoparticles.

A different approach, one that is closer to the work presented in this thesis, was taken by Elliott and coworkers who investigated pNIPAM as a potential carrier for the tuberculosis drug isoniazid.[211] In this case, the carrier is not a particle or hydrogel but a polymer brush grafted from a planar substrate. pNIPAM was grafted from silicon with a dry thickness of about 30 nm, and immersed in D_2O showed a LCST of ∼34 °C. AFM measurements indicated that the presence of a 5 vol% solution of isoniazid slightly decreased the thickness of the extended brush and delayed the onset of the phase transition. The endpoint of the transition and thickness of the collapsed brush, however, did not appear to be affected. Neutron reflectometry was then utilised to determine the density profile of the brush at different temperatures and the impact of isoniazid. Below the LCST (23 °C), the brush was extended with and without the drug. The results indicated though that there might be a layer of higher density closer to the interface in both cases. Midway through the collapse (34 °C) the polymer brush was best described with a two layer model consisting of a dense brush near the interface and a less dense layer further from the interface. This vertical phase separation was referred to as a bilayer collapse. The dense layer was found to be thinner in the presence of the drug although that was ruled to be a possible consequence of the shifted phase transition. The collapsed layer at 46 °C was

modelled with one layer in both cases and had a thickness of 41 nm and 45 nm with and without the drug, respectively. At low temperatures, below the LCST, the isoniazid concentration was found to be on average 5.7 ± 0.5 vol% inside the polymer layer at a bulk concentration of 5 vol%. Isoniazid thus has a stronger affinity towards the polymer than water. The average concentration inside the brush was 9.6 ± 1.0 vol% above the LCST. Although the numbers might indicate an accumulation of the drug at high temperature, it should be noted that the decrease in the pNIPAM volume fraction matches the increase in the concentration of isoniazid. The amount of the cargo inside the brush is thus constant across the phase transition. pNIPAM is consequently able to bind very small quantities of isoniazid but it is not possible to release the drug by triggering a phase transition.

4.3 Results

In this section, I will describe and discuss the effect of temperature on the TIR Raman spectra of pNIPAM grafted films. One aim of this study is to characterise the spectral changes induced by the rupture of hydrogen bonds during the pNIPAM phase transition, and better understand the underlying mechanism. The second aim of this preliminary study is to determine the temperatures at which the two isotherms of adsorption of cargoes will be collected. The idea is to compare the binding constant of a given cargo onto two very different states of hydration of the polymer film. Then, the adsorption isotherms of various cargoes will be measured at these two temperatures and will be compared to the isotherms collected on free silica to deduce the effectiveness of uptake and release of the polymer films.

4.3.1 Band assignment of the pNIPAM Raman spectrum

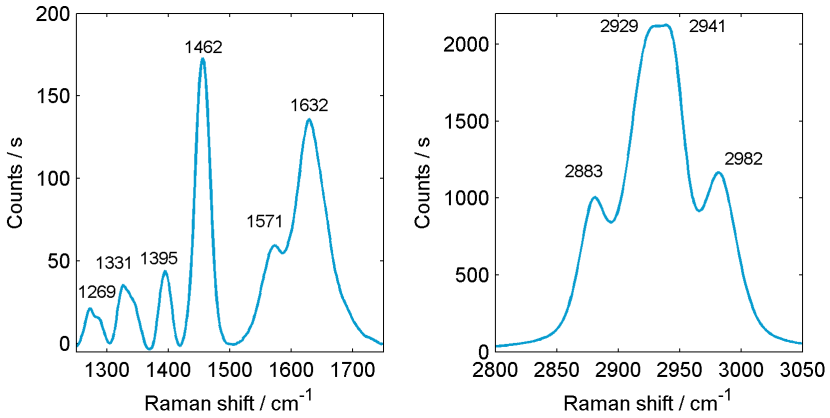

Figure 4.4: TIR Raman spectrum of a grafted pNIPAM film in the fingerprint region (left) and CH region (right), in the Sy polarisation.

Figure 4.4 shows the SY-polarised Raman spectrum of a pNIPAM film grafted onto a silica hemisphere at the silica-water interface. The main features in the Raman spectrum of pNIPAM are located in the 2800–3050 cm^{-1} range. Four main peaks are resolved and have been assigned to CH stretches. The band at 2982 cm^{-1} has been assigned to a methyl antisymmetric stretch,[212,213] while the symmetric stretch

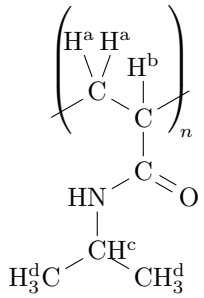

Figure 4.5: Structure of pNIPAM. The superscript letters are used to label the different hydrogen atoms listed in ta.1ble 4.1.

arises at $2883\,\mathrm{cm}^{-1}$.[212,213] The band at $2941\,\mathrm{cm}^{-1}$ is assigned to the methylene antisymmetric stretch.[213] Other others have assigned it to the methylene symmetric stretch,[212] however, based on polarised Raman spectra, I conclude that the former assignment is more likely. Finally, the band around $2929\,\mathrm{cm}^{-1}$ is assigned to a Fermi resonance of the methyl stretch. The remaining CH stretches including those of the methine group (C−H^{b} and C−H^{c}) are buried under these bands. The assigned peaks of the CH region are listed in table 4.1 with their peak positions and normalised intensities. Due to the number of Fermi resonances in the CH region, much of the intensity in the centre of this region is likely due to the Fermi resonances rather than fundamental modes. Figure 4.5 shows the the structure of pNIPAM and identifies the hydrogen atoms listed in the table.

Table 4.1: Comparison of the peak position arising from from pNIPAM.

Assignment	Peak position / cm^{-1}	Normalised intensity
CH_3 symmetric stretch,[213] H^{d}	2883	0.47
CH_3 Fermi resonance, H^{d}	2929	0.98
CH_2 antisymmetric stretch,[213] H^{a}	2941	1.00
CH_3 antisymmetric stretch,[212,213] H^{d}	2982	0.56

In the 1300–1800 cm^{-1} region, 6 peaks are resolved. The Amide III (1270 cm^{-1}) is resolved even though it has a weak Raman contribution. The bands at 1331 cm^{-1} and at 1395 cm^{-1} are tentatively assigned to an antisymmetric deformation of the isopropyl group. The band at 1462 cm^{-1} is tentatively assigned to a methylene scissoring mode. The bands at 1571 cm^{-1} and 1632 cm^{-1} correspond to the Amide II and Amide I bands, respectively.

The Amide I, II and III refer to a combination of two vibrations, the C−N stretch and the C=O stretch. The Amide I band mainly probes the C=O stretch near 1650 cm^{-1}. The Amide II band is sensitive to the N−H bend (60 %) and the C−N stretch (40 %). The Amide III mostly probes the C−N stretch and the N−H bend.[180]

4.3.2 Influence of temperature on poly(*N*-isopropylacrylamide) films

The influence of temperature on the spectrum of pNIPAM films in water has been studied. Raman spectra were recorded at temperatures ranging from 10 °C to 55 °C, starting at 10 °C. At each temperature, the sample cell was given 15 minutes to equilibrate before the measurement. As the spectrum of water changes with temperature, a reference spectrum was recorded for each temperature. Figure 4.6 shows the Raman spectra of a pNIPAM brush at different temperatures after the subtraction of the corresponding water background spectrum. The dry thickness of this brush is estimated to be 60 nm. This value is based on ellipsometry measurements of a brush grafted from a silicon wafer placed in the reacting mixture alongside the silica hemisphere that was used as the substrate for the brush shown below.

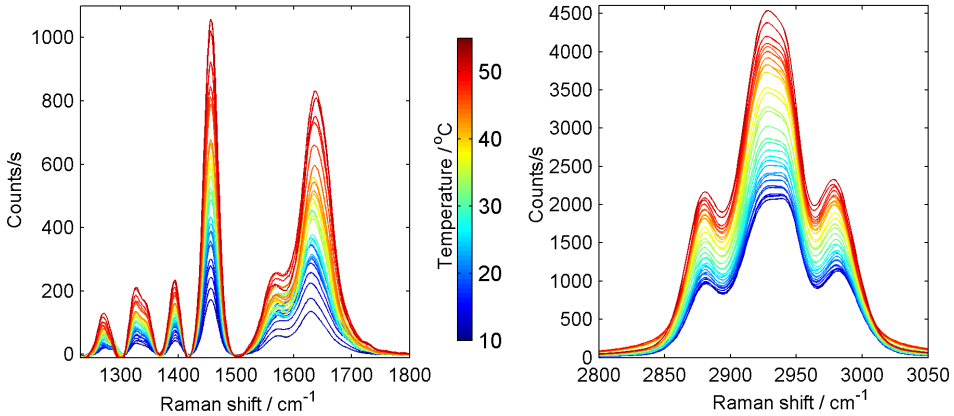

Figure 4.6: TIR Raman spectra of a grafted pNIPAM layer in the CH and CO regions, collected at different temperatures ranging from 10 °C to 55 °C. The brush has an estimated dry thickness of 60 nm.

The rise of temperature inside the cell triggers several spectral changes in terms of positions and intensities. The change of intensities during the transition is observed in both spectral regions. At the same time changes in positions of individual signals are recorded. All changes are described in the sections to follow.

Changes in intensities during phase transition

Figure 4.7 shows the amplitudes of CH stretches of pNIPAM at temperatures increasing from 10 °C to 55 °C. These intensities were calculated from the integrated TIR Raman spectra in the CH region and normalised to the intensity calculated at 10 °C. Spectra were also collected while decreasing the temperature and the corresponding amplitudes are shown in blue.

As the temperature increased, the signal amplitude in the CH region increased. This could be due to a collapse of the film where the chains move closer to the interface. As outlined in section 1.5.3, the square of the amplitude of electrical field of the evanescent wave is highest at the interface and decays exponentially with increasing distance. The observed increase in signal intensity is therefore consistent

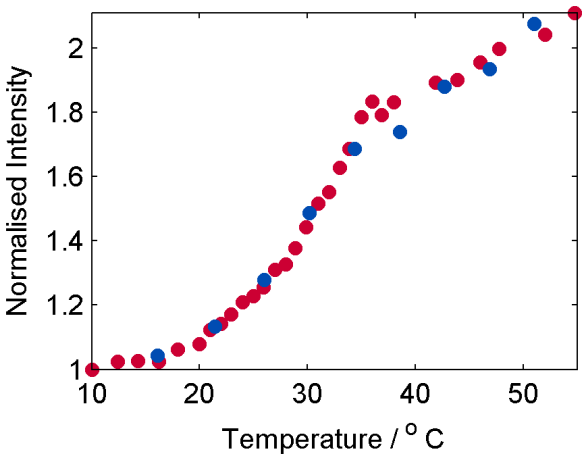

Figure 4.7: Change in intensity of the TIR Raman spectrum of a grafted pNIPAM layer as a function of temperature. These changes are probed during a temperature rise (●) and fall (●).

with the pNIPAM chains collapsing onto the substrate. The lack of a plateau at high temperatures implies that this process is not completed at 55 °C.

The curve shows two distinct regions: between 10 °C and 35 °C, the signal intensity increases rapidly with temperature. Above 35 °C, the increase slows down and becomes linear. There are two possible explanations for this behaviour: One is that the inner parts of the chains, close to the substrate, collapse first leading to the observed rapid increase in signal intensity as TIR Raman spectroscopy is more sensitive towards material closest to the interface. The outer parts of the chains are then collapsing at higher temperatures. A similar behaviour was reported for pNIPAM grafted from curved substrates.[207,208] The smaller increase in signal intensity could then be a combination of the lower sensitivity towards those changes as well as the possibly lower chain density of the polymer's outer region. The second explanation is that the chains are collapsing uniformly perpendicular to surface and that the change in the signal increase is due to a slowing down of the transition. It is not possible to exclude either explanation based on this data alone.

There is a good overlap between the two curves obtained during the temperature rise and fall. No hysteresis was observed implying that the transition is truly reversible. The pNIPAM film is elastic and can return to its initial density and thickness after the collapse.

Changes in the band position of C−H stretches during the phase transition

Figure 4.8 shows the variation of the positions of C−H stretches as a function of temperature. The position of all peaks shifted towards lower Raman shifts with increasing temperature. This change has previously been attributed to a dehydration.[180] The reduction in C−H···OH_2 interactions leads to an extension of the C−H and a signal shift to lower wavenumbers.

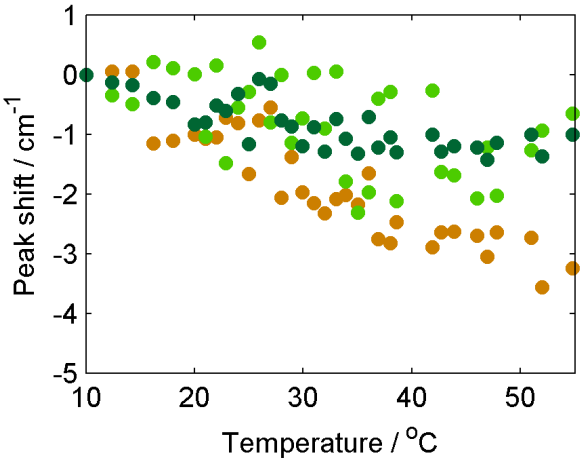

Figure 4.8: Change in peak position in the CH region of the TIR Raman spectrum of a grafted pNIPAM layer as a function of temperature. The position of the antisymmetric methyl stretch (●), the Fermi resonance of the methyl stretch (●) and the antisymmetric methylene stretch (●) are sensitive to the increase in temperature.

Changes in the fingerprint region during the pNIPAM phase transition

Figure 4.9 shows the changes in the Raman shift of the methyl deformation as well as the Amide I and II band positions (1400–1800 cm^{-1}) as a function of temperature. Each band was fitted using a Gaussian-Lorentzian blend. Whereas the position of the methyl deformation does not change across the range of temperatures studied, the position of the Amide II shifts downwards ($-12\,cm^{-1}$) while the position of the Amide I shifts upwards ($+8\,cm^{-1}$). Such observations have already been made on the study of pNIPAM solutions by another Raman spectroscopy technique.[214]

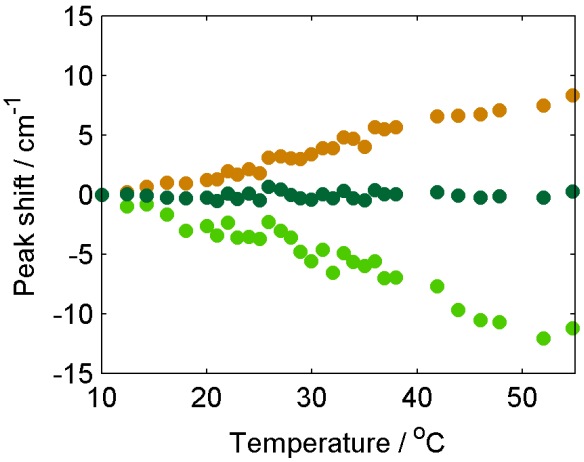

Figure 4.9: Changes in peak position in the fingerprint region of the TIR Raman spectrum of a grafted pNIPAM layer as a function of temperature.The positions of the Amide I (●) and the Amide II (●) bands are sensitive to the increase in temperature. The position of the methylene stretch (●) does not change.

Amide II The downshift of the Amide II band during the dehydration of pNIPAM has previously been reported and attributed to the loss of hydrogen bonds with water.[180] By comparing the signal shifts in pNIPAM and pNIPAM-d, Ahmed *et al.* showed that water is bonded as N−H···OH_2 rather than C−N···H−O−H at low temperatures.[214]

Amide I The upshift of the Amide I band can be explained by the presence of three peaks. At all temperatures, the Amide I band can be decomposed into three bands of fixed position and width, of which only one increases in amplitude. These three bands are located at 1614 cm^{-1}, 1631 cm^{-1} and 1650 cm^{-1}.[197] The band at 1614 cm^{-1} arises from a fully hydrated amide, with two water molecules onto the carbonyl oxygen and a third molecule of water onto the N−H site. The band at 1631 cm^{-1} arises from a partially hydrated amide, with only two water molecules per amide. The band at 1650 cm^{-1} is tentatively assigned to a fully dehydrated amide bond.

The relative amplitudes of the three Amide I bands are plotted as a function of the temperature on Figure 4.10. Assuming that all bands have equal Raman cross sections, the band at 1631 cm^{-1} becomes the main contributor from 30 °C. The band at 1650 cm^{-1} has the lowest contribution at all temperatures, suggesting that the majority of the amides remain hydrated. At 10 °C, 45 % of amides are fully hydrated. This percentage decreases gradually until it reaches 38 %. Hence, during the phase transition of the pNIPAM chains, the level of hydration of the amides is reduced while remaining fairly hydrated at all stages. This is in agreement with the picture of amide–water bonds being gradually replaced by amide–amide bonds as described in previous reports, although the initial proportion of fully hydrated amides is lower than reported for bulk pNIPAM.[214]

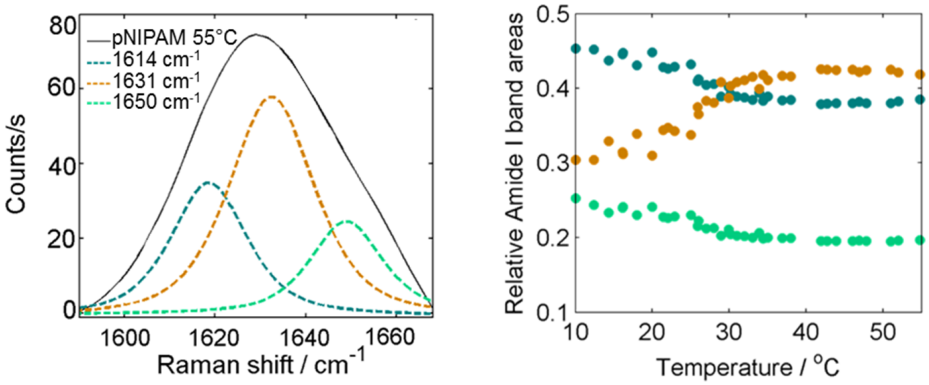

Figure 4.10: (a) Example of the peak fitting of the Amide I bands into 3 peaks of fixed positions: 1614 cm^{-1} (●), 1631 cm^{-1} (●) and 1650 cm^{-1} (●), following a method developed by Ahmed *et al.*[214] and Katsumoto *et al.*[197] (b) Change in relative amplitudes of the three Amide I bands of the TIR Raman spectrum of a grafted pNIPAM layer as a function of temperature.

A transition temperature can be determined by looking at the relative population

of fully and partially hydrated amides. Figure 4.11 shows the ratio of amplitudes of the Amide bands corresponding to the most and second most hydrated amide groups. The ratio increases from 0.7 at 10 °C up to 1.1 at 37 °C showing an increase in the relative amount of partially hydrated compared to fully hydrated amide groups. The ratio remains constant above this temperature. This could imply that the dehydration of the amide groups is finished at this point. The temperature matches the one at which the increase in the amplitude in the CH signals changes, see figure 4.7. As a consequence, the picture of a uniform collapsing of the pNIPAM chains is more likely than a vertical phase separation. In the case of a vertical phase separation, further changes in the hydration of the chains would have been expected.

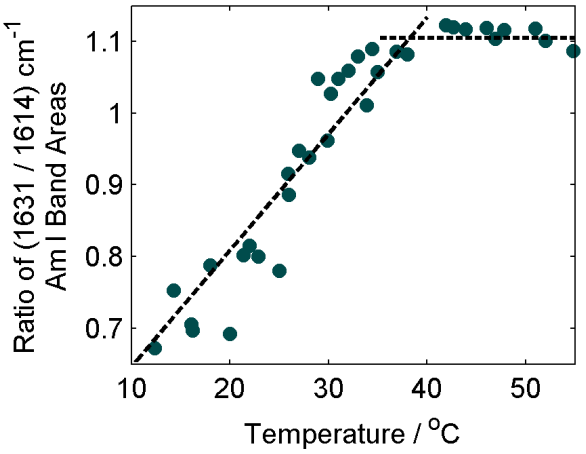

Figure 4.11: Ratio of amplitude of two Amide I bands as a function of temperature. The two Amide bands correspond to two partially hydrated amide function, with 3 bound water molecules (1614 cm^{-1}) or 2 bound water molecules (1631 cm^{-1}). The dashed lines are for visual guidance only.

Changes in Amide I and II band intensities during the phase transition

The intensities of the amide bands Amide I and Amide II change during the phase transition. The intensity of the Amide II band decreases while the intensity of the Amide I band increases. Recent density functional calculations [215] focussing on the orbitals of the amide of *N*-methylacetamide as a function of the number of water molecules per amide explains this observation. The results show that the formation of hydrogen bonds between the amides and the water molecules stabilises the resonant form [O=C−NH↔$^{-}$O−C=NH^{+}] inducing a change in the geometry of the amide bond, *i.e.* a shortening of the C−N bond and an elongation of the C=O bond. Also, the resonant form is more stable in a polar solvent. The ratio of intensity is a good indicator of the polarity of the solvent.

Figure 4.12 shows that the ratio of amplitudes of AmI/AmII increases with temperature. This highlights that the polarity inside the pNIPAM film decreases when the temperature increases and is in agreement with the replacement of amide–water hydrogen bonds with amide–amide bonds. This evolution follows the replacement of fully hydrated amides by partially hydrated amides. The polarity inside the film

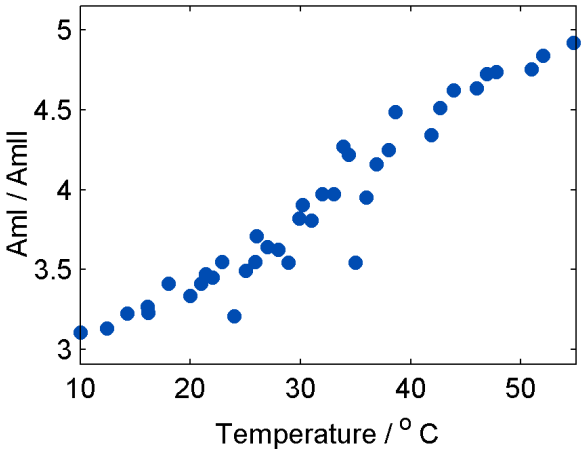

Figure 4.12: Variation of the AmI/AmII ratio as a function of temperature.

decreases gradually from 10 °C to 50 °C. The slope of increase in the AmI/AmII intensity ratio changes at around 24 °C.

Comparison with the spectral changes in the Amide I bands in *N*-methylacetamide

The impact of dehydration on the amide bonds can be modelled using a simple amide bond bearing molecule such as *N*-methylacetamide (NMA). NMA is highly soluble in water and the hydration of its amide bond can be varied easily by changing its concentration. Figure 4.13 shows the TIR Raman spectra of a range of NMA solutions in the CH and the CO regions. NMA does not adsorb onto silica and the Raman spectra arise purely from bulk NMA. As the concentration of NMA is increased

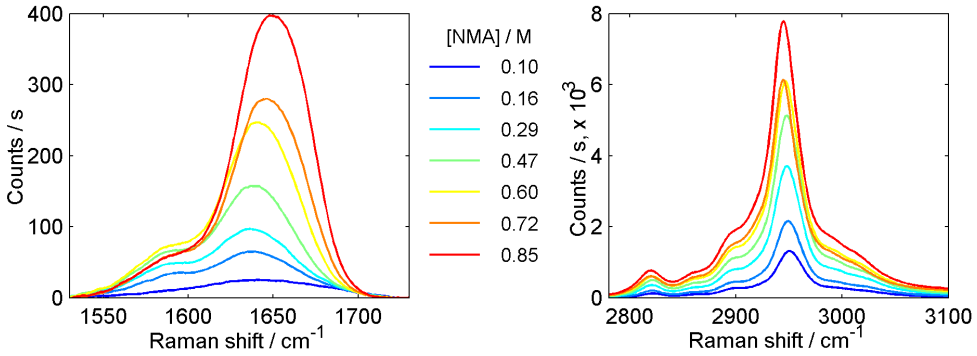

Figure 4.13: TIR Raman spectra of *N*-methylacetamide at different concentrations in the fingerprint (left) and CH (right) regions.

from 100 mM to 850 mM, the TIR Raman intensities in both regions increase. The shape of the spectrum in the amide region is changing corresponding to changes in the relative ratio of the Amide I bands and a change in peak position, very similar to what has been observed in pNIPAM. The increase in the relative amplitudes of the Am I band to Am II band with concentration is shown in figure 4.14. This behaviour matches the trend in pNIPAM films increasing temperature (see figure 4.12). This

confirms that this ratio change indicates the replacement of hydrogen bonds between C=O and water with inter- and intramolecular C=O···H−N hydrogen bonds. This matches the behaviour reported by Maeda *et al.*.[180]

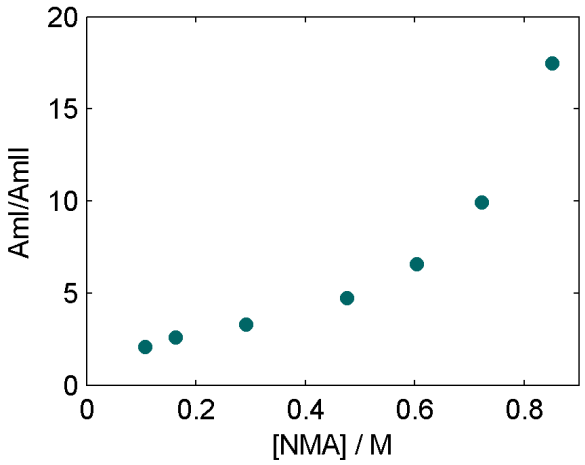

Figure 4.14: Change in relative amplitudes of the Amide I and Amide II bands of the TIR Raman spectrum of NMA solutions as a function of concentration.

Summary

The results presented in this section showed that the phase transition of surface-grafted pNIPAM is a complex process. The transition is less sharp than in pNIPAM solutions and a state with fully dehydrated amides has not been reached at 55 °C. At 10 °C, the largest fraction of amides are fully hydrated (with three bound water molecules). This fraction falls from 45 % to 38 % from 10 °C to 30 °C, while the proportion of partially hydrated amides become more preponderant. Fully dehydrated amides represent the smallest fraction at all temperatures. The amide I bands show that most of the amide dehydration is completed at 37 °C. Spectral features of the amide still continue to change at higher temperatures. In particular, the continuous increase of the Amide I/Amide II ratio across the studied temperature range indicates that the environment around the amide bonds continues to become less polar with increasing temperature. Experiments with NMA confirmed the connection between the Amide I/Amide II ratio and the hydration level of the amide bonds. In the CH region, the position of the methyl stretches are also gradually shifting towards the red in the range of temperature studied. This is in agreement with a gradual dehydration of the pNIPAM chain.

The positions of the individual Raman bands themselves and relative signal intensities prove to be a good indicator for the dehydration of the pNIPAM film. In parallel, the absolute intensities of the pNIPAM Raman signals increase with temperature signalling a collapse of the brush towards the interface during the phase transition.

For comparison, the temperature dependent integrated CH signals of the brush used as an example in this section is shown alongside the data of a shorter brush (dry thickness 13 nm) in figure 4.15. The behaviour is overall similar but the amplitude of

the change is smaller for the shorter film. This can be attributed to optical effects as the collapse of shorter films leads to smaller changes in thickness and therefore smaller changes in the electric field. The reason for such effects is the exponential decay of the evanescent wave — and consequently the Raman signal — with increasing distance from the surface. I decided to use the longer brush to study the interaction with cargo molecules since it might be able to capture a larger amount of cargo leading to higher signal intensities.

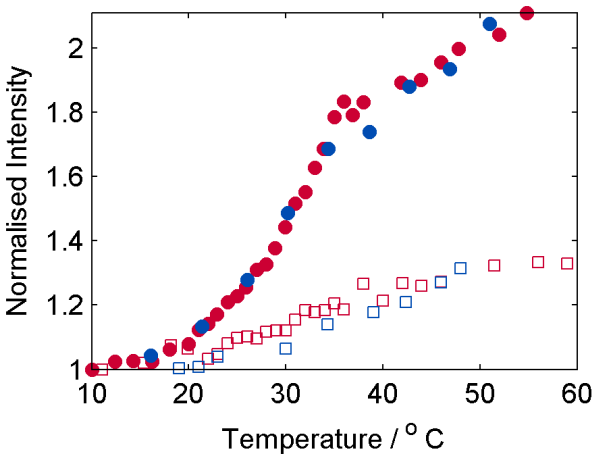

Figure 4.15: Change in intensity in the CH region of the TIR Raman spectrum of a long grafted pNIPAM layer (dry thickness 60 nm) (●) and a shorter film (dry thickness 13 nm) (□) as a function of temperature. These changes are probed during a temperature rise (● and □) and fall (● and □).

4.3.3 How to choose cargo molecules?

I wanted to explore three types of binding between pNIPAM and the cargo molecule: hydrophobicity, hydrogen bonding and specific ion interactions. In order to be able to detect small quantities of the cargo molecules inside the polymer layer, I have favoured molecules that show strong and sharp Raman signals. Further details on the selection process can be found in this section.

Hydrophobic interactions

Hydrophobic interactions are expected between the backbone of the pNIPAM chains and hydrophobic cargo molecules. At high temperatures, amides are less hydrated which is in agreement with the picture of a film becoming more hydrophobic. On the other hand, at lower temperatures, more hydrogen bonds are formed between the chains. This network of hydrogen bonds could act as a good shield from hydrophobic moieties of cargo molecules. The table shows a series of molecules with high solubility in water yet bearing a hydrophobic moiety. The partition coefficient between octane and water has been taken as a good reference of hydrophobicity.

Table 4.2: Partition coefficients between octanol and water for potential cargoes preselected for their Raman visible moieties.

Molecule	logP
cholesterol	7.00
decanoic acid	4.09
metoproclamide	2.62
hydrobenzoic acid	1.30
benzylamine	1.10
benzamide	0.64
procainamide	0.88
caffeine	−0.07
adenine	−0.09
guanine	−0.91
isoleucine	−1.70

Cross referencing the table 4.2 with the detection limits with our system, benzylamine appears to be the best compromise between an easily detectable cargo (its detection limit being as low as $0.1\,\mu mol\,m^{-2}$) with a large water solubility range and a potent hydrophobicity via its benzene ring. However, in presence of benzylamine, grafted pNIPAM layers tend to get permanently detached from the substrate. Figure 4.16 shows the decay of the pNIPAM features after the introduction of benzylamine. The incompatibility with the pNIPAM layers consequently disqualifies this compound as a potential cargo molecule. Benzamide was subsequently identified as a good alternative. Similar to benzylamine, this molecule also possesses a hydrophobic benzene ring as well as an amide group. It, however, does not damage pNIPAM layers.

Hydrogen bonding

The formation of hydrogen bonds is another potential method of binding cargo molecules to the polymer brush. Table 4.3 shows the potential of a series of candidates to bind with hydrogen bonds. The candidates were selected based on the number of possible hydrogen bonds.

Table 4.3: List of possible hydrogen bonding cargoes giving the number of hydrogen bond donor and acceptor sites.

Molecule	H Donor	H Acceptor	log P
lysine	5	4	−3.00
valine	3	2	−2.30
metoproclamide	4	2	2.62
urea	1	2	−2.11
malonamide	2	2	/

Malonamide was an interesting choice for two reasons. First, it has two binding sites allowing a high interaction potential with the hydrated form of the pNIPAM film. In

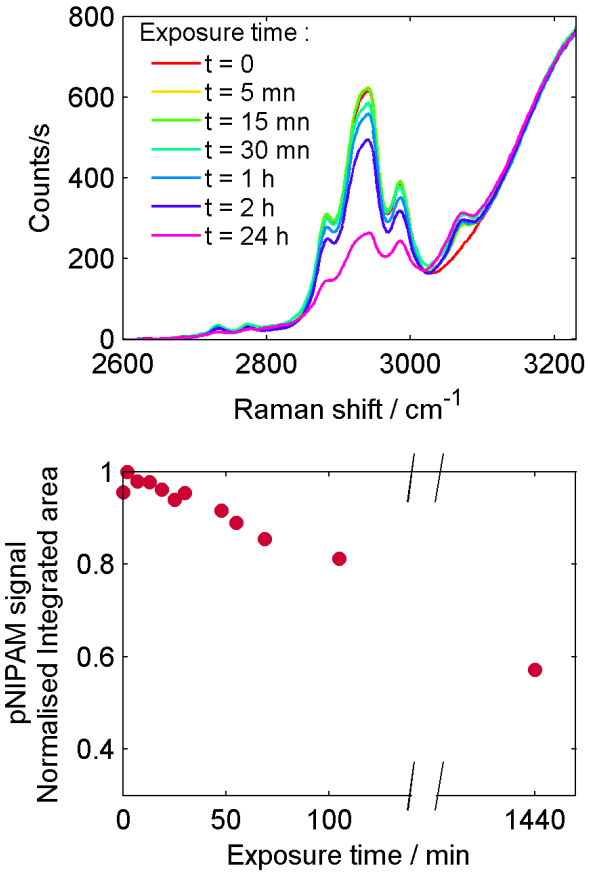

Figure 4.16: Degradation of a pNIPAM layer in contact with a solution of benzylamine (2 mM) followed by TIR Raman over time. A $t = 0$, the red spectrum shows a pNIPAM layer and a water band. After the introduction of a 2 mM solution of benzylamine, an additional band originating from the phenyl ring of benzylamine appears at 3080 cm^{-1} and the pNIPAM C−H stretches start to decrease in amplitude with time. After 1 day, benzylamine is rinsed away and half of the layer has disappeared. Not all spectra are shown in the left hand side for clarity.

addition, it can be easily deuterated, thus increasing its detection limit which means it is easily detectable at low concentrations (as low as 1 µmol m^{-2}). The deuteration of the protons in the β position of both amides can be achieved in D_2O at a pD of 9. The deuteration is followed by NMR and full exchange is achieved after one day (see Appendix). The solution was neutralised by the addition of NaOD. Deuterated malonamide is retrieved by evaporating the water slowly in a lyophilisator.

Specific ion interactions

Potassium thiocyanate was identified as another possible cargo molecule. Since it is an ionic species, potassium thiocyanate can potentially bind to the pNIPAM layer through specific interactions with the polymer's amide groups. Thiocyanate exhibits an intense Raman signal at 2060 cm^{-1} which means it is easily detectable with a low detection limit of 0.5 µmol m^{-2}. The signal position itself is of interest as well since

it depends on the molecule's oxidation state. It might thus be possible to follow the binding of potassium thiocyanate through changes in the peak position.

Conclusion

Three cargo molecules were chosen based on their potential for binding to pNIPAM through different types of interactions. Benzamide was chosen for being a good compromise between solubility in water, its safety towards the pNIPAM film and its potential to bind to a pNIPAM film via hydrophobic interactions. Deuterated malonamide was chosen because of its ability to form hydrogen bonds whilst potassium thiocyanate was identified as a candidate since it might bind through specific ion interactions. Each molecule shows strong Raman signals that are different from the ones originating from grafted pNIPAM films (see Table 4.4). Their presence in the polymer film can thus be easily deduced through TIR Raman spectroscopy. The Raman spectra of the cargo molecules are shown alongside pNIPAM in figure 4.17. The results of the experiments probing the interactions between those molecules and pNIPAM are shown in the next section.

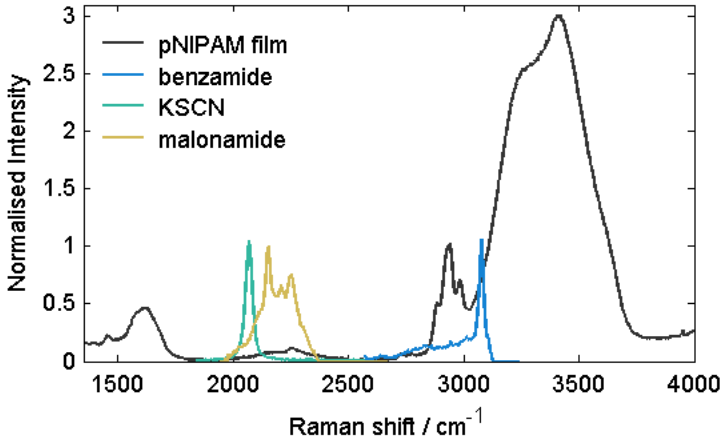

Figure 4.17: Normalised Raman spectra of a pNIPAM film and the three selected cargo molecules.

Table 4.4: Target Raman bands of the model cargo molecules and their calculated detection limit.

Cargo molecule	Raman band / cm^{-1}	Detection limit / $\mu mol\,m^{-2}$
benzamide	3080	0.1
d-malonamide	2150	1.4
KSCN	2060	0.5

4.3.4 Interaction between a poly(*N*-isopropylacrylamide) film and cargo molecules

This section presents the results of the interaction of pNIPAM films with the aforementioned potential cargo molecules. Equilibrium adsorption isotherms were collected

at temperatures below and above the phase transition of the pNIPAM brushes, and are visualised with blue and red dots, respectively. In addition to the recorded signal intensities, each figure features a dotted line indicating the intensity of the cargo molecule's Raman signal as a function of the bulk concentration. A detailed description of experimental details is given in section 2.1.3.

Interaction between a poly(*N*-isopropylacrylamide) film and benzamide

The interaction of benzamide with pNIPAM was studied over a concentration range from 10 to 90 mM. The resulting adsorption isotherms for 20 °C and 40 °C are shown in figure 4.18. The increased concentration of benzamide inside the brush compared to the bulk phase shows that the molecule adsorbs onto the polymer brush. The bound amount of benzamide is calculated from the difference between an isotherm on clean silica and the equilibrium adsorption isotherm on the pNIPAM brush. The resulting surface excess plot is shown on the right of figure 4.18.

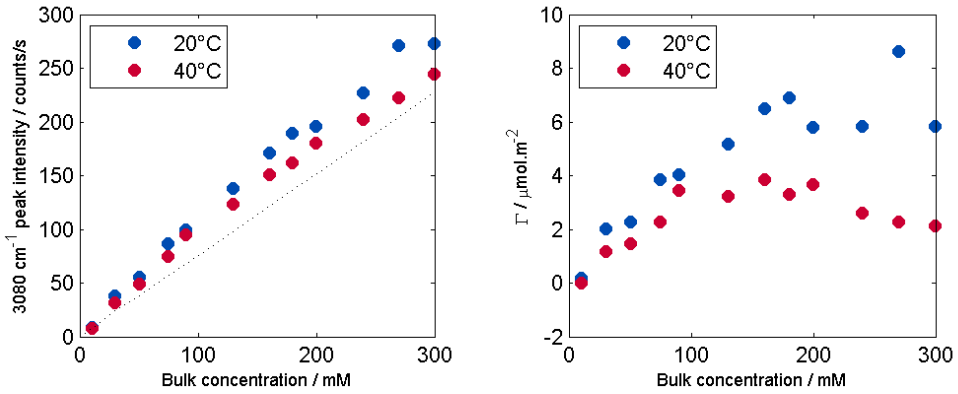

Figure 4.18: Adsorption isotherm of benzamide onto pNIPAM below (●) and above (●) the pNIPAM phase transition temperature. The dotted line shows the signal intensity expected if the bulk concentration continued up to the surface (left). The bound amount of benzamide is calculated from the difference between an isotherm on clean silica and the equilibrium adsorption isotherm on the pNIPAM brush (right).

At both temperatures, the surface excess of benzamide increases with increasing bulk concentration. The surface excess of benzamide reaches 4.0 µmol m^{-2} and 3.4 µmol m^{-2} at 20 °C and 40 °C, respectively, for a bulk concentration of 90 mM.

Interaction between a poly(*N*-isopropylacrylamide) film and d-malonamide

The adsorption of d-malonamide onto pNIPAM was studied for concentrations ranging from 5 to 300 mM at 20 °C and 40 °C. The resulting isotherms are shown in figure 4.19.

At both temperatures, the amount of d-malonamide at the interface is about the same in the presence of the pNIPAM film as on clean silica. This observation implies that d-malonamide does not adsorb onto pNIPAM whichever state of hydration it is in. The negative values indicate an excluded volume for d-malonamide from the surface due to the presence of the pNIPAM film. Therefore, the attractive potential

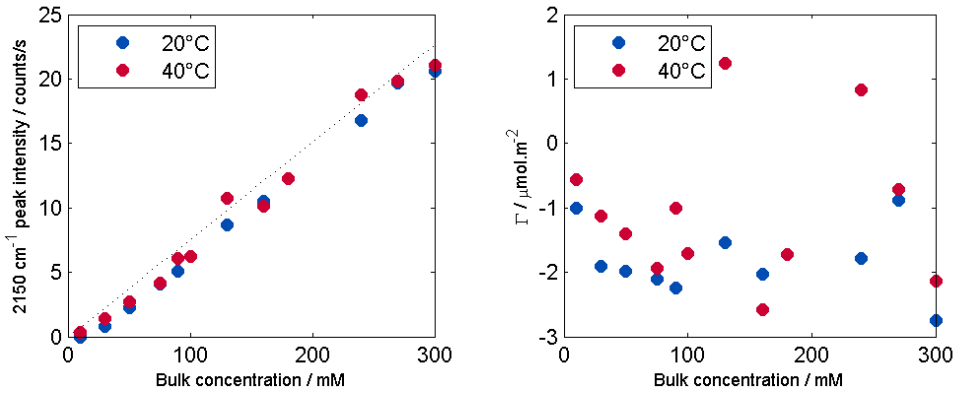

Figure 4.19: Adsorption isotherm of d-malonamide onto pNIPAM below (●) and above (●) the pNIPAM phase transition temperature. The dotted line shows the signal intensity expected if the bulk concentration continued up to the surface (left). The difference in d-malonamide concentration between the isotherms on pNIPAM and silica (right). Negative values indicate an excluded volume from the surface due to the presence of the pNIPAM film.

of forming hydrogen bonds between the amide moieties is not high enough to compete with the entropic penalty of concentrating d-malonamide close to the interface.

On a separate note, the overlap between the data at 20 °C and 40 °C shows that the impact of a change in the refractive index of the polymer layer during the phase transition is minimal.

Interaction between a poly(*N*-isopropylacrylamide) film and potassium thiocyanate

The adsorption isotherms of potassium thiocyanate are presented in figure 4.20. The isotherms were generated through spectra recorded at concentrations ranging from 10 to 214 mM at 20 °C and 40 °C. Similarly to what has been observed with

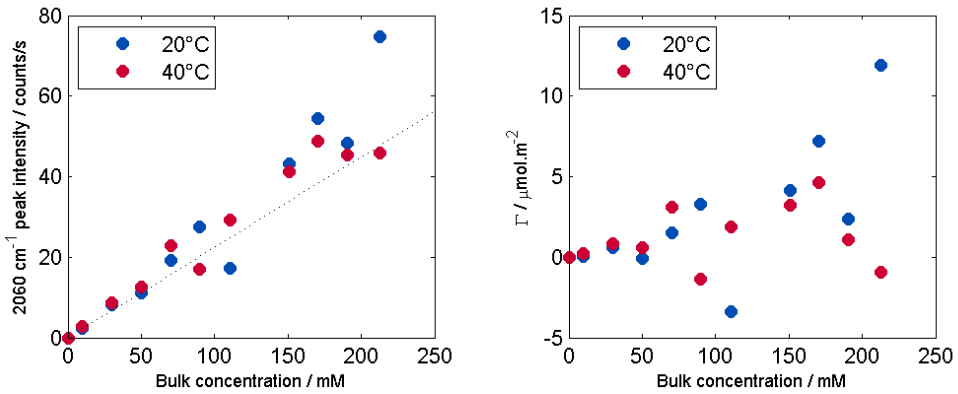

Figure 4.20: Adsorption isotherm of potassium thiocyanate onto pNIPAM below (●) and above (●) the pNIPAM transition temperature. The dotted line shows the signal intensity expected if the bulk concentration continued up to the surface.

d-malonamide, potassium thiocyanate does not bind onto pNIPAM in either state of hydration. In addition, there was no change in the peak position of the thiocyanate

stretch or in the pNIPAM spectrum at any KSCN concentration. The position of the thiocyanate stretch is sensitive to its state of oxidation.[216] Thus, if potassium thiocyanate were to bind onto the electrophilic site of the amide of pNIPAM as inferred by Sainant *et al.*, the position of the band would have changed during the adsorption. Therefore both the band position and intensity of the thiocyanate stretch imply no interaction between the anion and the amide function. This is in disagreement with a recent paper investigating the potential of vibrational spectroscopy to measure the specific ion binding effect onto amides and hence proteins. In their study, Cremer *et al.* used IR Spectroscopy to detect changes in the Amide I stretching bands in the presence of anions, inferring a binding effect.[217] A shift in the position in the Amide I is visible in the presence of several anions including potassium thiocyanate but at very high concentrations (close to $5\,\mathrm{mol\,L^{-1}}$). The previous section on the effect of dehydration on this amide stretch has shown the sensitivity of the technique towards the hydrogen bonding network of the amide. Also the independent detection of the thiocyanate anion also shows no accumulation or changes in the band position, implying no adsorption or bonding.

4.4 Conclusion

In this chapter, I have shown that TIR Raman spectroscopy is a viable method for studying pNIPAM brushes. The phase transition inside the brush can be detected through an increase in the Raman signal intensity as the chains are collapsing onto the silica surface. The position of CH stretches gives information on the hydration of the brush at different temperatures. An increasing redshift shows that the hydration of the brush decreases with increasing temperature. The Amide I and II bands prove to be highly sensitive to hydrogen bonding. The Amide I band was shown to be composed of three different bands, corresponding to different levels of hydration. With increasing temperature, the amide signal indicating full hydration decreased in intensity. At the same time, the signal associated with partially hydrated amide groups increased in intensity. The phase transition inside a dense pNIPAM film was shown to be more gradual when compared to the phase transition in bulk pNIPAM. The data implied a two-step process that can be explained through the slowing down of the transition above 37 °C. The composition of the Amide I band does not change above this temperature and the increase in the intensity of the CH signals decreases.

A range of potential cargo molecules was investigated. The molecules were chosen based on the driving force behind their possible adsorption: hydrophobicity, polarity and hydrogen bonding. The cargoes were furthermore required to not be harmful to the polymer and exhibit a low detection limit. None of the investigated molecules showed selective binding to either state of the polymer brush. Potassium thiocyanate and d-malonamide did not bind onto either state of pNIPAM. The driving adsorption force was not strong enough to overbalance the entropic penalty of trapping a molecule close to the interface and inside a polymer film. Benzamide bound onto pNIPAM below and above the phase transition temperature, and only showed small differences at high benzamide concentrations. pNIPAM is thus hydrophobic enough in both states for benzamide to favour adsorption. Hydrophobic interactions therefore seem

to be the only driving force for the adsorption of the investigated cargo molecules onto pNIPAM.

The next chapter will explore a different type of surface-grafted polymer: the polypeptide polyvaline. This polymer is expected to be thermoresponsive in water due to the presence of an isopropyl group while being less hydrophobic than pNIPAM. Such a system might show different affinity towards hydrophobic molecules depending on its phase.

Chapter 5: Polyvaline films

5.1 Introduction

The previous chapter has shown that adsorption onto pNIPAM was driven by hydrophobic interactions and therefore was not selective enough for a temperature stimulated release of a cargo. This chapter will explore the potential of a less hydrophobic layer: a grafted film of polyvaline. Polyvaline is expected to be thermoresponsive in water due to the presence of an isopropyl group while being less hydrophobic than pNIPAM. The aim of this chapter is to examine the potential of polyvaline films to take up and release a cargo molecule to and from a coated surface. In the first part of this chapter, I will summarise the relevant literature on polyvaline and polyaminoacids. Then, I will present and discuss my results on the interactions between the polymer film and the studied cargo molecules.

5.2 Review

5.2.1 Grafted polyaminoacids

Proteins are essential to biological activities controlling the structure and function of cells. They are made of long chains of amino acids called polyaminoacids. Synthetic polypeptides have received growing interest since they are good models for studying the peptide bonds and are much easier to synthesise than actual proteins. They also have great potential for therapeutic and biotechnological applications such as tissue engineering and drug delivery.[218] One important factor for the interest in polypeptides as biological applications is their potential biocompatibility and biodegradability.[219] Similarly to polymers like pNIPAM, there has been a significant interest in grafted polypeptides to combine the properties of the polymer and the supporting substrate.[220]

There are overall three main techniques for the synthesis of polypeptides brushes: The first two methods are grafting to and grafting from which are outlined in section 2.7. Grafting from is commonly achieved through ring-opening polymerisation of α-amino acid N-carboxyanhydrids (NCAs).[219] NCA vapour deposition is the third option and was first developed by Chang and Frank.[221] It is a solvent-free technique where NCA monomers are polymerised through vapour deposition. The layer thickness is tuned through temperature, pressure and reaction time.[222] Some research, however, indicates that this approach might not be suitable for the synthesis

of polyvaline brushes.[223]

One of the few studies on grafted polyvaline was published by Wang and coworkers in 2010 who prepared D- and L-valine based polymers on silicon via ATRP.[224] Cell adhesion experiments showed an increased cyctocompatibility of L-polyvaline where cells adhered, grew and spread better than on D-polyvaline. Follow-up work showed a similar behaviour for alanine- and leucine-based polymers.[225] They, however, did not directly determine the conformation of the grafted chains but repeated the synthesis in bulk and carried out CD measurements on polymer solutions. The CD measurements showed that the chirality of the D- and L-valine was preserved in the respective polymers. This work is a part of a wider effort to develop chiral polymer-based materials with possible applications as anti-fouling coatings, chiral separators in drug synthesis and chiral sensors.[226]

It is worth mentioning that the research on the development of bioinspired and biomimetic materials is not limited to polypeptides but extends to polypeptoids.[227,228] This class of polymers has the same backbone as polypeptides but side chains are attached to the nitrogen rather than the α-carbon. They thus do not form hydrogen bonds in the backbone and show properties dominated by the side chains.

5.2.2 Spectroscopy of polyvaline and other polyaminoacids

A wide range of techniques is available for the study of polypeptide films. Techniques such as ellipsometry,[229,230] AFM,[224,225,231] and XPS[232,233] determine the thickness, topography and composition of the brushes, respectively. This section, however, will focus on CD and vibrational spectroscopy since they are more relevant to the work presented in this chapter.

CD spectroscopy is used to determine the conformation of grafted polypeptides although the measurements are not always carried out directly on the brushes. Instead, the synthesis is repeated in bulk and a solution of the resulting polymer is analysed.[224,225] In a different approach, the polymers are grafted from a quartz substrate which is then placed in the beam path of the spectrometer allowing the direct acquisition of CD spectra of the grafted polypeptide.[234,235] An example of the latter technique is the work by Yang *et al.* who grafted polymers of L-lysine from substrates such as silicon and quartz.[231] CD measurements on the polymer grafted from quartz revealed characteristic features of an α-helical secondary structure which transitioned to β-sheet and random coil structures in solutions of anionic polyelectrolytes. The advantage of this approach is that it is direct.

IR spectroscopy is a popular tool for probing the composition as well as secondary structure of polypeptides. It is possible to characterise grafted polypeptides but also bulk polypeptides.[236,237] Grafted polymers can be probed in the transmission mode if they are *e.g.* grafted from silicon[230,231,233,238] or through ATR-IR if they were grafted from an ATR crystal.[221] It is also possible to use IR spectroscopy for polypeptides grafted from particles.[220,239] One example is the work of Lee and coworkers who synthesised a range of grafted polypeptides through NCA vapour deposition.[223] The polypeptides grafted from silicon were characterised using FTIR spectroscopy in

transmission mode. The researchers were able to determine the secondary structures through characteristic Amide I and II signals for film thicknesses as low as 50 Å. This highlights the ability of vibrational spectroscopy to probe the secondary structure in polypeptides with a high sensitivity.

Raman spectroscopy has so far played a minor role in the characterisation of polypeptides in general and polyvaline in particular. One of the first Raman spectra of poly(L-valine) was published by Koenig *et al.* in 1971 who presented spectra of a range of synthetic polypeptides.[240] The spectrum showed a sharp and strong peak at 1667 cm^{-1} which was assigned to the polymer's anti-parallel β-sheet secondary structure. The signal was compared to the two bands at 1687 cm^{-1} and 1625 cm^{-1} in the IR spectrum of poly(L-valine) that are indicating the same structure. They furthermore recorded two strong peaks at 1455 cm^{-1} and 1462 cm^{-1} associated with asymmetric CH_3 deformations. Two weak lines at 1346 cm^{-1} and 1316 cm^{-1} were assigned to deformations of the $C_\beta-H$ and $C_\alpha-H$ groups, respectively. The work of Chen and coworkers confirmed these findings.[241]

Conformation studies on poly(L-valine) at different degrees of polymerisation (DP) were carried out by Fasman and coworkers.[242] Raman spectra of the pure polymer at low DP showed the distinct sharp peak at 1668 cm^{-1} characteristic of a β-sheet. At DPs above 500, a shoulder appeared at 1650 cm^{-1} indicating the formation of an α-helix. The proportion of α-helix only increased slowly with increasing DP and was judged to be low even at a DP of 1000. Their findings are similar to those reported by Itoh and coworkers who studied this effect with IR spectroscopy.[236]

As seen so far, the majority of the published work focusses on L-valine and poly(L-valine) where the polymer was consistently shown to be present in an anti-parallel β-sheet structure. Akaike and coworkers prepared polyvaline from L-valine and D-valine with varying L-valine contents ranging from 50 % to 100 %.[243] IR spectroscopic measurements of the solid polymers showed the strong peak at 1630 cm^{-1} and a weaker signal at 1690 cm^{-1}. Both peaks are characteristic of an anti-parallel β-sheet structure, showing that the introduction of D-valine does not alter the secondary structure of polyvaline. This is of importance since the polyvaline brushes used in this chapter are a mix of both enantiomers.

5.3 Results

In this section, I will describe and discuss the effect of temperature on the TIR Raman spectra of grafted polyvaline films. The aim of this study is to generate a thermoresponsive polymer film with two states that show a bigger difference in hydrophobicity than pNIPAM. The thermoresponse in pNIPAM is controlled through the disruption of the hydrogen network surrounding its isopropyl groups. I chose polyvaline as an alternative to pNIPAM since it also has the isopropyl groups but exhibits a lower hydrophobicity due to the absence of the CH_2 backbone. In the following sections, I will show a TIR Raman spectrum of polyvaline giving special attention to the Amide region since it reveals some features of self-organisation within the film. The response of the film towards changes in temperature is outlined in the subsequent

section. Finally, I will present the adsorption of three cargo molecules introduced in the previous chapter (benzamide, malonamide and potassium thiocyanate) onto polyvaline films.

5.3.1 Band assignment of the polyvaline Raman spectrum

At the beginning of this section, I will first introduce the Raman spectrum of valine. Its structure is shown in figure 5.1a. A spectrum of valine obtained from powdered DL-valine is shown in figure 5.2. The Raman spectrum of valine has been previously discussed elsewhere [244,245] and most band are well assigned. The Raman spectrum of a polyvaline film grafted onto a silica hemisphere at the silica-water interface is discussed afterwards.

(a) Valine (b) Polyvaline

Figure 5.1: Structures of valine and polyvaline.

The TIR Raman spectrum of valine

The Raman spectrum of valine is shown in figure 5.2 and the peak assignment summarised in table 5.1. Within the fingerprint region shown on the left, the band at $1275\,\mathrm{cm}^{-1}$ corresponds to a deformation of the CH unit. The two signals at $1329\,\mathrm{cm}^{-1}$ and $1353\,\mathrm{cm}^{-1}$ can be assigned to the $C_\alpha-H$ and $C_\beta-H$ groups, respectively. The three bands at $1398\,\mathrm{cm}^{-1}$, $1425\,\mathrm{cm}^{-1}$ and $1455\,\mathrm{cm}^{-1}$ correspond to bending modes of the methyl groups with the latter being an antisymmetric band. The C−N stretch is detected at $1512\,\mathrm{cm}^{-1}$. The three signals associated with stretches of the carboxylic group are located at $1566\,\mathrm{cm}^{-1}$, $1595\,\mathrm{cm}^{-1}$ and $1631\,\mathrm{cm}^{-1}$.

Five bands are visible in the CH region shown on the right of figure 5.2. The band at $2884\,\mathrm{cm}^{-1}$ corresponds to a combination of the CH_3 and CH stretches. [153] The band at $2913\,\mathrm{cm}^{-1}$ corresponds to a methyl symmetric stretch, while the bands at $2952\,\mathrm{cm}^{-1}$ and $2973\,\mathrm{cm}^{-1}$ are assigned to CH stretches. Finally, the band at $2996\,\mathrm{cm}^{-1}$ is assigned to either stretches of the NH_3 group or antisymmetric CH_3 stretch. [244] Because this signal disappears during polymerisation (see below), it is more likely that it belongs to the NH_3 group.

The TIR Raman spectrum of grafted polyvaline

The background-subtracted Raman spectrum of polyvaline recorded in SY polarisation is shown in figure 5.3. Table 5.2 summarises the peak assignment. The dominant peak in the fingerprint region (left) is located at $1667\,\mathrm{cm}^{-1}$ and belongs to the Amide I band. Its peak position is characteristic for a β-sheet (see section 5.2.2). The Amide II region between $1535\,\mathrm{cm}^{-1}$ and $1620\,\mathrm{cm}^{-1}$ is not well resolved.

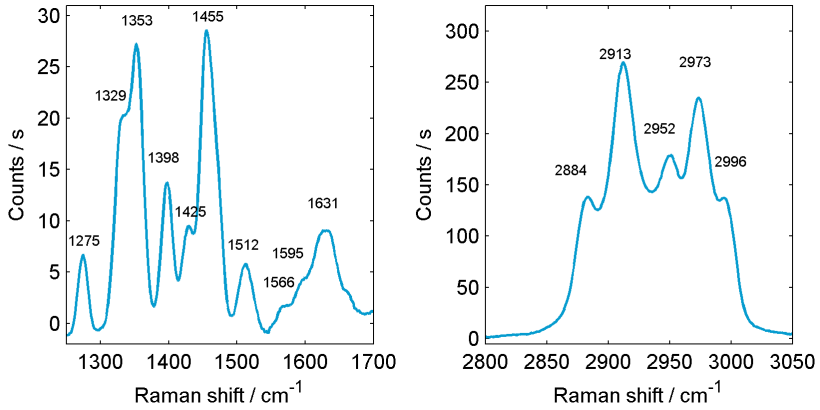

Figure 5.2: TIR Raman spectrum of valine powder in the fingerprint region (left) and CH region (right), recorded in SY polarisation.

Table 5.1: Assignment of the Raman bands of valine. Intensities are normalised to the the symmetric methyl stretch at 2913 cm^{-1}.

cm^{-1}	Intensity	Assignment
2996	0.50	$\nu(NH_3)$ or $\nu_{as}(CH_3)$ [244]
2973	0.87	$\nu(CH)$ [244]
2952	0.66	$\nu(CH)$ [244]
2913	1.00	$\nu_s(CH_3)$ [244]
2884	0.51	$\nu(CH_3) + \nu(CH)$ [153]
1631	0.03	$\nu_{as}(C{=}O)$
1595	0.02	$\nu_s(C{=}O)$
1566	0.01	$\nu_s(CO_2^-)$
1512	0.02	$\nu(N{-}C)$
1455	0.11	$\delta_{as}(CH_3)$
1425	0.04	$\delta(CH_3)$
1398	0.05	$\delta(CH_3)$
1353	0.10	$\delta(C_\beta{-}H)$
1329	0.08	$\delta(C_\alpha{-}H)$
1275	0.02	$\delta(C{-}H)$

The diffuse Raman scattering in this region is characteristic for polyvaline. [240] The symmetric and antisymmetric bending modes of the methyl groups are located at 1396 cm^{-1} and 1458 cm^{-1}, respectively. The signals at 1316 cm^{-1} and 1348 cm^{-1} are assigned to the $C_\alpha{-}H$ and $C_\beta{-}H$ groups, respectively. Finally, the signal at 1281 cm^{-1} is assigned to the Amide III band.

Four peaks are resolved in the CH region of polyvaline, shown on the right of figure 5.3. Three bands assigned to the methyl symmetric stretch are located at 2876 cm^{-1}, 2902 cm^{-1} and 2937 cm^{-1}. The band at 2968 cm^{-1} is assigned to the CH_3 antisymmetric stretch. The shoulder at 2855 cm^{-1} is assigned to a symmetric $C{-}H$ stretch.

5.3.2 Secondary structure of polyvaline in grafted films

The secondary structure of proteins is of utmost importance for their functions. Over the years, a range of tools has been developed to accurately evaluate the spatial

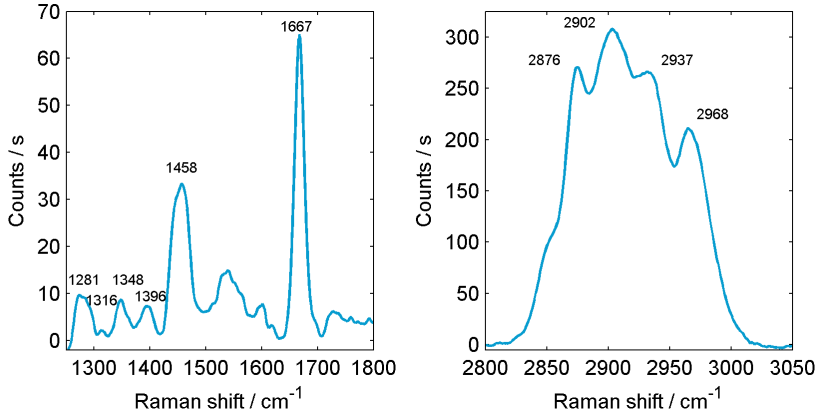

Figure 5.3: SY-polarised TIR Raman spectrum of a grafted polyvaline film in the fingerprint region (left) and CH region (right).

Table 5.2: Assignment of the Raman bands of polyvaline. Intensities are normalised to the the symmetric methyl stretch at 2902 cm^{-1}.

cm^{-1}	Intensity	Assignment
2968	0.68	$\nu_{as}(CH_3)$
2937	0.86	$\nu_s(CH_3)$
2902	1.00	$\nu_s(CH_3)$
2876	0.88	$\nu_s(CH_3)$
2855	0.32	ν_s(C–H) [153]
1667	0.21	ν(C=O) (Amide I) [240]
1535–1620		(Amide II) [240]
1458	0.10	$\delta_{as}(CH_3)$ [240]
1396	0.02	$\delta_s(CH_3)$ [240]
1348	0.03	$\delta(C_\beta–H)$ [240]
1316	0.01	$\delta(C_\alpha–H)$ [240]
1281	0.03	δ(N–H), ν(C–C_α), ν(N–C) (Amide III) [240]

arrangements of biomacromolecules. CD Spectroscopy is a standard method used in biochemistry to measure the structure of a protein or a synthesised polypeptide.

Since polyvaline is not soluble in a CD transparent liquid (deionised water and various kinds of buffer) at room temperature, it was not possible to simply fill a cuvette with a polyvaline solution and record a CD spectrum. I thus decided to graft a polyvaline film from the inside of a cuvette in order to gain access to structural information of such a film. After subtraction of the water background, the CD spectrum of polyvaline was obtained and shown in figure 5.4.

The structure of polyvaline could be a combination of alpha helices, beta sheet segments and random coils. Since each structure has a specific CD signal (see figure 2.22 in chapter 2), the CD spectrum of polyvaline is a convolution of these signals. The maximum just above 200 nm is consistent with a beta sheet. The absence of a negative signal at 215 nm, however, implies that the secondary structure is not a pure beta sheet but a mixture of different structures. In the next step, the CD data was further analysed using the DichroWeb online service provided by Wallace of Birkbeck College, University of London. [246] The analysis, which compares the measured spectrum

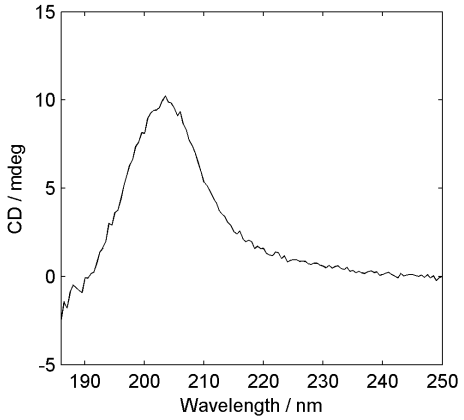

Figure 5.4: CD spectrum of a grafted-from polyvaline film.

to a library of CD spectra of proteins of known structures, is capable of extracting a percentage of each basic structure in the sample. The analysis revealed that the synthesised film consists mainly of an equal mixture of beta sheet and random coil (48 %) but also a small amount of alpha helix (4 %). The recorded CD spectrum is rather noisy since it originates from a thin film. I believe the 4 % alpha helix might thus be a consequence of noise in the CD spectrum. The website does not return values indicating the goodness of the fit such as r^2, making it difficult to assess the confidence in the assignment.

TIR Raman spectroscopy and Circular Dichroism Spectroscopy are consistent with self assembly of polyvaline chains inside the grafted film. The self assembly is consistent with a mixture of beta sheet and random coil structure. This formation of intermolecular amide bonds is a potential deactivator of the polyvaline binding sites. With the neighbouring amide being a chelatant for the amide, its potential for forming hydrogen bonds with cargo molecules may be limited.

On the other hand, this additional intermolecular interaction could potentially act as a trap for cargo molecules by limiting their diffusion out of the film. To do so, it is necessary to activate and deactivate the formation of the beta sheet strands. Urea was identified as a potential candidate since it is a small molecule with two amide functions and might thus be able to disrupt a hydrogen bond by inserting itself between the two connected functions and separating for example the two strands of a helix or breaking a beta sheet. To test this hypothesis, a polyvaline film was left in contact with a 50 mM solution of urea in deionised water for two hours. A Raman spectrum was recorded subsequently and showed no changes whatsoever. I concluded that urea was not able to disrupt the structure of the grafted polyvaline film.

This result was in disagreement with a recently published paper [247] by Cremer *et al.* aimed at detecting the direct binding of urea onto amide bonds. They used pNIPAM as a model system of biomacromolecules and gel permeation chromatography and Fourier Transform Infrared Spectroscopy. They related an increase in the Stokes radii of the pNIPAM chains in presence of urea to a swelling due to the crosslinking of pNIPAM chains by urea. Also, they used FTIR and isotope labelling

to detect the hydrogen bonding between urea and the amide of pNIPAM. Using C^{13}-labeled urea, they observed a shift in the amide bond of pNIPAM in presence of a 6 M urea solution. I exposed a polyvaline film to a 50 mM solution of urea to investigate whether it is able to trigger a disruption in the hydrogen bond network of the polymer, and a change in the 1667 cm^{-1} and 1535 cm^{-1} band. The Raman spectrum of the film, however, did not show any changes.

Using the secondary structure of the polyvaline grafted film as a way to selectively encapsulate or deliver a cargo molecule was consequently not an option. Therefore, I decided to continue with a similar strategy as used with pNIPAM i.e. triggering a change in the hydrogen bond network through a temperature rise.

5.3.3 Influence of temperature on polyvaline films

The influence of temperature on the spectrum of polyvaline films was studied by recording Raman spectra at temperatures ranging from 10 °C to 70 °C. In between measurements, the sample cell was warmed up to the next temperature point and given 15 minutes upon reaching the set point to equilibrate before the measurement. The background-subtracted Raman spectra of a polyvaline film at different temperatures are shown in figure 5.5.

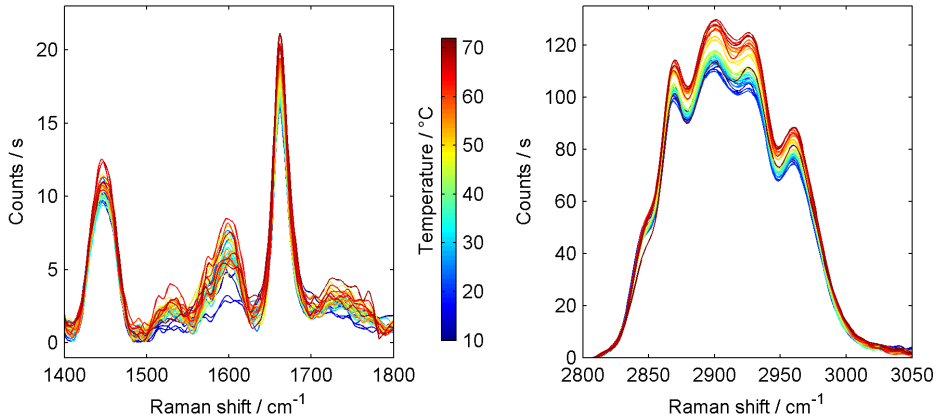

Figure 5.5: SY-polarised TIR Raman spectra of a grafted polyvaline layer in the CO (left) and CH (right) regions, collected at different temperatures ranging from 10 °C to 70 °C.

The increase of the signals in the CH region with temperature is shown in figure 5.6 and indicates a contraction of the polymer film towards the interface. This entropy-driven phase transition is milder in polyvaline than in pNIPAM and shows no clear transition temperature between 10 °C and 70 °C. The transition appears to be shifted to higher temperatures which is consistent with polyvaline being less hydrophobic than pNIPAM. The entropic penalty of hydrating the monomer is lower in polyvaline leading to the upwards shift in transition temperature.

Figure 5.7 shows that the shape of the amide band at 1667 cm^{-1} associated with a β-sheet structure is not very sensitive to a change of temperature. This implies that there is no significant change to the polymer's secondary structure over this temperature range.

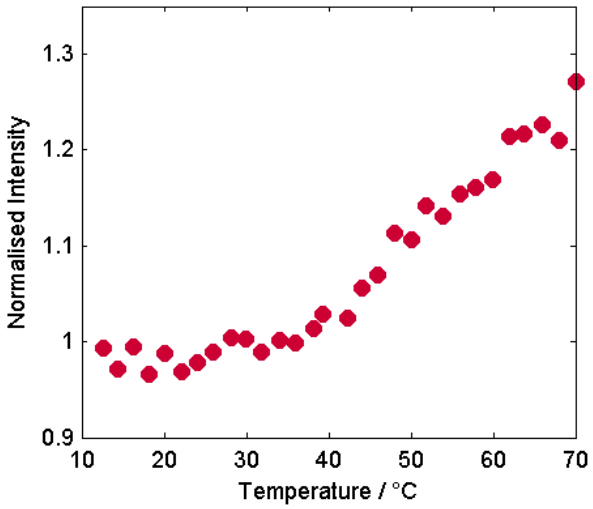

Figure 5.6: Change in intensity of the CH region in the TIR Raman spectrum of a grafted polyvaline layer as a function of temperature.

To check this hypothesis, I recorded a Raman image of the film (see figure 5.8) by choosing the filter angles so that I could overlap the distribution of the 1667 cm^{-1} band (in green) with the CH stretches of polyvaline across the surface. Table 5.3 shows the centres and FWHM of the transmission bands for the chosen filter angles. The two distributions are overlapping over the sampled area and show a rather homogeneous distribution of the beta sheet across the polyvaline film.

Table 5.3: Centres and FWHM of the transmission bands of the tunable filter for the angles used to reconstruct the images shown in figure 5.8.

Filter angle	centre / cm^{-1}	FWHM / cm^{-1}
0°	2938	507
10°	2850	509
15°	2750	511
35°	2048	530
40°	1813	541

The results showed that the synthesised films are homogeneous and exhibit a thermoresponsive behaviour. Based on the findings of the temperature study, I decided to study cargo adsorption between 20 °C and 50 °C. The high temperature was chosen as a compromise between having a temperature as high as possible to get the biggest difference between the two states of the polymer and the long-term stability of the layer to avoid degradation.

5.3.4 Interaction between polyvaline films and cargo molecules

This section summarises the results of the interactions between polyvaline films and three different cargo molecules: benzamide, deuterated malonamide and potassium thiocyanate. The choice of cargo molecules is explained in detail in section 4.3.3. In short, the molecules were chosen based on their potential for binding to

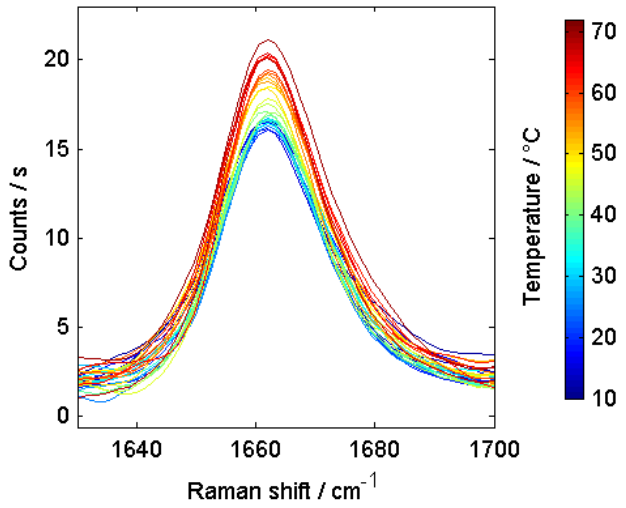

Figure 5.7: TIR Raman spectra of the Amide I band at 1667 cm^{-1} as a function of the temperature.

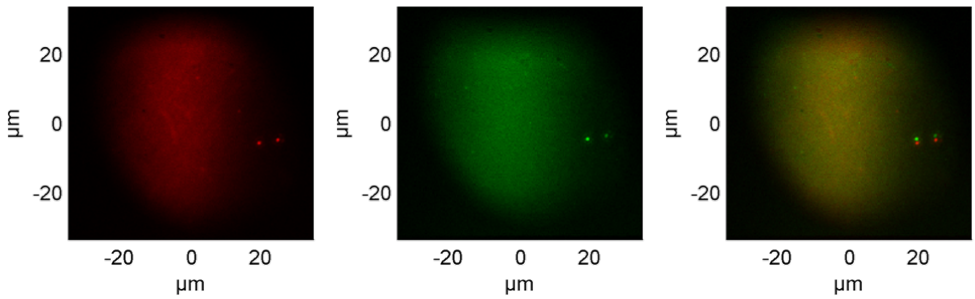

Figure 5.8: TIR Raman image of a polyvaline film. The distribution of the CH stretches onto the surface (left), the 1667 cm^{-1} band assigned to a beta sheet (center) and the overlap of both (right).

polyvaline through different types of interactions. For each cargo molecule, an equilibrium adsorption isotherm was collected at 20 °C and 50 °C. Throughout this section, data recorded at low and high temperature is visualised with blue and red dots, respectively. To aid the interpretation of the results, the Raman signal intensity of the cargo molecules is plotted as a dotted line as a function of the bulk concentration alongside the isotherms.

Interaction between a polyvaline film and benzamide

The adsorption isotherms for benzamide on polyvaline are shown in figure 5.9. The isotherms were generated from spectra recorded at concentrations ranging from 10 mM to 90 mM at 20 °C and 50 °C.

The data overall shows a small accumulation of benzamide inside the polyvaline film at both temperatures at high bulk concentrations. As shown on the right of figure 5.9, the adsorbed amount increases with increasing bulk concentration until approximately 2.3 µmol m^{-2} and 1.6 µmol m^{-2} at a bulk concentration of 90 mM at 20 °C and 50 °C, respectively. Since similar small quantities of benzamide are adsorbed

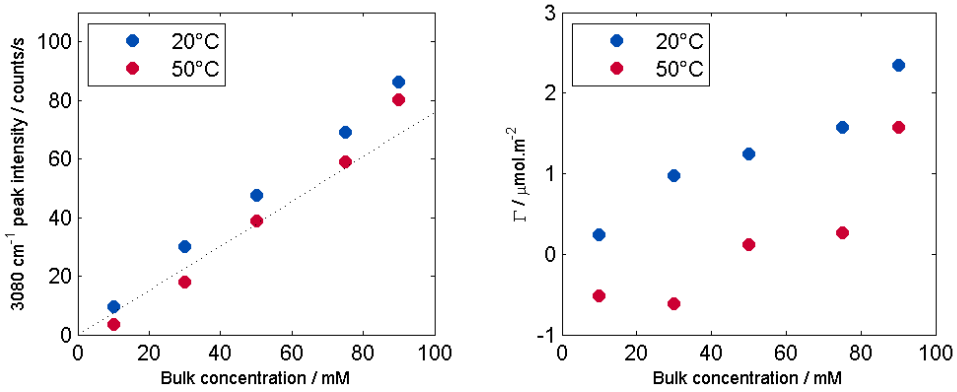

Figure 5.9: Adsorption isotherm of benzamide onto polyvaline below (●) and above (●) the polyvaline phase transition temperature. The dotted line shows the signal intensity expected if the bulk concentration continued up to the surface (left). The bound amount of benzamide is calculated from the difference between an isotherm on clean silica and the equilibrium adsorption isotherm on the polyvaline brush (right).

at both temperatures, it will not be possible to trigger the uptake of release of this molecule through temperature changes. The adsorbed amounts are similar to the ones observed for pNIPAM films as shown in section 4.3.4 (4.0 µmol m^{-2} at 20 °C and 3.4 µmol m^{-2} at 40 °C). The observed difference is a consequence of polyvaline being less hydrophobic than pNIPAM. This behaviour shows that the adsorption onto polyvaline is still driven by hydrophobic forces.

Interaction between a polyvaline film and d-malonamide

d-malonamide was used in concentrations between 10 mM and 300 mM to study its adsorption to polyvaline at 20 °C and 50 °C. The resulting isotherms are shown in figure 5.10. Throughout the range of concentrations investigated, d-malonamide shows a slightly increased presence in the polymer compared to the bulk concentration.

Approximately 2.0 ± 0.6 µmol m^{-2} and 2.0 ± 0.8 µmol m^{-2} adsorbed at 20 °C and 50 °C, respectively. There is no significant impact of the bulk concentration on the adsorbed amount. Although the isotherms show that d-malonamide can bind to polyvaline in small quantities, the results further indicate that it is not possible to release the cargo by either cooling or heating the polymer. In addition, the adsorption of similar amounts at high and low concentration implies that the attractive potential of forming hydrogen bonds between the amide moieties does not change significantly over the studied temperature range.

Interaction between a polyvaline film and potassium thiocyanate

The adsorption of potassium thiocyanate onto polyvaline was studied for concentrations ranging from 10 mM to 270 mM at 20 °C and 50 °C. The resulting isotherms are presented in figure 5.11 alongside the expected Raman intensity of KSCN as a function of bulk concentration. The isotherms were generated from spectra recorded at concentrations ranging from 2 to 280 mM at 20 °C and 2 to 170 mM at 50 °C. Above these concentrations, the grafted polyvaline film is degrading. This could be

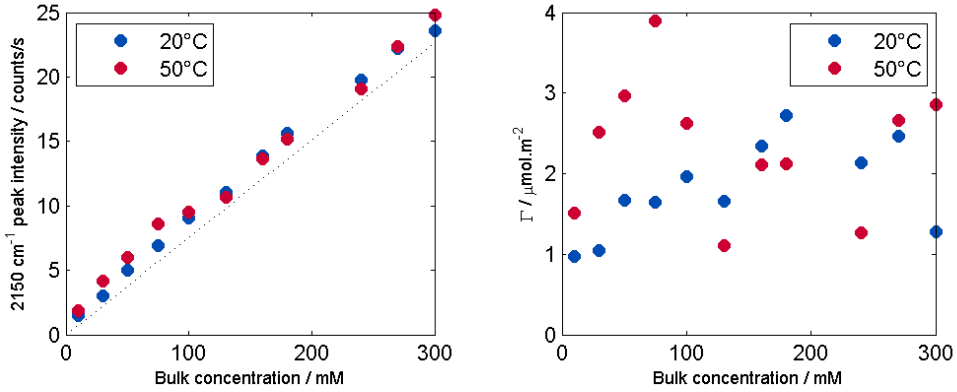

Figure 5.10: Adsorption isotherm of d-malonamide onto polyvaline below (●) and above (●) the polyvaline phase transition temperature. The dotted line shows the signal intensity expected if the bulk concentration continued up to the surface (left). The bound amount of d-malonamide is calculated from the difference between an isotherm on clean silica and the equilibrium adsorption isotherm on the polyvaline brush (right).

due to the reduction of the hydroxysilane bonds by the SCN^- anion, favoured at higher temperatures.

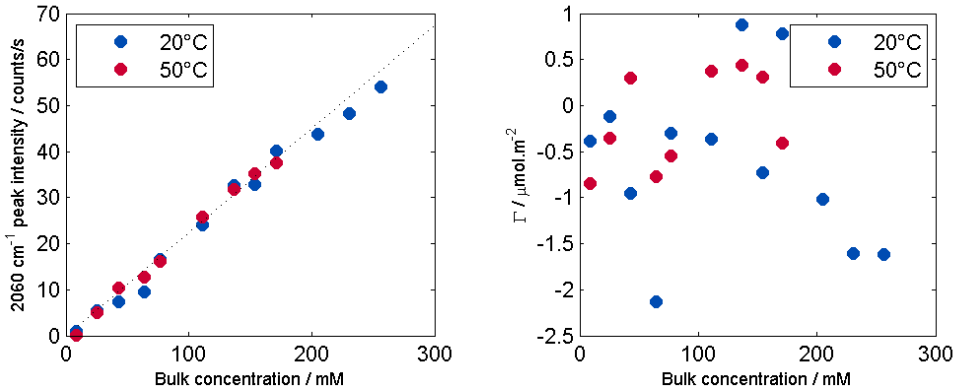

Figure 5.11: Adsorption isotherm of KSCN onto polyvaline below (●) and above (●) the polyvaline phase transition temperature. The dotted line shows the signal intensity expected if the bulk concentration continued up to the surface (left). The bound amount of KSCN is calculated from the difference between an isotherm on clean silica and the equilibrium adsorption isotherm on the polyvaline brush (right).

Over the investigated range, the concentration of potassium thiocyanate inside the polyvaline brush is equal to the bulk phase at both temperatures. The cargo does thus not adsorb onto polyvaline. It is consequently not possible to capture potassium thiocyanate using a polyvaline film and to release it subsequently by changing the temperature.

5.4 Conclusion

In this chapter, I presented polyvaline films grafted from a silica surface and their behaviour during temperature changes and in the presence of cargo molecules.

Polyvaline was synthesised to provide a less hydrophobic alternative to pNIPAM and to give more importance to the network of hydrogen bonds.

TIR Raman spectroscopy was again used to study the phase transition within the polymer brush. Similar to pNIPAM, an increase in the Raman signal intensity with temperature showed a contraction of the chains onto the silica surface. This change was more gradual and of a smaller magnitude than the one observed for pNIPAM.

The interaction with three potential cargo molecules with polyvaline was studied. Benzamide, d-malonamide and potassium thiocyanate were previously investigated as potential cargo molecules for pNIPAM brushes but did not show selective binding to either state of the polymer. Benzamide and d-malonamide showed some binding to polyvaline but at similar low levels at high and low temperature. The molecules can therefore not be released through temperature changes. Potassium thiocyanate did not adsorb to the polyvaline films. Overall, the hydrogen bonds within the polyvaline brush could not be replaced with hydrogen bonds between polyvaline and the cargo molecules. Figure 5.12 shows that no changes are observed in the Amide region of polyvaline in the presence of all cargoes. This demonstrates the absence of association between the amides and the cargoes. The next step in the design of a carrier polymer

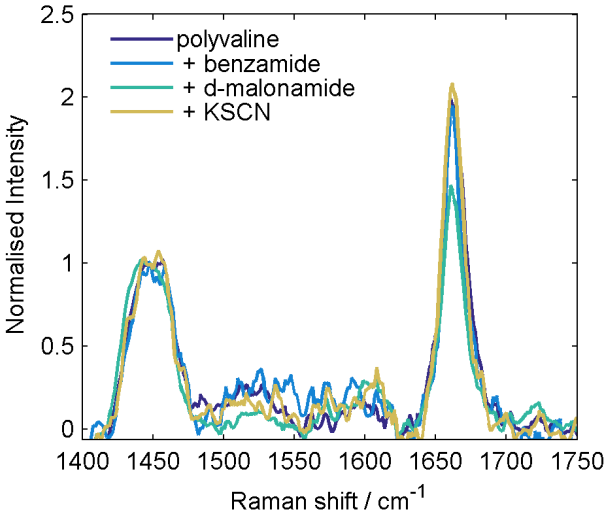

Figure 5.12: TIR Raman spectra of a polyvaline film in the fingerprint region at 20 °C in the presence of the three cargo molecules at a bulk concentration of 100 mM. Spectra were normalised to the CH_3 bending.

is the development of a block-copolymer. A polymer consisting of a charged block at the interface and a thermoresponsive block at the other end could be able to capture cargo molecules and release them following a temperature change.

Chapter 6: pDMAEMA-*b*-pNIPAM films

6.1 Introduction

This chapter will present the work on the grafted diblock copolymer poly((2-dimethylamino) ethyl methacrylate)-*b*-poly(*N*-isopropylacrylamide) (pDMAEMA-*b*-pNIPAM). The previous two chapters showed that three cargo molecules — benzamide, d-malonamide and potassium thiocyanate — did not show selective binding to grafted pNIPAM or polyvaline films. The idea behind using this copolymer is to achieve adsorption through electrostatic interactions via pDMAEMA, mediated by pNIPAM. This chapter will first give a review on some of the work on grafted copolymers and introduce pDMAEMA. The results part presents the TIR Raman spectrum of the diblock copolymer film and the changes during the temperature-induced phase transition. The last part shows the interactions between the copolymer film and the three cargo molecules in water.

6.2 Review

Extensive research is carried out developing functional copolymers responding to a range of external stimuli including temperature, pH, ionic strength and light.[248] The combination of the functionalities of different polymers in one molecule through copolymerisation leads to multi-stimuli responsive systems. These polymers have the potential to deliver the complex responses required in a wide range of applications.[249]

A wide variety of systems combines the thermoresponsive polymer pNIPAM with a range of polymers. pH responsive polymers such as polyacrylic acid[250,251] and chitosan[252] are often combined with pNIPAM to get dual response – temperature and pH. Other research associates pNIPAM with biocompatible polymers including poly(ethylene glycol),[253] dextran[254] and DL-lactide[255] to design systems fit for clinical applications such as drug delivery. Comonomers can also be added to pNIPAM to shift its phase transition temperature.[256]

Since the focus of this thesis is on vibrational spectroscopy, it is worth discussing the work of Plamper *et al.* who conducted an IR-spectroscopic study on the impact of copolymerisation on the phase transition of pNIPAM and poly(*N*,*N*-diethyl acrylamide) (pDEAA).[257] Both homopolymers show phase transitions at around 30 °C albeit sharp in pNIPAM and broad in pDEAA. Homopolymers of pNIPAM

and pDEAA, mixtures of both, block copolymers and statistical polymers of similar molecular weights were synthesised and dissolved in D_2O. Cloud point turbidity measurements showed a lower LCST for the mixture of homopolymers at 23.9 °C compared to 28.8 °C and 26.3 °C for pure pNIPAM and pDEAA, respectively. The statistical copolymer showed the lowest LCST (16 °C) whereas the diblock copolymer exhibited a LCST (28.6 °C) close to the one of pNIPAM. IR spectroscopy showed a higher contribution of the 1640 cm^{-1} band in the Amide I region of the statistical copolymer and the mixture of homopolymers than in the homopolymers on their own. This is thought to be a consequence of a less hydrophilic environment for the carbonyl functions which can be due to additional hydrogen bonding between the polymer chains. The diblock copolymer, however, behaves as an ideal copolymer where the Amide I band is an average of the contributions of both homopolymers. A closer look at changes in the IR spectrum during the phase transition shows a decrease in the 1600 cm^{-1} band intensity for all polymers, indicating a reduction in hydrogen bonding between the polymers and water. The slope of the decrease changes close to the phase transition. At this point, the solvation is so far reduced that the polymers aggregate. The signal at 1620 cm^{-1}, assigned to amide carbonyls in a mixed hydrophilic/hydrophobic surrounding, increases in all cases. A step-wise increase is seen in the 1640 cm^{-1} band at the phase transition, indicating an increase in inter-polymer hydrogen bonding. It follows from their findings that the properties of block copolymers can resemble the averaged properties of the homopolymers.

6.2.1 Poly((2-dimethylamino)ethyl methacrylate) (pDMAEMA)

I chose pDMAEMA as the inner block since it is charged in the pH range that is workable without hydrolysing the silane layer on which the polymer layer is grown.

Previous work on grafted pDMAEMA includes the study of Moglianetti and coworkers on the conformation of pDMAEMA films in aqueous solutions of various pH.[258] They used neutron reflectometry to measure the density profile of layers of pDMAEMA. At all pH, the volume fraction profile could be modelled by a Gaussian distribution, with a dense core close ot the interface and a loose tail. A possible explanation for such a profile is the presence of short chains close to the interface which increases the density in this area. At pH 7 and 9, the segment distribution of the brush is in agreement with the quasi neutral regime for high density grafted weak polyelectrolytes described by Zhulina and Borisov.[259] In this regime, the segments are weakly charged and stretch out from the surface in a similar fashion as neutral brushes. In a previous study,[260] pDMAEMA was estimated to enter the quasi neutral regime at a pH of 7, which is close to the pK_a of the monomer in aqueous solutions ($pK_a = 7 - 7.5$ [261]). The brush is even more stretched at pH 3 as the excluded volume effect between the protonated monomers is stronger than at higher pH. Water remains a good solvent over the whole pH range studied and no collapse has been observed.

In addition to the pH-responsive behaviour, pDMAEMA can also be thermoresponsive. The transition temperature of aqueous pDMAEMA solutions was shown to

be highly pH-dependent.[262] At pH 7 the transition temperature is at about 80 °C and decreases with increasing pH. At same time, the molecular weight of the polymer starts to influence the transition as well. For example at pH 10, the temperature can vary between 25 °C and 45 °C depending on the molecular weight. A similar behaviour was observed for pDMAEMA grafted from silicon by Thomas *et al.*[263] who carried out AFM measurements on the film at different pH. The film thickness increased when decreasing the pH to 2. At the same time, the transition temperature shifted from 60 °C at pH 10 to 75 °C at pH 4. This behaviour was interpreted as a consequence of the protonation of the amine groups at low pH, leading to increased hydration, and repulsive electrostatic and steric interactions between the polymer chains. As a consequence, the phase transition is delayed in acidic environments. A similar behaviour was reported by Jia and coworkers who grafted pDMAEMA from gold.[264]

Although a phase transition has been reported for free and grafted pDMAEMA, my experiments with the pDMAEMA-*b*-pNIPAM diblock copolymer will be at conditions where no such transition is expected. The pH will be slightly acidic due to CO_2 dissolved in Milli-Q water. The temperature will not exceed 50 °C.

Another factor influencing the transition temperature is the presence of a comonomer. Yuk and coworkers have, for example, used ethyl acrylamide (EMA) as a comonomer of DMAEMA. pEMA has a LCST above 80 °C in neutral pH but the copolymerisation with DMAEMA results in a copolymer with a transition temperature of just 4 °C.[265] The researchers investigated the potential of such a system to release insulin on demand. They embedded insulin in a matrix of pDMAEMA-co-pEMA and transferred it to a glucose-containing solution. Aliquots were removed at various times and the glucose concentration measured with liquid chromatography. The presence of an excess of glucose was shown to protonate the amino groups of pDMAEMA. The polymer swelled as a consequence, releasing insulin. The rate of the insulin release was governed by the glucose concentration. Several load and release cycles were shown although responsiveness of the copolymer decreased after several cycles.

6.2.2 Surface-grafted copolymers

Analogous to homopolymers, block copolymers are of interest for the development of smart surfaces and can be grafted from and to substrates. Surface-grafting is not limited to diblock copolymers but can be extended to *e.g.* triblock copolymer systems.[266,267] This section will review some of the work published on surface-grafted copolymers containing pNIPAM or pDMAEMA. This includes statistical and diblock copolymers.

The work of Cunliffe and coworkers on bacteria adhesion to polymer-coated surfaces shows how copolymerisation can be used to tune the properties of a responsive polymer.[268] The researchers grafted pNIPAM and statistical copolymers of *N*-isopropylacrylamide with acrylamide as well as *N*-*tert*-butylacrylamide from glass surfaces. The introduction of the hydrophobic *N*-*tert*-butylacrylamide lowered the

phase transition temperature from 32 °C to 20 °C while the addition of the hydrophilic acrylamide increased the LCST to 42 °C. To measure the adhesion of bacteria onto the films, the coated surfaces were left in contact with solutions of dye-labelled bacteria for 24 h at 5 °C and 37 °C. The amount of cells adsorbed onto the surface was determined through fluorescence microscopy. The substrates showed a higher amount of bacteria when the adsorption happened above the polymer's phase transition temperature. Gram positive and Gram negative bacteria cells both attached more strongly onto hydrophobic interfaces. These two observations suggested the attachment is driven by the hydrophobicity of the substrate rather than specific interactions between the substrate and the bacteria.

A similar study on cell adhesion on films of pNIPAM-based copolymers was carried out by Ebara *et al.* in 2003.[251] pNIPAM and statistical copolymers of NIPAM with acrylic acid (AA) as well as with 2-carboxyisopropylacrylamide (CIPAAm) were grafted to polystyrene cell culture dishes. Using CIPAAm instead of the popular AA avoids the rise in the phase transition temperature and the dampening of the transition. Cell spreading measurements were carried out at 37 °C (above the LCST) and the progress monitored through phase contrast microscopy. pNIPAM and pNIPAM-*co*-pCIPAAm showed similar cell spreading while none was observed on pNIPAM-*co*-pAA. The cell spreading was hindered on pNIPAM-*co*-pAA by excessive surface hydration due to the introduction of the acrylic acid group. Cell lifting experiment at 20 °C showed a faster detachment from pNIPAM-*co*-pCIPAAm compared to pure pNIPAM. This behaviour is a consequence of the hydrophilic carboxyl group microenvironment of CIPAAm leading to an accelerated grafted surface hydration. This dependence of cell behaviour on the hydrophobicity of the grafted film matches the observations by Cunliffe and coworkers.

The temperature-induced collapse of pNIPAM chains formed the basis of bactericidal and bacteria repellent copolymers developed by Wang and coworkers.[269] The hierarchical structure consisted of a poly(sulfobetaine methacrylate) (pSBMA) block grafted from silicon and a second block containing a statistical copolymer formed by NIPAM and 2-carboxyethyl acrylate. The antibiotic molecule vancomycin (Van) was chemically bound to the second block. The block copolymer thus consists of an antifouling inner block and a thermoresponsive antibacterial outer block. Below its LCST (36.5 °C), the statistical copolymer is extended, exposing Van. This leads to antibacterial behaviour, killing bacteria that adsorb to the brush. Raising the temperature above the LCST leads to a collapse of the pNIPAM-based block burying the antibiotic and exposing the pSBMA block. This block can thus now repel bacteria from the surface. The structure therefore overcomes the limitation of traditional contact-killing antibacterial surfaces where adhesion of dead bacteria compromises the antibacterial activity. Blood cells are also repelled which is of interest for biomedical applications such as implants. The results show that the collapse of the outer layer in a grafted block copolymer can expose the bottom layer to the surface which then governs the interactions with the environment.

The effect of block length in grafted block copolymers on solvent response was investigated by Xu and coworkers.[270] They first grafted poly(*n*-butyl methacrylate)

(pBMA) of constant length from silicon and then added a second block of pDMAEMA with a thickness gradient. The solvent response was studied by immersing the substrates in water or hexane for 30 minutes before drying them and measuring the static water contact angle. After water treatment, the contact angle reduces with increasing pDMAEMA length, quickly reaching the contact angle of the homopolymer. The same behaviour was observed for three different lengths of pBMA. Following hexane treatment, the contact angle decreases only at higher pDMAEMA lengths. For the longest pBMA block, the contact angle did not reach the values of a pDMAEMA homopolymer over the range of pDMAEMA lengths studied. In the case of water treatment, the behaviour is explained by a collapse of the pBMA segment and the domination of the surface properties by the extended pDMAEMA block. The situation is reversed following the hexane treatment. For short pDMAEMA segments, the collapsed pDMAEMA block can be covered by the pBMA block. This becomes more difficult with increasing pDMAEMA length until a region is reached where the surface properties are always controlled by the pDMAEMA block. This research highlights the possibility of using solvent quality as a stimulus for giving the bulk phase increased access to the inner block of a grafted diblock copolymer. This could be of potential use for controlling the capture and release of cargo molecules in a diblock film.

In a more applied study, Nagase *et al.* have used diblock-coated chromatography columns for the separation of biomolecules.[271] Statistical and diblock copolymers consisting of 3-acrylamidopropyl trimethylammonium chloride (APTAC) and NIPAM were grafted from silica beads. In the diblock copolymer, pAPTAC formed the inner block whereas the outer block consisted of pNIPAM. Stainless steel columns were filled with the coated beads forming the stationary phase and the retention time of several biomolecules was measured as a function of temperature. Acidic compounds such as adenosine nucleotides were retained by all copolymers. Diblock copolymers, however, showed a stronger retention than the statistical copolymer. No retention was observed for the case of a column with pNIPAM-modified silica beads. Hydrophobic molecules such as steroids showed a weaker retention in both copolymer-based columns compared to pure NIPAM-based columns. This was explained through a lowered hydrophobicity inside the copolymers due to APTAC. In pNIPAM-based columns, the retention of steroids increases with temperature due to the increased hydrophobicity of the polymer. In contrast, the copolymers show a lower retention at higher temperature. Experiments with mixtures of milk proteins and the pNIPAM-*b*-pAPTAC column showed the potential of this stationary phase. At 40 °C, acidic proteins like α-lactalbumin were retained while others, including lactoferrin, eluded. Upon cooling of the column to 10 °C, all proteins that previously adsorbed to the polymer eluted. Thermoresponsive diblock copolymers are thus an interesting choice for the separation of organic mixtures utilising the thermoresponsive change in hydrophobicity of pNIPAM.

6.3 Results

In this section, I will present the results on the work on grafted poly((2-dimethylamino) ethyl methacrylate)-*b*-poly(*N*-isopropylacrylamide) (pDMAEMA-*b*-pNIPAM) films. The first part will focus on the Raman spectrum of the polymer and the impact of temperature. The second part shows the adsorption of the three cargo molecules (benzamide, malonamide and potassium thiocyanate) onto the block copolymer.

6.3.1 Band assignment of the pDMAEMA-*b*-pNIPAM film

This section begins with the introduction of the Raman spectrum of poly((2-dimethylamino) ethyl methacrylate), pDMAEMA, along with a proposed peak assignment. The structure of pDMAEMA which forms the first block of the copolymer, is shown in figure 6.1. The Raman spectrum of pDMAEMA-*b*-pNIPAM grafted from fused silica in the CH and fingerprint regions is shown later in figure 6.3.

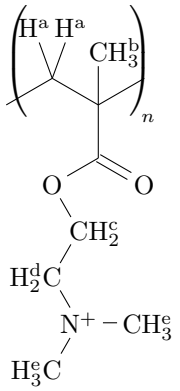

Figure 6.1: Structure of poly((2-dimethylamino) ethyl methacrylate) (pDMAEMA), the first block of the polymer film.

The TIR Raman spectrum of pDMAEMA

The background-subtracted Raman spectrum of pDMAEMA recorded in SY polarisation is shown in 6.2. Table 6.1 summarises the peak assignment discussed in this section. Three main bands are resolved in the fingerprint region (left). The main band located at 1451 cm^{-1} and its shoulder at 1406 cm^{-1} are assigned to bending of the methylene and methyl groups, in the side chain and along the polymer backbone.[272,273] The band located at 1714 cm^{-1} is assigned to C=O stretching.

Several peaks are resolved in the CH region shown on the right of figure 6.2. The strongest stretches are located at 2944 cm^{-1} and 2961 cm^{-1}. The former is assigned to the symmetric stretch of the methylene of the side chain, closest to the oxygen atom (denoted with the letter c in figure 6.1). The latter has also been observed by Thomas *et al.* in polymethyl methacrylate and was assigned to a combination of the symmetric stretch of the methyl in α position and the antisymmetric stretch of the methylene of the backbone.[272] The band at 3005 cm^{-1} is assigned to the antisymmetric stretch of the methyl group in α position,[272] while the peaks at 3030 cm^{-1} and 3050 cm^{-1} are assigned to the symmetric and antisymmetric stretch of the methyl in the dimethylammonium group respectively. The stretches at 2894 cm^{-1} and 2856 cm^{-1} are

assigned to a methylene stretch of the side chain antisymmetric and symmetric respectively.[159] The symmetric stretch of the methylene of the backbone is located at 2884 cm^{-1}.[273] The band at 2800 cm^{-1} is tentatively assigned to an overtone of bending of the methylene and methyl groups.

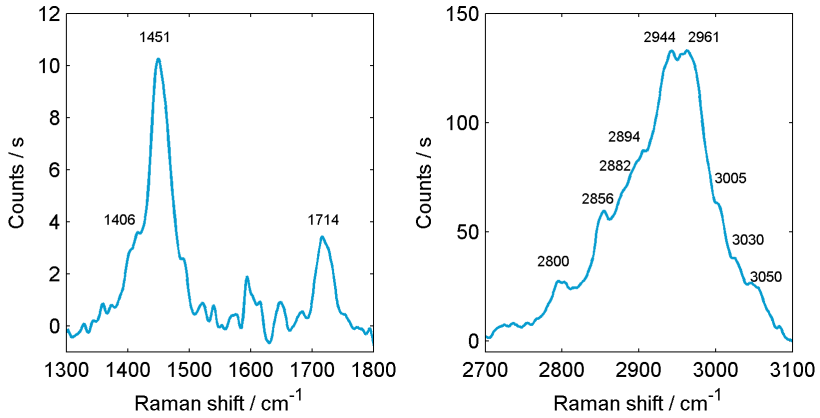

Figure 6.2: SY-polarised TIR Raman spectrum of a grafted pDMAEMA film in the fingerprint region (left) and CH region (right).

Table 6.1: Assignment of the Raman bands of pDMAEMA. Intensities are normalised to the band at 2944 cm^{-1}.

cm^{-1}	Intensity	Assignment
3050	0.19	$\nu_{as}(CH_3{}^{e})$ [159]
3030	0.29	$\nu_{s}(CH_3{}^{e})$ [159]
3005	0.45	$\nu_{as}(CH_3{}^{b})$ [272]
2961	1.00	$\nu_{s}(CH_3{}^{b})$ and $\nu_{as}(CH_2{}^{a})$ [272]
2944	1.00	$\nu_{s}(CH_2{}^{c})$ [273]
2894	0.66	$\nu_{as}(CH_2{}^{d})$ [159]
2884	0.53	$\nu_{s}(CH_2{}^{a})$ [273]
2856	0.45	$\nu_{s}(CH_2{}^{d})$ [159]
2800	0.21	overtone of $\delta(CH_3)$
1714	0.02	ν(C=O)
1451	0.08	$\delta(CH_3)$ [272]
1406	0.03	$\delta(CH_3)$ [272]

The TIR Raman spectrum of pDMAEMA-*b*-pNIPAM

The Raman spectrum of a pDMAEMA-*b*-pNIPAM film recorded in SY polarisation is shown in figure 6.3. In the fingerprint region, the band at 1450 cm^{-1} corresponding to CH_3 bending is still the dominant feature. The band associated to C=O stretching inside the pDMAEMA block is located at 1726 cm^{-1}. The band around 1650 cm^{-1} is similar to the Amide I band found in pNIPAM. The signal assigned to the antisymmetric deformation of the isopropyl group of pNIPAM can be found at 1311 cm^{-1}. It is more difficult to assign individual peaks in the CH region but some features of pDMAEMA are still visible. This includes the shoulder at 2962 cm^{-1} assigned to a combination of the symmetric stretch of the methyl in α position and the antisymmetric stretch of the methylene of the backbone, as well as the bending overtone at 2800 cm^{-1}.

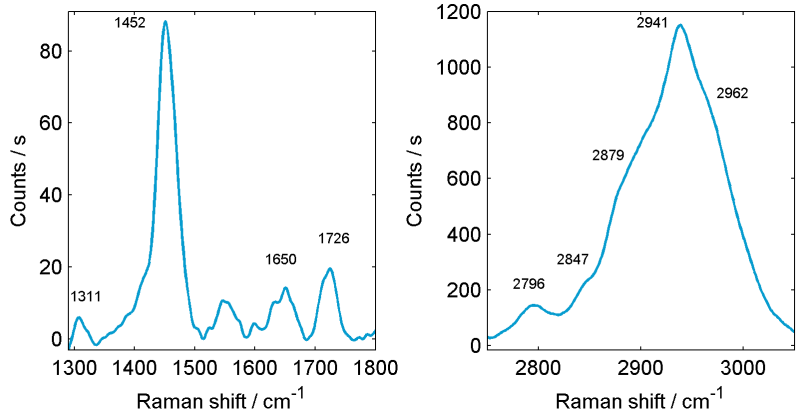

Figure 6.3: SY-polarised TIR Raman spectrum of a grafted pDMAEMA-*b*-pNIPAM film in the fingerprint region (left) and CH region (right).

The plot in figure 6.4 shows the overlap between the diblock Raman spectrum and spectra obtained from the separate blocks. The latter spectra of surface grafted pNIPAM and pDMAEMA are also shown in figures 4.4 and 6.3, respectively. The two spectra were scaled and combined to overlap with the pDMAEMA-*b*-pNIPAM spectrum. While the resulting spectrum does not match the spectrum of the diblock perfectly, it shows that the main features of the pDMAEMA-*b*-pNIPAM spectrum arise from a combination of spectra of the two blocks.

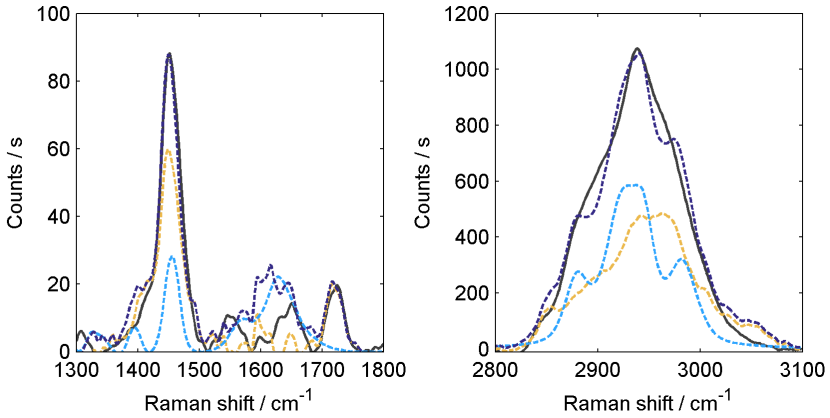

Figure 6.4: SY-polarised TIR Raman spectrum of a grafted pDMAEMA-*b*-pNIPAM film in the fingerprint region (left) and CH region (right). The spectrum of the diblock copolymer is shown in black alongside scaled spectra of pDMAEMA (dashed yellow), pNIPAM (dashed light blue), and the sum of both (dashed dark blue).

The uniformity of the diblock film was assessed by TIR Raman imaging of the polymer at the silica-water interface. Figure 6.5 shows the distribution of pDMAEMA-*b*-pNIPAM and water. Table 6.2 shows the centres and FWHM of the transmission bands for the chosen filter angles. There are a number of high-intensity spots in the polymer image indicating a non-uniform layer. At the same time, the water image shows areas of very low intensity. The image on the right of the figure shows that the two features are overlapping. We can conclude that the polymer has areas of increased intensity that could stem from a higher density or increased film thickness. I believe

that it is unlikely that these features are caused by adsorbed polymer chains that are not chemically bound to the substrates. All initiator molecules should be bound to the surface and the substrate has been washed and sonicated extensively in a good solvent (water) between the synthesis and the measurements. The polymerisation is thus less controlled than the polymerisation of *e.g.* pNIPAM.

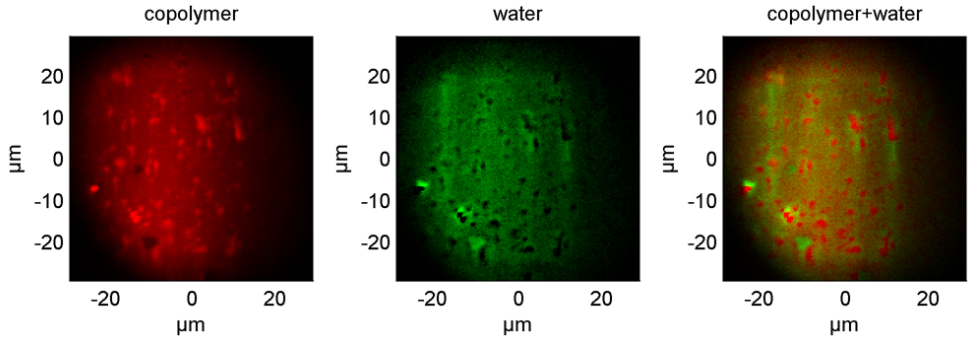

Figure 6.5: TIR Raman images of a pDMAEMA-*b*-pNIPAM film at the silica–water interface. The copolymer is shown in red and water in green.

Table 6.2: Centres and FWHM of the transmission bands of the tunable filter for the angles used to reconstruct the images shown in figure 6.5.

Filter angle	centre / cm^{-1}	FWHM / cm^{-1}
0°	2938	507
5°	2911	507
10°	2850	509
15°	2750	511
20°	2621	513

6.3.2 Influence of temperature on a pDMAEMA-*b*-pNIPAM film

The influence of temperature on the spectrum of pDMAEMA-*b*-pNIPAM films was studied by recording Raman spectra at temperatures ranging from 15 °C to 49 °C. In between measurements, the sample cell was warmed up to the next temperature point and given 10 minutes upon reaching the set point to equilibrate before the measurement. The background-subtracted Raman spectra of a pDMAEMA-*b*-pNIPAM film at different temperatures are shown in figure 6.6.

An increase in the intensity of Raman bands with increasing temperature is observed in the fingerprint and CH region. Within the fingerprint region, a signal increase is observed in the Amide I region around 1650 cm^{-1} and in the band at 1452 cm^{-1} assigned to a methylene scissoring mode. Similar increases were also observed during the phase transition of grafted pNIPAM presented in section 4.3.2. The band associated with the ester group of pDMAEMA ($\sim$1727 cm^{-1}) shows a smaller increase in intensity than the amide. This is consistent with the absence of thermoresponsive behaviour in the pDMAEMA block. As it is closer to the interface, even a small movement towards it would have resulted in a stronger signal increase. The

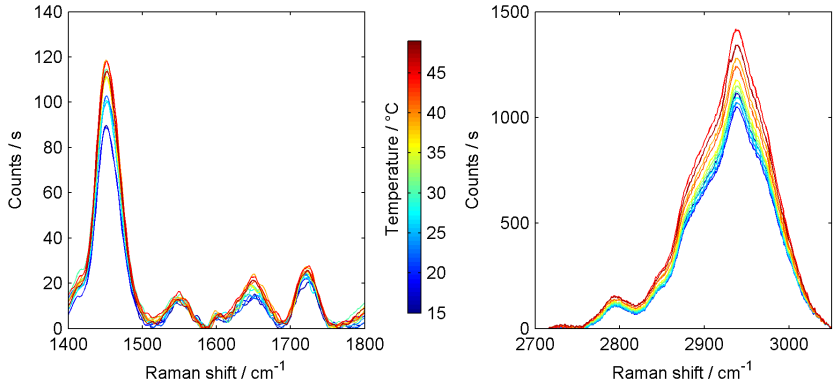

Figure 6.6: SY-polarised TIR Raman spectra of a pDMAEMA-*b*-pNIPAM film in the CO (left) and CH (right) regions, collected at different temperatures ranging from 15 °C to 49 °C.

increase of the signals in the CH region with temperature is shown in figure 6.7 and indicates a contraction of the polymer film towards the interface. The variability in the data can be attributed to the non-uniform polymer distribution shown in figure 6.5. Small changes in the hemisphere position during the temperature ramp might lead to different signal intensities as different areas are probed. The behaviour matches the one of grafted pNIPAM during the temperature increase but with a magnitude similar to a thin film (see figure 4.15). No shift of the peak positions was observed in the CH region. A pNIPAM film is expected to show a shift towards lower wavenumbers during the temperature increase. This change, however, was shown to be mild ($-0.1\,\mathrm{cm}^{-1}/°\mathrm{C}$, section 4.3.2). It is thus possible that it was not detected for the weaker transition in pDMAEMA-*b*-pNIPAM.

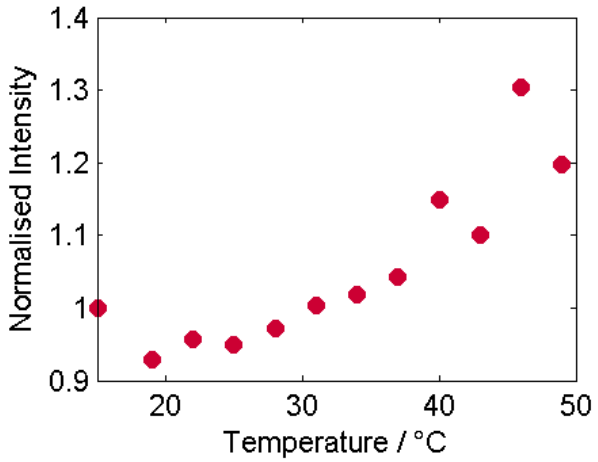

Figure 6.7: Change in intensity of the CH region in the TIR Raman spectrum of a grafted pDMAEMA-*b*-pNIPAM layer as a function of temperature.

The phase transition in the pDMAEMA-*b*-pNIPAM film shows feature changes similar to grafted pNIPAM. This confirms that the pNIPAM block is thermoresponsive. It is not possible to determine a clear transition temperature since the changes are happening more gradually than in a pure pNIPAM film. This could be an op-

tical effect as the pNIPAM chains are further away from the interface compared to chapter 4. As outlined in chapter 1, the sensitivity of TIR Raman spectroscopy drops exponentially with the distance from the interface, reducing the impact of changes in pNIPAM on the recorded spectrum. An additional contribution to the observed behaviour could be the hydrophilic pDMAEMA block shifting the phase transition of the pNIPAM block towards higher temperatures. A similar effect has been reported by Cunliffe *et al.* although for statistical copolymers of *N*-isopropylacrylamide and acrylamide.[268] The potential impact of the pDMAEMA block on the phase transition of pNIPAM could be investigated by studying temperature-induced changes in free pDMAEMA-*b*-pNIPAM. Based on this behaviour, I decided to study cargo adsorption between 20 °C and 45 °C. This temperature range will allow me to probe the biggest difference between the two states of pDMAEMA-*b*-pNIPAM.

6.3.3 Interaction between pDMAEMA-*b*-pNIPAM films and cargo molecules

This section summarises the results of the interactions between pDMAEMA-*b*-pNIPAM films and benzamide, deuterated malonamide and potassium thiocyanate. The two uncharged cargos (benzamide and d-malonamide) are studied even though mainly electrostatic interactions are expected with the diblock copolymer in order to better compare this polymer the previous ones. An equilibrium adsorption isotherm was collected for each cargo molecule at 20 °C and 45 °C. Data recorded at low and high temperature is visualised with blue and red dots, respectively, alongside a dotted line showing the Raman signal intensity of the cargo molecules as a function of the bulk concentration.

Interaction between a pDMAEMA-*b*-pNIPAM film and benzamide

The adsorption isotherms for benzamide on a pDMAEMA-*b*-pNIPAM film were recorded at concentrations ranging from 11 mM to 60 mM at 20 °C and 45 °C. The data is shown in figure 6.8.

Across the isotherms, the concentration of benzamide is increased inside the polymer brush. The surface excess increases linearly with increasing bulk concentration at both temperatures in the range of concentrations studied. The surface excess is similar at both temperatures and reaches 50 µmol m^{-2} and 46 µmol m^{-2} at a bulk concentration of 60 mM at 20 °C and 45 °C, respectively.

pNIPAM and polyvaline showed a slight enrichment of benzamide inside the films that did not change significantly with temperature. The surface excess on the pDMAEMA-*b*-pNIPAM film, however, was an order of magnitude higher than it was for pNIPAM and polyvaline. Still, similar quantities of benzamide are adsorbing at both temperatures. Release kinetics might still differ between 20 °C and 45 °C depending on whether the cargo has to diffuse through an open or a collapsed pNIPAM layer. The binding mechanism is not clear since no changes were observed in the fingerprint region.

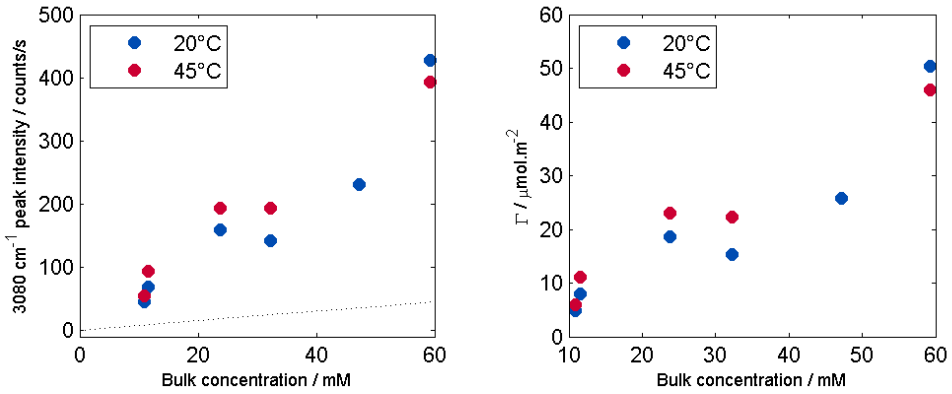

Figure 6.8: Adsorption isotherm of benzamide onto pDMAEMA-*b*-pNIPAM at 20 °C (●) and 45 °C (●). The dotted line shows the signal intensity expected if the bulk concentration continued up to the surface (left). The bound amount of benzamide is calculated from the difference between an isotherm on clean silica and the equilibrium adsorption isotherm on the pDMAEMA-*b*-pNIPAM brush (right).

Interaction between a pDMAEMA-*b*-pNIPAM film and d-malonamide

The interactions between a pDMAEMA-*b*-pNIPAM film and d-malonamide was studied for concentrations ranging from 10 mM to 250 mM at 20 °C and 10 mM to 180 mM at 45 °C. The resulting isotherms are shown in figure 6.9.

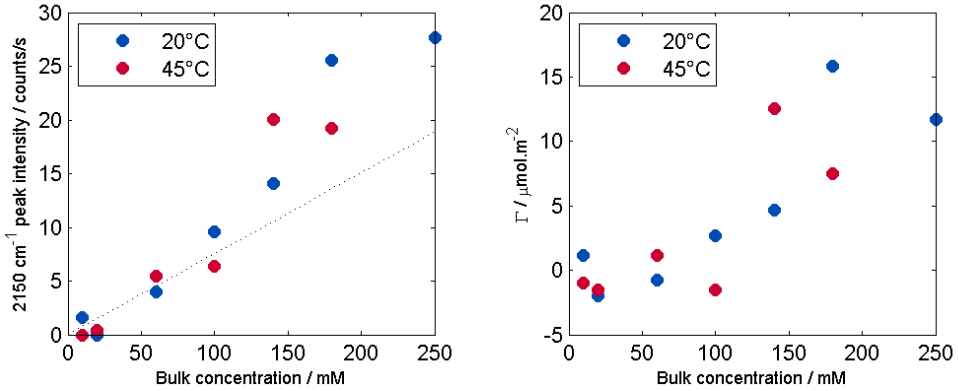

Figure 6.9: Adsorption isotherm of d-malonamide onto pDMAEMA-*b*-pNIPAM at 20 °C (●) and 45 °C (●). The dotted line shows the signal intensity expected if the bulk concentration continued up to the surface (left). The bound amount of d-malonamide is calculated from the difference between an isotherm on clean silica and the equilibrium adsorption isotherm on the polyvaline brush (right).

At low temperature, the concentration of d-malonamide inside the layer is increased compared to the bulk concentration. This difference increases with increasing bulk concentration and a surface excess of 12 µmol m^{-2} is reached at a bulk concentration of 250 mM. A similar behaviour is recorded at 45 °C where the concentration of malonamide in the film starts at a bulk concentration of 150 mM to reach a surface coverage between 5 and 12 µmol m^{-2}. As a consequence, it could be possible to capture d-malonamide at both low and high temperatures. Similarly to benzamide, the collapsed pNIPAM layer might lead to different release kinetics.

No change were detected in the band position of the C−D stretch of d-malonamide or in the C=O stretch of the diblock polymer. This suggests that the binding is not though hydrogen bond formation between malonamide and the polymer.

Interaction between a pDMAEMA-*b*-pNIPAM film and potassium thiocyanate

The interactions between potassium thiocyanate and a pDMAEMA-*b*-pNIPAM film were studied for concentrations ranging between 10 mM and 250 mM at 20 °C and 45 °C. The calculated isotherms are presented in figure 6.10 together with the expected Raman intensity of KSCN as a function of bulk concentration.

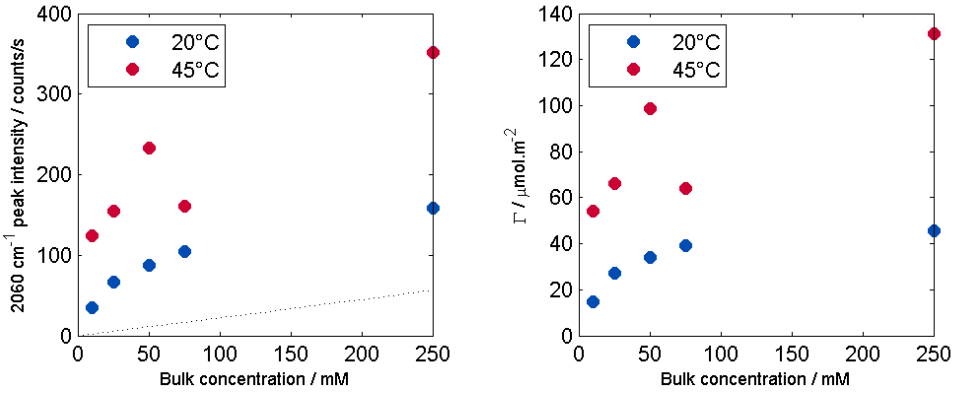

Figure 6.10: Adsorption isotherm of KSCN onto a pDMAEMA-*b*-pNIPAM film at 20 °C (●) and 45 °C (●). The dotted line shows the signal intensity expected if the bulk concentration continued up to the surface (left). The bound amount of KSCN is calculated from the difference between an isotherm on clean silica and the equilibrium adsorption isotherm on the diblock brush (right).

The isotherms show that potassium thiocyanate binds strongly to the pDMAEMA-*b*-pNIPAM film at both temperatures. The concentrations inside the film are significantly higher than the bulk concentration. This difference increases with increasing bulk concentration. This increase in surface excess appears to reduce at higher bulk concentrations at 20 °C. The surface excess first increases from 15 to 39 µmol m^{-2} between bulk concentrations of 10 and 75 mM and reaches 45 µmol m^{-2} at 250 mM. The data suggests that a concentration limit inside the brush is reached but more data points are necessary to confirm this assumption. The surface excess at 45 °C is consistently higher than at 20 °C. The surface excess also increases with bulk concentration over the entire range studied and reaches 131 µmol m^{-2} at 250 mM.

Potassium thiocyanate did not show any binding onto pNIPAM or polyvaline films. This behaviour is in stark contrast to the results for pDMAEMA-*b*-pNIPAM. The data presented in this section suggests that it would be possible to load a film of pDMAEMA-*b*-pNIPAM with KSCN at 45 °C and release a fraction of this cargo by reducing the temperature to 20 °C.

There were no changes in the fingerprint region of pDMAEMA-*b*-pNIPAM during the adsorption of KSCN. Binding to the amide or methacrylate groups is expected to

lead to changes in this region. There was also no change in the peak shape or position of the SCN^- signal at 2060 cm^{-1}.

Figure 6.11 shows Raman images of the pDMAEMA-*b*-pNIPAM film in contact with a 250 mM solution of KSCN at 20 °C and 45 °C. The centres and FWHM of the transmission bands for the filter angles used for those images are summarised in table 6.3. The images of the polymer show high intensity areas as seen in figure 6.5 above. The KSCN image shows a relatively uniform distribution across the image. This implies that the cargo is not more concentrated in the parts of the polymer that show a higher intensity. The image overlapping the two distributions consequently has red spots in the areas where the polymer shows a higher intensity. The uniform distribution of KSCN is not due to contributions of the bulk phase since the amount of the molecule inside the brush is significantly higher than the bulk concentration (see figure 6.10).

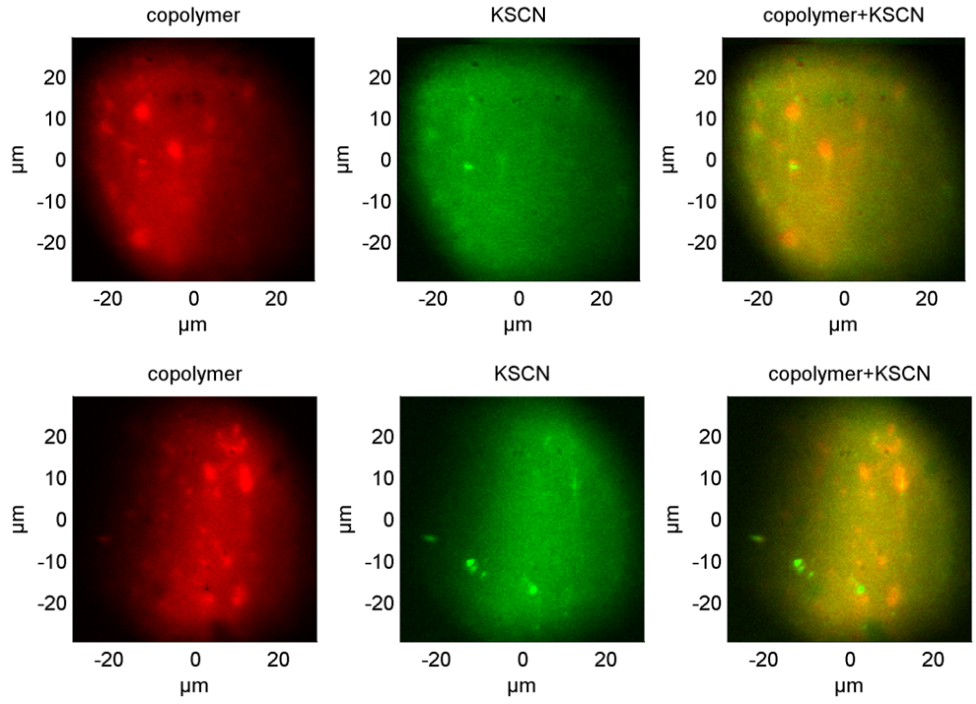

Figure 6.11: TIR Raman images of a pDMAEMA-*b*-pNIPAM film and KSCN at 20 °C (top) and 45 °C (bottom)

Table 6.3: Centres and FWHM of the transmission bands of the tunable filter for the angles used to reconstruct the images shown in figure 6.11.

Filter angle	centre / cm^{-1}	FWHM / cm^{-1}
0°	2938	507
10°	2850	509
15°	2750	511
30°	2271	523
35°	2048	530

6.4 Conclusion

In this chapter, I presented films of a block copolymer poly((2-dimethylamino) ethyl methacrylate)-*b*-poly(*N*-isopropylacrylamide) grafted from a silica surface. TIR Raman spectroscopy was used once again to study the impact of temperature changes on the polymer and its interaction with cargo molecules. pDMAEMA-*b*-pNIPAM was designed to provide a stronger driving force for adsorption using long range electrostatic and dipolar interactions. TIR Raman imaging showed that the layer was less uniform than the pNIPAM and polyvaline films shown in the previous chapters.

The pDMAEMA-*b*-pNIPAM layer was found to be thermoresponsive. The transition was however milder than in pure pNIPAM films and no clear temperature transition was found. This is consistent with the general behaviour of polymer films observed in this thesis. Based on the temperature behaviour, 20 °C and 45 °C were chosen for the study of the adsorption of cargoes onto the films.

The interaction between the layer and the three cargo molecules was studied. In contrast with pNIPAM and polyvaline, all the cargoes studied were found to adsorb onto the layer. Benzamide adsorbed onto a pDMAEMA-*b*-pNIPAM layer at both temperatures and reached a surface coverage of 50 µmol m^{-2} at a bulk concentration of 60 mM. d-malonamide was also found to adsorb to the polymer at both temperatures albeit with a smaller surface coverage of 12 µmol m^{-2} at 250 mM. Out of the three cargo molecules, potassium thiocyanate binds the strongest onto pDMAEMA-*b*-pNIPAM films. It binds onto both states of the polymer but more strongly at higher temperature (up to 130 µmol m^{-2} at 250 mM at 45 °C). TIR Raman images showed that KSCN was uniformly distributed in the layer and was not adsorbing more strongly onto spots of higher polymer density.

This chapter has demonstrated that pDMAEMA-*b*-pNIPAM is capable of binding relatively large amounts of certain cargo molecules. The degree of adsorption changes with temperature, showing that pDMAEMA-*b*-pNIPAM is a potential candidate for the temperature-dependent capture and release of cargo molecules.

Chapter 7: Conclusion

Smart surfaces have attracted a lot of interest as they have the potential to deliver a complex response to stimulation in a wide range of fields from biomedical applications to material science. A lot of work — both experimental and theoretical — has been carried out in order to understand the underlying mechanisms. This thesis seeks to aid the development of soft matter-based surfaces by designing methods for monitoring the uptake and release of cargo from thermoresponsive systems.

As part of this thesis, I developed synthetic methods for grafting three polymers — pNIPAM, polyvaline and pDMAEMA-*b*-pNIPAM — from silica substrates. I then studied their temperature response and their interactions with three cargo molecules: benzamide, d-malonamide and KSCN. I furthermore presented a procedure for the coadsorption of DDAB and d-SDS to silica. TIR Raman spectroscopy proved to be a powerful technique for probing the phase transition in grafted polymers, showing changes on a molecular level such as the dehydration of amide groups. Through isotherms, it was possible to gain quantitative and qualitative information on the species at the solid-water interface. The technique was sensitive enough to detect low cargo surface excess in the range of µmol m^{-2}. The filter-based Raman imaging proved to be a useful tool to assess the spatial distribution of the components on substrate, providing *e.g.* information on the homogeneity of surface grafted polymers. It was of particular use for the diblock copolymer where it revealed that the synthesis resulted in inhomogeneous films while the distribution of adsorbed cargo did not match the polymer topography.

The work on mixtures of DDAB and d-SDS showed that mixed vesicles of cationic and anionic surfactants can be used to transport an anionic surfactant to a negatively charged surface. On its own, d-SDS does not adsorb to silica but, together with DDAB, the inter-surfactant interactions overcome the repulsion between d-SDS and silica leading to a coadsorption of the two surfactant species. TIR Raman spectroscopy revealed that the composition of the mixed layer does not follow the surfactant-ratio in bulk. The highest amount of d-SDS adsorbs from mixtures where its concentration in the bulk phase is just below the equimolar ratio. A mechanism for this behaviour was proposed where the concentration of free DDAB is low enough to not change the charge of silica significantly during its adsorption. This would otherwise prevent the mixed vesicles from fusing to the surface. At the same time, the mixed vesicles are still overall positively charged and thus able to fuse to the surface.

The work on pNIPAM layers showed that the temperature-induced phase trans-

ition was broader than the one observed in bulk, as expected. Even though the hydrophobicity of the pNIPAM layer changed across the phase transition, it did not lead to selective adsorption of any of the studied cargo molecules. This is potentially caused by pNIPAM being too hydrophobic in either state, preventing selective cargo adsorption. The next step was the study of polyvaline which is less hydrophobic than pNIPAM but is also expected to show some thermoresponsive behaviour due to the presence of isopropyl groups. The adsorption of cargo molecules, however, was comparable to the observation with pNIPAM. This led to the development of the diblock copolymer pDMAEMA-*b*-pNIPAM. The aim was that cargoes could interact with the cationic bottom layer, pDMAEMA, while the conformation of the top layer, pNIPAM, restricts diffusion between the bottom of the polymer and the bulk phase. The surface excess of each cargo was larger than observed for pNIPAM and polyvaline. In the case of potassium thiocyanate, the surface excess was nearly double at 45 °C compared to 20 °C. TIR Raman spectroscopy indicated some chain collapse at high temperatures which was expected to lead to a smaller amount of KSCN inside the layer. At the same time, no changes were observed in the CH region during the transition or the adsorption. This implies that there was no major change of structure in the layer such as a migration of the top layer towards the interface exposing the pDMAEMA block, as had been reported by Wang *et al.* for another pNIPAM-based diblock copolymer.[269]

The findings on the interactions between the diblock copolymer pDMAEMA-*b*-pNIPAM and the cargo molecules highlight the sensitivity of TIR Raman spectroscopy and its ability to detect cargo molecules bound to surface-grafted polymer films. It follows that the lack of observed selective binding of the cargo molecules to layers of pNIPAM and polyvaline is not due to an insufficient sensitivity of TIR Raman spectroscopy. The three different cargo molecules studied in this work are thus not binding to surface-grafted layers of either pNIPAM or polyvaline.

While TIR Raman spectroscopy allowed the quantitative detection of *e.g.* cargo molecules, it might be necessary to employ complementary techniques to gain a full understanding of the processes in the polymer layers. For example, *in situ* AFM measurements can reveal in layer's topography. Neutron reflectometry could provide information on the changes in the layer profile during temperature increase and cargo adsorption. The method for grafting polymers from silane-terminated silica imposes limitations on the accessible pH-range to ∼5–7. Working outside this range can cause hydrolysis of the silane groups leading to the detachment of polymer chains. Alternatives need to be investigated if an extension of the pH range is desired.

I believe that this thesis presents useful methodologies and techniques for the study of responsive films at interfaces and their interactions with cargo molecules. The multilayer model has the potential to be a useful tool for determining thin film thicknesses as part of TIR Raman measurements. However, more work is required to validate its results. The synthetic protocols presented here can be valuable for the preparation of similar responsive systems. Future work should focus on diblock copolymers such as pDMAEMA-*b*-pNIPAM since it showed the highest potential for cargo capture and release. It will be interesting to study the kinetics of KSCN adsorp-

tion and release from pDMAEMA-*b*-pNIPAM. Experiments could include mixtures of cargoes to study competitive adsorption onto the polymer. It should be possible to carry out these studies with the techniques employed in this thesis. As mentioned above, a detailed study of structural changes might, however, require a wider range of techniques. Theoretical work might also provide valuable insight into intra- and inter-polymer as well as polymer-cargo interactions. Together the different techniques will aid the design of novel responsive cargo-polymer systems.

Chapter 8: Appendix

NMR of N-carboxyanhydride of valine

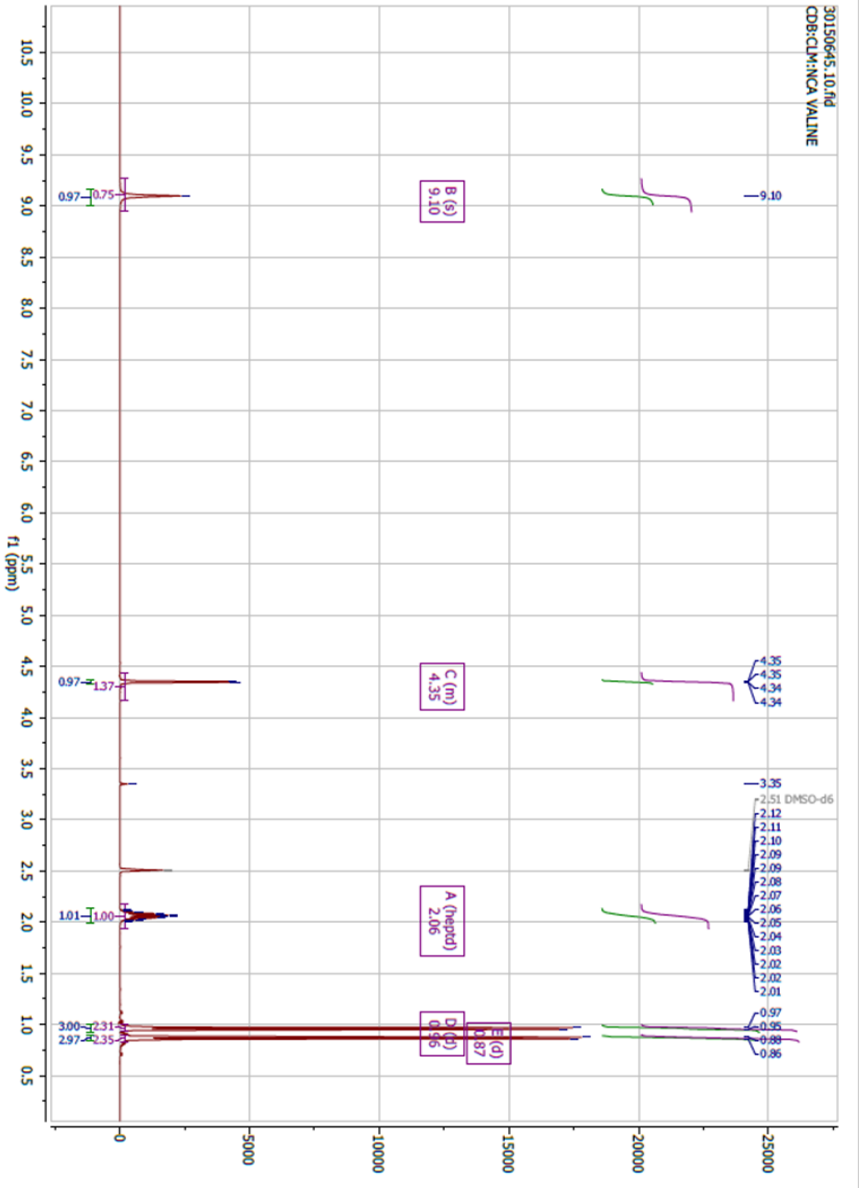

Figure 8.1: NMR spectrum of N-carboxyanhydride of valine.

Deuteration of malonamide

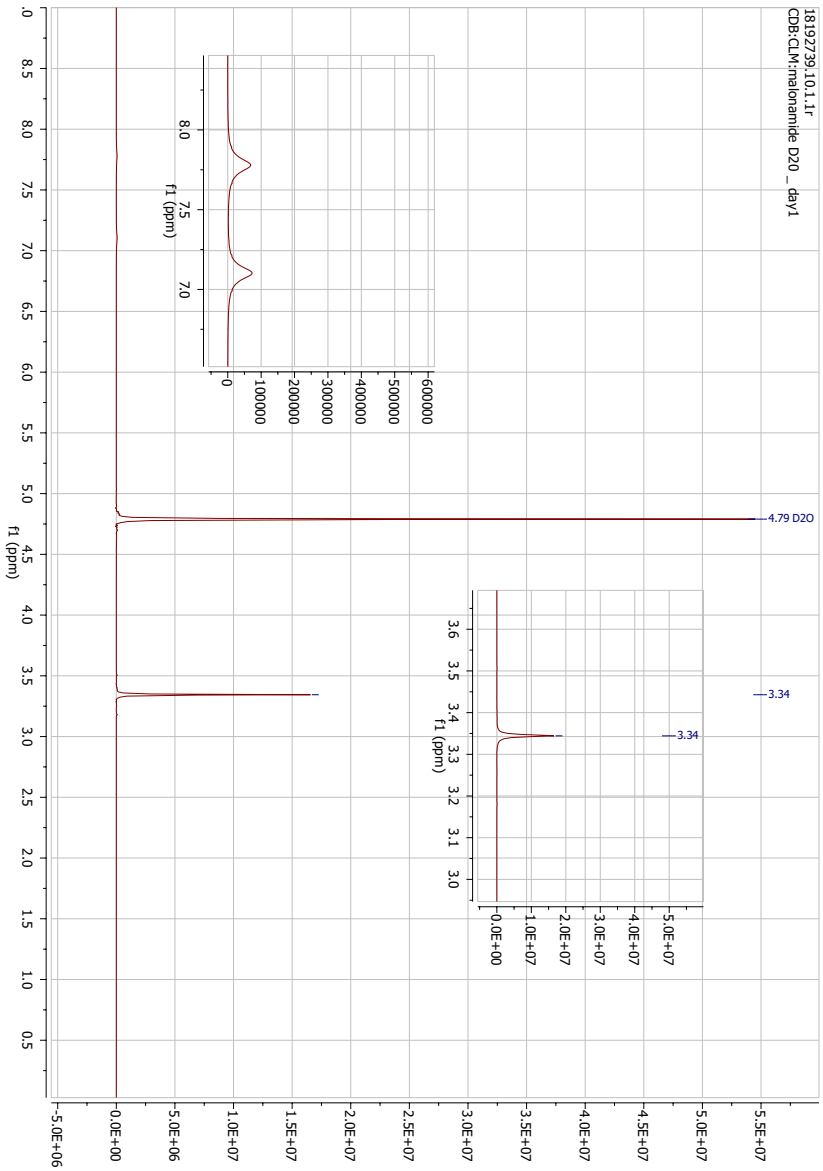

Figure 8.2: NMR spectrum of malonamide in D2O at pD=5

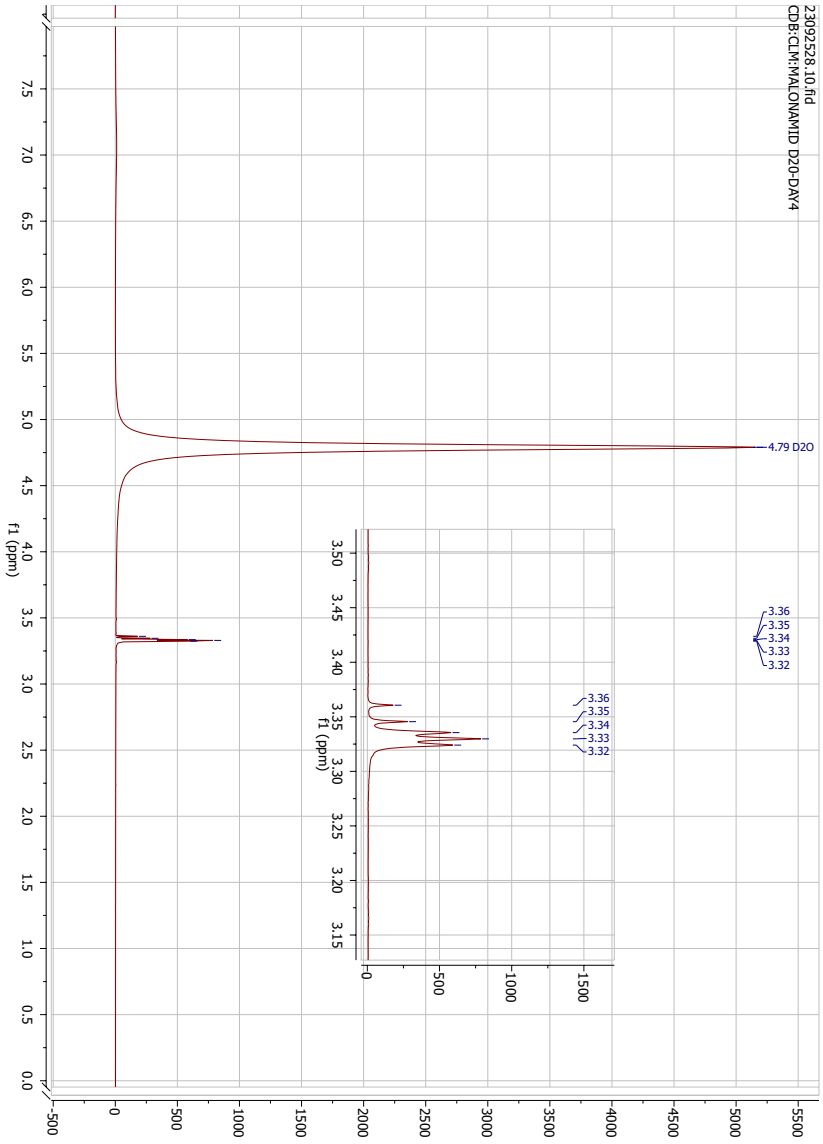

Figure 8.3: NMR spectrum of d-malonamide in D_2O after 4 days at pD=8

Bibliography

[1] A.-L. Kjoniksen, K. Zhu, R. Pamies, and B. Nystrom. Temperature-Induced Formation and Contraction of Micelle-Like Aggregates in Aqueous Solutions of Thermoresponsive Short-Chain Copolymers. *The Journal of Physical Chemistry B*, 112(11):3294–3299, 2008.

[2] R. V. Joshi, C. E. Nelson, K. M. Poole, M. C. Skala, and C. L. Duvall. Dual pH- and temperature-responsive microparticles for protein delivery to ischemic tissues. *Acta Biomaterialia*, 9(5):6526–6534, 2013.

[3] X. Yin, A. S. Hoffman, and P. S. Stayton. Poly(N-isopropylacrylamide-co-propylacrylic acid) Copolymers That Respond Sharply to Temperature and pH. *Biomacromolecules*, 7(5):1381–1385, 2006.

[4] Z. Pang, W. Lu, H. Gao, K. Hu, J. Chen, C. Zhang, X. Gao, X. Jiang, and C. Zhu. Preparation and brain delivery property of biodegradable polymersomes conjugated with OX26. *Journal of Controlled Release*, 128(2):120–127, 2008.

[5] J. Rosselgong, A. Blanazs, P. Chambon, M. Williams, M. Semsarilar, J. Madsen, G. Battaglia, and S. P. Armes. Thiol-Functionalized Block Copolymer Vesicles. *ACS Macro Letters*, 1(8):1041–1045, 2012.

[6] R. N. Netz and D. Andelman. Neutral and charged polymers at interfaces. *Physics Reports*, 380(1):1 – 95, 2003.

[7] A. R. Khokhlov, A. Y. Grosberg, and V. S. Pande. *Statistical Physics of Macromolecules*. Springer, 1994.

[8] P. J. Flory. *Principles of Polymer Chemistry*. Cornell University, 1953.

[9] Z. Lei, S. Yang, and E.-Q. Chen. Membrane rigidity induced by grafted polymer brush. *Soft Matter*, 11:1376–1385, 2015.

[10] A. Karim, S. K. Satija, J. F. Douglas, J. F. Ankner, and L. J. Fetters. Neutron reflectivity study of the density profile of a model end-grafted polymer brush: Influence of solvent quality. *Phys. Rev. Lett.*, 73:3407–3410, Dec 1994.

[11] M. S. Kent, L. T. Lee, B. J. Factor, F. Rondelez, and G. S. Smith. Tethered chains in good solvent conditions: An experimental study involving langmuir diblock copolymer monolayers. *The Journal of Chemical Physics*, 103(6):2320–2342, 1995.

[12] D. M. Jones, A. A. Brown, and W. T. S. Huck. Surface-initiated polymerizations in aqueous media: Effect of initiator density. *Langmuir*, 18(4):1265–1269, 2002.

[13] Y. Liu, V. Klep, B. Zdyrko, and I. Luzinov. Synthesis of high-density grafted polymer layers with thickness and grafting density gradients. *Langmuir*, 21(25):11806–11813, 2005.

[14] A. Kostruba, M. Ohar, B. Kulyk, O. Zolobko, and Y. Stetsyshyn. Surface modification by grafted sensitive polymer brushes: An ellipsometric study of their properties. *Applied Surface Science*, 276:340–346, 2013.

[15] J. Habicht, M. Schmidt, J. Ruhe, and D. Johannsmann. Swelling of thick polymer brushes investigated with ellipsometry. *Langmuir*, 15(7):2460–2465, 1999.

[16] Y. E. Ghoussoub, M. Zerball, H. M. Fares, J. F. Ankner, R. von Klitzing, and J. B. Schlenoff. Ion distribution in dry polyelectrolyte multilayers: a neutron reflectometry study. *Soft Matter*, 14:1699–1708, 2018.

[17] M. Lösche, J. Schmitt, G. Decher, W. G. Bouwman, and K. Kjaer. Detailed structure of molecularly thin polyelectrolyte multilayer films on solid substrates as revealed by neutron reflectometry. *Macromolecules*, 31(25):8893–8906, 1998.

[18] X. Sun, E. Bouchaud, A. Lapp, B. Farnoux, M. Daoud, and G. Jannink. Profiles of adsorbed polymer layers observed by neutron reflection. *Europhysics Letters*, 6(3):207, 1988.

[19] C.-H. Lee, Y.-M. Yang, K.-L. Leu, H.-Y. Lin, C.-H. Liang, and C.-H. Chang. Exploring physical stability characteristics of positively charged catanionic vesicle/dna complexes. *Colloid and Polymer Science*, 293(8):2239–2247, 2015.

[20] G. Zhang and C. Wu. Quartz Crystal Microbalance Studies on Conformational Change of Polymer Chains at Interface. *Macromolecular Rapid Communications*, 30(4-5):328–335, 2009.

[21] G. Dunér, E. Thormann, and A. Dėdinaitė. Quartz crystal microbalance with dissipation (qcm-d) studies of the viscoelastic response from a continuously growing grafted polyelectrolyte layer. *Journal of Colloid and Interface Science*, 408:229–234, 2013.

[22] D. Tabor and H. S. Winterton. Surface forces: Direct measurement of normal and retarded van der waals forces. *Nature*, 219:1120–1121, 1986.

[23] J. N. Israelachvili and G. E. Adams. Direct measurement of long range forces between two mica surfaces in aqueous kno3 solutions. *Nature*, 262:774–776, 1976.

[24] N. Myshkin and A. Kovalev. Adhesion and surface forces in polymer tribology - a review. *Friction*, 6(2):143–155, 2018.

[25] D. Kleshchanok, R. Tuinier, and P. R. Lang. Direct measurements of polymer-induced forces. *Journal of Physics: Condensed Matter*, 20(7):073101, 2008.

[26] S. R. Sheth and D. Leckband. Measurements of attractive forces between proteins and end-grafted poly(ethylene glycol) chains. *Proceedings of the National Academy of Sciences*, 94(16):8399–8404, 1997.

[27] L. Zhang, H. Zeng, and Q. Liu. Probing Molecular and Surface Interactions of Comb-Type Polymer Polystyrene-*graft*-poly(ethylene oxide) (PS-*g*-PEO) with an SFA. *The Journal of Physical Chemistry C*, 116(33):17554–17562, 2012.

[28] G. F. Belder, G. ten Brinke, and G. Hadziioannou. Influence of Anchor Block Size on the Thickness of Adsorbed Block Copolymer Layers. *Langmuir*, 13(15):4102–4105, 1997.

[29] S. Kidoaki, S. Ohya, Y. Nakayama, and T. Matsuda. Thermoresponsive Structural Change of a Poly(*N*-isopropylacrylamide) Graft Layer Measured with an Atomic Force Microscope. *Langmuir*, 17(8):2402–2407, 2001.

[30] S. Yamamoto, M. Ejaz, Y. Tsujii, and T. Fukuda. Surface Interaction Forces of Well-Defined, High-Density Polymer Brushes Studied by Atomic Force Microscopy. 2. Effect of Graft Density. *Macromolecules*, 33(15):5608–5612, 2000.

[31] T. W. Kelley, P. A. Schorr, K. D. Johnson, M. Tirrell, and C. D. Frisbie. Direct force measurements at polymer brush surfaces by atomic force microscopy. *Macromolecules*, 31(13):4297–4300, 1998.

[32] V. Freger, J. Gilron, and S. Belfer. Tfc polyamide membranes modified by grafting of hydrophilic polymers: an ft-ir/afm/tem study. *Journal of Membrane Science*, 209(1):283–292, 2002.

[33] Y.-F. Yang, Y. Li, Q.-L. Li, L.-S. Wan, and Z.-K. Xu. Surface hydrophilization of microporous polypropylene membrane by grafting zwitterionic polymer for anti-biofouling. *Journal of Membrane Science*, 362(1):255–264, 2010.

[34] Y. Tsuda, A. Kikuchi, M. Yamato, Y. Sakurai, M. Umezu, and T. Okano. Control of cell adhesion and detachment using temperature and thermoresponsive copolymer grafted culture surfaces. *Journal of Biomedical Materials Research Part A*, 69A(1):70–78, 2004.

[35] Y. Tsuda, A. Kikuchi, M. Yamato, A. Nakao, Y. Sakurai, M. Umezu, and T. Okano. The use of patterned dual thermoresponsive surfaces for the collective recovery as co-cultured cell sheets. *Biomaterials*, 26(14):1885–1893, 2005.

[36] H. Takahashi, M. Nakayama, M. Yamato, and T. Okano. Controlled chain length and graft density of thermoresponsive polymer brushes for optimizing cell sheet harvest. *Biomacromolecules*, 11(8):1991–1999, 2010.

[37] R. R. Patil, S. Turgman-Cohen, J. Šrogl, D. Kiserow, and J. Genzer. On-demand degrafting and the study of molecular weight and grafting density of poly(methyl methacrylate) brushes on flat silica substrates. *Langmuir*, 31(8):2372–2381, 2015.

[38] G. Tiwari, R. Tiwari, B. Sriwastawa, L. Bhati, S. Pandey, P. Pandey, and S. Bannerjee. Drug delivery systems: An updated review. *International Journal of Pharmaceutical Investigation*, 2(1):2–11, 2012.

[39] S. Zhang, Y. Zhou, W. Nie, L. Song, J. Li, and B. Yang. Fabrication of uniform "smart" magnetic microcapsules and their controlled release of sodium salicylate. *Journal of Materials Chemistry B*, 1:4331–4337, 2013.

[40] A. Kroning, A. Furchner, D. Aulich, E. Bittrich, S. Rauch, P. Uhlmann, K.-J. Eichhorn, M. Seeber, I. Luzinov, S. M. Kilbey, B. S. Lokitz, S. Minko, and K. Hinrichs. In situ infrared ellipsometry for protein adsorption studies on ultrathin smart polymer brushes in aqueous environment. *ACS Applied Materials & Interfaces*, 7(23):12430–12439, 2015.

[41] G. Huang, J. Gao, Z. Hu, J. V. St. John, B. C. Ponder, and D. Moro. Controlled drug release from hydrogel nanoparticle networks. *Journal of Controlled Release*, 94(2):303–311, 2004.

[42] X.-Z. Zhang, D.-Q. Wu, and C. C. Chu. Synthesis, characterization and controlled drug release of thermosensitive IPN–PNIPAAm hydrogels. *Biomaterials*, 25(17):3793–3805, 2004.

[43] E. Hecht. *Optics*. Pearson, 5th edition, 2017.

[44] D. A. Beattie, S. A. Winget, and C. D. Bain. Raman Scattering from Confined Liquid Films in the Sub-Nanometre Regime. *Tribology Letters*, 27(159), 2007.

[45] P. Atkins and R. Friedman. *Molecular Quantum Mechanics*. Oxford University Press, 4th edition, 2005.

[46] D. A. Long. *The Raman Effect: A Unified Treatment of the Theory of Raman Scattering by Molecules*. Wiley-Blackwell, 2002.

[47] P. F. Bernath. *Spectra of Atoms and Molecules*. Oxford University Press, 2nd edition, 2005.

[48] M. Possiwan. *Private communication*.

[49] Y. Brasse, M. B. Müller, M. Karg, C. Kuttner, T. A. F. König, and A. Fery. Magnetic and Electric Resonances in Particle-to-Film-Coupled Functional Nanostructures. *ACS Applied Materials & Interfaces*, 10(3):3133–3141, 2018.

[50] G. M. Hale and M. R. Querry. Optical Constants of Water in the 200-nm to 200-μm Wavelength Region. *Applied Optics*, 12(3):555–563, Mar 1973.

[51] M. J. Citra and P.H. Axelsen. Determination of molecular order in supported lipid membranes by internal reflection fourier transform infrared spectroscopy. *Biophysical Journal*, 71(4):1796–1805, 1996.

[52] T. A. McKeague. *Private communication*.

[53] C. B. Walsh and E. I. Franses. Thickness and quality of spin-coated polymer films by two-angle ellipsometry. *Thin Solid Films*, 347(1):167–177, 1999.

[54] C. Xue, N. Yonet-Tanyeri, N. Brouette, M. Sferrazza, P. V. Braun, and D. E. Leckband. Protein adsorption on poly(n-isopropylacrylamide) brushes: dependence on grafting density and chain collapse. *Langmuir*, 27:8810–8, 2011.

[55] B. A. Humphreys, J. D. Willott, T. J. Murdoch, G. B. Webber, and E. J. Wanless. Specific ion modulated thermoresponse of poly(N-isopropylacrylamide) brushes. *Physical Chemistry Chemical Physics*, 18:6037–6046, 2016.

[56] C. Z. Tan. Determination of refractive index of silica glass for infrared wavelengths by ir spectroscopy. *Journal of Non-Crystalline Solids*, 223(1):158–163, 1998.

[57] N. J. Greenfield. Using circular dichroism spectra to estimate protein secondary structure. *Nature protocols*, 1:2876–2890, 2006.

[58] B. J. H. Kuipers and H. Gruppen. Prediction of molar extinction coefficients of proteins and peptides using uv absorption of the constituent amino acids at 214 nm to enable quantitative reverse phase high-performance liquid chromatography-mass spectrometry analysis. *Journal of Agricultural and Food Chemistry*, 55(14):5445–5451, 2007.

[59] S. Mori and H. G. Barth. *Size Exclusion Chromatography*. Springer Laboratory, 1999.

[60] Y. Kondo, H. Uchiyama, N. Yoshino, K. Nishiyama, and M. Abe. Spontaneous vesicle formation from aqueous solutions of didodecyldimethylammonium bromide and sodium dodecyl sulfate mixtures. *Langmuir*, 11(7):2380–2384, 1995.

[61] V. Ramesh and M. M. Labes. Influence of disc-rod-sphere phase transitions in nematic lyotropics on a unimolecular isomerization reaction. *Journal of the American Chemical Society*, 109(11):3228–3231, 1987.

[62] K. J. Mysels. Surface tension of solutions of pure sodium dodecyl sulfate. *Langmuir*, 2(4):423–428, 1986.

[63] L. A. M. Rupert, D. Hoekstra, and J. B. F. N. Engberts. Fusogenic behavior of didodecyldimethylammonium bromide bilayer vesicles. *Journal of the American Chemical Society*, 107(9):2628–2631, 1985.

[64] E. F. Marques, A. Khan, and B. Lindman. A calorimetric study of the gel-to-liquid crystal transition in catanionic surfactant vesicles. *Thermochimica Acta*, 394(1):31–37, 2002. Festschrift Dedicated to Dr. Richard B. Kemp on the Occasion of his 60th Birthday . Calorimetry : A Tool in Health and Environmental Studies .

[65] H. Tang, N. Arulsamy, M. Radosz, Y. Shen, N. V. Tsarevsky, W. A. Braunecker, W. Tang, and K. Matyjaszewski. Highly Active Copper-Based Catalyst for Atom Transfer Radical Polymerization. *Journal of the American Chemical Society*, 128(50):16277–16285, 2006.

[66] H. Suzuki, H. M. Nurul, T. Seki, T. Kawamoto, H. Haga, K. Kawabata, and Y. Takeoka. Precise Synthesis and Physicochemical Properties of High-Density Polymer Brushes designed with Poly(*N*-isopropylacrylamide). *Macromolecules*, 43(23):9945–9956, 2010.

[67] J. N. Kizhakkedathu, R. Norris-Jones, and D. E. Brooks. Synthesis of Well-Defined Environmentally Responsive Polymer Brushes by Aqueous ATRP. *Macromolecules*, 37(3):734–743, 2004.

[68] J. N. Kizhakkedathu and D. E. Brooks. Synthesis of Poly(*N*,*N*-dimethylacrylamide) Brushes from Charged Polymeric Surfaces by Aqueous ATRP: Effect of Surface Initiator Concentration. *Macromolecules*, 36(3):591–598, 2003.

[69] K. N. Jayachandran, A. Takacs-Cox, and D. E. Brooks. Synthesis and Characterization of Polymer Brushes of Poly(*N*,*N*-dimethylacrylamide) from Polystyrene Latex by Aqueous Atom Transfer Radical Polymerization. *Macromolecules*, 35(11):4247–4257, 2002.

[70] I. B. Malham and L. Bureau. Density effects on collapse, compression, and adhesion of thermoresponsive polymer brushes. *Langmuir*, 26(7):4762–4768, 2010.

[71] B. Mao, L.-H. Gan, Y.-Y. Gan, X. Li, P. Ravi, and K.-C. Tam. Controlled polymerizations of 2-(dialkylamino)ethyl methacrylates and their block copolymers in protic solvents at ambient temperature via ATRP. *Journal of Polymer Science Part A: Polymer Chemistry*, 42(20):5161–5169, 2004.

[72] Q. Yan, H. Zhang, and Y. Zhao. Co2-switchable supramolecular block glycopolypeptide assemblies. *ACS Macro Letters*, 3(5):472–476, 2014.

[73] J. N. Israelachvili. *Intermolecular and Surface Forces*. Academic Press: San Diego, 1992.

[74] D. M. Small, editor. *The Physical Chemistry of Lipids*. Plenum, NY, 1986.

[75] C. Tanford. Micelle shape and size. *The Journal of Physical Chemistry*, 76(21):3020–3024, 1972.

[76] V. V. Dhawan and M. S. Nagarsenker. Catanionic systems in nanotherapeutics – biophysical aspects and novel trends in drug delivery applications. *Journal of Controlled Release*, 266:331–345, 2017.

[77] A. Lohani and A. Verma. Vesicles: Potential nano carriers for the delivery of skin cosmetics. *Journal of Cosmetic and Laser Therapy*, 19(8):485–493, 2017.

[78] T. Bramer, N. Dew, and K. Edsman. Pharmaceutical applications for catanionic mixtures. *Journal of Pharmacy and Pharmacology*, 59(10):1319–1334, 2007.

[79] B. György, M. E. Hung, X. O. Breakefield, and J. N. Leonard. Therapeutic applications of extracellular vesicles: clinical promise and open questions. *Annual Review of Pharmacology and Toxicology*, 55(1):439–464, 2015.

[80] H. B. Mohamed, S. M. El-Shanawany, M. A. Hamad, and M. Elsabahy. Niosomes: A strategy toward prevention of clinically significant drug incompatibilities. *Scientific Reports*, 7(1):6340, 2017.

[81] T. Taylor, P. Davidson, B. Bruce, and J. Weiss. Liposomal nanocapsules in food science and agriculture. *Critical Reviews in Food Science and Nutrition*, 45:587–605, 2005.

[82] M. Nuruzzaman, M. M. Rahman, Y. Liu, and R. Naidu. Nanoencapsulation, nano-guard for pesticides: A new window for safe application. *Journal of Agricultural and Food Chemistry*, 64(7):1447–1483, 2016.

[83] L. Juhlin. Retention of Particles by the Reticulo Endothelial System. *Acta Physiologica Scandinavica*, 48(1):78–87, 1960.

[84] R. Bazak, M. Houri, S. El Achy, W. Hussein, and T. Refaat. Passive targeting of nanoparticles to cancer: A comprehensive review of the literature. *Molecular and Clinical Oncology*, 2:904–908, 2014.

[85] A. L. Petersen, A. E. Hansen, A. Gabizon, and T. L. Andresen. Liposome imaging agents in personalized medicine. *Advanced Drug Delivery Reviews*, 64(13):1417–1435, 2012. Personalized nanomedicine.

[86] M. Howard, B. J. Zern, A. C. Anselmo, V. V. Shuvaev, S. Mitragotri, and V. Muzykantov. Vascular targeting of nanocarriers: Perplexing aspects of the seemingly straightforward paradigm. *ACS Nano*, 8(5):4100–4132, 2014.

[87] X. Liu, H. Li, Y. Chen, Q. Jin, K. Ren, and J. Ji. Mixed-charge nanoparticles for long circulation, low reticuloendothelial system clearance, and high tumor accumulation. *Advanced Healthcare Materials*, 3(9):1439–1447, 2014.

[88] A. Akbarzadeh, R. Rezaei-Sadabady, S. Davaran, S. W. Joo, N. Zarghami, Y. Hanifehpour, M. Samiei, M. Kouhi, and K. Nejati-Koshki. Liposome: classification, preparation, and applications. *Nanoscale Research Letters*, 8(1):102, 2013.

[89] H. Talsma, M. J. van Steenbergen, J. C. H. Borchert, and D. J. A. Crommelin. A novel technique for the one-step preparation of liposomes and nonionic surfactant vesicles without the use of organic solvents. liposome formation in a continuous gas stream: The bubble method. *Journal of Pharmaceutical Sciences*, 83(3):276–280, 1994.

[90] J. S. Wilkhu, D. Ouyang, M. J. Kirchmeier, D. E. Anderson, and Y. Perrie. Investigating the role of cholesterol in the formation of non-ionic surfactant based bilayer vesicles: Thermal analysis and molecular dynamics. *International Journal of Pharmaceutics*, 461(1):331–341, 2014.

[91] M. H. Nematollahi, A. Pardakhty, M. Torkzadeh-Mahanai, M. Mehrabani, and G. Asadikaram. Changes in physical and chemical properties of niosome membrane induced by cholesterol: a promising approach for niosome bilayer intervention. *RSC Advances*, 7:49463–49472, 2017.

[92] G. P. Kumar and P. Rajeshwarrao. Nonionic surfactant vesicular systems for effective drug delivery—an overview. *Acta Pharmaceutica Sinica B*, 1(4):208–219, 2011.

[93] S. Moghassemi and A. Hadjizadeh. Nano-niosomes as nanoscale drug delivery systems: An illustrated review. *Journal of Controlled Release*, 185:22–36, 2014.

[94] E. F. Marques, O. Regev, A. Khan, and B. Lindman. Self-organization of double-chained and pseudodouble-chained surfactants: counterion and geometry effects. *Advances in Colloid and Interface Science*, 100-102:83–104, 2003.

[95] M. C. Jennings, K. P. C. Minbiole, and W. M. Wuest. Quaternary ammonium compounds: An antimicrobial mainstay and platform for innovation to address bacterial resistance. *ACS Infectious Diseases*, 1(7):288–303, 2015.

[96] A. J. McBain, R. G. Ledder, L. E. Moore, C. E. Catrenich, and P. Gilbert. Effects of Quaternary-Ammonium-Based Formulations on Bacterial Community Dynamics and Antimicrobial Susceptibility. *Applied and Environmental Microbiology*, 70:3449–3456, 2004.

[97] N. R. Biswal and S. Paria. Wetting of PTFE and Glass Surfaces by Aqueous Solutions of Cationic and Anionic Double-Chain Surfactants. *Industrial & Engineering Chemistry Research*, 51(30):10172–10178, 2012.

[98] H. Kunieda and K. Shinoda. Solution behavior of dialkyldimethylammonium chloride in water. basic properties of antistatic fabric softeners. *The Journal of Physical Chemistry*, 82(15):1710–1714, 1978.

[99] P. Jokela, B. Joensson, and A. Khan. Phase equilibria of catanionic surfactant-water systems. *The Journal of Physical Chemistry*, 91(12):3291–3298, 1987.

[100] C. Tondre and C. Caillet. Properties of the amphiphilic films in mixed cationic/anionic vesicles: a comprehensive view from a literature analysis. *Advances in colloid and interface science*, 93(1-3):115–134, 2001.

[101] G. Bealle, J. Jestin, and D. Carriere. Osmotically induced deformation of capsid-like icosa- hedral vesicles. *Soft Matter*, 2011.

[102] C. C. Villa, N. M. Correa, J. J. Silber, F. Moyano, and R. D. Falcone. Singularities in the physicochemical properties of spontaneous AOT-BHD unilamellar vesicles in comparison with DOPC vesicles. *Physical Chemistry Chemical Physics*, 17:17112–17121, 2015.

[103] K. Manna and A. K. Panda. *Catanionic Surfactants: Novel Surrogates of Phospholipids*, chapter 83, pages 1020–1043. Wiley-Blackwell, 2016.

[104] L. R. Arriaga, D. Varade, D. Carriere, W. Drenckhan, and D. Langevin. Adsorption, Organization, and Rheology of Catanionic Layers at the Air/Water Interface. *Langmuir*, 29(10):3214–3222, 2013.

[105] X. Wang, E. J. Danoff, N. A. Sinkov, J.-H. Lee, S. R. Raghavan, and D. S. English. Highly efficient capture and long-term encapsulation of dye by catanionic surfactant vesicles. *Langmuir*, 22(15):6461–6464, 2006.

[106] N. Dew, T. Bramer, and K. Edsman. Catanionic aggregates formed from drugs and lauric or capric acids enable prolonged release from gels. *Journal of Colloid and Interface Science*, 323(2):386–394, 2008.

[107] E. F. Marques, R. O. Brito, S. G. Silva, J. E. Rodríguez-Borges, M. L. do Vale, P. Gomes, M. J. Araújo, and O. Sröderman. Spontaneous Vesicle Formation in Catanionic Mixtures of Amino Acid-Based Surfactants: Chain Length Symmetry Effects. *Langmuir*, 24(19):11009–11017, 2008.

[108] E. W. Kaler, A. K. Murthy, B. E. Rodriguez, and J. A. Zasadzinski. Spontaneous vesicle formation in aqueous mixtures of single-tailed surfactants. *Science*, 245(4924):1371–1374, 1989.

[109] L. M. Bergström, S. Skoglund, K. Edwards, J. Eriksson, and I. Grillo. Spontaneous Transformations between Surfactant Bilayers of Different Topologies Observed in Mixtures of Sodium Octyl Sulfate and Hexadecyltrimethylammonium Bromide. *Langmuir*, 30(14):3928–3938, 2014.

[110] H.-T. Jung, S. Y. Lee, E. W. Kaler, B. Coldren, and J. A. Zasadzinski. Gaussian curvature and the equilibrium among bilayer cylinders, spheres, and discs. *Proceedings of the National Academy of Sciences*, 99(24):15318–15322, 2002.

[111] H. T. Jung, B. Coldren, J. A. Zasadzinski, D. J. Iampietro, and E. W. Kaler. The origins of stability of spontaneous vesicles. *Proceedings of the National Academy of Sciences*, 98(4):1353–1357, 2001.

[112] L. L. Brasher, K. L. Herrington, and E. W. Kaler. Electrostatic Effects on the Phase Behavior of Aqueous Cetyltrimethylammonium Bromide and Sodium Octyl Sulfate Mixtures with Added Sodium Bromide. *Langmuir*, 11:4267–4277, 1995.

[113] B. Coldren, R. van Zanten, M. J. Mackel, J. A. Zasadzinski, and H.-T. Jung. From vesicle size distributions to bilayer elasticity via cryo-transmission and freeze-fracture electron microscopy. *Langmuir*, 19(14):5632–5639, 2003.

[114] M. T. Yatcilla, K. L. Herrington, L. L. Brasher, E. W. Kaler, S. Chiruvolu, and J. A. Zasadzinski. Phase Behavior of Aqueous Mixtures of Cetyltrimethylammonium Bromide (CTAB) and Sodium Octyl Sulfate (SOS). *The Journal of Physical Chemistry*, 100(14):5874–5879, 1996.

[115] E. Kaler, K. Herrington, D. Iampietro, B. Coldren, H. Jung, and J. Zasadzinski. *Mixed Surfactant Systems, 2nd ed., Revised and Expanded*, volume 124 of *Surfactant Science Series*. Marcel Dekker: New York, 2005.

[116] E. J. Danoff, X. Wang, S.-H. Tung, N. A. Sinkov, A. M. Kemme, S. R. Raghavan, and D. S. English. Surfactant vesicles for high-efficiency capture and separation of charged organic solutes. *Langmuir*, 23(17):8965–8971, 2007.

[117] C. Caillet, M. Hebrant, and C. Tondre. Sodium octyl sulfate/cetyltrimethylammonium bromide catanionic vesicles: Aggregate composition and probe encapsulation. *Langmuir*, 16(23):9099–9102, 2000.

[118] Y. Jiang, F. Li, Y. Luan, W. Cao, X. Ji, L. Zhao, L. Zhang, and Z. Li. Formation of drug/surfactant catanionic vesicles and their application in sustained drug release. *International Journal of Pharmaceutics*, 436(1):806–814, 2012.

[119] R. P. Richter, R. Bérat, and A. R. Brisson. Formation of solid-supported lipid bilayers: An integrated view. *Langmuir*, 22(8):3497–3505, 2006.

[120] A. A. Brian and H. M. McConnell. Allogeneic stimulation of cytotoxic t cells by supported planar membranes. *Proceedings of the National Academy of Sciences*, 81(19):6159–6163, 1984.

[121] R. Richter, A Mukhopadhyay, and A. Brisson. Pathways of lipid vesicle deposition on solid surfaces: A combined qcm-d and afm study. *Biophysical Journal*, 85(5):3035–3047, 2003.

[122] R. P. Richter and A. R. Brisson. Following the formation of supported lipid bilayers on mica: a study combining afm, qcm-d, and ellipsometry. *Biophysical journal*, 88(5):3422–3433, 2005.

[123] C. Lee and C. D. Bain. Raman spectra of planar supported lipid bilayers. *Biochimica et Biophysica Acta (BBA) - Biomembranes*, 1711(1):59–71, 2005.

[124] V. P. Zhdanov and B. Kasemo. Comments on Rupture of Adsorbed Vesicles. *Langmuir*, 17(12):3518–3521, 2001.

[125] G. P. Cherepanov. *Fracture: A topical encyclopedia of current knowledge*. Krieger Publishing Company, 1998.

[126] Z. V. Leonenko, A. Carnini, and D. T. Cramb. *Biochimica et Biophysica Acta*, 1509:131–147, 2000.

[127] U. Seifert. Configurations of fluid membranes and vesicles. *Advances in Physics*, 46(1):13–137, 1997.

[128] W. Helfrich. Elastic Properties of Lipid Bilayers Theory and Possible Experiments. *Zeitschrift für Naturforschung C*, 28:693–703, 1973.

[129] I. Reviakine and A. Brisson. Formation of supported phospholipid bilayers from unilamellar vesicles investigated by atomic force microscopy. *Langmuir*, 16(4):1806–1815, 2000.

[130] P. Nollert, H. Kiefer, and F. Jähnig. Lipid vesicle adsorption versus formation of planar bilayers on solid surfaces. *Biophysical Journal*, 69(4):1447–1455, 1995.

[131] J. Ekeroth, P. Konradsson, and F. Höök. Bivalent-ion-mediated vesicle adsorption and controlled supported phospholipid bilayer formation on molecular phosphate and sulfate layers on gold. *Langmuir*, 18(21):7923–7929, 2002.

[132] K. C. Weng, J. J. R. Stalgren, D. J. Duval, S. H. Risbud, and C. Frank. Fluid biomembranes Supported on Nanoporous Aerogel Xerogel Substrates. *Langmuir*, 20(17):7232–7239, 2004.

[133] P. S. Cremer and S. G. Boxer. Formation and spreading of lipid bilayers on planar glass supports. *The Journal of Physical Chemistry B*, 103(13):2554–2559, 1999.

[134] R. P. Richter, N. Maury, and A. R. Brisson. On the Effect of the Solid Support on the Interleaflet Distribution of Lipids in Supported Lipid Bilayers. *Langmuir*, 21(1):299–304, 2005.

[135] R. P. Richter, J. L. K. Him, B. Tessier, C. Tessier, and A. R. Brisson. On the kinetics of adsorption and two-dimensional self-assembly of annexin A5 on supported lipid bilayers. *Biophysical journal*, 89(5):3372–3385, 2005.

[136] T. Kunitake and Y. Okahata. A totally synthetic bilayer membrane. *Journal of the American Chemical Society*, 99(11):3860–3861, 1977.

[137] E. Feitosa, R. D. Adati, and F. R. Alves. Thermal and phase behavior of didodecyldimethylammonium bromide aqueous dispersions. *Colloids and Surfaces A: Physicochemical and Engineering Aspects*, 480:253–259, 2015.

[138] S. Manne and H. E. Gaubt. Molecular organization of surfactants at solid-liauid interfaces. *Science*, 270(5241):1480–1482, 1995.

[139] J. C. Schulz, G. G. Warr, P. D. Butler, and W. A. Hamilton. Adsorbed layer structure of cationic surfactants on quartz. *Physical Review E*, 63:041604, 2001.

[140] A. Blom, G. Warr, and A. Nelson. Structure of mixed DTAB/DDAB adsorbed layers on quartz: A neutron reflectometry and atomic force microscopy study. *Colloids and Surfaces A: Physicochemical and Engineering Aspects*, 310:1–8, 2007.

[141] L. R. Griffin, K. L. Browning, C. L. Truscott, L. A. Clifton, J. Webster, and S. M. Clarke. A comparison of didodecyldimethylammonium bromide adsorbed at mica/water and silica/water interfaces using neutron reflection. *Journal of Colloid and Interface Science*, 478:365–373, 2016.

[142] M. S. Johal, E. W. Usadi, and P. B. Davies. Coadsorption of didodecyldimethylammonium bromide and dodecan-1-ol on a hydrophobic surface studied by sum frequency spectroscopy. *Faraday Discussions*, 104:231–243, 1996.

[143] P. Dynarowics, W. Jawień, J. Miñones Trillo, N. Vila Romeu, and O. Conde Mouzo. Surface properties of didodecyldimethylammonium bromide adsorbed and spread at the water/air interface. *Journal of Colloid and Interface Science*, 174(2):518–520, 1995.

[144] E. Feitosa, F. R. Alves, A. Niemiec, M. E. C. D. Real Oliveira, E. M. S. Castanheira, and A. L. F. Baptista. Cationic Liposomes in Mixed Didodecyldimethylammonium Bromide and Dioctadecyldimethylammonium Brom-

ide Aqueous Dispersions Studied by Differential Scanning Calorimetry, Nile Red Fluorescence, and Turbidity. *Langmuir*, 22(8):3579–3585, 2006.

[145] E. F. Marques, O. Regev, A. Khan, M. da Graça Miguel, and B. Lindman. Vesicle Formation and General Phase Behavior in the Catanionic Mixture SDS-DDAB-Water. The Anionic-Rich Side. *The Journal of Physical Chemistry B*, 102(35):6746–6758, 1998.

[146] E. F. Marques, O. Regev, A. Khan, M. da Graça Miguel, and B. Lindman. Vesicle Formation and General Phase Behavior in the Catanionic Mixture SDS-DDAB-Water. The Cationic-Rich Side. *The Journal of Physical Chemistry B*, 103(39):8353–8363, 1999.

[147] Z. Liao and J. E. Pemberton. Raman spectral conformational order indicators in perdeuterated alkyl chain systems. *The Journal of Physical Chemistry A*, 110(51):13744–13753, 2006.

[148] J. Churchwell. *TIR-Raman Spectroscopy of Model Supported Lipid Bilayers*. PhD thesis, Durham University, 2014.

[149] E. Tyrode and J. Hedberg. A Comparative Study of the CD and CH Stretching Spectral Regions of Typical Surfactants Systems Using VSFS: Orientation Analysis of the Terminal CH_3 and CD_3 Groups. *The Journal of Physical Chemistry C*, 116(1):1080–1091, 2012.

[150] E. A. G. Aniansson, S. N. Wall, M. Almgren, H. Hoffmann, I. Kielmann, W. Ulbricht, R. Zana, J. Lang, and C. Tondre. Theory of the kinetics of micellar equilibria and quantitative interpretation of chemical relaxation studies of micellar solutions of ionic surfactants. *The Journal of Physical Chemistry*, 80(9):905–922, 1976.

[151] F. E. Stanley, A. M. Warner, E. Schneiderman, and A. M. Stalcup. Rapid determination of surfactant critical micelle concentrations using pressure-driven flow with capillary electrophoresis instrumentation. *Journal of chromatography. A*, 1216:8431–8434, 2009.

[152] M. S. Akhter. Effect of acetamide on the critical micelle concentration of aqueous solutions of some surfactants. *Colloids and Surfaces A: Physicochemical and Engineering Aspects*, 121(2):103–109, 1997.

[153] R. G. Snyder, S. L. Hsu, and S. Krimm. Vibrational spectra in the CH stretching region and the structure of the polymethylene chain. *Spectrochimica Acta Part A: Molecular Spectroscopy*, 34(4):395–406, 1978.

[154] S. Segota, S. Heimer, and D. Tezak. New catanionic mixtures of dodecyldimethylammonium bromide/sodium dodecylbenzenesulphonate/water: I. surface properties of dispersed particles. *Colloids and Surfaces A: Physicochemical and Engineering Aspects*, 274(1):91–99, 2006.

[155] M. Cardenas, H. Wacklin, R. A. Campbell, and T. Nylander. Structure of DNA-Cationic Surfactant Complexes at Hydrophobically Modified and Hydrophilic Silica Surfaces as Revealed by Neutron Reflectometry. *Langmuir*, 27:12506–12514, 2011.

[156] B. H. Bijsterbosch. Characterization of silica surfaces by adsorption from solution. investigations into the mechanism of adsorption of cationic surfactants. *Journal of Colloid and Interface Science*, 47(1):186–198, 1974.

[157] Y. Gao, J. Du, and T. Gu. Hemimicelle formation of cationic surfactants at the silica gel-water interface. *J. Chem. Soc., Faraday Trans. 1*, 83:2671–2679, 1987.

[158] P. Somasundaran and D. W. Fuerstenau. Mechanisms of alkyl sulfonate adsorption at the alumina-water interface. *The Journal of Physical Chemistry*, 70(1):90–96, 1966.

[159] E. Tyrode, M. W. Rutland, and C. D. Bain. Adsorption of CTAB on Hydrophilic Silica Studied by Linear and Nonlinear Optical Spectroscopy. *Journal of the American Chemical Society*, 130(51):17434–17445, 2008.

[160] C. J. Orendorff, M. W. Ducey, and J. E. Pemberton. Quantitative Correlation of Raman Spectral Indicators in Determining Conformational Order in Alkyl Chains. *The Journal of Physical Chemistry A*, 106(30):6991–6998, 2002.

[161] M. Heskins and J. E. Guillet. Solution Properties of Poly(*N*-isopropylacrylamide). *Journal of Macromolecular Science: Part A - Chemistry*, 2(8):1441–1455, 1968.

[162] A. Larsson, D. Kuckling, and M. Schönhoff. 1H NMR of thermoreversible polymers in solution and at interfaces: the influence of charged groups on the phase transition. *Colloids and Surfaces A: Physicochemical and Engineering Aspects*, 190(1):185–192, 2001.

[163] J Spěváček. Phase Separation in Aqueous Polymer Solutions as Studied by NMR Methods. *Macromolecular Symposia*, 222(1):1–14, 2005.

[164] F. M. Winnik, M. F. Ottaviani, S. H. Bossman, W. Pan, M. Garcia-Garibay, and N. J. Turro. Phase separation of poly(*N*-isopropylacrylamide) in water: a spectroscopic study of a polymer tagged with a fluorescent dye and a spin label. *The Journal of Physical Chemistry*, 97(49):12998–13005, 1993.

[165] H. Ohta, I. Ando, S. Fujishige, and K. Kubota. Molecular motion and 1H NMR relaxation of aqueous poly(*N*-isopropylacrylamide) solution under high pressure. *Journal of Polymer Science Part B: Polymer Physics*, 29(8):963–968, 1991.

[166] C. Wu and X. Wang. Globule-to-Coil Transition of a Single Homopolymer Chain in Solution. *Physical Review Letters*, 80:4092–4094, 1998.

[167] G. Zhang and C. Wu. The Water/Methanol Complexation Induced Reentrant Coil-to-Globule-to-Coil Transition of Individual Homopolymer Chains in

Extremely Dilute Solution. *Journal of the American Chemical Society*, 123(7):1376–1380, 2001.

[168] C. Wu. A comparison between the "coil-to-globule" transition of linear chains and the "volume phase transition" of spherical microgels. *Polymer*, 39(19):4609–4619, 1998.

[169] K. Kubota, S. Fujishige, and I. Ando. Single-chain transition of poly(*N*-isopropylacrylamide) in water. *The Journal of Physical Chemistry*, 94(12):5154–5158, 1990.

[170] K. Kubota, S. Fujishige, and I. Ando. Solution Properties of Poly(*N*-isopropylacrylamide) in Water. *Polymer Journal*, 22:15, January 1990.

[171] X. Wang, X. Qiu, and C. Wu. Comparison of the Coil-to-Globule and the Globule-to-Coil Transitions of a Single Poly(*N*-isopropylacrylamide) Homopolymer Chain in Water. *Macromolecules*, 31(9):2972–2976, 1998.

[172] S. Fujishige, K. Kubota, and I. Ando. Phase transition of aqueous solutions of poly(*N*-isopropylacrylamide) and poly(*N*-isopropylmethacrylamide). *The Journal of Physical Chemistry*, 93(8):3311–3313, 1989.

[173] Z. Tong, F. Zeng, X. Zheng, and T. Sato. Inverse Molecular Weight Dependence of Cloud Points for Aqueous Poly(*N*-isopropylacrylamide) Solutions. *Macromolecules*, 32(13):4488–4490, 1999.

[174] Y. Ding, X. Ye, and G. Zhang. Microcalorimetric Investigation on Aggregation and Dissolution of Poly(*N*-isopropylacrylamide) Chains in Water. *Macromolecules*, 38(3):904–908, 2005.

[175] Y. Xia, N. A. D. Burke, and H. D. H. Stöver. End Group Effect on the Thermal Response of Narrow-Disperse Poly(*N*-isopropylacrylamide) Prepared by Atom Transfer Radical Polymerization. *Macromolecules*, 39(6):2275–2283, 2006.

[176] F. M. Winnik. Fluorescence studies of aqueous solutions of poly(*N*-isopropylacrylamide) below and above their LCST. *Macromolecules*, 23(1):233–242, 1990.

[177] R. Walter, J. Rička, C. Quellet, R. Nyffenegger, and T. Binkert. Coil-Globule Transition of Poly(*N*-isopropylacrylamide): A Study of Polymer-Surfactant Association. *Macromolecules*, 29(11):4019–4028, 1996.

[178] Y. Maeda, T. Nakamura, and I. Ikeda. Changes in the Hydration States of Poly(*N*-*n*-propylmethacrylamide) and Poly(*N*-isopropylmethacrylamide) during Their Phase Transitions in Water Observed by FTIR Spectroscopy. *Macromolecules*, 34(23):8246–8251, 2001.

[179] Y. Katsumoto, T. Tanaka, H. Sato, and Y. Ozaki. Conformational Change of Poly(*N*-isopropylacrylamide) during the Coil-Globule Transition Investigated by Attenuated Total Reflection/Infrared Spectroscopy and Density Functional Theory Calculation. *The Journal of Physical Chemistry A*, 106(14):3429–3435, 2002.

[180] Y. Maeda, T. Higuchi, and I. Ikeda. Change in Hydration State during the Coil-Globule Transition of Aqueous Solutions of Poly(*N*-isopropylacrylamide) as Evidenced by FTIR Spectroscopy. *Langmuir*, 16(19):7503–7509, 2000.

[181] A. Percot, X. X. Zhu, and M. Lafleur. A simple FTIR spectroscopic method for the determination of the lower critical solution temperature of *N*-isopropylacrylamide copolymers and related hydrogels. *Journal of Polymer Science Part B: Polymer Physics*, 38(7):907–915, 2000.

[182] T. Terada, T. Inaba, H. Kitano, Y. Maeda, and N. Tsukida. Raman spectroscopic study on water in aqueous solutions of temperature-responsive polymers: Poly(*N*-isopropylacrylamide) and poly[*N*-(3-ethoxypropyl)acrylamide]. *Macromolecular Chemistry and Physics*, 195(9):3261–3270, 1994.

[183] Y. Maeda, H. Yamamoto, and I. Ikeda. Phase Separation of Aqueous Solutions of Poly(*N*-isopropylacrylamide) Investigated by Confocal Raman Microscopy. *Macromolecules*, 36(14):5055–5057, 2003.

[184] F. Tanaka. *Polymer Physics: Applications to Molecular Association and Thermoreversible Gelation*. Cambridge University Press, 2011.

[185] W.J. Moore. *Basic Physical Chemistry*. Prentice-Hall, NJ, 1983.

[186] C. K. Chee, S. Rimmer, I. Soutar, and L. Swanson. Time-resolved fluorescence anisotropy studies of the temperature-induced intramolecular conformational transition of poly(*N*-isopropylacrylamide) in dilute aqueous solution. *Polymer*, 38(2):483–486, 1997.

[187] Y. Okada and F. Tanaka. Cooperative Hydration, Chain Collapse, and Flat LCST Behavior in Aqueous Poly(*N*-isopropylacrylamide) Solutions. *Macromolecules*, 38(10):4465–4471, 2005.

[188] A. Halperin, M. Kröger, and F. M. Winnik. Poly(*N*-isopropylacrylamide) Phase Diagrams: Fifty Years of Research. *Angewandte Chemie International Edition*, 54(51):15342–15367, 2015.

[189] X. Zhou, J. Li, C. Wu, and B. Zheng. Constructing the Phase Diagram of an Aqueous Solution of Poly(*N*-isopropyl acrylamide) by Controlled Microevaporation in a Nanoliter Microchamber. *Macromolecular Rapid Communications*, 29(16):1363–1367, 2008.

[190] H. G. Schild, M. Muthukumar, and D. A. Tirrell. Cononsolvency in mixed aqueous solutions of poly(*N*-isopropylacrylamide). *Macromolecules*, 24(4):948–952, 1991.

[191] F. M. Winnik, M. F. Ottaviani, S. H. Bossmann, W. Pan, M. Garcia-Garibay, and N. J. Turro. Cononsolvency of poly(*N*-isopropylacrylamide): a look at spin-labeled polymers in mixtures of water and tetrahydrofuran. *Macromolecules*, 26(17):4577–4585, 1993.

[192] G. Dalkas, K. Pagonis, and G. Bokias. Control of the lower critical solution temperature-type cononsolvency properties of poly(*N*-isopropylacrylamide) in water-dioxane mixtures through copolymerisation with acrylamide. *Polymer*, 47:243–248, 2006.

[193] S. Hirotsu. Critical points of the volume phase transition in *N*-isopropylacrylamide gels. *The Journal of Chemical Physics*, 88(1):427–431, 1988.

[194] C. M. Mukherji, D.and Marques and K. Kremer. Polymer collapse in miscible good solvents is a generic phenomenon driven by preferential adsorption. *Nature Communications*, 5:4882, 2014.

[195] F. Rodríguez-Ropero, T. Hajari, and N. F. A. van der Vegt. Mechanism of Polymer Collapse in Miscible Good Solvents. *The Journal of Physical Chemistry B*, 119(51):15780–15788, 2015.

[196] A. Pica and G. Graziano. An alternative explanation of the cononsolvency of poly(*N*-isopropylacrylamide) in water-methanol solutions. *Physical Chemistry Chemical Physics*, 18:25601–25608, 2016.

[197] Y. Katsumoto, T. Tanaka, K. Ihara, M. Koyama, and Y. Ozaki. Contribution of Intramolecular C=O···H-N Hydrogen Bonding to the Solvent-Induced Reentrant Phase Separation of Poly(*N*-isopropylacrylamide). *The Journal of Physical Chemistry B*, 111(44):12730–12737, 2007.

[198] J. Dybal, M. Trchová, and P. Schmidt. The role of water in structural changes of poly(*N*-isopropylacrylamide) and poly(*N*-isopropylmethacrylamide) studied by FTIR, Raman spectroscopy and quantum chemical calculations. *Vibrational Spectroscopy*, 51(1):44–51, 2009.

[199] Y. Tang, Y. Ding, and G. Zhang. Role of Methyl in the Phase Transition of Poly(*N*-isopropylmethacrylamide). *The Journal of Physical Chemistry B*, 112(29):8447–8451, 2008.

[200] B. Sun, Y. Lin, P. Wu, and H. W. Siesler. A FTIR and 2D-IR Spectroscopic Study on the Microdynamics Phase Separation Mechanism of the Poly(*N*-isopropylacrylamide) Aqueous Solution. *Macromolecules*, 41(4):1512–1520, 2008.

[201] M. Füllbrandt, E. Ermilova, A. Asadujjaman, R. Hölzel, F. F. Bier, R. von Klitzing, and A. Schönhals. Dynamics of Linear Poly(*N*-isopropylacrylamide) in Water around the Phase Transition Investigated by Dielectric Relaxation Spectroscopy. *The Journal of Physical Chemistry B*, 118(13):3750–3759, 2014.

[202] J. Zhang and R. Pelton. The dynamic behavior of poly(*N*-isopropylacrylamide) at the air/water interface. *Colloids and Surfaces A: Physicochemical and Engineering Aspects*, 156(1):111–122, 1999.

[203] K. N. Plunkett, X. Zhu, J. S. Moore, and D. E. Leckband. PNIPAM Chain Collapse Depends on the Molecular Weight and Grafting Density. *Langmuir*, 22(9):4259–4266, 2006.

[204] H. Yim, M. S. Kent, S. Satija, S. Mendez, S. S. Balamurugan, S. Balamurugan, and G. P. Lopez. Study of the conformational change of poly(*N*-isopropylacrylamide)-grafted chains in water with neutron reflection: Molecular weight dependence at high grafting density. *Journal of Polymer Science Part B: Polymer Physics*, 42(17):3302–3310, 2004.

[205] N. Ishida and S. Biggs. Effect of Grafting Density on Phase Transition Behavior for Poly(*N*-isopropylacryamide) Brushes in Aqueous Solutions Studied by AFM and QCM-D. *Macromolecules*, 43(17):7269–7276, 2010.

[206] B.-C. Choi, S. Choi, and D. E. Leckband. Poly(*N*-isopropyl acrylamide) Brush Topography: Dependence on Grafting Conditions and Temperature. *Langmuir*, 29(19):5841–5850, 2013.

[207] H. Tang, B. Zhang, and P. Wu. On the two-step phase transition behavior of the Poly(*N*-isopropylacrylamide) (PNIPAM) brush: different zones with different orders. *Soft Matter*, 10:7278–7284, 2014.

[208] J. Zhao, J. Shan, G. Van Assche, H. Tenhu, and B. Van Mele. Demixing and Remixing Kinetics in Aqueous Dispersions of Poly(*N*-isopropylacrylamide) (PNIPAM) Brushes Bound to Gold Nanoparticles Studied by Means of Modulated Temperature Differential Scanning Calorimetry. *Macromolecules*, 42(14):5317–5327, 2009.

[209] J. Zhang, H. Chen, L. Xu, and Y. Gu. The targeted behavior of thermally responsive nanohydrogel evaluated by NIR system in mouse model. *Journal of Controlled Release*, 131(1):34–40, 2008.

[210] Y.-Z. You, K. K. Kalebaila, S. L. Brock, and D. Oupický. Temperature-Controlled Uptake and Release in PNIPAM-Modified Porous Silica Nanoparticles. *Chemistry of Materials*, 20(10):3354–3359, 2008.

[211] L. C. C. Elliott, B. Jing, B. Akgun, Y. Zhu, P. W. Bohn, and S. K. Fullerton-Shirey. Loading and Distribution of a Model Small Molecule Drug in Poly(*N*-isopropylacrylamide) Brushes: a Neutron Reflectometry and AFM Study. *Langmuir*, 29(10):3259–3268, 2013.

[212] H. Yamauchi and Y. Maeda. LCST and UCST Behavior of Poly(*N*-isopropylacrylamide) in DMSO/Water Mixed Solvents Studied by IR and Micro-Raman Spectroscopy. *The Journal of Physical Chemistry B*, 111(45):12964–12968, 2007.

[213] Y. Tsuboi, M. Nishino, and N. Kitamura. Laser-Induced Reversible Volume Phase Transition of a Poly(*N*-isopropylacrylamide) Gel Explored by Raman Microspectroscopy. *Polymer Journal*, 40:367, March 2008.

[214] Z. Ahmed, E. A. Gooding, K. V. Pimenov, L. Wang, and S. A. Asher. UV Resonance Raman Determination of Molecular Mechanism of Poly(*N*-Isopropylacrylamide) Volume Phase Transition. *The Journal of Physical Chemistry. B*, 113(13):4248–4256, 2009.

[215] N. S. Myshakina, Z. Ahmed, and S. A. Asher. Dependence of Amide Vibrations on Hydrogen Bonding. *The Journal of Physical Chemistry B*, 112(38):11873–11877, 2008.

[216] M. G. Sainant, K. Kunimatsu, R. Viswanathan, H. Seki, C. Pacchioni, P. S. Bagus, and M. R. Philpott. In situ vibrational spectroscopy of adsorbed thiocyanate on silver electrodes: Experiment and theory. *Langmuir*, 1987.

[217] X. Chen, T. Yang, S. Kataoka, and P. S. Cremer. Specific Ion Effects on Interfacial Water Structure near Macromolecules. *Journal of the American Chemical Society*, 129(40):12272–12279, 2007.

[218] J. Huang and A. Heise. Stimuli responsive synthetic polypeptides derived from N-carboxyanhydride (NCA) polymerisation. *Chemical Society Reviews*, 42:7373–7390, 2013.

[219] Y. Shen, Z. Li, and H.-A. Klok. Polypeptide brushes grown via surface-initiated ring-opening polymerization of α-amino acid *N*-carboxyanhydrides. *Chinese Journal of Polymer Science*, 33(7):931–946, Jul 2015.

[220] J. D. Lunn and D. F. Shantz. Peptide Brush-Ordered Mesoporous Silica Nanocomposite Materials. *Chemistry of Materials*, 21(15):3638–3648, 2009.

[221] Y.-C. Chang and C. W. Frank. Vapor Deposition-Polymerization of α-Amino Acid *N*-Carboxy Anhydride on the Silicon(100) Native Oxide Surface. *Langmuir*, 14(2):326–334, 1998.

[222] R. H. Wieringa, E. A. Siesling, P. F. M. Geurts, P. J. Werkman, E. J. Vorenkamp, V. Erb, M. Stamm, and A. J. Schouten. Surface Grafting of Poly(l-glutamates). 1. Synthesis and Characterization. *Langmuir*, 17(21):6477–6484, 2001.

[223] N. H. Lee and C. W. Frank. Surface-Initiated Vapor Polymerization of Various α-Amino Acids. *Langmuir*, 19(4):1295–1303, 2003.

[224] X. Wang, H. Gan, T. Sun, B. Su, H. Fuchs, D. Vestweber, and S. Butz. Stereochemistry triggered differential cell behaviours on chiral polymer surfaces. *Soft Matter*, 6:3851–3855, 2010.

[225] X. Wang, H. Gan, M. Zhang, and T. Sun. Modulating Cell Behaviors on Chiral Polymer Brush Films with Different Hydrophobic Side Groups. *Langmuir*, 28(5):2791–2798, 2012.

[226] M. M. Li, G. Y. Qing, M. X. Zhang, and T. L. Sun. Chiral polymer-based biointerface materials. *Science China Chemistry*, 57(4):540–551, 2014.

[227] J. Sun and R. N. Zuckermann. Peptoid Polymers: A Highly Designable Bioinspired Material. *ACS Nano*, 7(6):4715–4732, 2013.

[228] M. Schneider, C. Fetsch, I. Amin, R. Jordan, and R. Luxenhofer. Polypeptoid Brushes by Surface-Initiated Polymerization of N-Substituted Glycine *N*-Carboxyanhydrides. *Langmuir*, 29(23):6983–6988, 2013.

[229] J. Luijten, E. J. Vorenkamp, and A. J. Schouten. Reversible Helix Sense Inversion in Surface-Grafted Poly(β-phenethyl-l-aspartate) Films. *Langmuir*, 23(21):10772–10778, 2007.

[230] C.-T. Yang, Y. Wang, and Y.-C. Chang. Effect of Solvents and Temperature on the Conformation of Poly(β-benzyl-l-aspartate) Brushes. *Biomacromolecules*, 11(5):1308–1313, 2010.

[231] C.-T. Yang, Y. Wang, S. Yu, and Y.-C. I. Chang. Controlled Molecular Organization of Surface Macromolecular Assemblies Based on Stimuli-Responsive Polypeptide Brushes. *Biomacromolecules*, 10(1):58–65, 2009.

[232] R. H. Wieringa and A. J. Schouten. Oriented Thin Film Formation by Surface Graft Polymerization of γ-Methyl l-Glutamate *N*-Carboxyanhydride in the Melt. *Macromolecules*, 29(8):3032–3034, 1996.

[233] A. Heise, H. Menzel, H. Yim, M. D. Foster, R. H. Wieringa, A. J. Schouten, V. Erb, and M. Stamm. Grafting of Polypeptides on Solid Substrates by Initiation of *N*-Carboxyanhydride Polymerization by Amino-Terminated Self-Assembled Monolayers. *Langmuir*, 13(4):723–728, 1997.

[234] Y. Wang and Y. C. Chang. Synthesis and Conformational Transition of Surface-Tethered Polypeptide: Poly(l-lysine). *Macromolecules*, 36(17):6511–6518, 2003.

[235] J. Wang, M. I. Gibson, R. Barbey, S.-J. Xiao, and H.-A. Klok. Nonfouling Polypeptide Brushes via Surface-initiated Polymerization of N^{ϵ}-oligo(ethylene glycol)succinate-L-lysine *N*-carboxyanhydride. *Macromolecular Rapid Communications*, 30(9-10):845–850, 2009.

[236] K. Itoh and G. D. Fasman. Poly(L-valine). Conformational dependence on the degree of polymerization: Infrared studies. *Biopolymers*, 14(8):1755–1767, 1975.

[237] L. Burman, P. Tandon, V. D. Gupta, S. Rastogi, and S. Srivastava. Heat capacity and normal modes of poly (l-valine) in relation to spectra of oligovalines. *Biopolymers*, 38(1):53–67, 1996.

[238] R. H. Wieringa, E. A. Siesling, P. J. Werkman, H. J. Angerman, E. J. Vorenkamp, and A. J. Schouten. Surface Grafting of Poly(l-glutamates). 2. Helix Orientation. *Langmuir*, 17(21):6485–6490, 2001.

[239] Z. Xu, Y. Feng, X. Liu, M. Guan, C. Zhao, and H. Zhang. Synthesis and characterization of Fe_3O_4@SiO_2@poly-l-alanine, peptide brush–magnetic microspheres through NCA chemistry for drug delivery and enrichment of BSA. *Colloids and Surfaces B: Biointerfaces*, 81(2):503 – 507, 2010.

[240] J. L. Koenig and P. L. Sutton. Raman scattering of some synthetic polypeptides: Poly(γ-benzyl L-glutamate), poly-L-leucine, poly-L-valine, and poly-L-serine. *Biopolymers*, 10(1):89–106, 1971.

[241] M. C. Chen and R. C. Lord. Laser-excited Raman spectroscopy of biomolecules. VI. Polypeptides as conformational models. *Journal of the American Chemical Society*, 96(15):4750–4752, 1974.

[242] G. D. Fasman, K. Itoh, C. S. Liu, and R. C. Lord. Laser-Raman spectroscopy of biomolecules. XI. Conformational study of poly(L-valine) and copolymers of L-valine and L-alanine. *Biopolymers*, 17(1):125–143, 1978.

[243] T. Akaike, S. Inoue, and K. Itoh. Conformaion of poly(DL-valine) obtained by the polymerization of the *N*-carboxy anhydride. *Biopolymers*, 15(9):1863–1868, 1976.

[244] J. A. Lima, P. T. C. Freire, R. J. C. Lima, A. J. D. Moreno, J. Mendes Filho, and F. E. A. Melo. Raman scattering of L-valine crystals. *Journal of Raman Spectroscopy*, 36(11):1076–1081, 2005.

[245] G. Zhu, G. Zhu, Q. Fan, and X. Wan. Raman spectra of amino acids and their aqueous solutions. *Spectrochimica Acta Part A: Molecular and Biomolecular Spectroscopy*, 78(3):1187–1195, 2011.

[246] L. Whitmore and B. A. Wallace. DICHROWEB, an online server for protein secondary structure analyses from circular dichroism spectroscopic data. *Nucleic Acids Research*, 32(suppl2):W668–W673, 2004.

[247] L. B. Sagle, Y. Zhang, V. A. Litosh, X. Chen, Y. Cho, and P. S. Cremer. Investigating the hydrogen-bonding model of urea denaturation. *Journal of the American Chemical Society*, 131(26):9304–9310, 2009.

[248] Z. M. O. Rzaev, S. Dinçer, and E. Pişkin. Functional copolymers of *N*-isopropylacrylamide for bioengineering applications. *Progress in Polymer Science*, 32(5):534–595, 2007.

[249] P. Schattling, F. D. Jochum, and P. Theato. Multi-stimuli responsive polymers – the all-in-one talents. *Polym. Chem.*, 5:25–36, 2014.

[250] C. M. Schilli, M. Zhang, E. Rizzardo, S. H. Thang, Y. K. Chong, K. Edwards, G. Karlsson, and A. H. E. Müller. A New Double-Responsive Block Copolymer Synthesized via RAFT Polymerization: Poly(*N*-isopropylacrylamide)-block-poly(acrylic acid). *Macromolecules*, 37(21):7861–7866, 2004.

[251] M. Ebara, M. Yamato, M. Hirose, T. Aoyagi, A. Kikuchi, K. Sakai, and T. Okano. Copolymerization of 2-Carboxyisopropylacrylamide with *N*-Isopropylacrylamide Accelerates Cell Detachment from Grafted Surfaces by Reducing Temperature. *Biomacromolecules*, 4(2):344–349, 2003.

[252] S. Y. Kim, S. M. Cho, Y. M. Lee, and S. J. Kim. Thermo- and pH-responsive behaviors of graft copolymer and blend based on chitosan and *N*-isopropylacrylamide. *Journal of Applied Polymer Science*, 78(7):1381–1391, 2000.

[253] M. D. C. Topp, P. J. Dijkstra, H. Talsma, and J. Feijen. Thermosensitive Micelle-Forming Block Copolymers of Poly(ethylene glycol) and Poly(*N*-isopropylacrylamide). *Macromolecules*, 30(26):8518–8520, 1997.

[254] L-Q. Wang, K. Tu, Y. Li, J. Zhang, L. Jiang, and Z. Zhang. Synthesis and characterization of temperature responsive graft copolymers of dextran with poly(*N*-isopropylacrylamide). *Reactive and Functional Polymers*, 53(1):19 – 27, 2002.

[255] F. Kohori, K. Sakai, T. Aoyagi, M. Yokoyama, Y. Sakurai, and T. Okano. Preparation and characterization of thermally responsive block copolymer micelles comprising poly(*N*-isopropylacrylamide-*b*-dl-lactide). *Journal of Controlled Release*, 55(1):87–98, 1998.

[256] J. Virtanen and H. Tenhu. Thermal Properties of Poly(*N*-isopropylacrylamide)-*g*-poly(ethylene oxide) in Aqueous Solutions: Influence of the Number and Distribution of the Grafts. *Macromolecules*, 33(16):5970–5975, 2000.

[257] F. A. Plamper, A. A. Steinschulte, C. H. Hofmann, N. Drude, O. Mergel, C. Herbert, M. Erberich, B. Schulte, R. Winter, and W. Richtering. Toward Copolymers with Ideal Thermosensitivity: Solution Properties of Linear, Well-Defined Polymers of *N*-Isopropyl Acrylamide and *N*,*N*-Diethyl Acrylamide. *Macromolecules*, 45(19):8021–8026, 2012.

[258] M. Moglianetti, J. R. P. Webster, S. Edmondson, S. P. Armes, and S. Titmuss. Neutron Reflectivity Study of the Structure of pH-Responsive Polymer Brushes Grown from a Macroinitiator at the Sapphire-Water Interface. *Langmuir*, 26(15):12684–12689, 2010.

[259] E. B. Zhulina and O. V. Borisov. Polyelectrolytes Grafted to Curved Surfaces. *Macromolecules*, 29(7):2618–2626, 1996.

[260] S. Sanjuan, P. Perrin, N. Pantoustier, and Y. Tran. Synthesis and Swelling Behavior of pH-Responsive Polybase Brushes. *Langmuir*, 23(10):5769–5778, 2007.

[261] V. Bütün, S. P. Armes, and N. C. Billingham. Synthesis and aqueous solution properties of near-monodisperse tertiary amine methacrylate homopolymers and diblock copolymers. *Polymer*, 42(14):5993–6008, 2001.

[262] F. A. Plamper, M. Ruppel, A. Schmalz, O. Borisov, M. Ballauff, and A. H. E. Müller. Tuning the Thermoresponsive Properties of Weak Polyelectrolytes: Aqueous Solutions of Star-Shaped and Linear Poly(*N*,*N*-dimethylaminoethyl Methacrylate). *Macromolecules*, 40(23):8361–8366, 2007.

[263] M. Thomas, M. Gajda, C. Amiri Naini, S. Franzka, M. Ulbricht, and N. Hartmann. Poly(*N*,*N*-dimethylaminoethyl methacrylate) Brushes: pH-Dependent Switching Kinetics of a Surface-Grafted Thermoresponsive Polyelectrolyte. *Langmuir*, 31(49):13426–13432, 2015.

[264] A. Jia, H.and Wildes and S. Titmuss. Structure of pH-Responsive Polymer Brushes Grown at the Gold–Water Interface: Dependence on Grafting Density and Temperature. *Macromolecules*, 45(1):305–312, 2012.

[265] S. H. Yuk, S. H. Cho, and S. H. Lee. pH/Temperature-Responsive Polymer Composed of Poly((*N*,*N*-dimethylamino)ethyl methacrylate-co-ethylacrylamide). *Macromolecules*, 30(22):6856–6859, 1997.

[266] S. G. Boyes, W. J. Brittain, X. Weng, and S. Z. D. Cheng. Synthesis, Characterization, and Properties of ABA Type Triblock Copolymer Brushes of Styrene and Methyl Acrylate Prepared by Atom Transfer Radical Polymerization. *Macromolecules*, 35(13):4960–4967, 2002.

[267] W. Huang, J.-B. Kim, G. L. Baker, and M. L. Bruening. Preparation of amphiphilic triblock copolymer brushes for surface patterning. *Nanotechnology*, 14(10):1075, 2003.

[268] D. Cunliffe, C. de las Heras Alarcón, V. Peters, J. R. Smith, and C. Alexander. Thermoresponsive Surface-Grafted Poly(*N*-isopropylacrylamide) Copolymers: Effect of Phase Transitions on Protein and Bacterial Attachment. *Langmuir*, 19(7):2888–2899, 2003.

[269] X. Wang, S. Yan, L. Song, H. Shi, H. Yang, S. Luan, Y. Huang, J. Yin, A. F. Khan, and J. Zhao. Temperature-Responsive Hierarchical Polymer Brushes Switching from Bactericidal to Cell Repellency. *ACS Applied Materials & Interfaces*, 9(46):40930–40939, 2017.

[270] C. Xu, T. Wu, C. M. Drain, J. D. Batteas, M. J. Fasolka, and K. L. Beers. Effect of Block Length on Solvent Response of Block Copolymer Brushes: Combinatorial Study with Block Copolymer Brush Gradients. *Macromolecules*, 39(9):3359–3364, 2006.

[271] K. Nagase, J. Kobayashi, A. Kikuchi, Y. Akiyama, H. Kanazawa, and T. Okano. Protein separations via thermally responsive ionic block copolymer brush layers. *RSC Advances*, 6:26254–26263, 2016.

[272] K. J. Thomas, M. Sheeba, V. P. N. Nampoori, C. P. G. Vallabhan, and P. Radhakrishnan. Raman spectra of polymethyl methacrylate optical fibres excited by a 532 nm diode pumped solid state laser. *Journal of Optics A: Pure and Applied Optics*, 10(5):055303, 2008.

[273] Y. Maeda, H. Yamauchi, and T. Kubota. Confocal Micro-Raman and Infrared Spectroscopic Study on the Phase Separation of Aqueous Poly(2-(2-methoxyethoxy)ethyl (meth)acrylate) Solutions. *Langmuir*, 25(1):479–482, 2009.